Electronic properties of graphene heterostructures below 1K

A thesis submitted to the University of Manchester
for the degree of Doctor of Philosophy
in the Faculty of Science and Engineering

2022

Julien Barrier

Department of Physics and Astronomy
in the School of Natural Sciences

Blank page

Contents

Part II Experimental methods

Word count: 43533

Symbols & abbreviations

For more precise definition, refer to the page numbers indicated in brackets.

a graphene's lattice constant, 0.246 nm. (49)

$\mathcal{A}$ area, m^2.

B magnetic field, T.

B_0 magentic field with 1 flux piercing a characteristic area, T. (78)

B^* maximum magnetic field supporting ABS, T. (46)

B_{focusing} magnetic field required to focus electrons, T. (33)

C_{g} gate capacitance, µF. (73)

$\mathcal{D}$ diffusion constant, $\mathrm{cm}^2\,\mathrm{s}^{-1}$.

D electric displacement field, $\mathrm{V\,cm}^{-1}$. (74)

e electronic charge, $1.6 \times 10^{-19}\,\mathrm{C}$.

E electric field, $\mathrm{V\,m}^{-1}$. (25)

E_{f} Fermi energy, eV.

E_{J} Josephson energy, eV. (40)

E_{n} nth Landau level energy, eV (35)

E_{Th} Thouless energy, eV. (39)

$f(E)$ Fermi-Dirac distribution. (26)

G conductance, S. (30)

g degererancy factor.

h Planck constant, $6.63 \times 10^{-34}\,\mathrm{J\,s}$.

$\hbar$ reduced Planck constant $= h/2\pi$ =$1.05 \times 10^{-34}\,\mathrm{J\,s}$.

I current, A.

j current density, $\mathrm{A\,cm}^{-1}$. (26)

j_{c} critical current for a Fermi liquid, $\mathrm{A\,cm}^{-1}$.

j_{s} critical current density in a Josephson junction, $\mathrm{A\,cm}^{-1}$. (40)

J_{S} critical current spatial density, $\mathrm{A\,cm}^{-1}$ (81)

k_{B} Boltzmann constant, $= 1.38 \times 10^{-23}\,\mathrm{J\,K}^{-1}$

k_{f} Fermi wavenumber, cm^{-1}. (26)

ℓ mean free path, cm. (28)

l_{B} magnetic length, nm. (34)

L device length, cm. (30)
L_{E} characteristic length of the superconducting proximity effect, cm. (39)
m effective mass, kg.
m_{c} cyclotron mass, kg. (34)
n gate-induced electron density, cm^{-2}. (72)
n_0 density of secondary Dirac points, cm^{-2}. (77)
n_{BZF} effective electron density for Brown-Zak fermions, cm^{-2}. (112)
n_{c} electron density per Landau level, cm^{-2}. (35)
n_{H} Hall density, $= -B/e\rho_{\mathrm{xy}}$, cm^{-2}.
n_{s} electron density in the 2DEG, cm^2
$\mathcal{N}_{\mathrm{s}}$ density of states, $= m/\pi\hbar^2$.
p momentum, $\mathrm{kg\,m\,s}^{-1}$.
p number of flux penetrating a number of unit cell (see q). (106)
q number of superlattice unit cells penetrated by p fluxes. (106)
R resistance, Ω.
R_{b} resistance in the bend geometry. (32)
r_{c} cyclotron radius, m.
R_{n} normal resistance, Ω. (64)
T temperature, K.
T transmission coefficient of propagating modes. (31)
Tr transmission coefficient of a junction (64)
v_{f} Fermi velocity, $\mathrm{cm\,s}^{-1}$. (28)
v_{d} drift velocity, $\mathrm{cm\,s}^{-1}$. (25)
V voltage drop, V.
V_{H} Hall voltage, V. (30)
V_{x} longitudinal voltage, V. (30)
V_{n} voltage step of the nth Shapiro step, V. (46)
W device width, cm. (30)
δ moiré lattice mismatch. (75)
Δ bandgap, eV.
Δ superconducting gap, eV. (40)
ε_s energy in the Dirac cone eV. (51)
Λ effective length of electron-hole trajectories in a Josephson junction, cm. (41)
λ_{f} Fermi wavelength, cm. (45)
λ_{j} Josephson penetration depth, cm.(45)
λ_{sl} superlattice periodicity, nm. (76)
μ mobility, $\mathrm{cm}^2\,\mathrm{V}^{-1}\,\mathrm{s}^{-1}$. (27)
ν Landau filling index. (36)
ξ characteristic length scale, cm.
ξ_0 superconducting coherence length, cm. (38)
ξ_{n} thermal coherence length, cm. (39)

φ superconducting phase difference. (40)
ϕ_0 flux quantum, $= h/e$ for electrons and $= h/2e$ for Cooper pairs.
ρ sheet resistivity, Ω.
ρ_{xx} longitudinal resistivity, Ω. (29)
ρ_{xy} Hall resistivity, Ω. (29)
σ conductivity, S.
σ_{xx} longitudinal conductivity, S.
$\sigma_{xy} = \sigma_H$ Hall conductivity, S.
τ_m momentum relaxation time, s. (25)
$\omega_c/2\pi$ cyclotron frequency, s^{-1}. (34)

2DEG two-dimensional electron gas (25)
ABS Andreev bound states (41)
AR Andreev reflection (39)
BZF Brown-Zak fermions (105)
CAES Chiral Andreev edge states (65)
DP Dirac point (57)
hBN hexagonal boron nitride
LL Landau Level (35)
QHE Quantum Hall effect (36)
mtBG minimally twisted bilayer graphene
MA-tBG magic-angle twisted bilayer graphene
MAR multiple Andreev reflection (80)
MC mixing chamber (92)
NS normal metal - superconductor junction (38)
NP neutrality point (51)
SdHO Shubnikov-de Haas oscillations (35)
SQUID Superconducting quantum interference device (43)
tBG twisted bilayer graphene
tDBG twisted double bilayer graphene
tMBG twisted monolayer-bilayer graphene (146)
vdW van der Waals
vHS van Hove singularity (59)

List of devices measured

A number of devices were emasured in this thesis. This list enumerates different devices and fabrication parameters.

Table 0.1: List of graphene devices

	substrate	type	width (µm)	Fabricated by
G1	SiO_2	monolayer	4	Shuigang Xu
G2	hBN	bilayer	2	Shuigang Xu

Table 0.2: List of graphene superlattices

	width (µm)	angle (°)	gate capacitance (µF m^{-2})	Fabricated by
D1	17	0.4	101	Piran Kumaravadivel
D2	4	0	98	Matthew Holwill
D3	3	0.2	104	Na Xin
D4	3.2	0.5	96	Na Xin
D5	2	0.2	106	Roman Gorbachev
D6	2	0.3	98	Na Xin

Table 0.3: List of Josephson junctions

	SC	metal	length (nm)	width (µm)	N_{DW} [a]	Fabricated by
Ja	Nb	graphene	300	7	0	Moshe Ben Shalom
Jb	Nb	bilayer graphene	400	4	0	Moshe Ben Shalom
J1	NbTi	mtBG	200	1.5	1	Na Xin
J2	NbTi	mtBG	100	4	multiple	Na Xin
J3	NbTi	mtBG	150	1.5	2	Na Xin
J4	NbTi	mtBG	150	2	1	Na Xin
J5	NbTi	mtBG	150	0.5	8	Piran Kumaravadivel
J6	NbTi	mtBG	150	0.3	1	Piran Kumaravadivel
J7	NbTi	mtBG	150	4	6	Na Xin
J8	NbTi	bilayer graphene	100	1	0	Na Xin

[a] N_{DW} denotes the number of domain walls between two superconducting electrodes, for the case of minimally twisted bilayer graphene (mtBG).

Table 0.4: List of twisted monolayer-bilayer graphene (tMBG) devices

	twist angle (°)	width (µm)	Fabricated by
M1	1.22	1	Shuigang Xu
M2	1.47	1.5	Shuigang Xu
M3	1.30	2	Shuigang Xu
M4	0.99	5	Na Xin
M5	1.18	1	Shuigang Xu
M6	1.20	1	Shuigang Xu
M7	1.26	1.4	Shuigang Xu
M8	1.41	1.2	Shuigang Xu
M9	1.60	2.5	Nila Balakrishnan

Table 0.5: List of twisted multilayer devices

	N_{layers}	twist angle (°)	width (µm)	Fabricated by
S1	4	1.25, 10, 0.4		Shuigang Xu
S2	2	1.23		Shuigang Xu

List of Publications

The work presented in this thesis has been the subject of the following publications:

1. Y. Shi, S. Xu, Y. Yang, S. Slizovskiy, S. V. Morozov, S.-K. Son, S. Ozdemir, C. Mullan, J. Barrier, J. Yin, A. I. Berdyugin, B. A. Piot, T. Taniguchi, K. Watanabe, V. I. Fal'ko, K. S. Novoselov, A. K. G. Geim, and A. Mishchenko, *Electronic Phase Separation in Multilayer Rhombohedral Graphite*, Nature **584**, 210 (2020).
   JB's contribution: performed transport measurements, discussed results and reviewed the manuscript.
2. J. Barrier, P. Kumaravadivel, R. Krishna-Kumar, L. A. Ponomarenko, N. Xin, M. Holwill, C. Mullan, M. Kim, R. V. Gorbachev, M. D. Thompson, J. R. Prance, T. Taniguchi, K. Watanabe, I. V. Grigorieva, K. S. Novoselov, A. Mishchenko, V. I. Fal'ko, A. I. Berdyugin, and A. K. Geim, *Long-Range Ballistic Transport of Brown-Zak Fermions in Graphene Superlattices*, Nature Communications **11**, 5756 (2020).
   JB's contribution: performed transport measurements, analysed all data, discussed results and wrote the paper.
3. S. Xu, M. M. Al Ezzi, N. Balakrishnan, A. Garcia-Ruiz, B. Tsim, C. Mullan, J. Barrier, N. Xin, B. A. Piot, T. Taniguchi, K. Watanabe, A. Carvalho, A. Mishchenko, A. K. Geim, V. I. Fal'ko, S. Adam, A. H. Castro Neto, K. S. Novoselov, and Y. Shi, *Tuneable Van Hove Singularities and Correlated States in Twisted Monolayer-Bilayer Graphene*, Nature Physics (2021)
   JB's contribution: performed transport measurements, discussed results and reviewed the manuscript. Additional data were measured and analysed as part of this project. They were not published but presented in this thesis.
4. J. Barrier et al, *Proximity superconductivity in artificial quantum Hall edges - in preparation*
   JB's contribution: performed all measurements, analysed all data, discussed results and wrote the manuscript.
5. J. Barrier et al, *Screening-induced superconductivity in twisted multilayer graphene - in preparation*
   JB's contribution: performed transport measurements, analysed data, discussed results and wrote the manuscript.

Abstract

The past fifteen years have witnessed a dramatic evolution of condensed matter physics as a new class of materials has been explored: two-dimensional materials. These are extracted from layered crystals and thinned down to the atomic layer, revealing new electronic properties absent in the parent crystal. Graphene was the first of these two-dimensional materials to be extracted and remained the most studied as it is truly unique with a linear electronic dispersion hosting Dirac fermions, an anomalous quantum Hall effect and a valley degree of freedom to name a few. The development of graphene research and fabrication techniques enabled the creation of van der Waals heterostructures consisting of multiple two-dimensional sheets stacked together. These heterostructures can combine two different materials assembled in a chosen sequence to create stacks with designer properties. It is also possible to misalign the two lattices by a twist angle θ to create electronic properties unseen in nature. This thesis explores the electronic properties of van der Waals heterostructures made of graphene and hexagonal boron nitride (hBN) with different twist angles at cryogenic temperatures. The twist angles enable several properties based on the long-range superlattice period and the electronic hybridisation between two neighbouring electronic bands.

The experimental work consists of two parts. First, I study the effect of the superlattice potential on electronic properties. I present long-range superlattices with periods of more than 10 nm by aligning a graphene layer with hBN. This length scale is 100 times larger than the lattice constant of the parent graphene and can be made comparable with the magnetic length at high magnetic fields. In high-quality graphene superlattices in high magnetic fields, I explore the regime of Brown-Zak fermions. I find that they have ballistic motion and measure their degeneracy. Additionally, I present the superconducting proximity effect in superlattices made by stacking two graphene sheets at small angles. This kind of heterostructures is subject to strain-induced reconstruction, resulting in large domains separated by narrow conduction channels that are topologically protected against backscattering. The resulting proximity ef-

fect is found to withstand extremely high magnetic fields and is attributed to Andreev bound states propagating in the narrow domain walls.

The second part focuses on the band hybridisation occurring when two layers are stacked at a singular angle. I present twisted monolayer-bilayer graphene, a system in which the C_2 and time-reversal symmetries are spontaneously broken. I explore the correlated insulators created by band flattening and study the asymmetry relative to perpendicular electric fields applied to the layer. I also probe these flat bands under strong electric fields, shifting the Fermi surface out of equilibrium and study the interplay of high drift velocities with narrow bandwidths. Finally, I explore the effect of high twist angles on strong correlations. These high twists allow screening of electron-electron interactions. I notably observe the emergence of superconductivity as a result of band flattening driven by Coulomb screening. I explore this regime's limitations when the Fermi velocity becomes comparable to the superconducting condensate velocity.

Declaration

No portion of the work referred to in this thesis has been submitted in support of an application for another degree or qualification at this or any other university or other institute of learning.

Copyright Statement

Acknowledgements

During the past four years, I have received help from many people; I would like to take this opportunity to express my gratitude. First, I want to thank my supervisor Prof. Andre Geim who welcomed me into his lab and tirelessly continues to impulse research directions. Andre has a unique — optimistic — method of doing science, rapidly moving from project to project, scouting the field and selecting promising directions as they arise. Andre persuaded me that there is no better way to figure out if something is achievable or not than by trying hands-on; in these circumstances, theory would be of little help. I hope I could acquire a portion of his exceptional physical intuition and way of conducting experiments. Of course, I am grateful to him for constantly reminding me that there are no bad samples; there are only bad students (only about 5 % of the samples measured in the past four years are presented in this thesis).

Andre has been successful at attracting and retaining brilliant researchers around him. I want to thank Prof. Volodya Fal'ko, Prof. Irina Grigorieva, Prof. Artem Mishchenko and Prof. Kostya Novoselov. They have always been happy to discuss results and measurement techniques. Likewise, I am grateful for Dr Alexey Berduygin, who taught me the rudiments of electronic transport. Our knowledge and experience expanded as we measured devices and saw unexpected curves as they appeared on the screen. Working with you was a true pleasure.

This thesis would not have been possible without the talented individuals fabricating the devices I have been measuring: Prof. Rashid Jalil, Dr Piranavan Kumaravadivel, Dr David Perello, Dr Zefei Wu, Dr Na Xin, Dr Shuigang Xu and Dr Yaping Yang. Other dedicated physicists have contributed to acquiring data and discussing new physics: Dr Minsoo Kim, Ciaran Mullan, Dr Yanmeng Shi and Dr Jun Yin. Special thanks should be given to my collaborators at Lancaster University, who provided indispensable help with dilution refrigeration, thermometry and noise reduction: Dr Leonid Ponomarenko, Dr Jonathan Prance and Dr Michael Thompson. Likewise, the support from a

few theoreticians helped advance our understanding. I want to acknowledge the contribution of Dr Angelika Knothe and Dr Sergey Slizovskiy.

Technicians belong to a group of people without which research would not be possible. Special thanks to Dominic McCullagh and Mark Sellers, who relentlessly provide all the support and maintenance on cryogenic equipment in the Schuster building and Chris Hyde, Chris Livingston, and Dr Kunal Lulla in the National Graphene Institute (NGI). I also need to acknowledge the work of Polly Greensmith, Charlotte Hooson-Sykes and John Whittaker for their help in administrative processes. I would also like to thank Prof Roman Gorbachev and Dr Andrey Kretinin. They let me use their experimental facilities on the first floor of NGI and welcomed me into their weekly group meetings. These have been inspirational.

Dr Sylvain Gilat and Prof. Jean-François Joanny at ESPCI did their PhD with Nobel laureates (Lehn and De Gennes, respectively). They gave me invaluable advice before joining Manchester. I am grateful for their recommendations. Of course, a PhD would not be that fun without friends to share good times, celebrate papers, successful vivas, birthdays or anything that is deemed to be. On top of all those cited earlier, I would like to thank Bayo Akinpelu, Dr Adrian Ceferino, Dr Victor Hugo Guarochico-Moreira, Dr Sasha Kazantsev, Dr Roshan Krishna-Kumar, Dr Wenjun Kuang, Dr Tom Lane, Dr Lucas Mogg, Yulia Nikonova, Dr Servet Ozdemir, Pietro Steiner, Dr Harry Warring, Dr Astrid Weston, Dr Qian Yang and Dr Johana Zultak.

Finally, I thank my girlfriend, Maria Khan, for her endless patience. Thank you for supporting me during the most stressful parts!

The United Kingdom's Engineering and Physical Sciences Research Council (EPSRC-UK) supported this work.

Chapter 1
Introduction

The student I was at ESPCI Paris would categorise physics into two distinct areas: the microscopic and the macroscopic worlds. The microscopic world contains the building block of matter, such as molecules, atoms and electrons: objects that cannot be seen directly. These systems contain a sufficiently small number of excitation quanta that they should be described by the laws of quantum physics. Their wavelength and phase entirely define the behaviour of these excitations. The macroscopic world contains objects that can be seen with our eyes and would obey general intuition. They are generally described by the laws of classical physics or at least can be treated as semi-classical systems. For example, in usual — macroscopic — solid-state systems, electronic bands will be only filled up to a maximum energy: the Fermi energy and electrical conduction occurs because of the partial filling of the topmost band. This Fermi energy is associated with a maximum wavevector k_F, thus with a minimum wavelength $\lambda_\mathrm{F} = 2\pi/k_\mathrm{F}$. As only the electrons with energies close to the Fermi energy contribute to the conduction, the relevant length scale in a macroscopic metal will be λ_F, experimentally unreachable. Consequently, the translational invariance of the lattice leads to the formation of Bloch bands with a finite number of electronic states available per band [1–3]. Here the wavelength and phase of individual excitations have no importance in measurable phenomena.

There is, however, an intermediary area: *mesoscopic physics*, introduced in the 1980s, motivated by the need to miniaturise components in the electronic industry, shaping the advent of nanotechnology. Although they contain a very large number of atoms or electrons, mesoscopic systems are so small that they only host a few relevant excitations around equilibrium, so that their behaviour can be described as quantum mechanical. This is counterintuitive in systems that look dirty, messy, and jumbled with grubby leads connected to measurement instruments obeying the laws of classical physics, inevitably inducing decoherence. In these mesoscopic systems, the relevant length scale is usually a correlation length ξ like the mean free path — the distance an electron travels before its momentum is destroyed — or the phase relaxation length — the distance an electron travels before its phase is destroyed. Under

these length scales, the spectrum of excitations is discrete; therefore, the phase is preserved, and interference effects can be measured. Both these length scales can reach a few dozens of micrometres, allowing interference effects [4–6].

The most notable example of electron interference effects in mesoscopic systems is the behaviour of a ring-shaped conductor in a small magnetic field, the so-called Aharonov-Bohm effect [7]. Figure 1.1 shows the first example of such an electron interferometer, consisting of a ring that allows the current to pass through both arms from the top to the lower contact. In this system, electrons travelling along a path l acquire a phase shift $\Delta\varphi$ that can be obtained from the vector potential A: $\Delta\varphi = (e/\hbar)\int A \cdot \mathrm{d}l$. Notably, it can be derived that the phase difference is determined by the total magnetic flux ϕ enclosed in the area of the ring $\mathcal{A}$:

$$\Delta\varphi = \frac{e}{\hbar} B\mathcal{A} = 2\pi\frac{\phi}{\phi_0}, \tag{1.1}$$

where $\phi_0 = h/e$ is the *flux quantum*. Here the phase $\Delta\varphi$ is called the Aharonov-Bohm phase. As the magnetic field is changed, a set of magnetoresistance oscillations develop with a periodicity in multiples of ϕ_0 [6–9] (see fig 1.1). Although Aharonov and Bohm predicted this effect in 1959 [7], the development of controlled growth and advanced optical or electron-beam lithography techniques only allowed to create the small structures required for these observations in the 1980s. This spread in multiple research directions, including quantised conductance of quantum point contacts, quantum Hall effects (integer and fractional, superconductor and normal-super combination including Josephson junctions, Coulomb blockade and single-electron transistors, tunnelling cyclotron resonance, Gantmakher and Weiss oscillations to name a few [4–14]. The quantum Hall effect, discovered in 1980 [15], is another characteristic effect of mesoscopic physics where external electric and magnetic fields allow significant system manipulation. Applying a perpendicular magnetic field to a 2D electron gas allows the discretisation of the spectrum into a series of energy levels, opening a window into the basic properties of a given system. The exfoliation of graphene from pyrolitic graphite crystals in 2004 gave a new impetus to the field, as it introduced new opportunities to create 2D ballistic systems with an even larger number of experimentally tunable parameters. This new 2D age transformed the landscape of fundamental research in physics, allowing the demonstration of a wide variety of phenomena: Hall effects, valley physics, chiral quasiparticles, superfluidity, etc.

When I started my PhD, graphene research had already evolved into a vast field, with the peak already reached. Researchers had already mastered the art of exfoliating other 2D materials and stacking them together to create designer materials not found in nature [16–18]. All the low-hanging fruits of these so-called *van der Waals heterostructures* had already been harvested. That was without counting on the physics of Moiré superlattices that had just boomed.

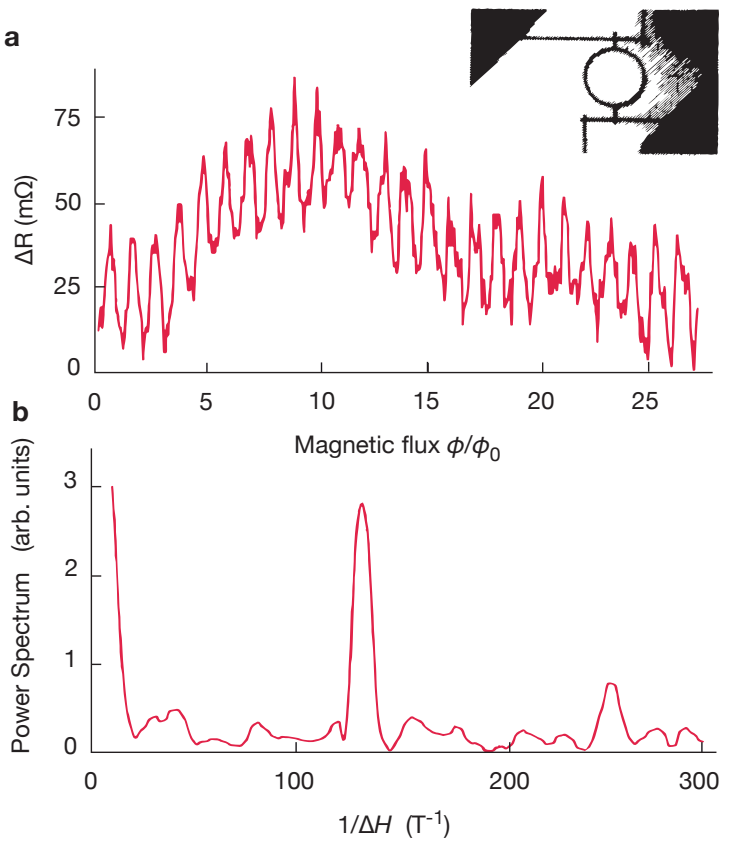

Fig. 1.1 Aharonov-Bohm interferences **a)** Magnetoresistance of the ring at T =10 mK. Inset: picture of the ring, inside diameter is 784 nm. **b** Fourier power spectrum containing peaks at h/e and $h/2e$. Data extracted from ref. [9]

Instead of stacking 2D materials like LEGO bricks, improvements in fabrication procedures allowed to add a twist between two layers, opening refreshing opportunities for fundamental physics owing to the delicate interplay between long-range effects from the superlattice and interlayer hybridisation. The most influential of these emergents effects is probably the discovery of correlated insulators and superconductivity when two graphene sheets are stacked together with a 1.05° twist. However, there are less impressive but nonetheless exciting results that can still be discovered. I hope this thesis gives a blueprint on some of the directions now within experimental reach. The energy of mesoscopic systems is discrete. Thermal energy may broaden these levels and smear all measurable effects. In order to prevent this, we shall pay particular attention to lowering the thermal energy $k_{\mathrm{B}}T$ below the characteristic energy of the excitations we are probing. As such, my investigations made use of a dilution refrigerator to measure electronic properties at temperatures in the order of 10 mK.

This thesis is organised as follows. Part I is a literature review of mesoscopic physics in graphene. It is composed of two chapters. **Chapter 2** is an introduction to mesoscopic transport. Here, I discuss diffusive and ballistic 2D electron gas and introduce experimental results on Josephson junctions. **Chapter 3** introduces graphene and graphene-based van der Waals heterostructure as a rich experimental platform. I discuss the main results from the literature. Part II is focused on experimental technicalities: **chapter 4** introduces measurement techniques of van der Waals heterostructures, encompassing the geometry of Hall bars, extraction of twist angles, gate capacitances and other device param-

eters. Reconstruction of the critical current spatial density in Josephson junctions is discussed. **Chapter 5** introduces low temperature measurements. As I have been in charge of maintaining and incrementally improving a dilution refrigerator, I discuss the main techniques to achieve electronic temperatures below 300 mK. The knowledgeable reader may skip parts I and II, although I hope newcomers to the field find value in them. Parts III and IV develop the results of my research, encompassing respectively the long-range superlattice effects created by a moiré potential and the interlayer hybridisation from interacting electrons resulting in correlation phenomena in which the Coulomb energy dominates over the quenched kinetic energy. **Chapter 6** introduces a family of ballistic quasiparticles, the Brown-Zak fermions, emerging at high magnetic fields due to the Aharonov-Bohm phase acquired in a superlattice. **Chapter 7** explores the quantisation of Brown-Zak fermions in small effective magnetic fields and their degeneracy. These two chapters present results published in ref. [19]. **Chapter 8** explores the consequences of inducing superconductivity in a moiré superlattice via the *proximity effect*. I engineered a supercurrent in quantum Hall states on the boundary of moiré domains similar to superconductivity in the quantum spin Hall regime, where each 1D channel can carry its own supercurrent. The results from this chapter are currently being prepared for publication. These three chapters discuss results that can be treated with a non-interacting single-particle picture. The following two chapters deal with phenomena originating when electron-electron interactions dominate their kinetic energy. **Chapter 9** introduces twisted monolayer-bilayer graphene as a new platform for studying strongly correlated systems. Van Hove singularities and the phase diagram are discussed. Some of these results were published as part of ref. [20]. **Chapter 10** presents superconductivity and screening effects in a 4-layer graphene heterostructure. These last two chapters contain data that have not been published by a lack of sufficient understanding of the underlying mechanisms. **Appendix A** details the fabrication of van der Waals heterostructures, a subject I have only treated in the first few months of this PhD.

Part I
Electronic transport in graphene

Blank page

Chapter 2
Mesoscopic transport

This chapter presents the basic properties of two-dimensional electron gas and the consequences of diffusive and ballistic transport on mesoscopic transport. A second part of the chapter focuses on superconductivity and the Josephson effect. The goal here is to provide enough background to understand the following chapters.

2.1 Properties of diffusive 2DEGs

This section describes the properties of a two-dimensional electron gas (2DEG) in the diffusive limit. Low scattering rates can be achieved in these systems —a fortiori graphene. The mobility at low temperature is a direct measurement of the momentum relaxation time that is limited only by impurities and defects. The mobility allows for a quantification of the defect concentration.

2.1.1 Drift velocity

At equilibrium, the conduction electrons of a 2DEG move randomly in all directions, resulting in a null current. If one applies an electric field $\boldsymbol{E}$ parallel to the plane of this 2DEG, electrons acquire a drift velocity $\boldsymbol{v}_\mathrm{d}$ in the direction of the force $e\boldsymbol{E}$ where e is the electron charge. In a steady state, the rate at which an electron receives momentum from the external electric field is equal to the rate at which it loses momentum $\boldsymbol{p}$ due to scattering forces and the drift velocity is defined as:

$$\boldsymbol{v}_\mathrm{d} = -\frac{e\boldsymbol{E}\tau_\mathrm{m}}{m}, \tag{2.1}$$

where m is the effective mass, and τ_m is the momentum relaxation time. One may rewrite equation 2.1 as $\boldsymbol{v}_\mathrm{d} = -\mu_\mathrm{e}\boldsymbol{E}$ where μ_e is the electron mobility defined as $\mu_\mathrm{e} = e\tau_\mathrm{m}/m$; together with the electron density n_s, it would

allow determining the Drude conductivity [4–6]. The current density $\boldsymbol{j}$ in a homogeneous conductor writes:

$$\boldsymbol{j} = e n_\mathrm{s} \boldsymbol{v}_\mathrm{d}. \tag{2.2}$$

Therefore, by rewriting eq. 2.2 with 2.1, one finds

$$\boldsymbol{j} = \frac{n_\mathrm{s} e^2 \tau_\mathrm{m}}{m} \boldsymbol{E} \equiv \sigma \boldsymbol{E}. \tag{2.3}$$

with σ the conductivity. That is an expression of Ohm's law.

Since all electrons acquire the same average drift velocity, this picture would suggest that the current induced by the electric field is carried by all the conduction electrons. At low temperatures, this is a misleading picture: the states that are more than a few times the thermal energy $k_\mathrm{B}T$ below the Fermi energy E_f are all filled; the energy of a conduction electron deep inside the Fermi sea (shown as the shaded blue area in figure 2.1) cannot change; only the electrons whose energies are close to E_f can contribute to the conductivity and vary from the Fermi-Dirac distribution: distribution of electrons among those at energies close to E_f can be different from the equilibrium Fermi-Dirac distribution $f(E)$.

$$f(E) = \frac{1}{1 + \exp\left[(E - E_\mathrm{f})/k_\mathrm{B}T\right]}. \tag{2.4}$$

An easier way to picture this is shown in figure 2.1: deep inside the Fermi sea ($k \ll k_\mathrm{f}$), nothing much happens when $k_\mathrm{d} < k_\mathrm{f}$ with k_f the Fermi wavenumber (in the linear regime): the states were occupied without the electric field and remain full upon application of the electric field. It is only near $\pm k_\mathrm{f}$ that empty states become filled or empty as a result of $\boldsymbol{E}$. From a single particle point of view, the electric field results in a drift velocity on all electrons; from a collective point of view, only the electrons between $-k_\mathrm{f}$ and $+k_\mathrm{f}$ move.

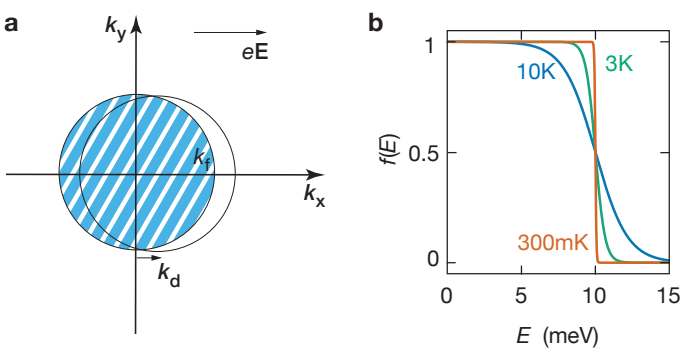

Fig. 2.1 Fermi sea. a) All states within a circle of radius k_f (shaded blue) are occupied at equilibrium. Under an electric field, the circle is shifted in the direction of $e\boldsymbol{E}$. **b)** Calculated Fermi-Dirac distribution at 0.3 K, 3 K and 10 K (orange, greend and blue lines, resp.) for E_f =10 meV representing the probability for an energy to be occupied.

Therefore the current is non-zero only within a few $k_{\mathrm{B}}T$ of the Fermi energy E_{f}: to understand the conduction properties at low temperature, a common simplification consists in studying the dynamics of electrons having energies close to the Fermi energy E_{f}.

Consequently, the current density can reflect the collective behaviour as follows:

$$\boldsymbol{j} = e\left(n_{\mathrm{s}}\frac{v_{\mathrm{d}}}{v_{\mathrm{f}}}\right)\boldsymbol{v}_{\mathrm{f}}. \tag{2.5}$$

Only a tiny fraction of the total electrons ($n_{\mathrm{s}}v_{\mathrm{d}}/v_{\mathrm{f}}$), those moving at the Fermi velocity, are able to carry the current.

2.1.2 Mobility

The mobility μ is the ratio of the drift velocity to the electric field:

$$\mu = \left|\frac{\boldsymbol{v}_{\mathrm{d}}}{\boldsymbol{E}}\right| = \frac{e\tau_{\mathrm{m}}}{m} = \frac{\sigma}{en_{\mathrm{s}}} \tag{2.6}$$

As described in section 6.2, the mobility can easily be measured in Hall bars, so it is a primary characterisation tool for 2DEGs — or, more generally, semiconducting and metallic films. Once the mobility is known, the momentum relaxation time τ_{m} can easily be deduced. In usual semiconductors, the momentum relaxation time increases with decreasing temperature due to the suppression of phonon scattering. However when impurity scattering is the dominant relaxation mechanism, the mobility remains constant as the temperature decreases. The sum of the drift current density $-\sigma\boldsymbol{E}/e$ and the diffusion current density $-D\nabla n_{\mathrm{s}}$ vanish in thermodynamic equilibrium ($\nabla\mu_{\mathrm{EC}} = 0$). At zero temperature, the electrochemical potential μ_{EC} is spatially constant:

$$\nabla\mu_{\mathrm{EC}} = e\boldsymbol{E} + \mathcal{N}_{\mathrm{s}}(E_{\mathrm{f}})^{-1}\nabla n_{\mathrm{s}} = 0. \tag{2.7}$$

Here $\mathcal{N}_{\mathrm{s}}(E)$ represents the density of states, this leads to the Einstein relation between the conductivity σ and the Fermi level properties.

$$\sigma = e^2\mathcal{N}_{\mathrm{s}}(E_{\mathrm{f}})\mathcal{D}. \tag{2.8}$$

Here $\mathcal{D}$ is a 2D diffusion constant. It is found by combining equations 2.6 and 2.8:

$$\mathcal{D} = \frac{n\mu}{e\mathcal{N}_{\mathrm{s}}(E_{\mathrm{f}})} = \frac{1}{2}v_{\mathrm{f}}^2\tau_{\mathrm{m}}, \tag{2.9}$$

where v_{f} is the Fermi velocity and τ_{m} the momentum relaxation time.

2.1.3 Mean free path

In a perfect crystal in the absence of electron-phonon and electron-electron interactions, the collective motion of electrons is similar to the diffusive behaviour of an ideal gas, where interactions between particles are negligible. Effects of the lattice and electron interactions do not appear in the usual equations describing the dynamics of electrons in the conduction band [4–6], although they are responsible for scattering and change of momentum. Instead, the interacting liquid is described by elementary excitations or quasiparticles. One uses the same equations to describe the system but incorporates interactions' effects into an effective mass m assumed to be spatially constant [3].

In the Drude model, the momentum relaxation time τ_m is related to the collision time τ_c with a relation of the form $1/\tau_\mathrm{m} \to \alpha_\mathrm{m}/\tau_\mathrm{c}$, where α_m is a number between 0 and 1 and denotes how effective is an individual collision in destroying momentum [4]. If collisions happen such that electrons are scattered only by a small angle, α_m is small, and the momentum relaxation time is much longer than the collision time. The mean free path ℓ is defined as the distance an electron travels before its initial momentum is destroyed:

$$\ell = v_\mathrm{f}\tau_\mathrm{m}, \tag{2.10}$$

where v_f is the Fermi velocity, given by:

$$v_\mathrm{f} = \frac{\hbar k_\mathrm{f}}{m} = \frac{\hbar}{m}\sqrt{\pi n_\mathrm{s}}. \tag{2.11}$$

It corresponds to the velocity of the fastest electrons moving near $T = 0$, that is, the velocity corresponding to a kinetic energy equal to the Fermi energy. The mean free path is given by:

$$\ell = \sigma\frac{\hbar}{e^2}\sqrt{\frac{\pi}{n_\mathrm{s}}}. \tag{2.12}$$

The Fermi velocity can reach $2 \times 10^7\,\mathrm{cm\,s^{-1}}$ for n_s =$5 \times 10^{11}\,\mathrm{cm^{-2}}$. Consequently, assuming a momentum relaxation time τ_m =100 ps, one obtains a mean free path ℓ =30 µm. This distance can be comparable to the size of mesoscopic devices. This will be detailed in section 6.2.

2.1.4 Transport in weak magnetic fields

As stated in section 2.1.2, Hall measurements are one of the most basic yet principal tools to characterise 2D materials. It enables us to deduce the carrier density n_s and mobility μ independently.

When a magnetic field B is applied to a 2DEG, a Lorentz force creates an electric field perpendicular to both the current and the magnetic field. As a result, the conductivity σ and the resistivity ρ become tensors:

$$\frac{m\boldsymbol{v_d}}{\tau_m} = e\left(\boldsymbol{E} + \boldsymbol{v_d} \times \boldsymbol{B}\right), \tag{2.13}$$

that is:

$$\begin{pmatrix} m/e\tau_m & -B \\ B & m/e\tau_m \end{pmatrix} \begin{pmatrix} v_x \\ v_y \end{pmatrix} = \begin{pmatrix} E_x \\ E_y \end{pmatrix}. \tag{2.14}$$

Here v_x and v_y are the x and y-components of the drift velocity, respectively, and E_x and E_y are the electric field components. From equation 2.2 one gets:

$$\begin{pmatrix} m/e\tau_m & -B \\ B & m/e\tau_m \end{pmatrix} \begin{pmatrix} j_x/en_s \\ j_y/en_s \end{pmatrix} = \begin{pmatrix} E_x \\ E_y \end{pmatrix}, \tag{2.15}$$

with j_x and j_y, the components of $\boldsymbol{j}$. This results in:

$$\begin{pmatrix} E_x \\ E_y \end{pmatrix} = \sigma^{-1} \begin{pmatrix} 1 & -\mu B \\ \mu B & 1 \end{pmatrix} \begin{pmatrix} j_x \\ j_y \end{pmatrix}, \tag{2.16}$$

with the conductivity and mobility defined earlier: $\sigma = en_s\mu$ and $\mu = e\tau_m/m$. Equally, a resistivity tensor can be defined from the relation:

$$\begin{pmatrix} E_x \\ E_y \end{pmatrix} = \begin{pmatrix} \rho_{xx} & \rho_{xy} \\ \rho_{yx} & \rho_{xx} \end{pmatrix} \begin{pmatrix} j_x \\ j_y \end{pmatrix}. \tag{2.17}$$

This yields the classical result for the longitudinal resistivity

$$\rho_{xx} = \sigma^{-1}, \tag{2.18}$$

and the Hall resistivity:

$$\rho_{yx} = -\rho_{xy} = \frac{\mu B}{\sigma} = \frac{B}{en_s}. \tag{2.19}$$

This is derived from the Drude model: the longitudinal resistance ρ_{xx} should be constant at low magnetic fields, while the Hall resistance ρ_{xy} increases linearly with the magnetic field. Note that ρ_{xy} depends only on n_s, the carrier density, but not on other parameters like the scattering time. For this reason, the Hall effect is a valuable experiment for measuring the density of carriers and the sign of their charges (electron or hole-like, e.g.).

Experimentally, the resistivity tensor can be measured from a *Hall bar* device, prepared as a rectangular sample, with a set uniform current flowing along the x-direction (see fig 2.2). Acquisition of the longitudinal voltage $V_x = V_1 - V_2$ allows one to obtain the longitudinal resistance and that of the transverse voltage $V_H = V_2 - V_3$, the Hall resistance.

Since the sample is assumed homogeneous, $j_y = 0$, one can write:

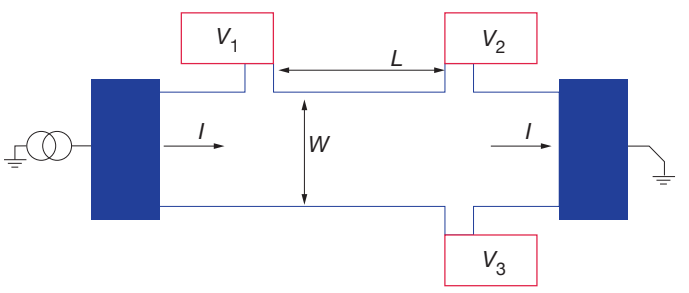

Fig. 2.2 Rectangular Hall bar (width W, length L) used for magnetoresistance measurement. The magnetic field is in the z-direction, perpendicular to the $x-y$ plane. Source and drain contacts are depicted as navy-filled rectangles; voltage probes contacts as red rectangles.

$$E_\mathrm{x} = \rho_\mathrm{xx} j_\mathrm{x} \qquad \text{and} \qquad E_\mathrm{y} = \rho_\mathrm{xy} j_\mathrm{x}. \tag{2.20}$$

It immediately follows that $I = j_\mathrm{x} W$ and $V_\mathrm{x} = E_\mathrm{x} L$ and $V_\mathrm{H} = E_\mathrm{y} W$, with L and W the device length and width, respectively. Therefore resistivities ρ_xx and ρ_xy can be expressed as a function of the longitudinal and transverse voltages:

$$\rho_\mathrm{xx} = \frac{V_\mathrm{x}}{I}\frac{W}{L} \qquad \text{and} \qquad \rho_\mathrm{xy} = \frac{V_\mathrm{H}}{I}. \tag{2.21}$$

Finally, it is easy to obtain the carrier density n_s and mobility μ from the low field longitudinal and Hall resitivities using equations 2.22 and 2.23

$$n_\mathrm{s} = \left(e\frac{\mathrm{d}\rho_\mathrm{yx}}{\mathrm{d}B}\right)^{-1} = \frac{I/e}{\mathrm{d}V_\mathrm{H}/\mathrm{d}B}, \tag{2.22}$$

and

$$\mu = \frac{1}{e n_\mathrm{s} \rho_\mathrm{xx}} = \frac{I/e}{n_\mathrm{s} V_\mathrm{x} W/L}. \tag{2.23}$$

2.2 Ballistic transport

2.2.1 Conductance

It appears here that the conductance G is an easily accessible quantity through measurements, as it relates the total current to the voltage drop: $I = GV$, while the conductivity relates the local current density to the electric field $\boldsymbol{j} = \sigma \boldsymbol{E}$. For large and homogeneous 2DEG, the conductance and conductivity are related through the width W and length L of the sample:

$$\sigma = G\frac{W}{L}. \tag{2.24}$$

This formula is valid as long as W and L are much larger than the mean free path ℓ, i.e. in the diffusive transport regime(see fig. 2.3). The ballistic transport

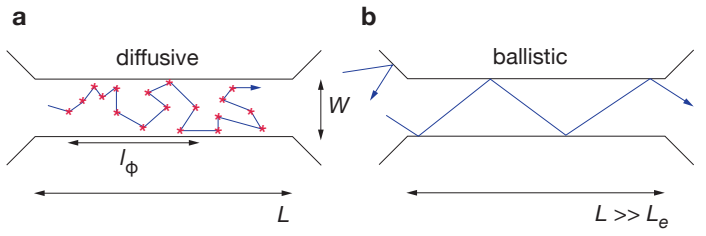

Fig. 2.3 Electron trajectories (blue arrows) for diffusive (a) and ballistic (b) transport regimes. Red dots correspond to sacttering centres. Taken from [6]

regime is reached when the device quality is improved so that $\ell > L > W$. Here only the conductance plays a role; it can be found using the Landauer formula [4–6] for one propagating mode:

$$G = \frac{e^2}{h} T. \tag{2.25}$$

Here T is the transmission probability of propagating modes at the Fermi level (also referred to as quantum channels). In this equation, the conductance does not depend on the sample length; therefore, the conductivity loses its meaning.

In the ballistic regime, the sample is so clean and temperature low enough that the momentum relaxation does not occur inside the conductor; the scattering of electrons at the sample boundaries limits the current, rather than impurity scattering. The consequence is that the Einstein relation 2.8 between the conductivity and the diffusion constant at the Fermi level, is no longer applicable in that form. The Landauer formula is an alternative relationship between the conductance and is a Fermi level property of the sample.

A perfect conductor's resistance originates from (i) the limited number of current-carrying modes and (ii) the mismatch between the number of modes in the conductor and the contacting leads. An essential consequence is that conductance becomes a quantised physical quantity, as depicted in figure 2.4. Here I show the conductance of a GaAs nanoconstriction measured as a function of gate voltage V_g, a parameter enabling control of the constriction's open

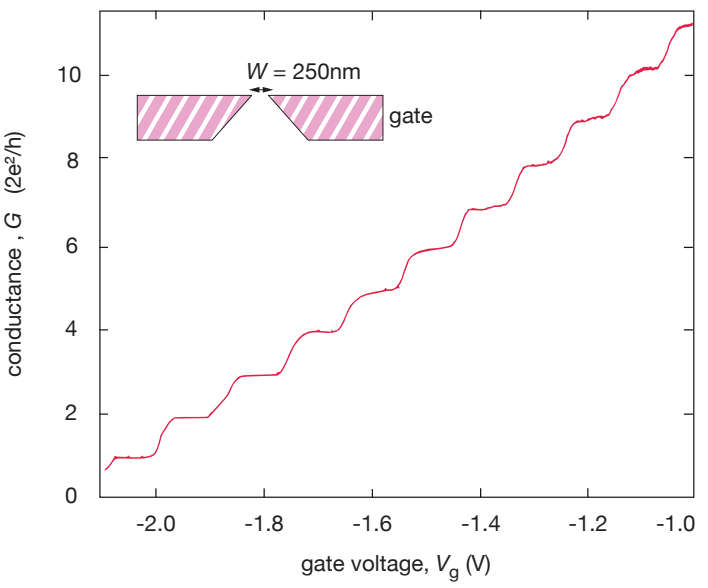

Fig. 2.4 Point contact conductance as a function of gate voltage defining the number of available modes. Inset: point-contact geometry. Data obtained from a GaAs nanoconstriction, extracted from ref [21].

modes' number. A sequence of plateaus with steps near integer multiples of $2e^2/h$ is observed, indicating conductance quantisation.

The Landauer-Büttiker formalism can be used to generalise this for a conductor with many terminals having different transmission probabilities but is beyond the scope of this work. I will here present a few experiments characteristic of ballistic transport.

2.2.2 Experimental signatures of ballistic transport

A few geometry-dependent magnetoresistance anomalies are a direct consequence of ballistic transport. Notably, with the ability to make devices smaller than the mean free path, Roukes et al. discovered in 1987 the quenching of the Hall effect in crosses [22], a consequence of the collimation effect [23, 24]. Other effects may appear, such as negative Hall resistance [25], bend resistance [6, 26, 27] or magnetic focusing. These phenomena can be qualitatively understood with semi-classical mechanisms [28]. I detail two of them: negative bend resistance and magnetic focusing, used in chapter 7 to prove the ballisticity of a novel quasiparticle family in graphene superlattices.

2.2.2.1 Negative bend resistance

In cross-shaped ballistic billiards samples, different mechanisms may appear. In the absence of a magnetic field, collimation and scrambling are key concepts, shown in figure 2.5a. An electron from the main channel and approaching the side probe will be reflected, and undergo multiple reflections before being directed to the contact opposite the injector. A consequence of this is that the probability for an electron to enter the right or left side probe is equal, resulting in the quenching of the Hall effect [6, 23–28].

In a magnetic field, the electrons undergo cyclotron trajectories: guiding takes over, as figure 2.5b. Guiding happens for magnetic fields corresponding to cyclotron radius smaller than the corner curvature's radius: $B \geq \hbar k_\mathrm{f}/er_\mathrm{corner}$. In this regime, the junction does not scatter the electron back into the channel: the absence of backscattering is a feature characteristic of the quantum Hall regime, as will be discussed in chapter 8.

Figure 2.5c shows the resulting negative resistance measured on high mobility GaAs 2DEG shaped into a cross with width W =100 nm. The bend resistance is defined as $R_\mathrm{b} = V_{3-4}/I_{1-2}$. At low magnetic fields, ballistic electrons injected from contact 1 shoot straight to contact 3 and accumulate, resulting in a negative resistance. As the magnetic field B is increased, guiding onto contact 2 happens. For small fields, large cyclotron orbits may be directed into all contacts with equal probabilities. When the cyclotron orbits

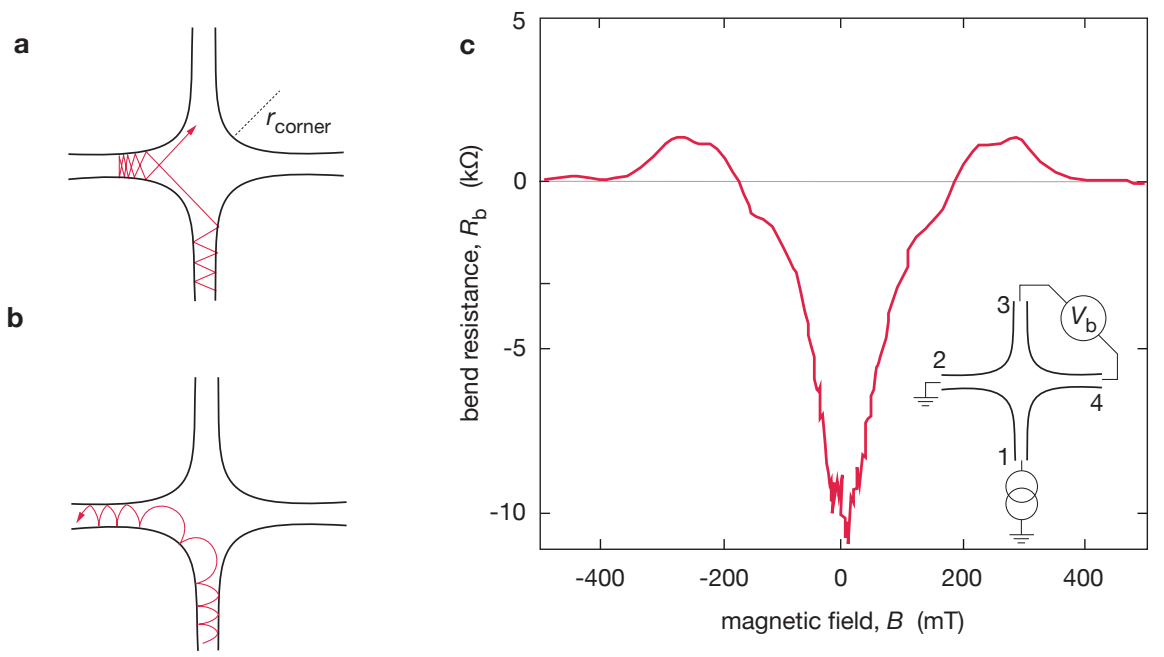

Fig. 2.5: Classical trajectories (red arrows) in an electron billiard, illustrating **a)** collimation and scrambling at $B \approx 0$ and **b)** magnetic guiding at finite B. **c)** experimental data with the geometry presented in the inset. r_{corner} represents the corner's curvature radius, defined in section 2.2.2.1. Data extracted from ref. [27]

become smaller than the cross width, all electrons are directed to contact 2: no electron is collimated into either 3 and 4, therefore $R_b = 0$.

2.2.2.2 Transverse magnetic focusing

The second effect is transverse magnetic focusing. It is analogous to the cross-resistance that measures the signal at the nearest contact to the injector instead of probing the voltage drop on the opposite electrode. Figure 2.6a shows the typical geometry to observe resonances as due to the magnetic focusing of electrons into the contact. The injector allows for injecting a divergent beam of electrons ballistically that reach the collector after one or more specular reflections at the boundary connecting i and c: these are skipping orbits (fig. 2.6b). Whenever L, the separation between the injector and collector, is an integer multiple of the cyclotron diameter, electron focusing results in a resistance maximum:

$$B_{\mathrm{focusing}} \equiv \left(\frac{2\hbar k_{\mathrm{f}}}{eL} \right) p. \tag{2.26}$$

Here $p-1$ is the number of rebounds on the edge ($p = 1$ corresponds to direct collimation without reflection, from injector to collector), $\hbar$ is the reduced Planck constant, e is the elementary charge and k_{f} is the Fermi momentum. For B_{focusing}, an electron trajectory matches the distance between injector and

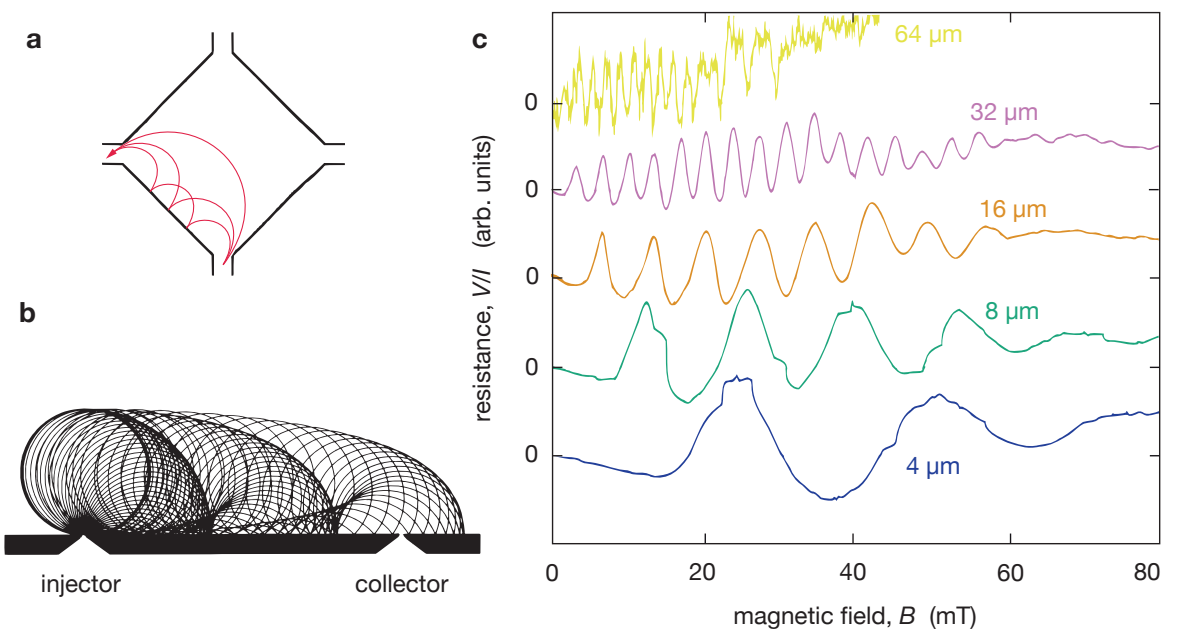

Fig. 2.6: Electron focusing: a) classical trajectories in an electron billiard, taken from ref. [6]. **b**) Classical electron focusing by the magnetic field; skipping orbits along the 2DEG boundary. Trajectories are drawn up to the third specular reflection. Extracted from ref. [29] **c**) Experimental electron focusing spectra at 0.3 K for five different injector-collector separations in high mobility material, taken from [30].

collector; therefore, a sharp resonance, seen as an oscillation maximum appears in the voltage signal. Examples of such resonances are shown in figure 2.6c.

2.2.3 High field magnetotransport

The classical equations of motion for an electron moving in 2D under the influence of a Lorentz force can be described in terms of the cyclotron frequency $\omega_c \equiv eB/m_c$ (m_c is the cyclotron mass). For weak fields and fast electrons, the radius of the cyclotron motion is large compared to the size of the wave packet. However, for high mobility 2DEG at sufficiently low temperature and sufficiently high magnetic field, the classical picture of section 2.1.4 breaks down because the orbits become small, and $\hbar\omega_c$ becomes significant.

In this problem, the length scale of interest is the magnetic length l_B corresponding to the area $2\pi l_B^2$ containing one quantum of magnetic flux $\phi_0 = h/e$:

$$l_B \equiv \sqrt{\frac{\hbar}{eB}}, \tag{2.27}$$

which is about 26 nm at 1T and decreases as $1/\sqrt{B}$. This notation shows the magnetic field as the density of magnetic flux through a 2DEG: $B = \phi_0/2\pi l_B^2$.

2.2.3.1 Landau levels and Shubnikov-de Haas oscillations

At low temperatures and high magnetic fields, the effects of quantisation start to be important. For electrons without scattering, the allowed energy levels become discrete Landau levels (LL):

$$E_{\mathrm{n}} = \left(n + \frac{1}{2}\right)\hbar\omega_{\mathrm{c}}. \tag{2.28}$$

The degeneracy for each LL is $p = BA/\phi_0 = A/2\pi l_{\mathrm{B}}^2$, corresponding to the number of flux quanta in the total area of the sample $A = WL$. Each Landau level can hold a carrier density $n_{\mathrm{c}} = 1/4\pi l_{\mathrm{B}}^2 = eB/h$. Experimentally, one may observe oscillations of the longitudinal resistivity ρ_{xx}: the Shubnikov-de Haas oscillations (SdHOs), corresponding to the Fermi level of the system passing through the discrete gaps.

Analytically, the step-like density of states associated with a 2DEG is:

$$\mathcal{N}_{\mathrm{s}}(E) = \frac{m}{\pi\hbar^2} f(E), \tag{2.29}$$

where $f(E)$ is the Fermi-Dirac density, defined in equation 2.4. This breaks down into a sequence of peaks separated by $\hbar\omega_{\mathrm{c}}$:

$$\mathcal{N}_{\mathrm{s}}(E, B) = \frac{2eB}{h} \sum_{\mathrm{n}} \delta\left(E - \hbar\omega_{\mathrm{c}}\left(n + \frac{1}{2}\right)\right). \tag{2.30}$$

It follows that the LL energies change when varying the magnetic field. Therefore, the resistivity oscillates whenever the Fermi level moves from one LL to another. Figure 2.7a shows examples of LL. In reality, scattering processes spread the LL in energy.

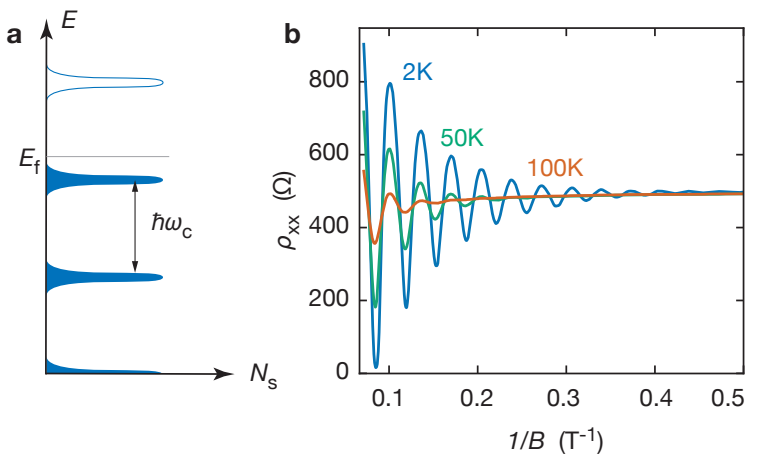

Fig. 2.7 Landau levels: a) density of states $N_{\mathrm{s}}(E, B)$ vs energy E for a 2DEG in a magnetic field. $E_{\mathrm{n}} = E_{\mathrm{s}} + (n + \frac{1}{2})\hbar\omega_{\mathrm{c}}$. **b)** Shubnikov-de Haas oscillations as a function of $1/B$ measured in a graphene 2DEG (device G1).

The general formula for SdHOs writes for a spin-degenerate 2DEG:

$$\rho_{\mathrm{xx}}(B, T) = \Delta\rho_{\mathrm{xx}}(B, T)\cos\left(2\pi\frac{B_\phi}{B} + \pi + \phi\right), \tag{2.31}$$

where $1/B_\phi = 2e/nh$ is the period of oscillations. With a finite temperature and sample imperfections, SdHOs amplitudes are damped by $\Delta\rho =$

$e^{-\mathscr{D}}\lambda(T)/\sinh\lambda(T)$ where $\mathscr{D} = \pi m_c/eB\tau_q$ is the Dingle factor is associated with the scattering time τ_q and $\lambda(T) = 2\pi^2 k_B T m_c/\hbar eB$ is the thermal factor, used to determine the cyclotron mass of charge carriers. The quantum scattering time τ_q enables the characterisation of a sample's quality. It is used instead of τ_m because it is sensitive to small-angle collisions, whereas τ_m primarily accounts for backscattering. Figure 2.7b shows an example of SdHOs.

At a given electron density, one may calculate the number of occupied LL by dividing eq. 2.30 by $2eB/h$. Consequently, a change in the magnetic field B results in variations in the number of occupied LL. Therefore at a fixed carrier density, crossing two successive peaks for fields B_1 and B_2 would allow getting the carrier density:

$$n_s = \frac{2e/h}{1/B_1 - 1/B_2}. \tag{2.32}$$

2.2.3.2 Quantum Hall effect and edge states

For a high-quality 2DEG, whenever $\omega_c\tau_q \gg 1$, the SdHOs evolve into the quantum Hall (QH) effect. At sufficiently high magnetic fields, one may observe a series of so-called QH plateaus: the Hall resistivity is quantised to the values:

$$\rho_{yx} = \frac{1}{\nu}\frac{h}{e^2}. \tag{2.33}$$

This quantisation does not depend on microscopic details such as the purity of the sample, the material or the presence of defects. One may rewrite the Hall resistivity as:

$$R_H = \frac{B}{n_s e} = \frac{h}{e^2}\frac{Be}{n_s h} = \frac{h}{e^2}\frac{B\mathcal{A}}{h/e}\frac{1}{n_s\mathcal{A}} = \frac{h}{e^2}\frac{\phi}{\phi_0}\frac{1}{N_e} = \frac{h}{e^2}\frac{N_\phi}{N_e}, \tag{2.34}$$

where $N_e = n\mathcal{A}$ is the number of electrons in the area $\mathcal{A}$ and N_ϕ is the number of flux quanta in the system. Therefore the quantum number ν can be seen as $\nu = N_e/N_\phi$, the number of electrons per flux quantum in the system. This ratio is usually referred to as the Landau level filling factor or, more simply, the filling factor.

Under these conditions, the bulk of the 2DEG is gapped similarly to band insulators. The family of allowed wave vectors is 1-dimensional, with the group velocity of opposite sign on the two edges of the sample. It corresponds to edge currents of opposite signs flowing on opposite sides. The semiclassical interpretation is that the current flows in a series of skipping orbits, with the circular motion interrupted by scattering at the device edge - see fig. 2.8. It corresponds in the Landauer picture to a number ν of 1D channels propagating for a Landau level index ν. The width of the conductor spatially separates these 1D states. For sufficiently wide devices, backscattering is suppressed because it requires electrons to jump from one edge to the other. As the two states do not

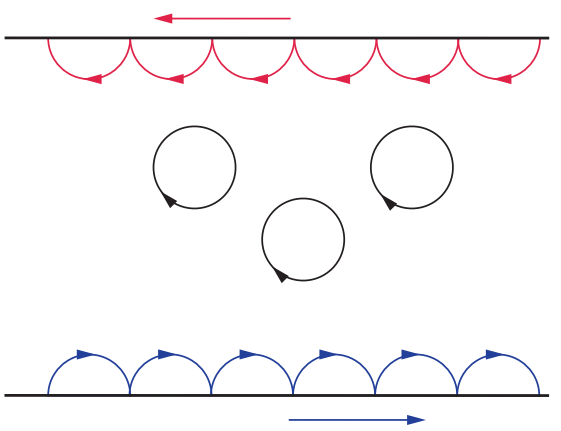

Fig. 2.8 Propagation of cyclotron orbits of electrons in the presence of a magnetic field pointing into the paper. Orbits are closed trajectories in the bulk. Collisions with the sample boundaries result in skipping orbits with non-zero drift velocities along the edges, pointing in opposite directions for opposite edges.

overlap, only forward scattering can happen, resulting in the disappearance of the longitudinal resistivity ρ_{xx} in the QH regime simultaneously with plateaus of the Hall resistivity ρ_{xy}. This chiral nature of the edge state is responsible for quantising the Hall conductance independently of disorder. In reality, the disorder is an essential component for the visibility of the Hall plateaus. When the Fermi energy E_f lies between LL, disorder would typically cause backscattering destroying the quantisation of σ_{xy}. Instead, disorder broadens the LL in the bulk and provides a reservoir of localised states allowing the chemical potential to vary smoothly with density; hence is responsible for the visibility of quantised values over a finite range of B or n.

2.3 Mesoscopic physics and superconductivity

So far, we considered the behaviour of normal electrons retaining a phase coherence over a certain length ξ of the order of device size, therefore creating interference effects between electrons in the same energy band. Let us now turn to the case of superconductivity. The superconducting state is characterised by a macroscopic wavefunction retaining its coherence over length scales much larger than in the normal state. Here we study how the normal and superconducting coherence couple together. While in a normal metal the conduction carriers are either electrons or holes, in a superconductor the conductivity is dominated by Cooper pairs, a composite particle formed by two bound electrons, with radically different properties. In this section, I review the literature showing that the combination of superconductivity with normal components hosts different exciting phenomena.

2.3.1 The superconducting proximity effect

When a normal metal and a superconductor are contacted (NS junction) with a clean enough interface, superconductivity can penetrate the normal metal over a length scale ξ_N. This is called the *proximity effect* [13]. For a clean metal, the probability of finding a Cooper pair at a distance of the interface decays exponentially. For a dirty metal (characterised by a mean free path lower than the superconducting coherence length ξ_0), the Cooper pairs' leakage is controlled by diffusion processes.

2.3.1.1 Andreev reflection

The Andreev reflection is the process through which an electron is transmitted through an NS interface. In the case of a normal-normal interface, a spin-up electron with an energy δE above the Fermi level is reflected as a spin-up electron with the same energy δE above the Fermi level. This is not the case for an NS interface. As in the ground state of the superconductor, electrons are bound together as Cooper pairs, one should equalise the chemical potential of two separate electrons in the normal metal and one Cooper pair in the superconductor. Transferring a spin-up electron with energy δE from the normal metal to the superconductor requires dragging a spin-down electron with energy $-\delta E$ to form a Cooper pair. This process can be seen differently: it leaves behind in the normal metal an antiparticle in the spin-down band with a momentum opposite to the picked-up electron. As a result, the Andreev reflection reflects an electron in the normal metal into an antiparticle with opposite momentum in the normal metal and transmits a Cooper pair in the superconductor [12, 31–33]. Figure 2.9 schematises the Andreev reflection for an energy δE created by biasing the NS interface with a voltage V.

The superconducting coherence length $\xi_0 = \hbar v_f/\Delta_0$ is the distance an electron travels in a time $\hbar/\Delta_0$, that is the time it takes for an electron with a spin up to be converted into a hole with spin down. It is possible to evaluate the variation in quasimomentum δp during the process. It would scale as $\mathrm{d}p/\mathrm{d}t$ times the time passed in the interface region ξ/v_f:

$$\delta p \sim \frac{\xi_0}{v}\frac{\Delta_0}{\xi} \sim p_0\frac{\Delta_0}{p_0 v} \sim p_0\frac{\Delta_0}{\epsilon_f} \ll p_0. \tag{2.35}$$

This means that for an Andreev reflection, the variation of the quasimomentum should be smaller than the quasimomentum itself. As the motion of electrons is directed away from the interface after the reflection, the quasiparticle should be transferred from one branch of the energy spectrum to the other: from a quasiparticle to an antiparticle with a close quasimomentum, i.e.

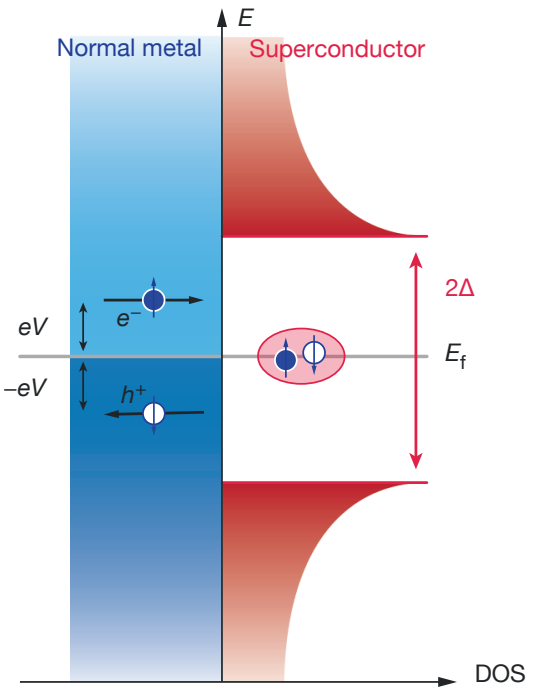

Fig. 2.9 Schematics of the Andreev reflection at a normal metal - superconductor interface. An electron from the conduction band with a total energy of $+eV$ within the superconducting gap 2Δ is reflected as a hole with energy $-eV$, forming a Cooper pair at the Fermi level E_f in the superconductor.

from an electron to a hole. The velocity of the reflected antiparticle $\boldsymbol{v}_\mathrm{ref}$ will be:

$$\boldsymbol{v}_\mathrm{ref} = \frac{\partial\left[v(p_0 - p)\right]}{\partial \boldsymbol{p}} = -\frac{v\boldsymbol{p}}{p} = -\boldsymbol{v}_\mathrm{inc}, \tag{2.36}$$

where $\boldsymbol{v}_\mathrm{inc}$ is the velocity of the incident particle. Upon reflection, the particle is converted to an antiparticle with energy and quasimomentum conserved. The velocity changes sign. This is a fundamentally distinct effect from the specular reflection of electrons, where only the normal component of the electron velocity changes sign at the interface. However, in the case of graphene junctions, Andreev reflection can be specular (see subsection 3.3.1).

Let us note that an electron with energy δE and wavevector $k_\mathrm{f} + \delta k$ will be reflected as a hole with energy $-\delta E$ and wavevector $k_\mathrm{f} - \delta k$. During the Andreev reflection, the reflected hole may acquire an intrinsic phase: $\delta\varphi = -\arccos(\delta E/\Delta_0)$. Additionally, the wavevector difference between the incident electron and the reflected hole will also result in a phase difference when the particles propagate in the normal metal. In the ballistic regime, this can be written as $2\delta k = 2\delta E/\hbar v_\mathrm{f}$. Consequently, the electron and hole will lose coherence at a distance $L_\mathrm{E} = \hbar v_\mathrm{f}/\delta E$ which is the characteristic length of the proximity effect in which the metal properties will be affected by the presence of the superconductor. In the diffusive regime (with a diffusion constant $\mathcal{D}$), it can be shown that $L_\mathrm{E} = \sqrt{\hbar\mathcal{D}/\delta E}$. Note that the characteristic length of the proximity effect depends upon the energy: in the metal at a distance d from the interface, the electron-hole pairs with energy higher than $E_\mathrm{Th} = \hbar\mathcal{D}/d^2$ will lose their coherence, whereas those with energy below E_Th will not. E_Th is called Thouless energy. At finite temperatures, the energy of electrons is of the order of the thermal energy $k_\mathrm{b}T$. It is then possible to define a thermal coherence length as $\xi_\mathrm{N} = \sqrt{\hbar\mathcal{D}/2\pi k_\mathrm{B}T}$.

2.3.1.2 Josephson junction: Cooper pair tunnelling

Here we consider an SNS junction [1], with the thickness of the metallic layer between the two superconductors thin enough so that there can be considerable overlap between the macroscopic wave functions of the two superconductors, therefore coupling between the two superconducting states. The overlap of the wave functions results in the coherent exchange of Cooper pairs, an effect known as the Josephson effect [12, 34, 35].

In the absence of a voltage, the phase difference $\varphi = (\phi_2 - \phi_1)$ between the two superconductors is time-independent. Therefore the current I_s through the superconducting contact is:

$$I_\mathrm{s} = I_\mathrm{c} \sin \varphi. \tag{2.37}$$

That is the first Josephson equation: the DC Josephson effect consists of a DC current crossing the normal metal without a voltage drop. The critical current I_c depends on the density of the Cooper pairs in the superconducting electrodes n_s, on the junction area A and the coupling constant $\mathcal{K}$ between the two superconductors: $I_\mathrm{c} = 2\mathcal{K}n/\hbar A$.

The second Josephson equation describes the evolution of the phase difference when a voltage drop V is applied to the junction:

$$\frac{\partial \varphi}{\partial t} = \frac{2eV}{\hbar}. \tag{2.38}$$

This equation means that Cooper pairs can tunnel without dissipation between the superconducting electrodes in the usual Josephson junction. The coupling is described by the Josephson energy $-E_\mathrm{J} \cos \varphi$, where E_J is the Josephson energy, defined as $E_\mathrm{J} = \hbar I_\mathrm{c}/2e$. It is related to the critical current of the junction, which can be expressed by the tunnelling resistance of the junction R_t and the energy gap of the superconductor Δ_0: $I_\mathrm{c}(T = 0) = \pi\Delta_0/(2eR_\mathrm{t})$. R_t can be seen as the transparency of the junction (see subsection 4.5.1). It corresponds to the total resistance of $1\,\mathrm{cm}^2$ of the junction area and has dimension of $\mathrm{s\,cm}$ (or $\Omega\,\mathrm{cm}^2$).

At $T = 0$, the critical current density in the Josephson junction can be expressed as a function of the transparency:

$$j_\mathrm{s} = \frac{\pi\Delta_0}{2eR_\mathrm{t}}. \tag{2.39}$$

---

[1] The Josephson effect originally described SIS junctions (superconductor - insulator - superconductor). The case of SNS junctions was found to be very similar [34]. As this thesis considers superconducting - graphene - junctions, we focus here on the case of SNS junctions.

2.3.1.3 Andreev bound states

The transfer of a Cooper pair through an SNS junction requires two Andreev reflections at opposite NS interfaces. It is a *double* Andreev process in which the involved electrons and holes retrace each other's trajectories, forming *Andreev bound states* (ABS).

The most common way to form ABS is when the electrons and hole involved in Andreev reflections have exactly opposite momenta: $\boldsymbol{p} = -\boldsymbol{p}'$. Their phases acquired along trajectories inside the normal metal cancel exactly, and ABSs are formed. For ballistic junctions, there is another way to find e^-–h^+ forming ABSs without retracing each other exactly. It corresponds to a small but non-zero probability of forming Andreev reflection at the contacts with slightly different reflection angles from the NS interface. In that case, if e^- and h^+ have slightly different momenta, as long as the carriers reside within the superconducting gap Δ_0 (i.e. $|p-p'|v_\mathrm{f} < \Delta_0$) and the phase shift acquired along the retracing e^-–h^+ trajectories, $(\phi_2 - \phi_1) = |p-p'|\Lambda/\hbar$ is small, then there can be ABS. Here Λ is the effective length of e^-–h^+ trajectories in the normal metal. This constraint reads:

$$\Delta_0 < hv_\mathrm{f}/\Lambda = E_\mathrm{Th}. \tag{2.40}$$

In this condition of misaligned e^-–h^+ trajectories, Λ is slightly larger than the device size L. For longer Λ, there can be no conventional Andreev-type trajectories that can contribute to the transfer of Cooper pairs[2].

There is another condition for the conversion of two electrons from a 2D metal into a Cooper pair: it necessitates $p_\mathrm{y} = -p'_\mathrm{y}$ (where y indice refers to direction parallel to the NS interface) and $p_\mathrm{x} = (\epsilon/v)\cos\theta$ and $p'_\mathrm{x} = (\epsilon'/v)\cos\theta'$, where θ and $\theta' = \theta - \delta\theta$ are the incident and reflected angles of the e^-–h^+ trajectories (see fig. 2.10). These last two conditions can be simplified as a single requirement:

$$\left| v_\mathrm{f}\sqrt{p_\mathrm{x}^2 + p_\mathrm{y}^2} - E_\mathrm{f} \right| < \Delta_0, \tag{2.41}$$

which can be interpreted as: the energies of charge carriers involved in ABS should reside within the gap. It is also required that the misalignment angle $\delta\theta = \theta' - \theta$ between ballistic e^- and h^+ trajectories forming ABS is very small:

$$\cot\theta' - \cot\theta \approx \frac{\theta' - \theta}{\sin^2\theta} < \frac{\Delta_0}{v_\mathrm{f}\cos\theta\, p \sin\theta}, \tag{2.42}$$

that can be simplified as [36]:

---

[2] We will show in the next chapter that unconventional Andreev bound states, such as mesoscopic Andreev edge states and chiral Andreev edge states, exist with longer Λ but here, we limit ourselves to the general case.

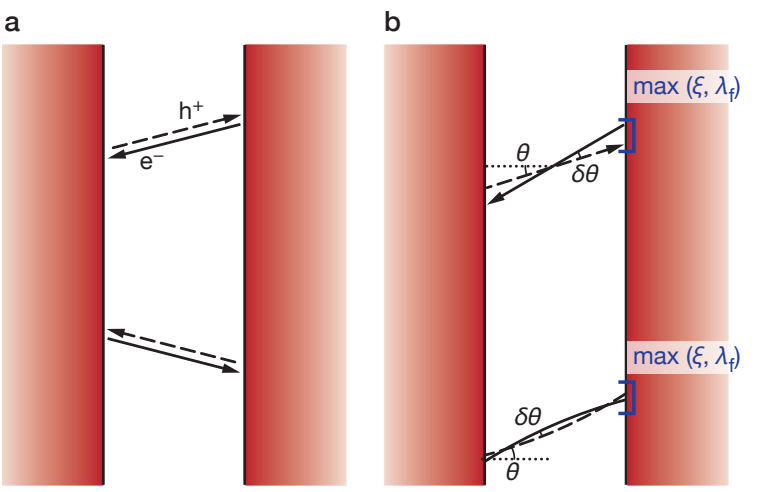

Fig. 2.10 ABS with allowed misalignment of contributing trajectories. a) e^-–h^+ trajectories for the standard double Andreev process. **b)** slightly misaligned e^-–h^+ trajectories that can also form ABS if their positions at the two NS interfaces are spatially close. Adapted from ref. [36].

$$\delta\theta < \frac{\Delta_0}{E_\mathrm{f}} \tan\theta. \tag{2.43}$$

Finally, there is another crucial requirement: for an electron to be reflected as a hole, the candidate electrons and holes should be sufficiently close to the contact: e^-–h^+ trajectories should not end up further away from each other than $\max(\xi_0, \lambda_\mathrm{f})$ where λ_f is the Fermi wavelength. This is because i) two electrons can only form a Cooper pair (of size given by the coherence length ξ_0) inside the superconducting contacts if they are at a distance smaller than ξ_0, and ii) two electrons' positions within a normal metal are indistinguishable if they are separated by less than λ_f.

Consequently one may write :

$$\frac{\delta\theta}{\cos^2\theta} < \frac{\max(\xi_0, \lambda_\mathrm{f})}{L}. \tag{2.44}$$

2.3.1.4 Effect of the temperature

At finite temperature, equation 2.39 reads [37]:

$$j_\mathrm{c} = \frac{\pi\Delta_0(T)}{2eR} \tanh\left(\frac{\Delta_0(T)}{2T}\right), \tag{2.45}$$

where the energy gap tempeature dependence is found from the BCS theory [14, 38, 39]:

$$\frac{\Delta(t)}{\Delta_0} = 1.74\sqrt{1 - \frac{T}{T_\mathrm{c}}}. \tag{2.46}$$

Note that there is an empirical relation between the energy gap Δ_0 at $T = 0$ and the critical temperature of a superconductor: $\Delta_0 = 1.76 k_\mathrm{B} T_\mathrm{c}$. So far, we have considered the case of *short* Josephson junctions, where the wavefunctions from the two superconductors overlap. The Josephson effect exists also for *long* Josephson junctions, in which the junction length L is longer than the superconducting coherence length ξ.

For the case of long junctions, Δ should be substituted with the Thouless Energy, E_Th [40], and the critical current evolves as:

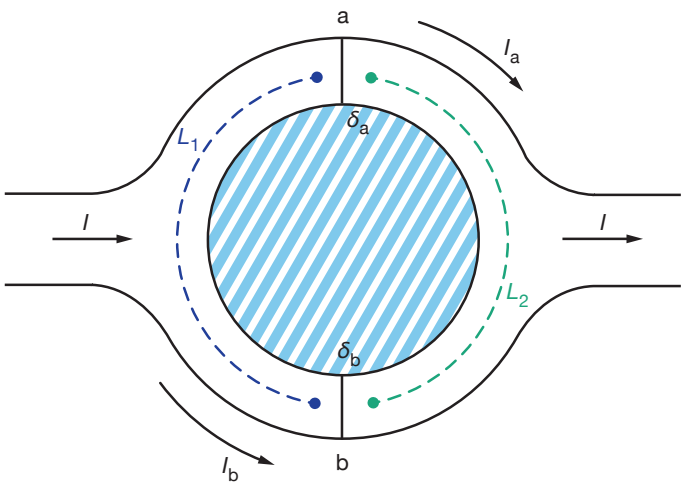

Fig. 2.11 Two parallel Josephson junctions with enclosed magnetic flux indicated by hatched area; phase changes are calculated along contours L_1 and L_2 assumed to begin and end at the weak links [14]

$$j_c \propto \exp(-k_B T/E_{Th}) \tag{2.47}$$

2.3.2 Effect of a magnetic field

Here I detail the effect of a magnetic field on the Josephson current. First, let me remind the dependence of the energy gap with temperature in the superconducting state to be used later:

$$\frac{\Delta(B)}{\Delta_0} = \sqrt{1 - \left(\frac{B}{H_{c2}}\right)^2}, \tag{2.48}$$

where H_{c2} is the critical field of the superconductor, at which superconductivity is destroyed.

The rest of this subsection is composed of three parts. First, I present the influence of a magnetic field B on the tunnelling of Cooper pairs in Josephson junctions by introducing interference of coherent waves. Second, I consider the case of junctions wide enough so that eddy currents can screen out the applied magnetic field. Third, I discuss the influence of the magnetic field on Andreev bound states.

2.3.2.1 Interference of coherent waves in small junctions

One may get a good physical picture by first considering two junctions (a and b) connected in parallel with superconducting leads such as the one in fig 2.11. Such a device is called a superconducting quantum interference device (SQUID). One may write the total current passing through the device as:

$$I = I_c(\sin\delta_a + \sin\delta_b) = 2I_c \cos\left(\frac{\delta_a - \delta_b}{2}\right) \sin\left(\frac{\delta_a + \delta_b}{2}\right), \tag{2.49}$$

where δ_a and δ_b denote the phase changes in the junctions a and b. The total phase difference $(\delta_\mathrm{a} - \delta_\mathrm{b})$ can be calculated by integrating along the contours L_1 and L_2 deep enough in the superconductor so that no current is flowing. The phase variations can be found as: $\varphi_i = -2e/\hbar \int_{\mathrm{L}_i} \boldsymbol{A} \cdot \mathrm{d}\boldsymbol{s}$ $(i = 1 \text{ or } 2)$. As $\delta_\mathrm{a} - \delta_\mathrm{b} = \varphi_1 + \varphi_2$, the phase difference between the two junctions is found as [14]:

$$\delta_\mathrm{a} - \delta_\mathrm{b} = \frac{2e}{\hbar} \oint ds \boldsymbol{A} \cdot \boldsymbol{s} = \frac{2e\phi}{\hbar}, \tag{2.50}$$

where ϕ is the magnetic flux. As a result, the field dependence of the critical current writes:

$$I = 2I_\mathrm{c} \sin\left(\frac{\delta_\mathrm{a} + \delta_\mathrm{b}}{2}\right) \cos\left(\pi \frac{\phi}{\phi_0}\right) = I_\mathrm{max} \cos\left(\pi \frac{\phi}{\phi_0}\right), \tag{2.51}$$

with $\phi_0 = h/2e$, the flux quantum. Measurements in SQUID-like structure are shown in figure 2.12 for a graphene-based SQUID [41], showing clear current oscillations as a function of the flux quantum.

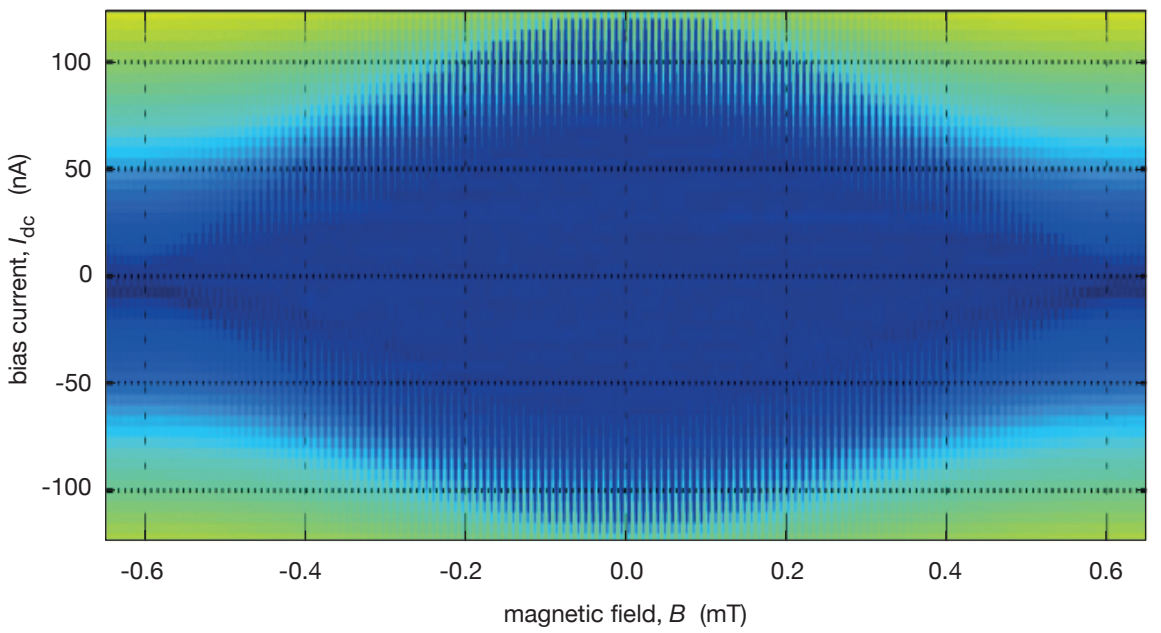

Fig. 2.12: Resistance $R(B, I_\mathrm{dc})$ of a SQUID. The device comprises a 210 µm^2 Niobium loop with two graphene Josephson junctions. The critical current oscillates with a period of 8.7 µT, corresponding to the flux penetrating an area of 230 µm^2, as in equation 2.51. colour scale: $|V_\mathrm{dc}|$ from 0 (navy) to 180 µV (lime). Map extracted from ref. [41]

In a single, thicker Josephson junction, analytically demonstrating the critical current as a function of the magnetic field can be achieved by replacing the summation over the two junctions by an integration over the junction width, resulting in a critical current of the form [42]:

$$I = I_\mathrm{max} \left| \frac{\sin(\pi\phi/\phi_0)}{\pi\phi/\phi_0} \right|. \tag{2.52}$$

Here ϕ is the flux trapped in the junction area. For a 2D junction, $\phi = \mathcal{A}B$ where B is the applied magnetic field, and $\mathcal{A}$ is the area of the junction. This form is similar to the Fraunhofer diffraction amplitude of a single slit: the common phenomenon between a Josephson junction and optical diffraction is the interference of coherent waves. The critical current from a 2D Josephson junction is shown in figure 2.13, following the relationship of equation 2.52.

2.3.2.2 Wide junctions and flux quantisation

In the previous subsection, I neglected the magnetic field contribution inside the junction. If the junction is large enough, this approximation is no longer valid as the Josephson current can generate a non-zero magnetic field screening out the applied field. A junction is wide if L is larger than the Josephson penetration depth λ_J; it is narrow if it is much smaller than λ_J, defined as:

$$\lambda_\mathrm{J} = \left(\frac{\phi_0}{8\pi^2 j_\mathrm{s} d}\right)^{1/2}. \tag{2.53}$$

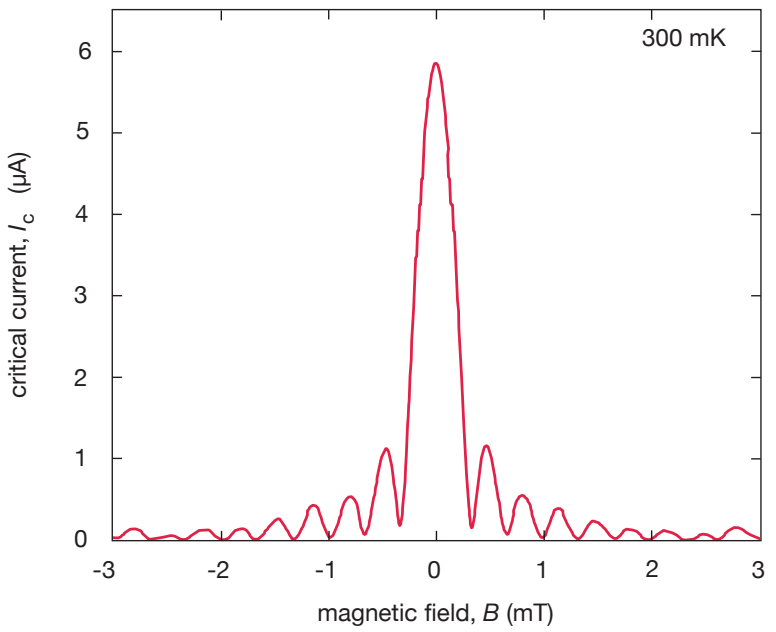

Fig. 2.13 Tunnel current $I_\mathrm{c}(B)$ through a Josephson junction. The magnetic field is applied perpendicular to the junction. Data measured by Mengjiang Zhu on device Ja.

Here d is the inductance of the Josephson junction that scales like the thickness of the normal metal. This length is in the order of 10^{-2} cm, much larger than the ordinary penetration depth of superconductors. In the case of wide junctions, these eddy currents are carried by Josephson vortices. These carry a single magnetic flux quantum inside the Josephson junction: $\phi = \phi_0$. As a result, one may see a Josephson junction as a 2D analogue of a type II superconductor with the Meissner effect. Vortices form from the external field $H = H_{\mathrm{c}1}$, which is the order of the average field in the vortex: $H_{\mathrm{c}1} \approx \phi_0/(d\lambda_\mathrm{J})$. The exact formula writes [35]:

$$H_{c1} = \frac{2\phi_0}{\pi^2 \lambda_J d}. \tag{2.54}$$

Above that field, the vortex concentration increases with the magnetic field. However, one may note that there is no transition to a normal state at any field H_{c2} since Josephson vortices have no normal core.

2.3.2.3 Andreev bound states in a magnetic field

A magnetic field suppresses the supercurrent resulting from Andreev bound states. Following similar consideration as in paragraph 2.3.1.3, it is possible to estimate $B*$ the field above which all ABSs are suppressed.

In a small magnetic field B, interference between Cooper pairs crossing the normal metal along different paths causes the supercurrent to vanish. When $\phi = B\mathcal{A} \sim \phi_0$, the Cooper pairs have broadly distributed phase shifts leading the supercurrent to oscillate and vanish periodically. For the case of large ballistic devices, B bends the e^-–h^+ trajectories, leading to misalignment such as Andreev-reflected electrons and holes do not retrace each other exactly [36,43,44], similarly to misaligned trajectories in fig. 2.10b. The condition of eq. 2.43 in the presence of a magnetic field can therefore be written as a function of the cyclotron radius $r_c = p_f/eB = \hbar k_f/eB$. It leads to a misalignment of $\delta\theta \sim L/r_c \cos\theta$, where L is the junction length.

Therefore, in order to support ABS in finite B, one needs:

$$r_c > \frac{E_f L}{\Delta_0}, \tag{2.55}$$

which is satisfied for $B < B^*$ where :

$$B^* \sim \frac{\Delta_0}{eLv_f}. \tag{2.56}$$

2.3.3 Effect of microwaves: the a.c. Josephson effect

Irradiation of a Josephson junction with an RF excitation of angular frequency ω_{rf} gives rise to constant-voltage steps in the DC IV curves for a series of voltages $V_n = n\hbar\omega_{rf}/2e$ [45]. These *Shapiro steps* are shown in figure 2.14 for a characteristic graphene Josephson junction. It can be understood easily by considering an ideal voltage bias $V = V_{dc} + V_{rf}\cos\omega_{rf}$ applied to the junction. Then the phase difference across the junction $\varphi = (\phi_2 - \phi_1)$ can be found through a time integration of equation 2.38:

$$\varphi(t) = \varphi_0 + \omega_J t + \frac{2eV_{rf}}{\hbar\omega_{rf}} \sin\omega_{rf} t. \tag{2.57}$$

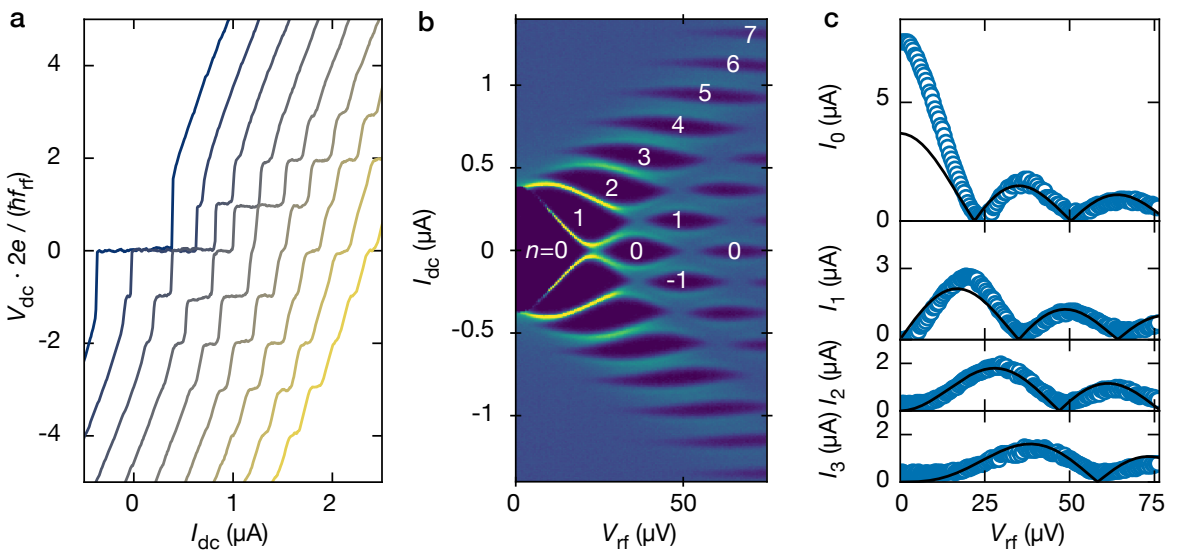

Fig. 2.14: Shapiro steps in a bilayer graphene Josephson junction (J8). a) constant voltage steps for varying RF power. **b)** corresponding dV/dI map showing zero resistance regions with Shapiro peaks as high resistance boundaries and **c)** Bessel function fit of V_n. Data measured at T_mc =20 mK and f_rf =4.5 GHz.

Here φ_0 is an integration constant and $\omega_\mathrm{J} \equiv 2eV_\mathrm{dc}/\hbar$. This phase modulation causes an AC supercurrent at the Josephson frequency ω_J and the side frequencies $\omega_\mathrm{J} \pm n\omega_\mathrm{rf}$. For most voltage biases, the AC supercurrent does not affect the DC IV characteristic, but whenever the condition $2eV = n\hbar\omega_\mathrm{rf}$ is fulfilled, one of the side frequencies will be zero. This expression can be inserted into the first Josephson equation $I = I_\mathrm{c} \sin\varphi$ and sin can be expanded as a sum of Bessel functions $\mathcal{J}_\mathrm{n}$:

$$I = I_\mathrm{c} \sum (-1)^n \mathcal{J}_\mathrm{n}(2eV_\mathrm{rf}/\hbar\omega_\mathrm{rf}) \sin[\varphi_0 + \omega_\mathrm{J} t - n\omega_\mathrm{rf} t]. \tag{2.58}$$

Note that the term in the sum contributes a dc component only when $\omega_\mathrm{J} = n\omega_\mathrm{rf}$, that is, when the dc voltage V_dc is at one of the values V_n:

$$V_\mathrm{n} = n\hbar\omega_\mathrm{rf}/2e. \tag{2.59}$$

These correspond to Shapiro steps. Now, one may include the normal current Vn/R, and therefore the total DC current in the nth Shapiro step can take any value in the following range:

$$\frac{V_\mathrm{n}}{R} - I_\mathrm{c}\mathcal{J}_\mathrm{n}(2eV_\mathrm{rf}/\hbar\omega_1) \;\leq\; I \;\leq\; \frac{V_\mathrm{n}}{R} + I_\mathrm{c}\mathcal{J}_\mathrm{n}(2eV_\mathrm{rf}/\hbar\omega_1). \tag{2.60}$$

That is, the half-width of the nth Shapiro step is defined by:

$$I_\mathrm{n} = I_\mathrm{c}\mathcal{J}_\mathrm{n}(2eV_1/\hbar\omega_\mathrm{rf}). \tag{2.61}$$

The $\mathcal{J}_\mathrm{n}(x)$ vary as x^n for small values of x. Consequently, when the RF voltage V_rf increases from 0 to a finite value, the lowest step appears before the second, etc. At higher x, $\mathcal{J}_\mathrm{n}(x)$ are oscillatory functions, decreasing as $x^{1/2}$

for large x. As a result, a given step will have an oscillatory width in I as the RF voltage varies.

The dc supercurrent in these Shapiro steps only exists for $V = V_{\mathrm{n}}$. For all voltages between the V_{n}, there is no dc effect of the supercurrent, as is the case for a voltage-biased junction free of irradiation. One may also look at the dV/dI characteristics. As in a junction free of RF irradiation, the resistance is zero below I_{c} and presents resistance maxima before entering a constant resistance regime where the superconductivity is destroyed. Similarly, at constant irradiation, there are multiple domains with a zero resistance and vertical Shapiro spikes occurring whenever the energy equals $2eV$ allowing a Cooper pair to go through the junction is equal to a multiple of the photon energy $\hbar\omega_{\mathrm{rf}}$.

Chapter 3
Graphene's structure and device properties

Graphene was first isolated on silicon oxide and shaped as a mesoscopic Hall bar to characterise its electronic properties. Eighteen years after its discovery, graphene research has vastly expanded, as new physical concepts arrived hand in hand with fabrication advances, but the kind of devices has remained similar. This chapter introduces the essential background necessary for graphene research. It discusses the properties of graphene-based van der Waals heterostructures that are necessary to understand the results of this thesis. The last section concerns the superconductivity induced in graphene via the proximity effect.

3.1 Graphene's electronic properties

From a theoretical point of view, graphene can be seen as a single plane from graphite, a material used as a moderator in nuclear reactors. For this reason, it was studied long before its discovery [46–50]. Its exfoliation in 2004 has allowed extensive experimental studies [51–54].

3.1.1 Dirac cones

The graphene structure is a hexagonal network of carbon atoms, as shown in figure 3.1. The triangular lattice has a basis composed of two atoms per unit cell, with lattice vectors:

$$\boldsymbol{a_1} = \frac{a}{2}\left(\sqrt{3}, 1\right), \qquad \boldsymbol{a_2} = \frac{a}{2}\left(\sqrt{3}, -1\right), \tag{3.1}$$

where $a \approx 0.246\,\text{nm}$ is the lattice constant. The nearest neighbour vectors resulting from these lattice vectors are:

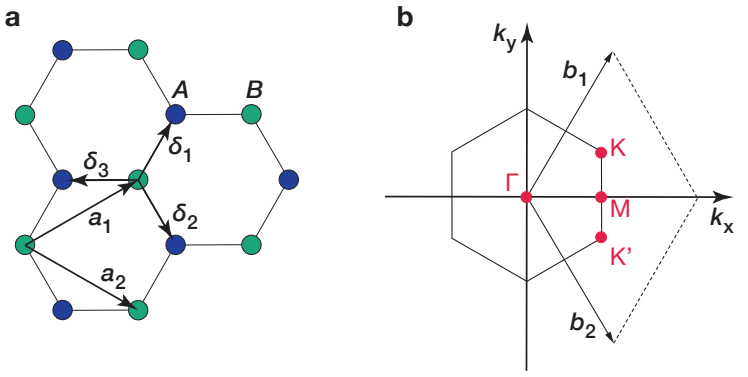

Fig. 3.1 Lattice structure of graphene: a) honeycomb lattice with two interpenetrating triangular lattices, and **b)** corresponding Brillouin zone. The Dirac cones are located at the K and K' points.

$$\boldsymbol{\delta_1} = \frac{a}{2}\left(1, \frac{1}{\sqrt{3}}\right), \qquad \boldsymbol{\delta_2} = \frac{a}{2}\left(1, -\frac{1}{\sqrt{3}}\right), \qquad \boldsymbol{\delta_3} = a\left(-\frac{1}{\sqrt{3}}, 0\right). \tag{3.2}$$

From these equations, it easily comes that the interatomic distance in graphene is $a/\sqrt{3} \approx 1.42\,\text{Å}$. The reciprocal lattice vectors are given by:

$$\boldsymbol{b_1} = \frac{2\pi}{a}\left(\frac{1}{\sqrt{3}}, 1\right), \qquad \boldsymbol{b_2} = \frac{2\pi}{a}\left(\frac{1}{\sqrt{3}}, -1\right). \tag{3.3}$$

The two points, K and K', located at the corners of the Brillouin zone, are critical in the physics of graphene. They are named Dirac points. Their position in momentum space is given by:

$$\boldsymbol{K} = \frac{4\pi}{3a}(0, 1), \qquad \boldsymbol{K'} = \frac{4\pi}{3a}(0, -1). \tag{3.4}$$

The stability of graphene's crystal is ensured by the sp^2 hybridised σ bond between the s, p_x and p_y orbitals from each carbon atom. From this, there is an unaffected p_z orbital perpendicular to the plane, forming covalent π bonds, giving rise to delocalised low-energy electronic states, crossing the Fermi level, therefore determining the electronic properties of graphene. As each p_z orbital has one electron, the π band is half-filled, resulting in large Coulomb energies and strong collective effects.

The band structure of graphene can therefore be calculated using a tight-binding approach [49, 50]. By taking into account only the nearest neighbour hopping, the tight-binding hamiltonian can be written in a basis of wave functions amplitudes on the $\boldsymbol{A}$ and $\boldsymbol{B}$ sublattices:

$$H(\boldsymbol{k}) = \begin{pmatrix} s_0 \sum_\text{j} \text{e}^{-i\boldsymbol{k}\cdot\boldsymbol{r}_\text{j}} & \gamma_0 \sum_\text{n} \text{e}^{-i\boldsymbol{k}\cdot\boldsymbol{\delta}_\text{n}} \\ \gamma_0 \sum_\text{n} \text{e}^{i\boldsymbol{k}\cdot\boldsymbol{\delta}_\text{n}} & s_0 \sum_\text{j} \text{e}^{-i\boldsymbol{k}\cdot\boldsymbol{r}_\text{j}} \end{pmatrix}, \tag{3.5}$$

where the sums are made over N unit cells, n is the index of the nearest neighbour and j of the second nearest neighbours. $\gamma_0 = -3.24\,\text{eV}$ is the overlap integral between the p_z orbitals [55], corresponding to nearest-neighbour hopping energy (hopping between different sublattices), and $s_0 = 0.0425\,\text{eV}$ is the nearest neighbour hopping energy (hopping in the same sublattice) [56]. The eigenvalues for this Hamiltonian can be expressed as [49, 50]:

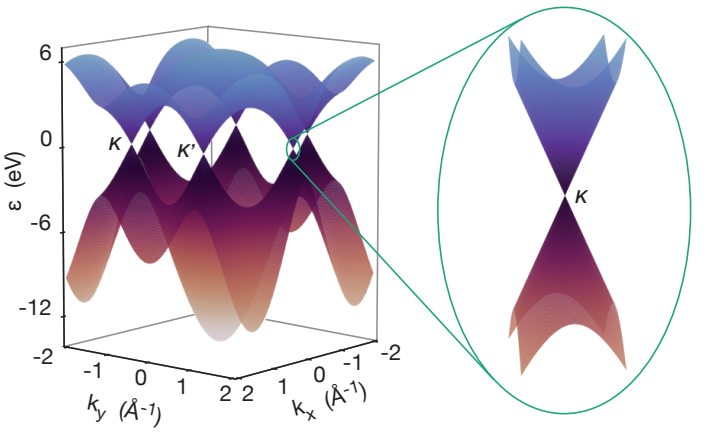

Fig. 3.2 Band structure of graphene. Energy spectrum calculated from equation 3.5. The valence band (red) and conduction band (blue) touch at six points at the Fermi level. The energies $\pm\gamma_0 - s_0$ correspond to van Hove singularities due to the saddle point located at the M point.

$$\varepsilon_{\pm}(\boldsymbol{k}) = \pm\gamma_0\sqrt{3 + f(k_\mathrm{x}, k_\mathrm{y})} - s_0 f(k_\mathrm{x}, k_\mathrm{y}), \tag{3.6}$$

with

$$f(k_\mathrm{x}, k_\mathrm{y}) = 4\cos\frac{\sqrt{3}ak_\mathrm{x}}{2}\cos\frac{ak_\mathrm{y}}{2} + 2\cos ak_\mathrm{y}. \tag{3.7}$$

The corresponding band structure is shown in figure 3.2. Figure 3.2 also shows a zoom-in around the K point. In this region, the dispersion can be obtained by expanding the band structure (eq. 3.5) close to the $\boldsymbol{K}$ vector [49] with $\boldsymbol{k} = \boldsymbol{K} + \boldsymbol{q}$ and $|\boldsymbol{q}| \ll |\boldsymbol{K}|$ is the momentum close to the Dirac point:

$$\varepsilon_s(\boldsymbol{q}) \approx sv_\mathrm{f}|\boldsymbol{q}|. \tag{3.8}$$

Here $s = \pm 1$ is the pseudospin that will be introduced in subsection 3.1.2. $\varepsilon_s(\boldsymbol{q})$ does not depend upon energy and is not quadratic in momentum, contrary to experimental systems described by the non-relativistic Scrödinger equation. Instead, ε_s is linear in $\boldsymbol{q}$: this is the Dirac equation describing ultrarelativistic particles. It is interesting for several reasons.First, the carriers near the Dirac points move at a constant speed, given by the Fermi velocity $v_\mathrm{f} = 3\gamma_0 a/2$, 300 times smaller than the speed of light c. Second, the electron dynamics in graphene can be described in terms of the Fermi velocity. The Dirac points (K and K') coincide with the charge neutrality, and the two carbon atoms in the unit cell each contribute one electron to the two bands; hence the Fermi energy $\boldsymbol{E_\mathrm{f}}$ lies precisely at the half-filled band. Third, the cyclotron mass m_c of massless carriers in graphene can be described by Einstein's (relativistic) equation $E = m_\mathrm{c}v_\mathrm{f}^2$. It makes graphene interesting in itself, but also allows the study of quantum electrodynamics (merger of quantum mechanics and relativity theory) in bench-top experiments.

3.1.2 Pseudospin and anomalous QHE

In equation 3.8, the energy of massless Dirac fermions includes a pseudospin factor s. It is an additional degree of freedom that is required as the honeycomb lattice possesses two different sublattices A and B. s can be seen as an index for the positive or negative part of the Dirac cones. It is tied to the $\boldsymbol{q}$ vector and therefore is analogous to the real spin of massless fermions and points towards the direction of propagation. Let us examine two cases: For $s = +1$, corresponding to the upper cone at $\boldsymbol{K}$, the states have a pseudospin parallel to $\boldsymbol{q}$ and correspond to right-handed Dirac fermions. For the case of $s = -1$, corresponding to anti-particles in the lower cone, the situation is reversed, i.e. $\boldsymbol{q}$ points towards the opposite direction: the situation corresponds to left-handed Dirac fermions. The chirality of graphene electrons in graphene has many implications in transport measurements; suppression of backscattering and the anomalous quantum Hall effect at high magnetic fields are some of them.

Graphene presents one set of SdHOs for both electrons and holes. Using standard fan diagrams [51–54] allows for determining fundamental SdHO frequency B_F. Both carrier types (electrons and holes) present the same linear dependence: $B_\mathrm{F} = \beta n$ where $\beta \approx 1.04 \times 10^{-15}\,\mathrm{T\,m^2}$ [53]. In theory, β is defined by a degeneracy factor g: $B_\mathrm{F} = \phi_0 n/g$ where ϕ_0 is the flux quantum. g was experimentally found to be equal to 4, corresponding to two spins and two valleys. The anomaly in SdHOs is their phase. In opposition to usual metals where the Landau levels correspond to longitudinal resistance $\rho_\mathrm{xx}(B)$ minima, graphene presents maxima at integer values of Landau filling factors ν. At high magnetic fields, SdHOs evolve into the quantum Hall effect. Instead of following the usual quantisation of σ_xy with the quantised filling factor $\nu = \pm gn$, with g the band degeneracy, the QHE in graphene is shifted by a half-integer (see fig. 3.3). The first plateau appears at $\sigma_\mathrm{xy} = 2e^2/h$, and others occur at the following:

$$\sigma_\mathrm{xy} = 4\frac{e^2}{h}\left(n + \frac{1}{2}\right). \tag{3.9}$$

The *odd* phase's origin is explained with the Berry phase (here, it is the phase electrons acquire during cyclotron motion). The 2π rotation between time-reversal pairs yields a Berry phase of π. This phase shift was explained theoretically [57–60], with a LL energy given by:

$$E_\mathrm{n} = \mathrm{sign}(n)\sqrt{2e\hbar v_\mathrm{f}^2|n|B}. \tag{3.10}$$

This equation allows a single LL with $n = 0$ and $E = 0$. σ_xy exhibits QHE plateaux when E_f falls between Landau levels and jumps of an amount ge^2/h with g the degeneracy, when E_f crosses a LL, with the time-reversal

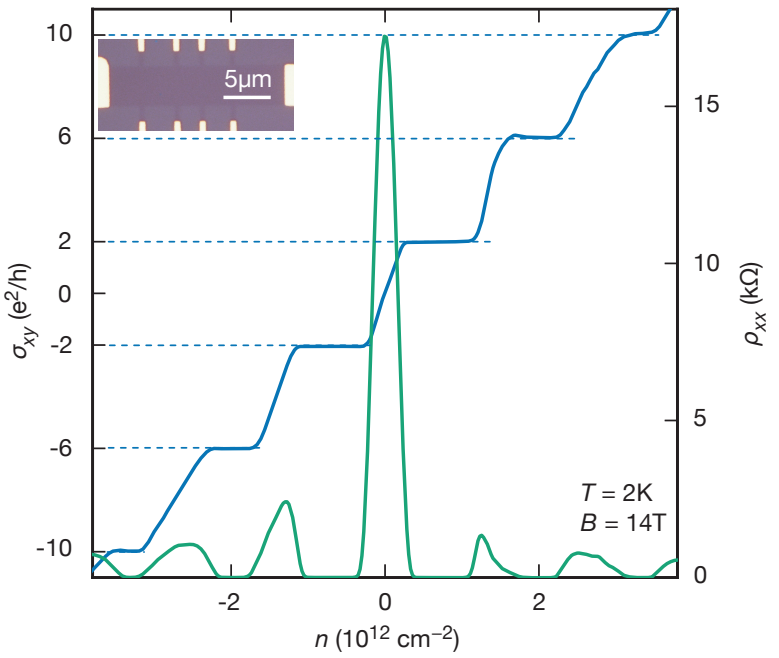

Fig. 3.3 QHE for massless Dirac fermions. Hall conductivity σ_{xy} and longitudinal resistivity ρ_{xx} as a function of the concentration for the graphene on SiO_2 Hall bar shown in the inset (device G1).

invariance guaranteeing particle-hole symmetry. As a result, σ_{xy} is an odd function in energy [48]: regardless of the magnetic field, the $n = 0$ LL is so robust that $E_0 = 0$ as long as the sublattice symmetry is preserved. It results in the first plateau at exactly $\sigma_{xy} = \pm ge^2/2h$ and the other plateaus for σ_{xy} increasing(decreasing) by an amount of ge^2/h as E_f crosses the next electron (hole) LL. Another effect of the Berry phase is that each scattering process and its time-reversal pair are dephased by π, resulting in destructive interferences. This suppresses back-scattering, allowing long electron mean free paths [17, 61, 62].

Finally, there is another exciting effect resulting from the pseudospin component. It is the unusual direction of the motion of charge carriers, locked into this extra quantum mechanical degree of freedom. As a result, backscattering is impossible as backward motion is locked into a different valley than forward motion. From that point of view, graphene is similar to the conducting surface layer of topological insulators, where the direction of motion of carriers is locked to their spin. This pseudospin can drive a so-called valley current in graphene devices [63]. That means that an applied voltage across the device gives rise to counter-propagating streams of carriers in graphene's two band structure valleys. The build-in chirality allows demonstrating an all-electrical valleytronic circuit. This valley-polarisation is understood in terms of the Berry phase: carriers in graphene accumulate a Berry phase of $\pi$for momentum-space circumnavigation of either valley (due to the 2π rotation of pseudospin locked to momentum). This is similar to the Aharonov-Bohm phase from a path in the field-free region around a solenoid.

3.1.3 Effective mass of Dirac fermions

The non-zero Berry's phase is related to the vanishing mass at the Dirac point. The effective carrier mass m_c can be extracted from the temperature dependence of the SdHOs at small magnetic fields. One may write the amplitude of the SdHOs $\Delta\sigma$ using the standard [11] expression of section 2.2.3.1:

$$\Delta\sigma = \frac{T}{\sinh(2\pi^2 k_B T m_c/\hbar e B)}. \tag{3.11}$$

Figure 3.4a shows the dependence of the fundamental SdHO amplitude versus temperature for two different carrier densities. From this is extracted the effective mass m_c as a function of the carrier density, shown in figure 3.4b.

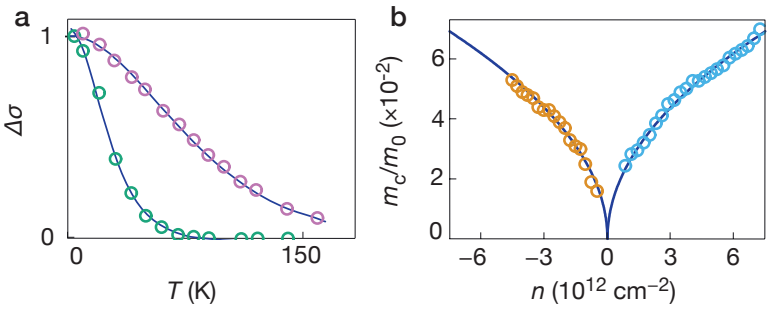

Fig. 3.4 Cyclotron mass in graphene. a) SdHO amplitude $\Delta\sigma(T)$ yielding $m_c = 0.069m_0$ and $m_c = 0.023m_0$. **b)** extracted cyclotron mass $m_c(n)$. Solid curves: best fits in both panels. Extracted from ref. [53].

The cyclotron mass is defined in the semiclassical approximation [2] as:

$$m_c = \frac{E_f}{v_f^2} = \frac{k_f}{v_f}. \tag{3.12}$$

As $n = k_f^2/\pi$, the effective mass carrier has a square root carrier density dependence, consistent with measurements:

$$m_c = \frac{\sqrt{\pi n}}{v_f}. \tag{3.13}$$

Fitting the square root dependence of the cyclotron mass allows us to estimate the Fermi velocity: $v_f \approx 1 \times 10^6\,\mathrm{m\,s^{-1}}$ and the hopping parameter $\gamma_0 \approx 3\,\mathrm{eV}$. A parabolic (Schrödinger) dispersion would imply a constant cyclotron mass. Therefore, the experimentally measured effective mass carrier dependence provides unequivocal evidence of the existence of massless Dirac fermions in graphene.

3.1.4 Multilayer graphene

When exfoliating graphene from highly-oriented pyrolitic graphite, it is possible to extract flakes with two or more atomic planes. In that case, the interlayer coupling changes the band structure drastically, depending on the

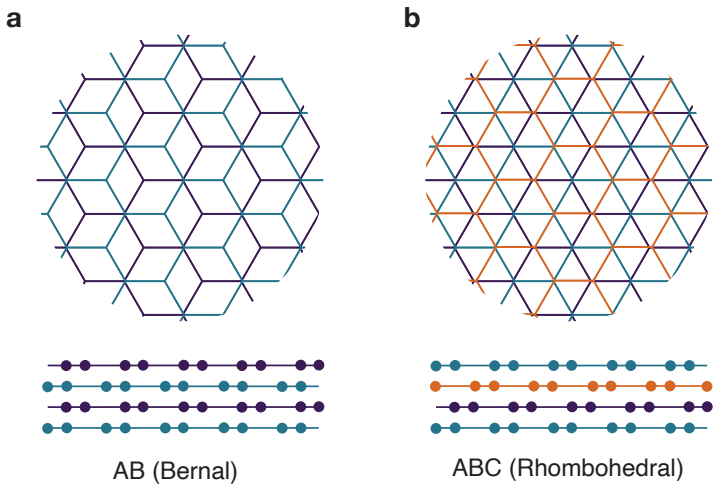

Fig. 3.5 Stacking arrangements for multilayer graphene. a) Bernal multilayer (most stable configuration) and **b)** Rhombohedral multilayer (less stable)

number of layers and the stacking order (see fig 3.5), as well as experimental results that can be measured. Bilayer graphene is probably the most interesting because, in experiments, the integer quantum Hall effect shows different anomalies like the one reported in monolayer graphene (e.g. LL are observed for $\nu = gn$) [50, 64, 65], and a gap opens between the conduction and valence band [66]. The magnitude of the gap can be enhanced upon applying an asymmetry between the two layers that can be achieved experimentally through a perpendicular electric field D (see methods, subsection 4.2.2 for details), as shown in figure 3.6. This gap can be inverted by switching the direction of the electric field D.

The size of the gap can be found from the temperature dependence of the resistivity ρ at sufficiently high temperatures [67–72]. At low temperature (below 50 K), ρ at the CNP in bilayer graphene is saturating at relatively low values, incompatible with a large gap found in theory papers [50, 66]. This was, at first, explained by remnant charge inhomogeneities resulting in enhanced hopping conductivity weakening the T dependence. However, it is now understood that the subgap conductivity originates from valley-polarised currents [73, 74]. These theories enable the valley current to propagate through the charge-neutral bulk, and was confirmed experimentally with significant non-local resistance measurements [63, 75–78].

More interestingly, stacking boundaries and edges also support a topological current. Applying two electric fields of two opposite directions in two neighbouring regions can create helical metallic quantum valley Hall kink states along the gates' boundary [78–80]. These quantum valley Hall kink states are chiral in each valley: the group velocities of the two valleys K and K' are opposite and immune from backscattering in the absence of a valley-mixing scattering mechanism. As a result, these domain boundaries can carry a ballistic valley-polarised current over long distances without dissipation [78, 79]. We will later see that such domains can be engineered with a twist angle instead of opposite polarity neighbouring gates, yielding similar results.

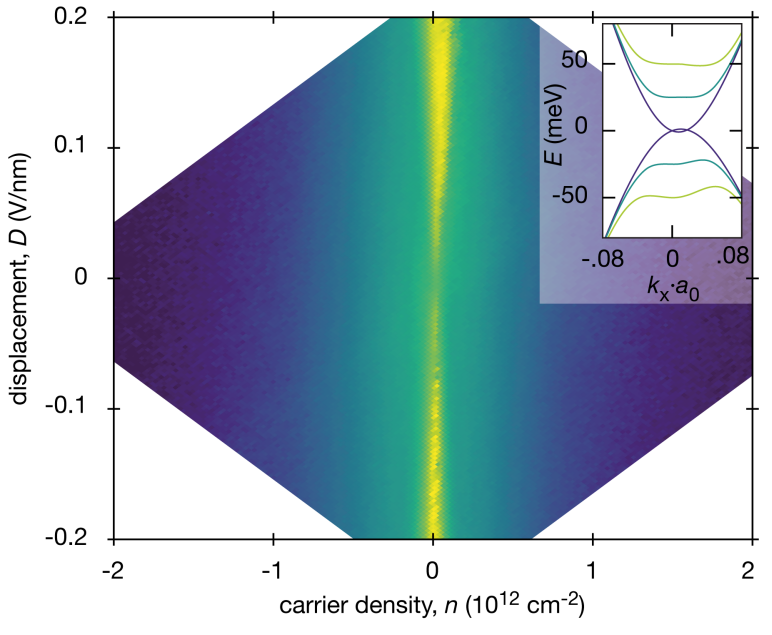

Fig. 3.6 $R_{xx}(n, D)$ **map** of a double-gated Bernal bilayer measured at 10 mK. Logarithmic colour scale: indigo (10 Ω) to yellow (4 kΩ). Inset: band structure near the Brillouin zone corner (a_0 =2.46 Å), for different perpendicular electric field, extracted from ref. [81]. Interlayer potentials of 100 meV (green), 50 meV (teal) and 0 meV (navy). Measured on device G2.

Finally, there have recently been a few interesting phenomena in rhombohedral graphene trilayers [82] and tetralayer [83] attributed to correlation physics. In thicker rhombohedral graphite films, we showed that the electronic states in the bulk are gapped, with electronic transport dominated by surface states [84]. It is particularly interesting as the topological nature of these surface states allows us to observe the quantum Hall effect despite a non-negligible thickness. Similarly to Bernal bilayer graphene, the application of a perpendicular displacement field opens a gap. However, the gap is present without the electric field for thinner films (below 10 layers). The study of trilayer films has benefitted from research on thicker films, showing a ground-state phase diagram characterised by a gap at high displacement, and phase transitions between different ferromagnetic isospin phases [85]. At lower temperatures, superconducting phases can be observed in a symmetric state, characterised by a spin-singlet pairing mechanism, and in a half-filled band with an unknown mechanism attributed to spin-triplet pairing [86]. This research gave a fresh look over Bernal bilayer graphene, where similar isospin phases could be observed, with superconductivity in a comparable half-filled band [81], attributed to a spin-triplet mechanism. These newer studies make Bernal bilayer a system of broad interest with a potential revival in the years to come.

3.2 van der Waals heterostructures

The exfoliation of graphene in 2004 was followed by increased efforts in exfoliating and measuring other two-dimensional atomic crystals [16] such as hexagonal boron nitride (hBN), transition metal dichalcogenides such as molybdenum disulphide (MoS_2) or tungsten diselenide (WSe_2) or various layered oxides. The most exciting about these new 2D materials is that it opens a venue to create

new materials by artificially stacking different layers on top of one another, as one would do with LEGOs [16, 18, 87]. In such a system, the compound layers are coupled with weak van der Waals forces, small enough to allow exfoliation but strong enough to keep the stacks together. Choosing the appropriate compounds, number of layers and alignment allows controlling the physical properties with the dream to create materials on demand. This thesis focuses on two types of van der Waals heterostructures based on graphene and hBN, exploring aligned graphene-hBN and twisted graphene multilayers.

3.2.1 Graphene-hBN heterostructures

One of the simplest and most studied van der Waals (vdW) heterostructures is graphene encapsulated between two hexagonal boron nitride (hBN) crystals. hBN has a hexagonal structure similar to graphene, where the A and B sublattices are occupied by boron and nitrogen atoms. Importantly, hBN is extracted from bulk crystals and is a direct bandgap semiconductor with an absorption band in the ultraviolet [88]. This makes it an ideal material to act as a dielectric encapsulation for graphene [89]. Encapsulation of graphene with hBN protects it from extrinsic disorder [90, 91], resulting in drastic improvements in the electronic quality compared to suspended devices, with micrometre-scale ballistic transport limited only by edge scattering. Soon after, hBN was used as gate dielectrics [92, 93] and tunnel barriers [94, 95]. Using hBN in such heterostructures gave new momentum to old phenomena, such as negative differential conductance [96, 97] and Coulomb drag [63], to allow exciton superfluids [98–100] or magnetophonons [101, 102].

There is a particular case when the crystallographic axes of graphene and hBN are intentionally aligned. The small (1.8%) mismatch between graphene and hBN crystal lattices results in a long-range periodic moiré potential. Superlattice potentials on 2DEGs have been a long-sought experimental platform [103], but efforts in this direction have been hampered by strong disorder and difficulties in creating potentials at the 10-100 nm range. The potential created by aligned hBN avoids these problems and results in profound changes in the electronic spectrum with a Brillouin-zone folding of the energy dispersion strongly modifying the electronic spectrum [87, 104–113]. This induces several original features like secondary Dirac points and van Hove singularities.

3.2.1.1 Secondary Dirac fermions

Figure 3.7 shows a typical density dependence of the resistivity ρ_{xx} and the Hall resistivity ρ_{xy} in a typical graphene-hBN superlattice. At zero doping, there is a sharp peak in the resistivity that corresponds to the main Dirac point. At $n =$

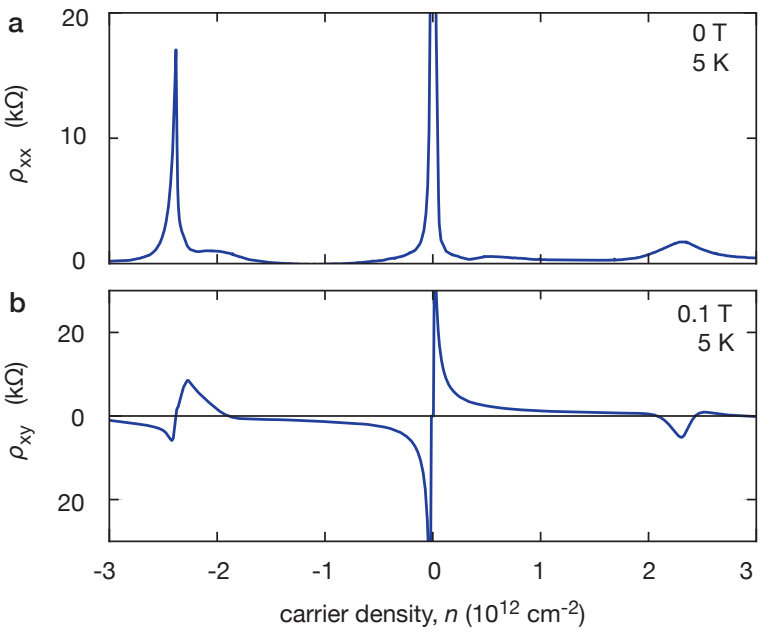

Fig. 3.7 Transport properties of Dirac fermions in a graphene-hBN superlattice (D6 with θ =0.3°) with positive and negative values of n correspond to electrons and holes, resp. **a)** longitudinal resistivity $\rho_{xx}(n)$ showing two satellite peaks around $2.5 \times 10^{12}\,\mathrm{cm}^{-2}$. **b)** Hall resistivity $\rho_{xy}(n)$ changes sign three times for both electrons and holes.

$\pm 2.5 \times 10^{12}\,\mathrm{cm}^{-2}$, there are two satellite peaks spaced equally from the main neutrality point. It was noted that the secondary DP is much more pronounced for holes than for electrons. Additionally, the Hall resistance diverges as the density approaches the ρ_{xx} maxima and shows a sign reversal. The sign change reflects a change of the majority carrier, both in the conduction and valence band. This feature is consistent for the main Dirac point and the satellite peaks.

It can be explained as the following: because of the band folding induced by the long-range superlattice, graphene-hBN superlattices possess a new set of Dirac points, a consequence of the Bloch's theorem. These secondary Dirac fermions have a reduced Fermi velocity [105, 114]. Figure 3.8a shows the calculated band structure of graphene-hBN superlattices with clear secondary Dirac points both in the conduction and valence bands. If the two crystal layers are close to perfect alignment, then the superlattice period is about 14 nm, which results in secondary Dirac points occurring at energies around 0.2 eV from the main Dirac point of graphene. That happens for electrostatic gating densities around $3 \times 10^{12}\,\mathrm{cm}^{-2}$. Note that the energies at which the secondary Dirac points occur are angle-dependent (see section 4.4 for further details. Indeed, the satellite peaks in the transport measurements correspond to the resistance as the Fermi level is tuned through the secondary Dirac points, consistent with the change of carrier types. This was confirmed via localised density of state (STM) measurements [106].

However, measurements of the Hall resistance also show three non-trivial changes of sign when tuning the Fermi energy away from the main Dirac point, both for holes and electrons. This is due to the presence of van Hove singularities in the density of states [105].

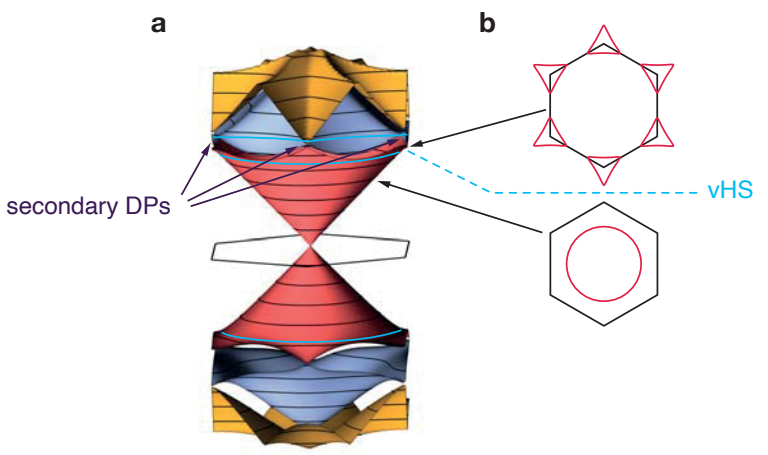

Fig. 3.8 Band structure of graphene aligned with hBN. a) band, extracted from ref. [115], with secondary Dirac points in the conduction band. **b)** fermi surface from the main miniband with vhs between a single annular fermi sea and six fermi pockets (indicated as red contours).

3.2.1.2 van Hove singularities

Van Hove singularities (vHS) are singularities in the density of state. They are usually associated with a change in the band curvature, i.e. a transition from an electron-like to a hole-like behaviour; therefore, $\rho_{xy}(\text{vHS}) = 0$. In condensed matter systems, they are attractive for a few reasons: electron-phonon coupling can get enhanced near a vHS, enabling superconductivity or affecting its stability [116]. They can also mediate deformations of the Fermi surface. Notably, vHS can trigger Landau-type symmetry-breaking phase transitions in the presence of deformations [117]. However, in most bulk materials, the chemical potential is not easily tunable across a wide enough energy range, so observing vHSs has been relatively rare. In graphene systems, however, there are promising candidates. In the graphene band structure (see figure 3.2), the merging of Dirac cones at the M point leads to vHSs, but the energy required to access them (2.7 eV) places them out of reach with transport experiments.

For graphene-hBN superlattices (or, more generally, twisted graphene multilayers), vHSs are readily accessible. In this system, they emerge due to electron-electron interactions strongly affecting the band structure. The vHSs occur whenever the Fermi surface topology changes, as shown in figure 3.8b. In graphene-hBN superlattices, the van Hove singularities happen on each side of the secondary Dirac points, and correspond to the edge of a new miniband, coinciding with a carrier type inversion. Close to the vHS, the Hall density $n_H = -B/eR_{xy}$ diverges logarithmically. However, this is not the case if the band becomes malleable as a result of strong electron-electron interactions [118, 119]. In that case, a gap may open upon crossing the vHS, meaning that n_H resets to zero in the newly created empty band, and beyond this point, n_H will increase linearly with n but offset from the origin of the gap [120]. This will be discussed in the case of Brown-Zak fermions in chap. 6.

3.2.1.3 Correlated states

Finally, the moiré potential created by hBN alignment can also influence the zero energy dispersion near charge neutrality. The superlattice potential breaks the inversion symmetry protecting graphene's spectrum [109, 121], an effect that could open a band gap at the Dirac point [105] with fundamental topological applications. For example, it was possible to create Berry curvature hot spots close to the Dirac point of graphene, allowing the study of topological currents [63].

For other graphene multilayers, hBN alignment also showed dramatic band modifications. For the case of Bernal bilayer graphene, hBN results in fractional quantum Hall states [122, 123]. In other twisted bilayer graphene, alignment [124, 125] results in ferromagnetism and a large anomalous Hall effect. Similarly, flat electronic bands emerged in rhombohedral graphene trilayers aligned with hBN, with correlated insulators appearing at integer filling of the moiré superlattice cell [126–128].

3.2.2 Twisted graphene layers

Similarly to stacking hBN on top of graphene with a controlled alignment, improvements in fabrication techniques have enabled new physics by twisting two graphene layers with a relative twist angle between them. This is very different from the case of semiconductor heterostructures like GaAs/AlGaAs, where the relative orientation between the two components cannot be controlled. The most visible structure is the formation of a relatively long-range moiré pattern. However, there have been rich physics due to modifications of the band structure induced by smaller Brillouin zones.

3.2.2.1 Small angles: atomic reconstruction

In the usual graphene monolayer, it is reasonable to assume that the lattice is rigid: the length of the C–C bond is always exactly 1.42 Å, and the interlayer distance is always 2.2 Å. This picture breaks down in twisted bilayer graphene, where the interlayer spacing can change depending on the stacking order, and relaxation effects can significantly affect the in-plane bonds. In bilayer graphene, there can be three different stacking types, each with a different energy profile, leading to different strains affecting the nearest-neighbour and interlayers distances(see fig. 3.9). The first type is *AA stacking* (or BB stacking), corresponding to almost perfect vertical alignment of the same sublattice site from both layers. The second stacking type is *AB stacking*, corresponding to the A atoms from the top layer vertically aligned with the B atoms from

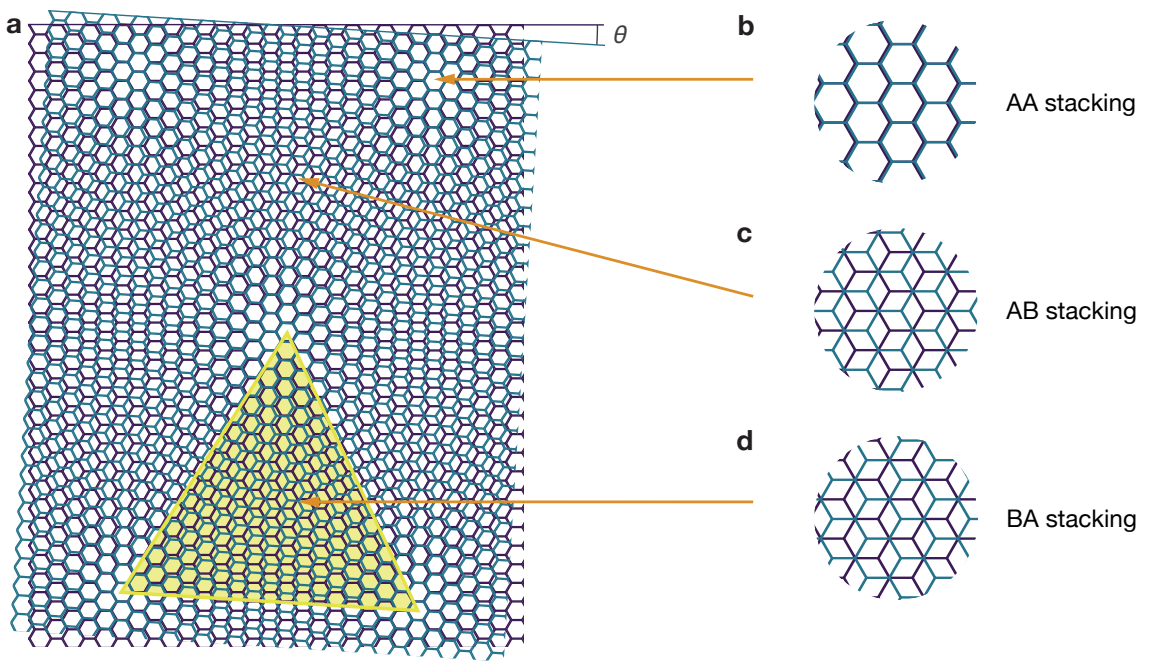

Fig. 3.9: Stacking types of graphene bilayers. a) long-range Moiré created by a twist angle θ, showing different stacking arrangements: AA **(b)**, AB **(c)** and BA **(d)**. For minimal values of θ, AB/BA regions will increase in size to span the entire yellow triangle of the panel (a).

the bottom layer. In this configuration, the top B and bottom A atoms are not aligned with any other atom. The last configuration is *BA stacking*: B atoms from the top layer are aligned with A atoms from the bottom layer. Similarly to AB stacking, the top A and bottom B atoms are not aligned.

In most cases, these three domain types would span over the same area, and the local stacking order evolves smoothly between the three cases. However, the AA stacking type is less energetically favourable because atoms sit directly on one another. As a result, the interlayer distance d_{AA} tends to be larger than $d_{\mathrm{AB}} = d_{\mathrm{BA}}$. It results in corrugations calculated to be as large as 30 pm [129, 130]. As a result, it becomes energetically favourable to distort atomic positions to minimise the span of AA regions, relaxing into AB-like stacking order that increases in size. However, distortion is also energetically costly; therefore, the equilibrium state results from a compromise between stacking energy and strain energies. Below twists angles of 0.4°, the importance of strain-induced atomic reconstruction becomes so great that it leads to the creation of giant triangular domains of commensurate alternating Bernal stacking [131]. These domains have been observed through AFM [131, 132] and also in transport measurements [133, 134].

These giant triangular Bernal domains are separated by domain walls that can be seen as incommensurate solitons [135, 136], or alternatively called kink states [79]. They correspond to local changes in the stacking configurations so that AB and BA domains have opposite Chern numbers under a uniform perpendicular electric field. The boundaries support valley-polarised helical

states [137–142]. As a result, whenever the AB/BA domains are gapped (see subsection 3.1.4), these gapless domain walls become the only conducting channel. This was shown in spatially-resolved density of states (STM) [132] and in electronic transport through the emergence of Aharonov-Bohm oscillations [134].

3.2.2.2 Magic angles

For large twist angles, the Dirac cones of the two graphene layers are relatively far away in momentum space, therefore their low-energy dispersion is minimally affected by the presence of a second layer. This is particularly useful to minimise corrugations and is a promising avenue for studying decoupled systems (see chapter 10). As the angle is decreased, the Dirac cones are moved closer to one another and interactions between electrons in the two neighbouring bands become non-negligible, resulting in interlayer hybridisation and renormalisation of the Fermi velocity. For a series of twist angles dubbed *magic angles*, the Fermi velocity v_f vanishes [143]. The largest of these magic angles happens at $\theta = 1.1°$.

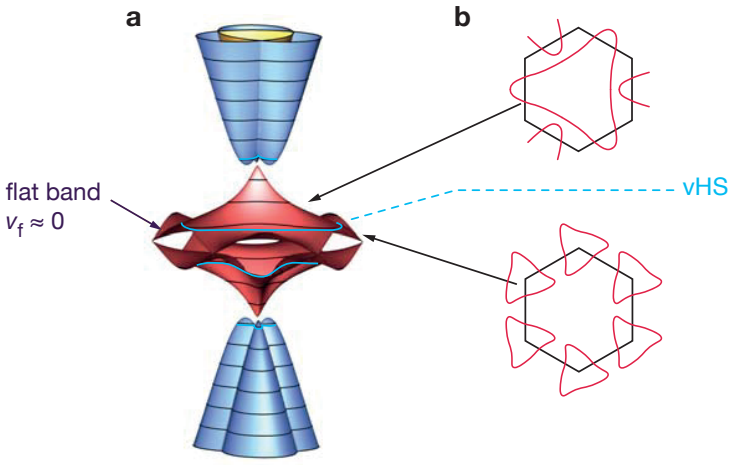

Fig. 3.10 Band structure close to the magic angle. a) band structure calculated for $\theta = 1.2°$. Extracted from ref. [115]. **b)** Fermi pockets above and below the first van Hove singularity. Extracted from ref. [144].

Figure 3.10a shows that, close to the magic angle, the Fermi velocity in the mini Brillouin zone corners is zero. At the magic angle, the states surrounding the K points are all concentrated in a very narrow energy range — a phenomenon called a flat band. The flatter the band, the greater the separation with higher energy bands. These flat bands emerged as a rich platform for exploring electronic interaction, giving rise to phases among which correlated insulators [145–147], superconductors [148–151], Chern insulators [119, 152] or orbital magnets [124, 125, 150]. In the first works, researchers used the Mott model to explain the origin of these states [153], but this was quickly contested, highlighting the need to include non-local correlations, which the Mott model does not [154, 155].

As shown in figure 3.10b, the spectrum contains two van Hove singularities separating a high-energy single-pocket Fermi surface centred at the Γ point from a low-energy two-pocket Fermi surface centred on the K and K' points [119, 144].

3.3 Proximity effect in graphene devices

Mesoscopic devices combining graphene and superconductors have been studied since the early days of graphene research [156–159], but it was only when ballistic devices [36,91,160–163] were achieved that sensible effects could be observed. The realisation of one-dimensional edge contacts, both with MoRe [163] and NbTi [36], was instrumental in observing of unusual Andreev physics.

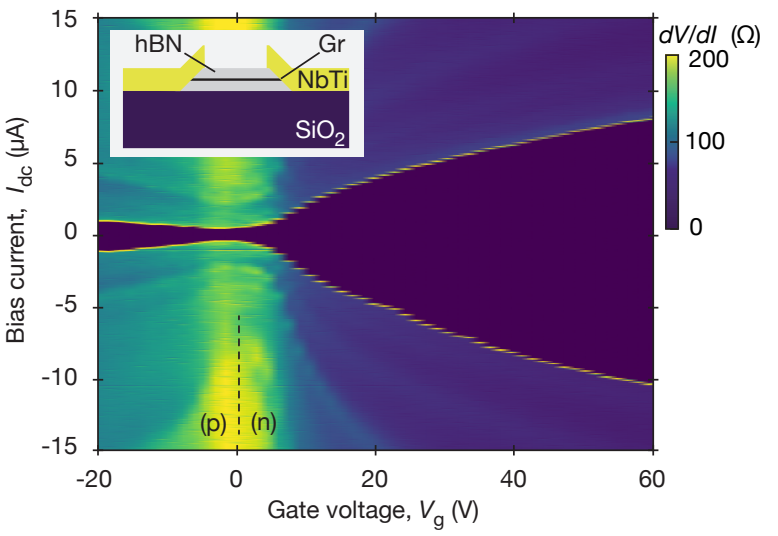

Fig. 3.11 $dV/dI(V_\mathrm{g}, I_\mathrm{dc})$ **map for a twisted bilayer graphene junction (device Jb)** measured at T_bath =300 mK. Inset: sketch of highly transparent 1D contacts. Map measured by Mengjiang Zhu.

In ballistic graphene Josephson junctions, it became possible to tune the density and change the type of junction. There are three different phases, as shown in figure 3.11: a hole-doped (p) regime with a relatively small critical current (I_c), in which phase-coherent interferences of electrons and holes carrying the Andreev bound states could be observed. The formation of a Fabry-Pérot cavity due to contact-induced n-type doping causes these interferences. This effect is also responsible for shifting the neutrality point to negative V_g, an effect most pronounced for devices with a small (<300 nm) graphene strip. Note that, the doping is uniform for ballistic devices away from the metal interface. There is also an electron-doped (n) regime with a much larger critical current, reaching values in excess of 10 µA at high gate voltages [36, 163]. At the DP there is a transition between ballistic and pseudo-diffusive evanescent transport [164]. The Fabry-Pérot behaviour consists of standing waves between the contacts, leading to pronounced oscillations in $R_\mathrm{n}(V_\mathrm{g})$ [36, 158, 159] in ballistic devices (not shown here).

For ballistic devices, the proximity effect can be observed in graphene junctions up to L =2.5 µm, with critical currents reaching densities above 5 µA m^{-1} in the shortest junctions at high electron density. High values of the critical current I_c indicate ballistic transport and low contact resistance (see section 4.5.1 for more information). In principle, I_c can reach the following value at low magnetic fields:

$$I_c = \alpha\Delta/eR_n, \tag{3.14}$$

where in theory $\alpha \approx 2.1$, although in experimental works, α was found to be slightly smaller [36]. For long junctions, one may also write the critical current as a function of the Thouless energy E_{Th} rather than the gap: $I_c \approx E_{Th}/eR_n$. Equation 3.14 can be inserted into the usual sinc dependence of the critical current resulting in an even lower critical current. Remember that the superconducting gap Δ depends on B, as shown in eq. 2.48, and R_n increases with the magnetic field.

3.3.1 Specular Andreev reflection

One of the peculiarities of graphene-superconductor junctions is that they can support specular Andreev reflections. In a standard NS interface, momentum conservation imposes that $p_e \sin\theta_i = p_h \sin\theta_r$ where p_e and p_h are total momenta of electrons and holes, θ_i is the incident angle of the incoming electron, and θ_r is the angle of the reflected electron. In that case, $E_f \gg \Delta$ and the reflected hole remains in the conduction band of the normal metal, thus carrying a momentum opposite to the incident electron, leading to a nearly perfect retro Andreev reflection: $\theta_r \approx -\theta_i$. This is different in the semimetal graphene, where the Fermi energy can be tuned such as $E_f \leq \Delta$. The energy difference between an electron and its reflected hole in an Andreev process is $2eV$. In the semimetal, the reflected hole can now appear in the valence band and thus travel in the same direction alongside the interface ($\theta_r > 0$). Whenever $E_f = 0$, the angle of the reflection is equal to the incidence angle: $\theta_r = \theta_i$. This phenomenon is called specular Andreev reflection [165,166] and was shown experimentally whenever $\Delta > eV > E_f$, with a crossover between intraband and interband Andreev reflection through tuning of the Fermi energy via electric field effect [167].

3.3.2 Josephson effect in moderate magnetic fields

With the use of graphene Josephson junctions and particularly ballistic devices, it has become possible to observe the persistence of superconductivity

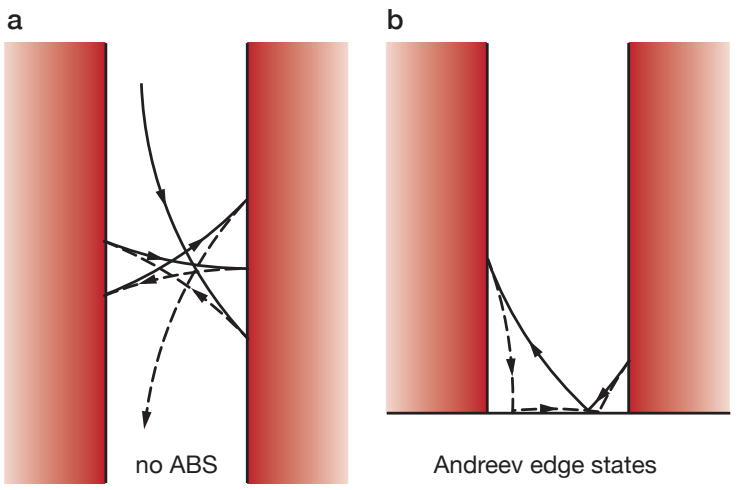

Fig. 3.12 Andreev states in moderate magnetic fields. a) open trajectories unable to form ABS. **b)** near-edge trajectories can close due to disorder-induced scattering, forming mesoscopic Andreev edge states. Figure adapted from ref. [36]

in moderate fields. In usual Josephson junctions, the proximity effect would be destroyed by perpendicular magnetic fields of the order of 10 mT, with a conventional Fraunhofer behaviour (see eq. 2.52). In graphene devices, it was shown that the supercurrent survives at fields up to 1 T, with small pockets ($I_c \approx$40 nA) appearing and disappearing randomly as a function of the magnetic field and carrier concentration.

In a moderate magnetic field, ballistic trajectories are bent, corresponding to cyclotron orbits. The trajectories combining segments of these orbits for $B > B*$, bouncing between the superconducting contacts, do not carry a supercurrent because the path to form such orbits is infinite (see an example of such orbits in fig. 3.12a.). The shape of these trajectories is quite general, forming never-ending star-shaped reflections unable to form Andreev bound states.

This is different near the junction edges. As shown in figure 3.12b, scattering from the graphene edges allows the existence of cyclotron orbits with close ends at both NS interfaces. As a result, despite having different lengths for the paths of electron and hole trajectories, these can transfer Cooper pairs via the formation of mesoscopic Andreev edge states [36]. This condition results in chaotic ballistic billiards [28, 168], with a current capacity close to the universal quantum limit $I_q \approx e\Delta/h$. Consequently, deviations from the standard Fraunhofer dependence can be observed from magnetic fields of $B \geq$5 mT, where random pockets of supercurrent appear instead of the usual oscillatory pattern, persisting up to 1 T.

3.3.3 Chiral Andreev edge states

The situation changes as soon as the cyclotron orbit becomes small enough to fit between the contacts without touching the interface ($r_c < L/2$). In graphene, this corresponds to:

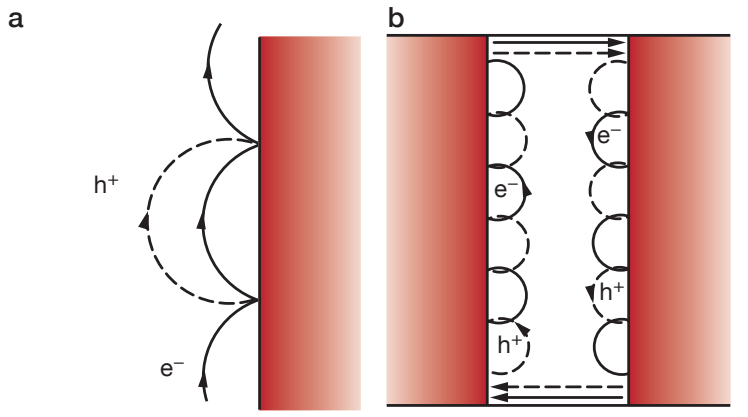

Fig. 3.13 Chiral Andreev edge state. a) semi-classical picture of electron and hole trajectories along the SN interface. **b)** CAES along the junction contour, forming hybrid electron-hole edge modes.

$$B > \frac{2\hbar}{eL}\sqrt{\pi n(V_g)}. \tag{3.15}$$

In this condition, transferring Cooper pairs through the usual Andreev bound states is impossible. There have been some proposals to engineer superconductivity in the quantum Hall regime through chiral Andreev edge states (CAES) [169–175], with early searches in semiconductor heterostructures focused on magneto-conductance oscillations [176–181]. More recently, ballistic graphene devices offered a new paradigm, allowing to mediate the supercurrent through chiral quantum Hall states [182–187].

In the quantum Hall regime, the bulk of the junction is gapped by Landau quantisation, and charge carriers can only be transferred from one contact to another via edge states. In this condition, both electron and hole states propagate in the same direction on a single edge; hence two edges are necessary to carry a supercurrent. It is a different situation from the mesoscopic Andreev edge states in moderate magnetic fields that are each carrying their own supercurrent. Semiclassically, CAES can be seen as skipping orbit trajectories in which an electron turns alternatively into a hole and then back into an electron upon successive Andreev reflections on the superconducting contacts (see fig. 3.13). Quantum mechanically, the CAES are a combination of Andreev reflections and quantum Hall edge states, yielding fermionic modes hybridising electrons and holes states, propagating chirally on opposite sides of the device and along with the graphene-superconductor interface. They are supported by superconducting correlations induced in quantum Hall edge states. These CAES allow to couple the two graphene-vacuum edge, allowing a supercurrent to be transmitted through the junction. These chiral Andreev edge states have first been observed as superconducting pockets in the quantum Hall regime [182] and later induced as either crossed Andreev reflection in the $\nu = 2$ QH state [184], inter-Landau level Andreev reflection in a split zeroth LL [185]. More recently, interferences of these chiral Andreev states were demonstrated through conductance oscillations on the quantum Hall edge [186].

Part II
Experimental methods

Blank page

Chapter 4
Measurement of van der Waals heterostructures

In this chapter, I present the main techniques used in this thesis. I start with basic electronic transport techniques and then give details on simple ways to measure a twist angle. However, different parameters can be varied throughout our experiments, namely the magnetic field B and the temperature T. The magnetic field is a straightforward parameter to vary thanks to a superconducting coil placed around the device, therefore not detailed here. The interested reader can refer to refs [188, 189]. The temperature necessitates more careful operation and is the next chapter's subject.

4.1 Transport measurements

The principles of electron transport are simple. Most of the time, it involves applying a small current in a device and measuring a voltage drop between two voltage probes while varying external parameters such as magnetic or electric field, charge density, temperature, bias current, etc.

4.1.1 Hall bars

Most devices are shaped as Hall bars to allow multiple measurement configurations (see, e.g. fig 4.1). In the standard measurement, a current I flows through the channel while a voltage drop V is measured from the side contacts. Such a configuration allows measuring the longitudinal resistance $\rho_{xx} = V/(IL/W)$ where W is the width of the channel and L is the distance between the voltage probes. Another typical geometry (that can be measured simultaneously) is the Hall geometry, consisting of measuring V_{xy} between contacts opposite to the sheet. The Hall resistance $R_{xy} = V_{xy}/I$ is directly related to the carrier density n (see eq. 2.19).

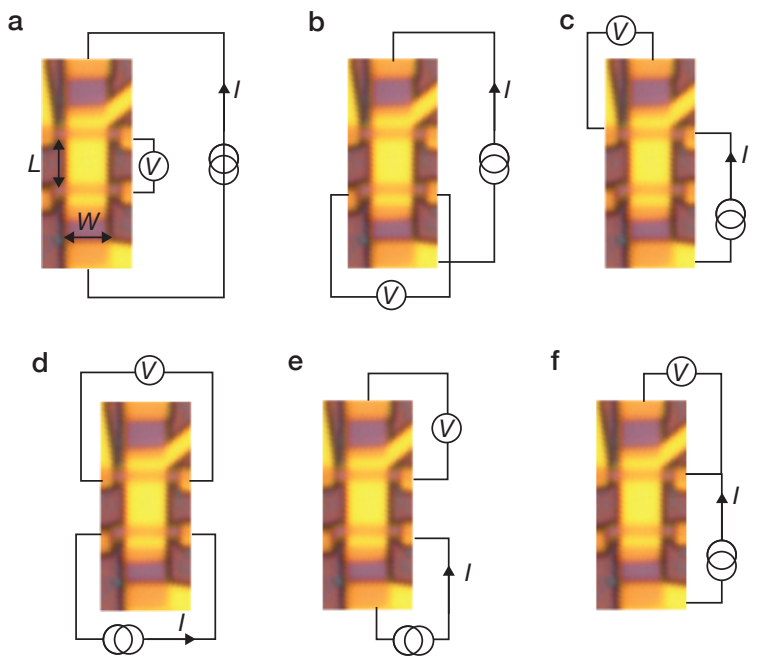

Fig. 4.1 Local and non-local measurement configurations. a) longitudinal resistance geometry. **b)** Hall geometry. **c)** bend geometry. **d and e)** non-local geometries and **f)** 3-probe geometry.

The bend geometry can also test if a device is ballistic. It is a modified version of the cross devices presented in section 2.2.2.1. Additionally, non-local geometries allow separating charge currents (dominating in local measurements) from the ohmic contribution. Two possibilities exist here. The first one (see fig. 4.1d) allows for minimising the ohmic contribution resulting from non-uniform current distribution in order to isolate the current contribution originating from flavour (spin or valley) diffusion [63, 190, 191]. In the second geometry (fig. 4.1e), the ohmic contribution is not small, allowing to probe magnetic focusing.

Finally, there is another configuration for which no results are shown in this thesis, but that is nonetheless useful to characterise devices prior to advanced measurements. It is the 3-terminal resistance which helps measuring contact resistance. Here, the idea is that the measured voltage drop V corresponds to the contact if the resistance of the region of the sample neighbouring the contact is small enough and can be ignored. This is the case in most graphene devices away from the neutrality point.

4.1.2 Lock-in technique

The devices presented in this thesis were measured with the standard lock-in measurement technique. One uses a low-frequency AC current passing through the device and measures the voltage drop at this exact frequency with the lock-in amplifier. Most of the results were acquired using the MFLI lock-ins from Zurich Instruments. The relatively high input impedance (10 MΩ) allows measuring signals without a preamplifier.

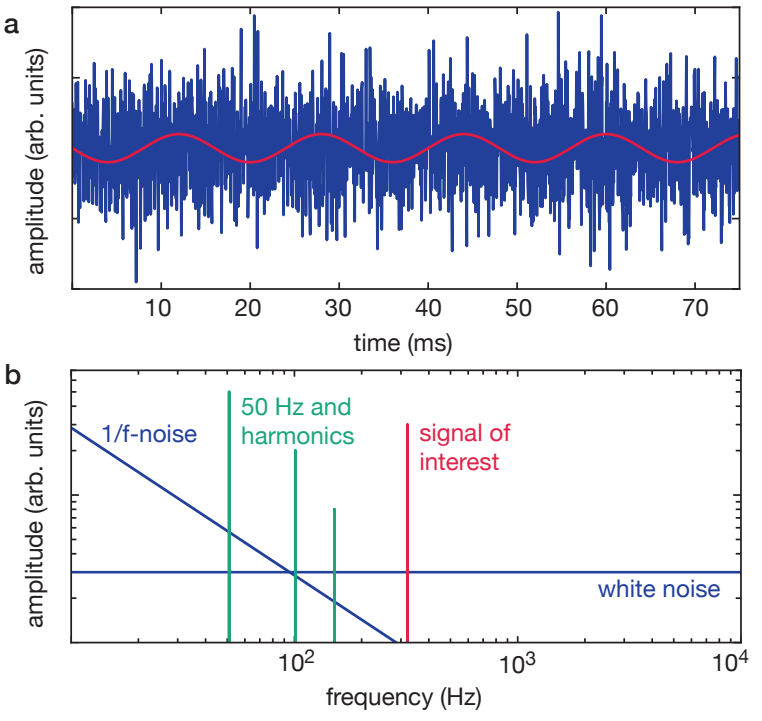

Fig. 4.2 Example of a noisy signal. a) signal at the frequency of interest (red) is hidden under a noisy background (blue). **b)** noise spectrum of the signal in (a). The measurement frequency (red) is chosen in a region with small background noise away from 50 Hz harmonics.

A lock-in amplifier is a powerful instrument that allows to measure AC voltages below the noise level. For example, the lock-in can extract the red signal in figure 4.2. The principle of operation is simple but necessitates a few precautions in choosing the proper signal. The lock-in uses a reference signal at frequency f_{ref} and multiplies the measured voltage drop by this reference signal. This measured signal is the sum of sine waves with different frequencies (see, e.g. the spectrum in fig. 4.2) of the form:

$$V_{\mathrm{meas}} = \sum_{\mathrm{i}} V_{\mathrm{i}} \sin\left(\frac{2\pi}{f_{\mathrm{i}}} t\right), \tag{4.1}$$

where V_{i} is the amplitude of the contribution with frequency f_{i}. This measured signal is then multiplied by the reference signal. Most of the time, f_{i} is not equal to f_{ref}, so the resulting product is zero. Whenever $f_{\mathrm{i}} = f_{\mathrm{ref}}$, the two functions are in phase, and the average value is equal to half the product of the amplitudes. This value is acquired. Adding filtering options allows getting rid of higher harmonics of f_{ref}. In practice, the multiplication by the reference signal is carried out over a finite time (the time constant, a parameter that can be varied between measurements, usually taken an order of magnitude above the signal periodicity).

A few precautions must be taken to ensure a good signal/noise ratio. The reference frequency is usually chosen in a region with small background noise, that is, in a clean white noise region above the 1/f noise and sufficiently far away from the 50 Hz harmonics from the mains. However, in mesoscopic devices, high contact resistances may result in AC coupling to parasitic capacitances, therefore altering the measurement at higher frequencies. For this reason, f_{ref} will be chosen as small as possible, usually between 30 Hz and 130 Hz.

4.1.3 Differential resistance

On top of the lock-in AC reference signal, a small DC current may be added to measure a differential resistance $\mathrm{d}V/\mathrm{d}I$. As a result, a current $I = I_0 + I_1 \sin(2\pi t/f_{\mathrm{ref}})$ is passed through the device under test, with a voltage $\mathrm{d}V$ measured by the lock-in amplifier. Here, I_0 is a DC component, and I_1 is the amplitude of the AC signal at the reference frequency. This technique is particularly useful for measuring superconducting characteristics (in Josephson junctions or superconducting devices) but also allows for inducing finite drift velocity. The measured voltage at the device's contacts can be approximated in the first order:

$$V(I) = V(I_0) + \left.\frac{\mathrm{d}V}{\mathrm{d}I}\right|_{I=I_0} I_1 \sin\left(\frac{2\pi}{f_{\mathrm{ref}}}t\right), \tag{4.2}$$

that is the sum of a DC component $V_{\mathrm{dc}} = V(I_0)$ and an AC signal $V_{\mathrm{ac}} = \mathrm{d}V/\mathrm{d}I|_{I=I_{\mathrm{dc}}}\, I_1 \sin(2\pi t/f_{\mathrm{ref}})$. The differential resistance is then defined as $dV/dI \equiv V_{\mathrm{ac}}/I_{\mathrm{ac}}$.

It is possible to source and measure the DC component with the same lock-in amplifier as the AC signal: the MFLI has auxiliary DC outputs and multiple demodulators; one of them can be set up with f_{ref} =0 Hz. Alternatively, I have used Keithley nanovolt-meters. As the lock-in sources a constant voltage, and the resistance of the devices under test can vary dramatically during a measurement, one has to use a voltage-current converter that usually places a high resistance in series. I used a homemade stabilised current source that takes the AC and DC voltages as input and mixes them to generate a low-noise source current. The amplitude of the AC excitation is chosen between 1 nA and 10 nA, depending on the measurement. The DC current is usually swept during measurements in a range from 10 nA to 20 000 nA.

4.2 Electrostatic effects

4.2.1 Field-effect

Graphene —and more generally, the van der Waals heterostructures based on graphene presented in this thesis— shows an ambipolar field effect. It means that both charge carrier types can be induced by applying a positive or negative gate voltage V_{g} through a dielectric on one side of the heterostructure. Applying a DC voltage across the gate induces a surface charge density:

$$n = \frac{V_{\mathrm{g}}\epsilon_0\epsilon_{\mathrm{r}}}{de}, \tag{4.3}$$

where d is the dielectric thickness (3.3 for hBN, 3.6 for SiO_2), ϵ and ϵ_r are the permittivities of free space and the dielectric, respectively. The gate acts as a parallel plate capacitor, where the voltage applied to the conductor (n-doped Si, Au or graphite) across a thin dielectric (hBN or SiO_2) induces a charge of opposite sign in the van der Waals heterostructure so that the Fermi level can be moved in the conduction or valence band. This is possible because our van der Waals heterostructures are thin enough so that the surface charge is not screened throughout the device, as is usually the case for bulk metals. That way, carrier concentrations of $1 \times 10^{13}\,\mathrm{cm}^{-2}$ can be achieved, corresponding to a shift of the Fermi level of about 350 meV.

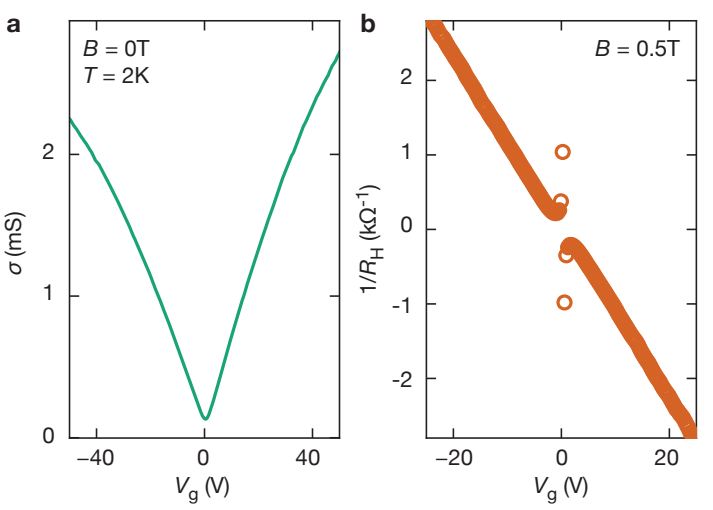

Fig. 4.3 Changes in graphene conductivity and Hall coefficient. a) σ as a function of the gate voltage V_g and **b)** Hall coefficient R_H. Curves were measured on the same device as figure 3.3 (G1).

Consequently, it is possible to define the gate capacitance C_g as $\epsilon_0\epsilon_r/d$. As the thickness d of the dielectric is relatively hard to measure, it is possible to find it experimentally by measuring the Hall resistance $R_H = B/ne$. That way, it becomes possible to extract both the type (electrons or holes) and density n of carriers. One can find the gate capacitance:

$$C_g = \frac{1}{V_g R_H}. \tag{4.4}$$

Additionally, it was experimentally shown [51, 53] that the DC conductivity of graphene depends linearly on the gate potential V_g (see fig 4.3a) for both polarities except close to the neutrality point and at high biases, and the Hall resistance changes sign at $V_g = V_0 \approx 0$, indicating that a substantial concentration of electrons (holes) can be induced by positive (negative, resp.) gate voltages. The gate capacitance calibration can only be found for regions where $\sigma \propto n$ and $R_H \propto 1/V_g$ in other heterostructures to avoid charge inhomogeneities and non-linear effects. The relation $\sigma \propto n$ can be obtained from the linearised Boltzmann equation [192, 193] with a relaxation-time approximation [50]:

$$\sigma_{xx} = 2\frac{e^2}{h}\frac{\pi v_f^2}{u_0^2}n, \tag{4.5}$$

where u_0 is the strength of the scattering potential. From that point, the carrier mobility can be extracted with the usual relationships (see chapter 2). For example, the mobility in graphene was found to be $15.000\,\mathrm{cm^2\,V^{-1}\,s^{-1}}$ in 2005 [53] and rapidly increased over several million with increasing device size and fabrication quality [19].

Consequently, the gate capacitance will be extracted by measuring the Hall resistance while sweeping the gate voltage under a small perpendicular magnetic field. If the regions of non-linearities are too large, the Hall coefficient can be corroborated by sweeping the magnetic field at a fixed gate voltage.

4.2.2 Double gates

For systems asymmetric relative to the axis orthogonal to the 2D structure (twisted trilayers, Bernal bilayer graphene, rhombohedral trilayer graphene, etc.), it is sometimes interesting to apply an electric field perpendicular to the plane. This can also be achieved through field-effect gating. Having two gates on top and bottom of the heterostructures allows to apply and tune independently and simultaneously the carrier concentration n and the transverse electric field D (called displacement field for reasons detailed in chapter 9). In a dual gate configuration, the application of a top (V_{tg}) and bottom (V_{bg}) gate voltages results in:

$$n = \frac{C_{\mathrm{tg}}V_{\mathrm{tg}} + C_{\mathrm{bg}}V_{\mathrm{bg}}}{e}, \tag{4.6}$$

and

$$|D| = \left|\frac{C_{\mathrm{tg}}V_{\mathrm{tg}} - C_{\mathrm{bg}}V_{\mathrm{bg}}}{2\epsilon_0}\right|, \tag{4.7}$$

where C_{tg} and C_{bg} are top and bottom gate capacitances, respectively. The sign of D is chosen arbitrarily for different heterostructures.

4.3 Thermal activation

In transport experiments, a resistance temperature dependence translates into a characteristic energy. For the case of insulating or semiconducting materials, one expects the resistance to decrease with temperature, as thermal excitations allow excitations to hop from the valence to the conduction band through the bandgap. Figure 4.4a shows an example of an insulating state in multilayer rhombohedral graphite, for which the resistivity decreases with temperature. The resistance change follows a function of the bandgap Δ:

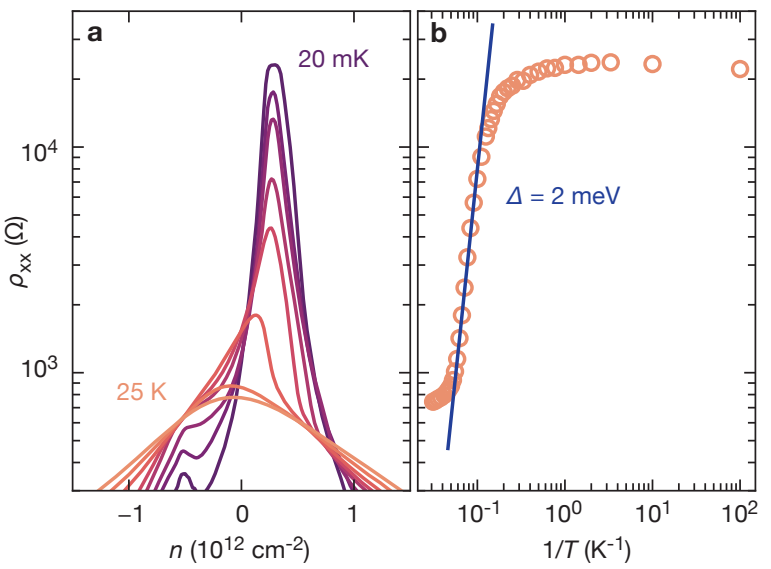

Fig. 4.4 Example of thermal activation gap of few-layer rhombohedral graphite. a) resistivity as a function of the density measured for various temperatures. **b)** Corresponding Arrhenius plot showing a 2 meV gap. Data published in ref. [84].

$$\log \rho = \log \rho_0 + \frac{\Delta}{2k_B T}. \tag{4.8}$$

By plotting ρ as a function of $1/T$ in a log-log scale (Arrhenius plot), it is possible to find the size of the gap Δ through a linear fit of $\rho(T)$. Here Δ is considered constant, but in reality, it depends on the temperature. In the region where $\rho(T)$ is linear, however, it can be assumed constant.

4.4 Moiré superlattices

In usual devices, small vibrations during fabrications, inaccuracies in transfer temperature, intrinsic strains within devices or other experimental variations can result in a twist angle between two atomic layers that is different from the target angle. On top of that, the twist angle can vary within a stack of about 0.5° within a few µm. The best way to know the twist angle in a device is to measure it via transport measurements. Here I give a few details on how to extract it. The first subsection introduces the relationship between the twist angle and the superlattice unit cell based on ref. [106] and the subsequent subsections give two methods to extract the twist angle from measurements.

4.4.1 Twist angle

All the lattices composing the van der Waals heterostructures presented in this thesis are hexagonal, so the resulting Moiré lattice is also hexagonal. In the reciprocal space, the resulting lattice points are shown in figure 4.5. Here we consider two reciprocal lattice vectors corresponding to two layers with a twist angle and a lattice constant difference. The reciprocal lattice vector corresponding to the first layer (in blue, e.g. graphene) can be chosen as $\boldsymbol{b}_1 = 2\pi/a(1, 0)$, where a is the lattice constant. The second layer has a lattice

mismatch $\delta = a_1/a_2 - 1$, where a_1 and a_2 denote the lattice constant of the top and bottom layers, respectively. As a result, the corresponding reciprocal lattice vector is shorter by an amount $(1+\delta)$, yielding (see red hexagon, e.g. hBN): $\boldsymbol{b}_2 = 2\pi/[(1+\delta)a](\cos\theta, \sin\theta)$. For the case of a twisted graphene bilayer, we note that $\delta = 0$, hence $|\boldsymbol{b}_2| = |\boldsymbol{b}_1|$.

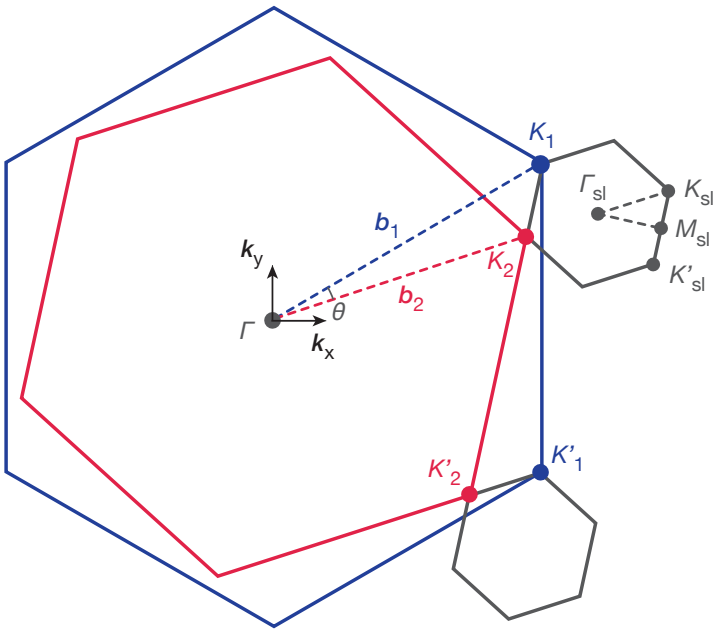

Fig. 4.5 The reciprocal space superlattice is defined by vectors $\boldsymbol{b}_1$ and $\boldsymbol{b}_2$. The shortest distance between these vectors forms the superlattice wavevector $\boldsymbol{k}_{\mathrm{sl}}$.

It is possible to define a new reciprocal lattice constant $\boldsymbol{k}_{\mathrm{sl}}$, defined as the vector connecting the two sets of reciprocal lattice vectors: $\boldsymbol{k}_{\mathrm{sl}} = \boldsymbol{b}_2 - \boldsymbol{b}_1$:

$$\boldsymbol{k}_{\mathrm{sl}} = \frac{2\pi}{a}\left(1 - \frac{\cos\theta}{1+\delta}, -\frac{\sin\theta}{1+\delta}\right). \tag{4.9}$$

Therefore, the superlattice wave vector is:

$$K_{\mathrm{sl}} = |\boldsymbol{k}_{\mathrm{sl}}| = \frac{2\pi}{a}\sqrt{\left(1 - \frac{\cos\theta}{1+\delta}\right)^2 + \left(\frac{\sin\theta}{1+\delta}\right)^2}, \tag{4.10}$$

and consequently, the superlattice periodicity in real space can be found as:

$$\lambda_{\mathrm{sl}} = \frac{2\pi}{\sin(\pi/3)K_{\mathrm{sl}}} = \frac{a(1+\delta)}{\sqrt{2(1+\delta)(1-\cos\theta)+\delta^2}}. \tag{4.11}$$

For the case of two identical layers twisted by an angle θ, this relationship simplifies to:

$$\lambda_{\mathrm{sl}} = \frac{a}{2\sin(\theta/2)}. \tag{4.12}$$

For small twist angles, i.e. $\theta \ll 1$, one can write:

$$\lambda_{\mathrm{sl}} \approx \frac{a}{\theta}. \tag{4.13}$$

In short, the superlattice wavelength is inversely proportional to the twist angle for small twists. As a result, it is virtually possible to achieve arbitrarily large superlattice periods (e.g. several 100 nm) for van der Waals heterostructures combining two layers with the same lattice constant (e.g. twisted bilayer graphene). However, for lattices with a mismatch δ, the maximum superlattice periodicity is limited by δ. The larger the lattice mismatch, the smaller the maximum wavelength. For example, on graphene-hBN superlattices, the largest possible superlattice constant is λ_{sl} =14 nm.

4.4.2 Position of secondary neutrality point

Two methods can be used to find the twist angle in graphene heterostructures—the first consists of looking at the position of secondary neutrality points.

The area of a superlattice unit cell spans a quadrilateral with sides λ_{sl}:

$$\mathcal{A}_{\mathrm{sl}} = \lambda_{\mathrm{sl}}^2 \cos\frac{\pi}{3} = \frac{\sqrt{3}}{2}\lambda_{\mathrm{sl}}^2. \tag{4.14}$$

For this area, each superlattice band in the reduced Brillouin zone can accommodate a carrier concentration $n_0 = 4/\mathcal{A}_{\mathrm{sl}}$, where 4 corresponds to the spin and valley degeneracies of graphene. As a result, the full filling carrier concentration is:

$$n_0 = \frac{8}{\sqrt{3}\lambda_{\mathrm{sl}}^2}. \tag{4.15}$$

Whenever the unit cell is filled with 4 electrons, that is, for n_0, a secondary Dirac point occurs [106–109]. As a result, the twist angle can be found as:

$$n_0 = \frac{8\sqrt{2(1+\delta)(1-\cos\theta)+\delta^2}}{\sqrt{3}a(1+\delta)}, \tag{4.16}$$

i.e.

$$\theta = \arccos\left[1 + \frac{\delta^2}{2(1+\delta)} - \frac{3a^2}{128}(1+\delta)n_0^2\right], \tag{4.17}$$

where n_0 is the position of the secondary Dirac point, a is the lattice constant (0.246 nm for graphene), and δ is the lattice mismatch (1.8 % for hBN). This relationship can be simplified for $\delta = 0$:

$$\theta = 2\arcsin\left[\frac{a}{8}\sqrt{\sqrt{3}n_0}\right], \tag{4.18}$$

and, for small angles $\theta \ll 1$:

$$\theta \approx a\sqrt{\frac{\sqrt{3}}{8}n_0}. \tag{4.19}$$

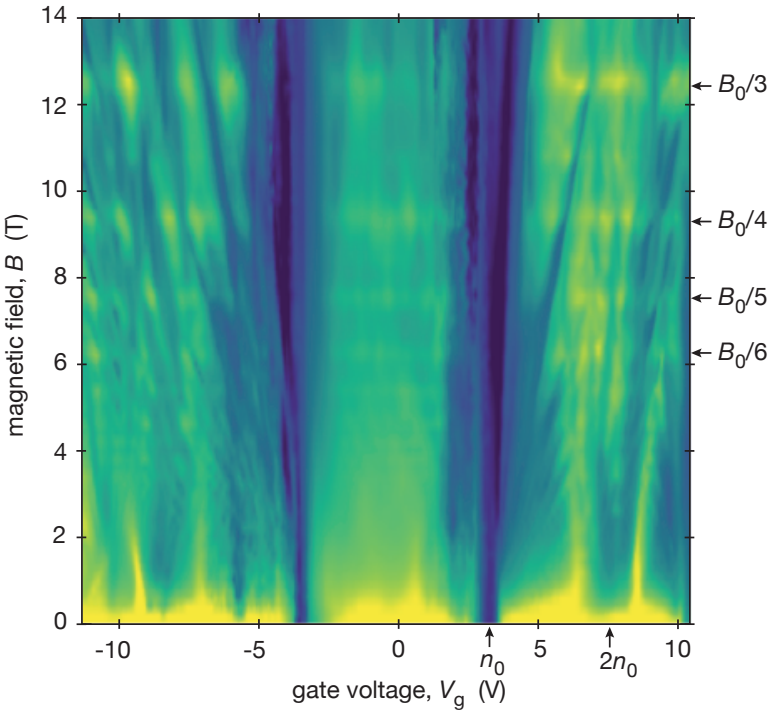

Fig. 4.6 Conductivity map of a 1.22° monolayer-bilayer graphene (device M1). B_0 and n_0 allowing extraction of the twist angle are highlighted.

4.4.3 Aharonov-Bohm effect or Brown-Zak fermions

Another way to find the twist angle is to use the Aharonov Bohm effect. Whenever the flux piercing through the area $\mathcal{A}_{\text{sl}}$ (or a multiple of) corresponds to one flux quantum $\phi_0 = h/e$, a set of magneto-oscillations periodic in B develop [134]. Aharonov-Bohm oscillations correspond to interferences between electronic states propagating along loops formed at the boundary between different superlattice cells.

As a result, the domain area is given by:

$$\mathcal{A}_{\text{sl}} = \phi_0/B_0, \tag{4.20}$$

where B_0 is the magnetic field corresponding to 1 flux quantum piercing one $\mathcal{A}_{\text{sl}}$. As the Aharonov-Bohm oscillations are periodic in B, it is possible to use ΔB in this formula. However, if $\mathcal{A}_{\text{sl}}$ becomes relatively small, B_0 might be too high to be found experimentally. In that case, it is possible to use a consequence of the Aharonov-Bohm effect: the Brown-Zak oscillations [194]. Whenever the flux piercing through the area $\mathcal{A}_{\text{sl}}$ is a multiple of the flux quantum, a set of magneto-oscillations develop, corresponding to conductance maxima, periodic in $1/B$. In that case, one may extract B_0 from the observation of conductance maxima at several fractions of B_0 (e.g. $B_0/2$, $B_0/3$, $B_0/4$).

Once B_0 is found, either for Aharonov-Bohm or Brown-Zak oscillations, one gets:

$$\theta = \arccos\left[1 + \frac{\delta^2}{2(1+\delta)} - \frac{\sqrt{3}}{4}a^2(1+\delta)\frac{B_0}{\phi_0}\right], \tag{4.21}$$

that can be reduced for the case of $\delta = 0$ as:

$$\theta = 2\arcsin\left[a\sqrt{\frac{\sqrt{3}}{8}\frac{B_0}{\phi_0}}\right]. \tag{4.22}$$

Figure 4.6 shows an example of Brown-Zak oscillations and secondary neutrality points to extract the twist angle in twisted monolayer-bilayer graphene.

4.5 Josephson junctions

4.5.1 Transparency of the NS interface

Before measuring a Josephson junction, it is important to characterise the quality of the contacts, that is, the superconductor-normal metal interface. Previous studies have shown that peculiar effects can only be expected in ballistic junctions. Here I explain a few methods to measure the quality of an NS interface based on measurements of the contact resistance R_c and multiple Andreev reflections (MAR).

4.5.1.1 Contact Resistance

For a ballistic device with superconducting contacts, the resistance in the normal state R_n (either at sufficiently high current bias to remove the superconductivity or at sufficiently high temperature) should be given by:

$$R_\mathrm{n} = R_\mathrm{q} + 2R_\mathrm{c}. \tag{4.23}$$

Here R_c is the contact resistance at each N-S interface and R_q is the quantum ballistic resistance, that can be determined for mesoscopic devices with the Sharvin formula (see section 2.2.1):

$$R_\mathrm{q} = \frac{1}{gM}\frac{h}{e^2}. \tag{4.24}$$

Here $g = 4$ comes from graphene's spin and valley degeneracy, M is the number of propagating electron modes: $M = \mathrm{int}(2W/\lambda_\mathrm{f})$ with the Fermi wavelength λ_f defined as $\lambda_\mathrm{f} = 2\sqrt{\pi/n} = 2\sqrt{\pi/C_\mathrm{g}V_\mathrm{g}}$. Figure 4.7 shows an example of the normal resistance for a graphene Josephson junction with the ballistic limit R_q indicated as a dashed line. In this kind of measurement, it is usually impossible to extract the carrier density through Hall measurements. As a result, one should find C_g from Landau fans or SdHOs at high n. The contact resistance is found by subtracting the quantum ballistic resistance from the normal resistance: $R_\mathrm{c} = (R_\mathrm{n} - R_\mathrm{q})/2$.

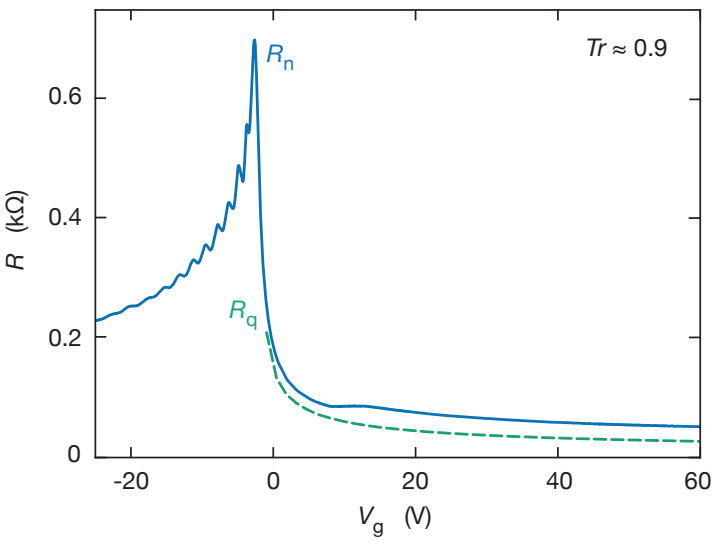

Fig. 4.7 Typical behaviour of a ballistic SGS junction: R_n measured at high T =12 K. The dashed curve shows calculated $R_q(n)$. Measured on device Ja

Once the contact resistance is known, it is possible to characterise the average transmission probability coefficient Tr given by [195]:

$$Tr = \frac{R_q}{R_q + R_c}. \tag{4.25}$$

For all the Josephson junctions presented in this thesis, I obtain Tr between 0.7 % and 0.9 %, corresponding to a highly transparent interface. Note that for hole dopings ($V_g < 0$), R_n is significantly higher, indicating a much smaller Tr as p-n junctions appear at the contacts, leading to partial reflection of electronic waves, resulting in the creation of Fabry-Pérot cavities [36].

4.5.1.2 Multiple Andreev reflections

In a Josephson junction without a decoherence mechanism in the normal metal, whenever $eV_{dc} < 2\Delta$, an Andreev pair traverses the junction successively from the left to the right superconductor and again from the right to the left superconductor. The number of times the Andreev reflection can happen is reflected as oscillatory features in the DC IV characteristics. It is easy to understand that this can be used to measure the superconducting contacts' transparency. Let us consider the behaviour of a single electron.

If $|eV_{dc}| > 2\Delta$, there can be no Andreev process; an electron normally escapes from the left contact to the right contact. As V_{dc} is decreased and $|eV_{dc}| = 2\Delta$, at least a single Andreev reflection becomes possible; an effective charge of $2e$ is transferred through the Josephson junction. When $|eV_{dc}| = 2\Delta/2$, two Andreev reflections happen simultaneously at each NS interface. Similarly, n Andreev reflections happen simultaneously whenever:

$$|eV_{dc}| = \frac{2\Delta}{n}, \qquad n \in \mathbb{N}. \tag{4.26}$$

Experimentally, these multiple Andreev reflections (MAR) result in a sharp dip in $\mathrm{d}V/\mathrm{d}I$ at values of V_{dc} given by equation 4.26 for superconductors with

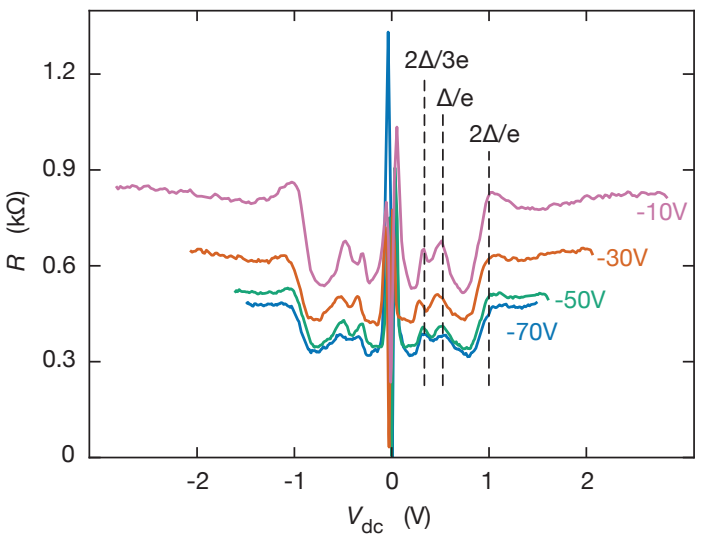

Fig. 4.8 Multiple Andreev reflections in a NbTi-graphene-NbTi Josephson junction: differential resistance $DV/\mathrm{d}I(V_{\mathrm{dc}})$ for different gate voltages, showing maxima associated with MAR. Curves were measured in a bilayer graphene junction at 300 mK. (device J8)

a long coherence length. For other superconductors, such as the NbTi used this thesis' junctions, MAR are observed as peaks in the $\mathrm{d}V/\mathrm{d}I$ characteristics [196]. The amplitude of these features (after normalising the differential resistance by the normal resistance) is independent of L/ξ, where L is the length of the junction and ξ is the coherence length in the normal metal: $\xi = \sqrt{\hbar D/\Delta}$ (with the diffusive constant $D = v_{\mathrm{F}}\ell/2$) [157]. The number of MAR experimentally observable depend on two factors: thermal noise and transparency of the NS interfaces.

The transparency dependence of the MAR can also give an estimate of the transmission coefficient [156, 157, 195], but this method is not as reliable as it depends on the chosen theoretical model [197, 198]. This method is not used here, but we note that the consistent observation of MAR further confirms the excellent transparency of the NS interfaces.

4.5.2 Extraction of the supercurrent density

In section 2.3.2, we assumed that the supercurrent density inside the junction is uniform, yielding a single-slit Fraunhofer interference in $I_{\mathrm{c}}^{max}(B)$. It is not always the case. Here I explain the method developed by Dynes and Fulton [199] and adapted for 2DEGs [200] to recover the supercurrent density from $I_{\mathrm{c}}^{max}(B)$ measurements.

Let us consider a 2D Josephson junction of width W in the x-direction and length L in the y-direction. The current propagates in the y-direction, and the density is assumed to vary only along the x-direction. One may write a normalised magnetic field β as:

$$\beta = \frac{2\pi(L + L_{\mathrm{c}})B}{\phi_0}, \tag{4.27}$$

where L_{c} is the length of the superconducting leads (to account for flux focusing, a consequence of the Meissner effect) and $\phi_0 = h/2e$ is the magnetic

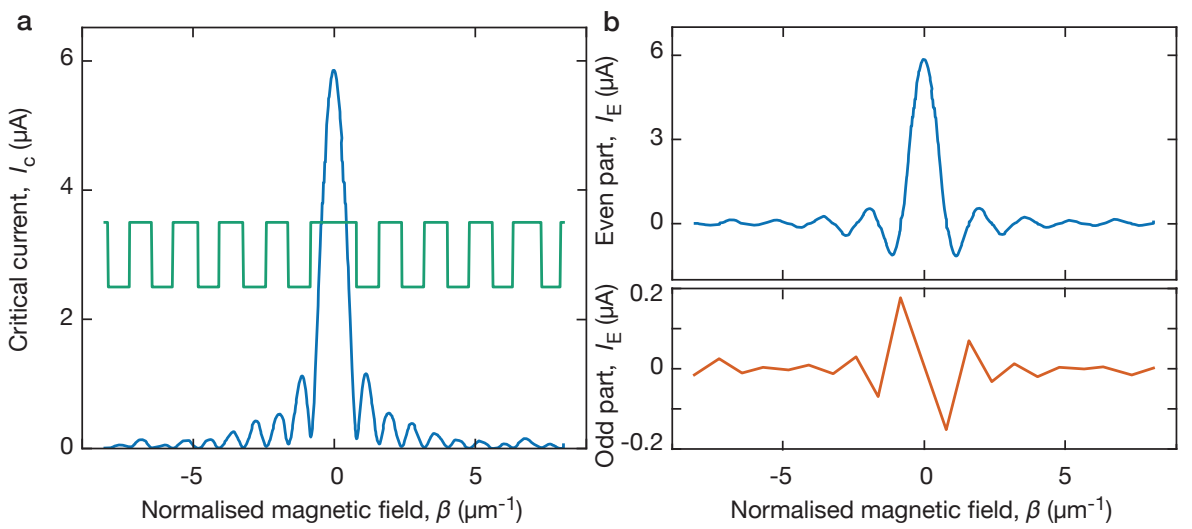

Fig. 4.9: Current reconstruction from extracted $I_c^{max}(\beta)$. a) extracted $I_c^{max}(\beta)$ from device Ja (blue) and flipper function (arb. units, green). **b)** $I_E(\beta)$ and $I_O(\beta)$ found using the Dynes and Fulton method.

flux quantum. For a given supercurrent density profile $J_S(x)$, the critical current is a complex function $\mathcal{J}_c(\beta)$ that can be found as the Fourier transform over the width of the junction:

$$\mathcal{J}_c(\beta) = \int_{-\infty}^{+\infty} dx J_S(x) e^{i\beta x}. \tag{4.28}$$

Experimentally, we can extract the magnitude of the complex supercurrent density $I_c^{max}(\beta) = |\mathcal{J}_c(\beta)|$. In order to recover $J_S(x)$, it is, therefore, necessary to find the complex critical current, that is, an even $I_E(\beta)$ and an odd part $I_O(\beta)$, such as:

$$\mathcal{J}_C(\beta) = I_E(\beta) + iI_O(\beta). \tag{4.29}$$

Let's start with an even current density: $I_O(\beta) = 0$. In that case, the odd part of $e^{i\beta x}$ vanishes in the integral of equation 4.28; one may write:

$$\mathcal{J}_C(\beta) = I_E(\beta) = \int_{-\infty}^{+\infty} dx J_E(x) cos\beta x, \tag{4.30}$$

where $J_E(x)$ is a real and positive symmetric distribution. As a result, $\mathcal{J}_C(\beta)$ is also real and typically alternates between positive and negative values at each zero crossing. One may recover the exact $I_E(\beta)$ by flipping the sign of every lobe in the observed $I_c^{max}(\beta)$.

Now let's add the imaginary, odd component on top of this function. We assume that $J_O(x)$ is relatively small. Its Fourier transform writes:

$$I_O(\beta) = \int_{-\infty}^{+\infty} dx J_O(x) \sin \beta x. \tag{4.31}$$

As a consequence, $I_E(\beta)$ dominates the observed critical current $I_c^{max}(\beta) = \sqrt{I_E^2(\beta) + I_O^2(\beta)}$ everywhere except at the minima. I obtain $I_E(\beta)$ by multiply-

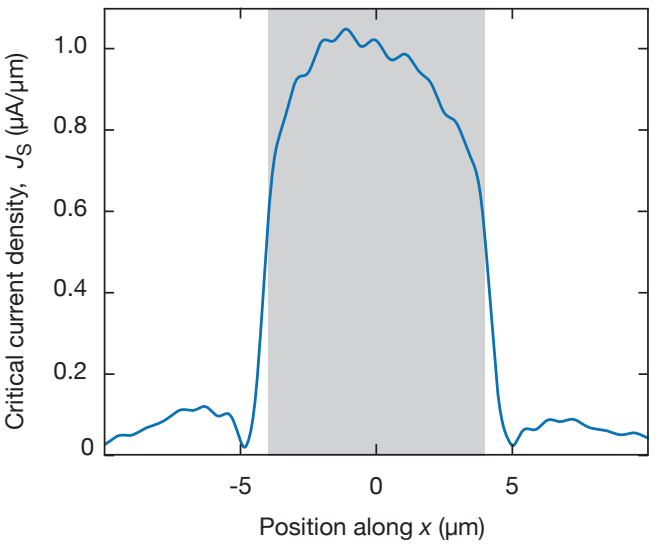

Fig. 4.10 Reconstructed critical current density for device Ja, based on the intermediary steps of figure 4.9.

ing $I_c^{max}(\beta)$ with a flipping function that switches the sign between consecutive lobes of the envelope function. When $I_E(\beta)$ is minimal but non-zero, $I_O(\beta)$ is non-negligible and dominates the critical current. $I_O(\beta)$ is then approximated by interpolating linearly between the minima of $I_c^{max}(\beta)$ and flipping the sign between lobes. Once $\mathcal{J}_c(\beta)$ is found, a Fourier transform over a range b of β gives the current density profile:

$$J_S(x) = \left| \frac{1}{2\pi} \int_{-b/2}^{b/2} d\beta \mathcal{J}_c(\beta) e^{-i\beta x} \right|. \tag{4.32}$$

Figure 4.9 shows the different steps to reconstruct the current distribution. Figure 4.10 shows the result of such a reconstruction in a Josephson junction made with minimally twisted bilayer graphene, and etched with a width W =500 nm.

4.5.3 RF irradiation

Shapiro steps are measured by irradiating a Josephson junction with microwave excitations. These are generated from an RF source (R&S SMB 100A) and transmitted to the inner vacuum chamber (IVC) via semi-rigid coaxial cables made of stainless steel (above 4 K) and NbTi alloy (below 4 K). The RF lines are thermally anchored to the different stages of the dilution refrigerator, using RF attenuators at different stages: 10 dB at 70 K and 4 K, 6 dB at 0.7 K and 0.3 K and 3 dB at the mixing chamber stage (10 mK), for a total attenuation of 35 dB. At the bottom end, an antenna consisting of an open-ended cable irradiates the device from roughly 1 cm. The transmission to the vacuum is enough to observe all the relevant effects.

Blank page

Chapter 5
Cryogenic techniques

Varying the temperature can allow an understanding of the behaviour of graphene heterostructures. Throughout my PhD, I have been in charge of a newly acquired dilution refrigerator, its maintenance and optimisation. This chapter introduces a few properties of liquid helium and mixtures of helium isotopes and showcases the operation of the dilution refrigerator.

5.1 Liquid Helium

Historically, low-temperature physics started with attempts to liquefy and solidify some gases. One of the aims was to find whether permanent gases exist. Nitrogen and Oxygen were first liquefied in 1883, enabling temperatures below 100 K. These advances were rapidly followed by a wide range of gases, the pinnacle of which was hydrogen, condensed by Dewar in 1898, allowing to reach temperatures as low as 13 kelvin. In 1908, Heike Kamerlingh Onnes liquefied the last gaseous element to be discovered: helium at 4.2 K. He later reached 0.83 K by pumping the vapour above a boiling ^{4}He bath. Accessing lower temperatures required more fundamental technologies, like magnetic refrigeration or adiabatic demagnetisation, that were proposed in the late 1920s to reach millikelvin temperatures temporarily. Later, another method was proposed, based on the dilution of the rare isotope ^{3}He by the common isotope ^{4}He: dilution refrigeration, allowed to reach a few millikelvin.

5.1.1 Isotopes & phase diagram

Here I cover a few properties of the two most stable isotopes of liquid helium at the heart of refrigeration techniques. ^{4}He is the most stable helium isotope. Its nucleus is composed of two protons and two neutrons. As each has anti-parallel nuclear spins, the total nuclear spin is $I = 0$: ^{4}He is a boson. On the other

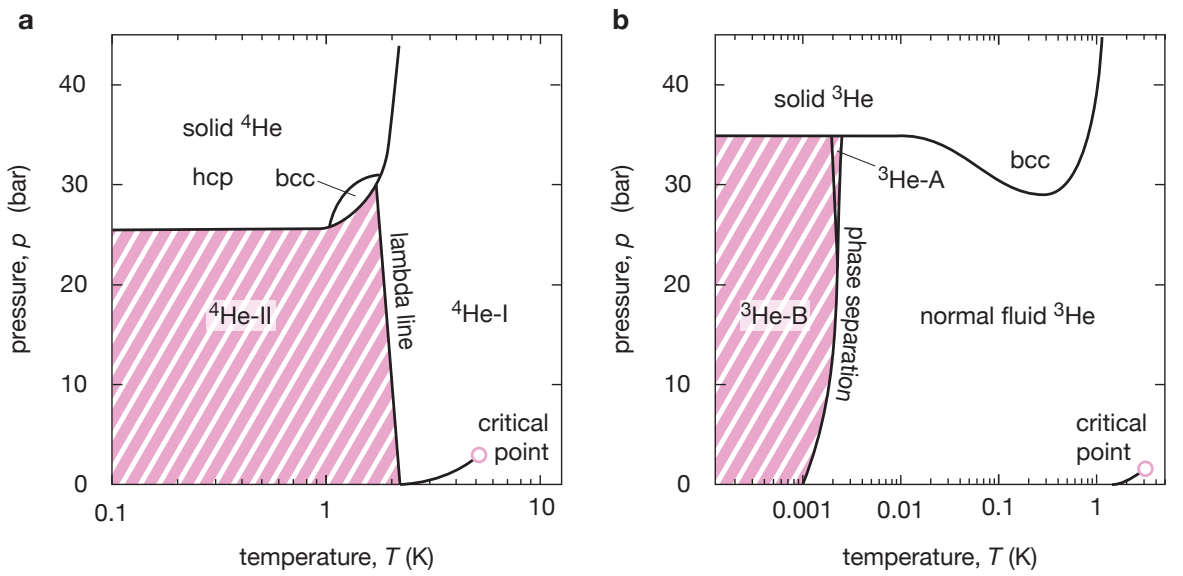

Fig. 5.1: Phase diagram of ^{4}He (a) and ^{3}He (b). Shaded regions correspond to superfluidity. ^{4}He-I represents the normal fluid phase, ^{4}He-II the superfluid phase. ^{3}He-A and ^{3}He-B are both superfluid phases. Adapted from refs [14, 201–203]

hand, ^{3}He has two protons and one neutron, so its total nuclear spin is $I = \frac{1}{2}$: ^{3}He atoms are fermions and obey Fermi-Dirac statistics. The difference in the statistics to describe these two isotopes results in considerable differences in their low-temperature behaviour. For example, pumping on a vapour of ^{4}He allows reaching temperatures of approximately 1 K and pumping on a vapour of ^{3}He allows reaching ≈0.3 K.

The different temperatures achievable from these two isotopes can be explained by the following: ^{3}He has a smaller atomic mass m than ^{4}He (3.02 u and 4.21 u, respectively); therefore, ^{3}He atoms have a larger zero-point energy $E_0 = h^2/8ma^2$ than ^{4}He (here, $a = (V_\mathrm{m}/\mathcal{N}_\mathrm{A})^{1/3}$ is the radius of the sphere in which the atoms are confined, $\mathcal{N}_\mathrm{A}$ is the Avogadro constant). This higher zero-point energy of ^{3}He gives rise to a lower boiling point, smaller density, smaller latent heat of evaporation and larger vapour pressure than its ^{4}He counterpart. Additionally, on the surface of ^{3}He, there is no film (see below); therefore, when pumping on ^{3}He, there is no heat leak or pumping load due to evaporation or the film (or eventually heat transfer along with the film). For this reason, ^{3}He baths can be pumped via wide tubes at the low-temperature end, whereas ^{4}He necessitate narrow constriction to suppress film flow.

Figure 5.1 shows the $p - T$ phase diagrams of ^{4}He and ^{3}He. Unlike all other liquids, both ^{4}He and ^{3}He do not become solid under their own vapour pressure. Instead, both isotopes remain liquid under normal pressures even at T =0 K. There are two liquid phases for ^{4}He: a normal fluid and a superfluid at temperatures below the lambda line. ^{3}He has two superfluid phases, with transition temperatures between 1 mK and 3 mK, three orders of magnitude below that of ^{4}He.

5.1.2 Superfluidity and lambda transition

At $T_\lambda = 2.17\,\mathrm{K}$ at ambient pressure, the specific heat of ^{4}He presents an abnormal, pronounced maximum with a discontinuity [204] called the lambda transition. It corresponds to a phase transition that can be understood as Bose-Einstein condensation. Above T_λ, ^{4}He behaves as a classical fluid (like a gas, owing to the low density). Below T_λ, ^{4}He is a superfluid: the fluid can flow through narrow capillaries without friction [205, 206].

Because ^{3}He obeys the Fermi-Dirac statistics and the Pauli principle, its liquid phase is analogous to that of a normal liquid: individual ^{3}He atoms cannot undergo the analogue of a Bose condensation into a superfluid state. There is no lambda transition. There are, however, weak attractive interactions between ^{3}He atoms in the liquid, giving rise to the pairing of two atoms at low temperatures, similar to the pairing of electrons to form Cooper pairs in a superconductor. As a result, ^{3}He undergoes a transition into a superfluid state at 0.92 mK at saturated vapour pressure. The properties of superfluid helium are not the topic of this thesis, and the reader may refer to textbooks for this: see refs. [14, 207–210]. However, a property is worth noting in the prospect of refrigeration techniques: a helium film forms on the surfaces above a bath of superfluid helium and on the walls of a container partly filled with liquid helium. It results from relatively strong van der Waals forces between the substrate and helium atoms driving the first atomic layer into a solid state and forcing liquid atoms to flow in a relatively thick layer. This solid film is usually immobile because of the low viscosity but can move in the superfluid state. Consequently, the levels of two connected partially filled ^{4}He containers will equalise through a frictionless flow of superfluid helium from one to the other. The superfluid film flow will later enhance evaporation of the ^{4}He bath because the superfluid will flow to hotter places and evaporate, siphoning the bath.

5.1.3 Cooling power

One can pump on the vapour above liquid ^{4}He to obtain temperatures below the standard (1 bar) boiling point [203]. It can be understood as follows: when atoms are pumped from the vapour phase, the most energetic atoms (the hottest) will leave the liquid and replenish the vapour. As a result, the mean energy of the liquid decreases, resulting in the liquid cooling down. Pumping on a bath moves n particles from the liquid to the vapour phase per unit of time. The cooling power $\dot{Q}$ is given by:

$$\dot{Q} = \dot{n}(H_\mathrm{l} - H_\mathrm{v}) = \dot{n}L, \tag{5.1}$$

where L is the latent heat of evaporation and H_l and H_v are the liquid and vapour phase enthalpies. Experimentally one may use a pump with a constant volume pumping speed $\dot{V}$, resulting in a mass flow $\dot{n}$ across the liquid-vapour boundary proportional to the vapour pressure P_v; hence the cooling power writes:

$$\dot{Q} \propto LP_\mathrm{v} \propto \mathrm{e}^{-1/T}. \tag{5.2}$$

The cooling power becomes less and less efficient as the temperature decreases. The absolute temperature minimum is achieved if all the liquid is evaporated. However, in practice, it is impossible to cool down as soon as the refrigeration from the atomic evaporation is balanced by external heat flowing onto the bath, i.e. ≈1.3 K for ^{4}He and 0.3 K for ^{3}He. Refrigeration of electronic devices by pumping on a helium bath was occasionally used in this thesis to measure devices down to 300 mK. To cool down even further, it is necessary to use liquid mixtures of ^{3}He and ^{4}He.

5.2 Liquid mixtures of ^{3}He and ^{4}He

In a mixture of ^{3}He and ^4He, superfluid ^{4}He acts as an inert background because it contains very few excitations. It influences only the effective mass of the interacting ^{3}He Fermi particles. Differences in the ^{3}He concentration results in different mean interaction energy and different properties of the fluid. Here I introduce the basic properties of ^{3}He–^{4}He mixtures that are important for understanding the operation of a dilution refrigerator.

5.2.1 The phase diagram

Figure 5.2 shows the phase diagram of liquid ^{3}He–^{4}He mixtures. There are three different regions: a mixture containing normal fluid ^{4}He, superfluid ^{4}He and a forbidden two-phase region (miscibility gap). Note that the lambda point is concentration-dependent: ^{4}He becomes superfluid at $T = 2.177\,\mathrm{K}$, and increasing the concentration of ^{3}He shifts the lambda point to lower temperatures. It is the case for concentrations in ^{3}He below 67.5 %, where ^{4}He superfluidity ceases to exist and the lambda point T_λ =867 mK meets the phase separation line. Below this temperature, the two isotopes are only miscible for certain limiting (temperature-dependent) concentrations. The shaded miscibility gap in figure 5.2 is a non-accessible unstable region where a mixture splits into two phases of concentrations given by the two branches of the phase separation curve. It means that if one cools down a helium mixture (with a ^{3}He concentration $x > 6.48\,\%$) to temperatures below 0.867 K, it will separate

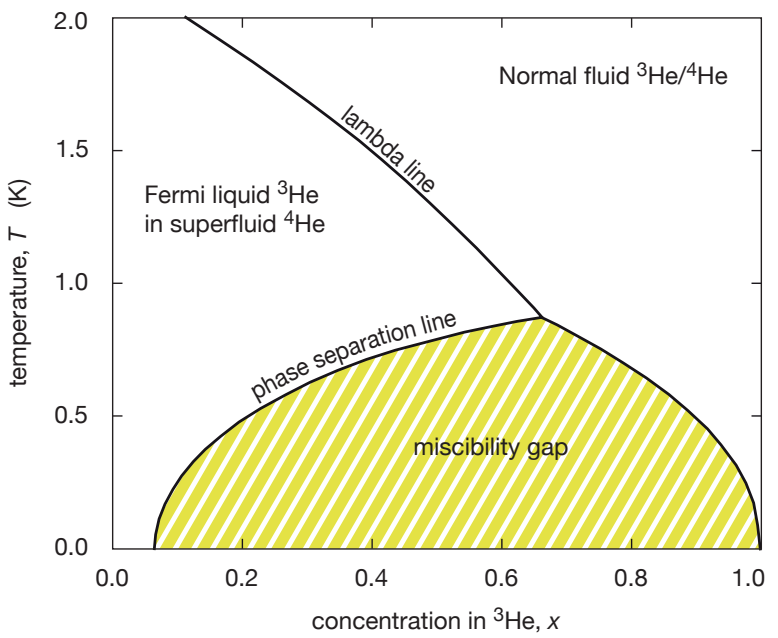

Fig. 5.2 Phase diagram of liquid mixtures of ^{3}He and ^{4}He. The shaded region marks the extent of the miscibility gap. Adapted from refs [14,203].

into two phases: one rich in ^{4}He and the other rich in ^{3}He. As ^{3}He has a lower density, the ^{3}He-rich fluid will stay on top of the other phase. Close to absolute zero, the ^{3}He-rich region will become pure ^{3}He, and the ^{4}He-rich phase will reach a constant concentration of 6.48 %, a necessary feature for the dilution refrigeration techniques shown later.

Importantly, in the ^{4}He-rich region (diluted phase), ^{4}He is superfluid and obeys Bose statistics, so there are essentially no excitations (phonon, rotons): the viscosity, entropy and specific heat vanish. As a result, the ^{3}He fermions can move through an inert ^{4}He superfluid background unhindered, as conduction electrons do in a metal crystal. ^{4}He contributes only to the volume of the liquid, therefore, to the interatomic distance between ^{3}He fermions, resulting in changes in the effective mass of the dissolved ^{3}He isotope. Under these conditions, ^{3}He can be treated as an interacting Fermi quasiparticle with a pressure equal to the osmotic pressure described below.

5.2.2 Finite solubility

The finite $x = 6.48\,\%$ solubility of ^{3}He in ^{4}He can be understood by considering two containers of pure ^{3}He and pure ^{4}He cooled down separately to 0 K before the liquids are put together and looking at the ^{3}He atoms. Because ^{3}He is lighter, it exhibits a larger zero-point motion and occupies a larger volume than ^{4}He. As a result, the first ^{3}He atoms will be closer to the ^{4}He atoms than the surrounding ^{3}He: the ^{3}He–^{4}He bonding will be stronger than the ^{3}He–^{3}He and ^{3}He will prefer to stay in the diluted phase.

It is necessary to find the binding energy to understand why the finite solubility is 6.48 %. Let us consider the chemical potential $\mu_{3,\mathrm{d}}$ of ^{3}He in ^{4}He and $E_3 = -\mu_{3,\mathrm{d}}$ is the binding energy of one ^{3}He atom in liquid ^{4}He (d

refers to the dilute phase). The binding energy of ^{3}He in ^{3}He is equal to the latent heat of evaporation of pure ^{3}He: $\mu_{3,\mathrm{c}} = -L_3$ (where c refers to the concentrated phase). As a result, E_3 should be greater than L_3. The first two ^{3}He atoms will occupy the lowest energy state $-E_3$ with anti-parallel spins, and additional ^{3}He atoms will have to obey the Pauli exclusion principle: they will occupy increasingly higher energy states. $\mu_{3,\mathrm{d}}$ should take into account the Fermi energy $E_\mathrm{f} = k_\mathrm{B}T_\mathrm{f}$, and the binding energy will increase with ^{3}He concentration. Considering that, at equilibrium, $\mu_{3,\mathrm{d}} = \mu_{3,\mathrm{c}}$, the equilibrium concentration of ^{3}He in ^{4}He at absolute zero should follow the equation:

$$-L_3 = -E_3(x) + k_\mathrm{B}T_\mathrm{f}(x), \tag{5.3}$$

where $x = x_3 = n_3/(n_3 + n_4)$ is the concentration of ^{3}He in ^{4}He, as shown in figure 5.2. This was calculated by Bardeen, Baym and Pines (BBP theory) [211, 212]. For x =6.48 %, the chemical potential equals that of ^{3}He in pure ^{3}He: that is, the finite solubility of ^{3}He in ^{4}He at 0 K.

5.2.3 Osmotic pressure

Consider now two containers of liquid helium mixtures with different ^{3}He concentrations connected via a superleak capillary. In the dilution fridge, we will see later that this constitutes the mixing chamber and the still [213]. If the system starts with equal levels in the two vessels, ^{4}He will flow through the superleak to equalise the ^{3}He concentration in both containers. As ^{3}He is not in a superfluid state, the high viscosity does not allow it to pass through the superleak and reduce the concentration gradient. For T =0 K, a concentration difference of 1 % would lead to a difference in height in the two containers of about 20 cm [14].

5.2.4 Cooling power of ^{3}He–^{4}He mixtures

The cooling process in a ^{3}He–^{4}He dilution refrigerator is achieved through the transfer of ^{3}He atoms from the pure ^{3}He phase to the dilute phase. In the peculiar phase diagram, finite solubility and osmotic pressure play an important role in achieving low temperatures. Equation 5.2 described the cooling power of an evaporating cryogenic liquid as exponentially decaying with temperature. For a helium mixture dilution process, the cooling power can be expressed as a function of the concentration x of the dilute phase and the mixing enthalpy ΔH that is the integral of the differences of the specific heats in the two phases: $\Delta H \propto \int \Delta C \mathrm{d}T$. Interestingly, $x \approx 0.0648$ is almost constant below 100 mK, contrary to the vapour density in an evaporating bath, where the

number of atoms decreases exponentially with the temperature. The cooling power temperature dependence writes:

$$\dot{Q} \propto x\Delta H \propto T^2. \tag{5.4}$$

This cooling power shows a much weaker temperature dependence than for an evaporation process, giving a substantial advantage for a ^{3}He–^{4}He dilution process.

5.3 The dilution refrigerator

The technique of dilution refrigeration relies on the specific properties of ^{3}He–^{4}He mixtures detailed in section 5.2. London, Clarke and Mendoza first proposed it in 1962 [14, 214], but it was only in 1965 that the first successful experiment was realised by Das, De Bruyn, Ouboter and Taconis [215], reaching a temperature of 220 mK. Today, dilution refrigerators are regularly used to access temperatures around 10 mK [216], but there is no theoretical lower bound on the temperature achievable through this process [213].

The maximum solubility of ^{3}He in ^{4}He depends on temperature and pressure (see sec. 5.2). As a result, the ^{3}He concentration is constant during cooling at sufficiently high temperatures. Below the phase separation line, the mixture separates into two different phases with concentrations following the phase separation line. Figure 5.3 shows the temperature and concentration dependence of different ^{3}He–^{4}He mixtures whilst cooling. The mixture in our refrigerator is composed of 20.45 % ^{3}He: the phase separation occurs at 470 mK and the lambda point at 1.86 K.

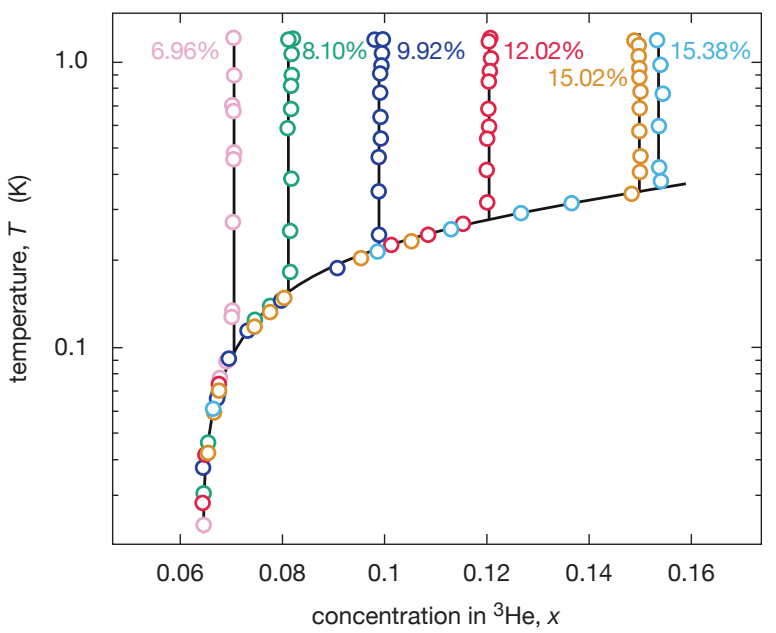

Fig. 5.3 Concentration and temperature dependence of ^{3}He dissolved in ^{4}He. The starting concentration of the ^{3}He is indicated at the top of each curve. Data extracted from refs [14, 217].

The cooling process occurs in the *mixing chamber*, transferring ^{3}He atoms from the concentrated (^{3}He-rich) phase into the dilute phase. Transferring one mole of ^{3}He to the dilute phase generates a heat of:

$$\Delta Q = T\Delta S = aT^2, \tag{5.5}$$

with $a = -84\,\mathrm{J\,K^{-2}}$. Continuously pumping ^{3}He away from the dilute phase in the mixing chamber allows cooling of the liquid, in the same way, that pumping away the vapour coming out of a cryogenic liquid. Feeding ^{3}He back to the concentrated phase allows for continuous operation of the dilution refrigerator. Figure 5.4 sketches the cold part of a ^{3}He–^{4}He dilution refrigerator. It consists of a *mixing chamber*, a *still* and a *counterflow heat exchanger*.

5.3.1 Mixing chamber and still

The dilution process occurs at the mixing chamber (MC) stage, and ^{3}He atoms are continuously removed from the dilute phase by distilling them off in the still. The MC and still constitute a system of two containers joined by a superleak (see subsection 5.2.3). In the initial stage of the cooling process, both the still and the MC are filled with the liquid ^{3}He–^{4}He mixture. The mixing chamber is cooled below 470 mK so that the mixture is phase-separated, with

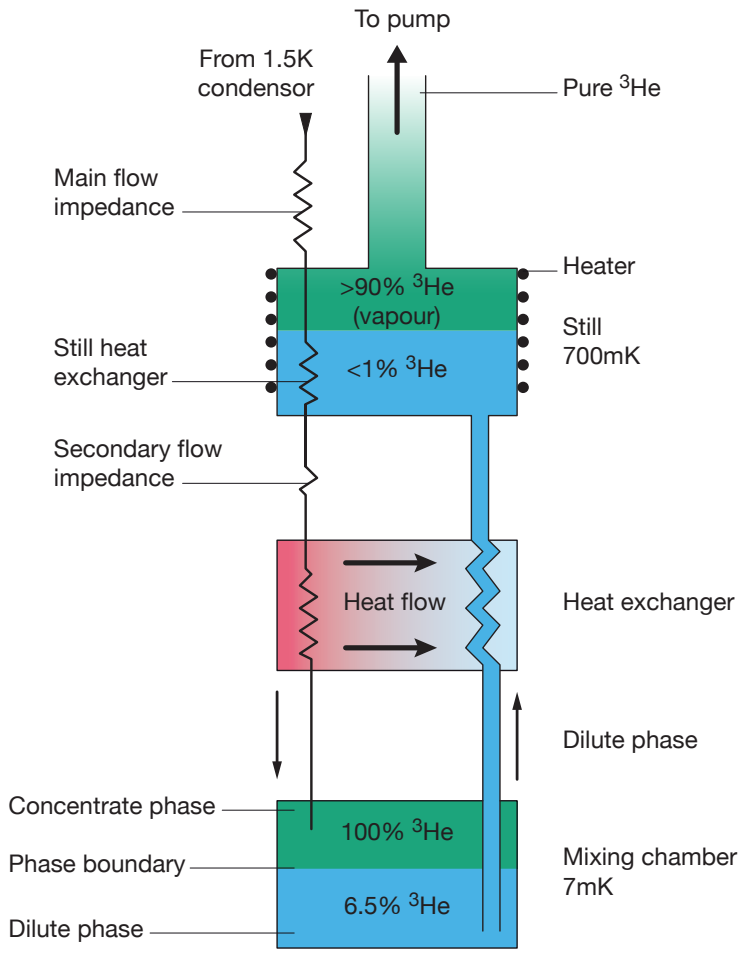

Fig. 5.4 Sketch of the inner ^{3}He–^{4}He circuit of the dilution refrigerator. Adapted from refs [14, 203]

the upper part of the MC filled with the concentrated phase and the lower part filled with the dilute phase.

Heat is applied to the still by means of an electrical current so that the liquid evaporates and the vapour is pumped away. The still temperature should be kept around 0.7 K to maximise the ^{3}He/^{4}He ratio. The lighter ^{3}He atoms are evaporated first, so their concentration is constantly reduced in the still. A pressure gradient develops between the chamber and the still as due to osmotic pressure; it is responsible for driving ^{3}He atoms from the concentrated phase to the dilute phase in the mixing chamber. The transfer of atoms from the concentrated phase to the dilute phase requires some energy (eq. 5.5) that is provided by the heat taken from the load: the process refrigerates. ^{3}He is then carried back into the mixing chamber to ensure the cycle never runs out.

The vapour in the still should be as close as possible to pure ^{3}He: the presence of ^{4}He can form a continuous film, driving unwanted heat into the MC. Additionally, the purer ^{3}He is in the concentrated phase, the more energy the dilution process can take from the load. In this cycle, there may be a considerable temperature difference between the different parts of the system. For example, the incoming ^{3}He from the condenser can be three times hotter than the ^{3}He moving out of the MC. Heat exchangers allow to cool down the incoming liquids.

5.3.2 Heat exchangers

The performance of the dilution fridge depends on how efficient the heat exchangers are in order to minimise the heat that reaches the MC and reduces its refrigeration power. The concentrated ^{3}He fluid flowing to the mixing chamber carries heat; the heat exchanger cools it down before entering the chamber. Figure 5.5 shows the two different heat exchangers used. They rely on the same principle: the specific heat of ^{3}He in the dilute phase is greater than that of pure ^{3}He; therefore, the dilute ^{3}He flowing out of the chamber is very effective at cooling the pure ^{3}He flowing into the MC. These two different heat exchangers are placed successively to form the counterflow heat exchanger.

Figure 5.5a shows a continuous heat exchanger consisting of a double-walled tube. The dilute phase flows in the outer tube. At the warm end, the concentrated phase flows into an inner capillary (secondary-flow impedance, preventing re-evaporation and ensuring that the pressure in the condenser builds up to liquefaction). After a few cm, the inner tube is rolled into a tight spiral. Figure 5.5b shows a step heat exchanger. The most important element here is the sintered silver layer attached to the copper-nickel foil, providing increased contact surface while reducing the thermal resistance. This layer divides the heat exchanger into two chambers, one in which the ^{3}He-rich phase flows, the

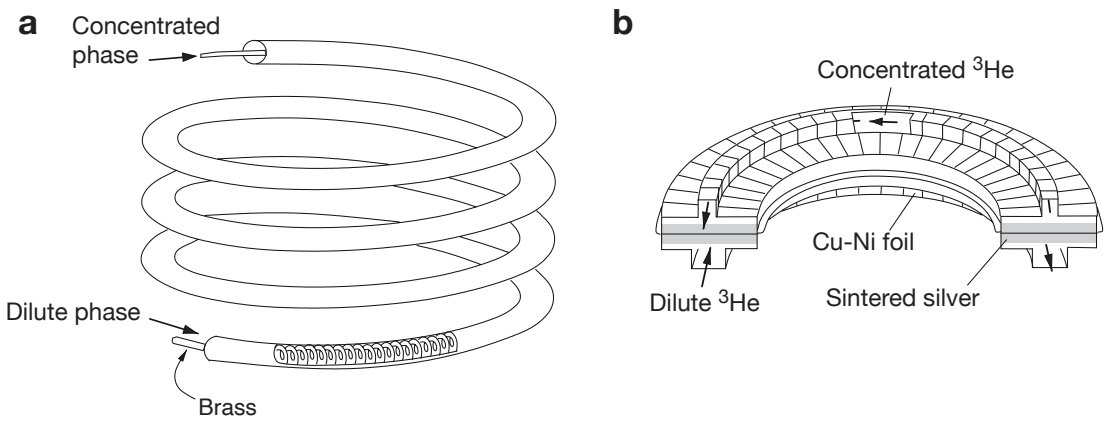

Fig. 5.5: Sketches of heat exchangers. a) continuous heat exchanger and **b)** cut through the cross-section of a step heat exchanger. Figures adapted from refs. [14, 203]

other flowing the dilute phase. Such a heat exchanger consists of five steps with different contact surfaces. It is used at the low-temperature end.

5.4 Experimental setup

The experimental system is composed of an Oxford Instrument dry dilution refrigerator that has been adapted to fit our needs. It is depicted in figure 5.6. Cooling to 10K is ensured with a *pulse tube cooler*, followed by mixture *condensing* to reach the base temperature.

5.4.1 Pulse tube cooler

Numerous types of cryogenic-free coolers exist; ours is based on a pulse tube cooler. This is composed of a compressor with a piston connected to a regenerator, itself connected to a hollow tube (the *pulse tube*) with heat exchangers at both ends [218]. This sort of cooler is based on smooth periodic adiabatic pressure variation. The regenerator is a large enough container filled with porous material with a high heat capacity. It absorbs heat from the gas pumped into the pulse tube, precooling it, stores the heat for half a cycle, and then transfers it back to outgoing cold gas in the second half of the cycle, cooling the regenerator. The compressor is connected to the warm end of the regenerator, providing the pressure oscillations driving the refrigerator.

The pulse tube transports heat against a temperature gradient through a process called surface heat pumping. In the first step of the cycle (compression phase), the refrigerant gas (helium) is compressed by flowing from the piston to the pulse tube. All the gaps initially in the tube will be adiabatically compressed closed to the hot end, resulting in a temperature increase. At the

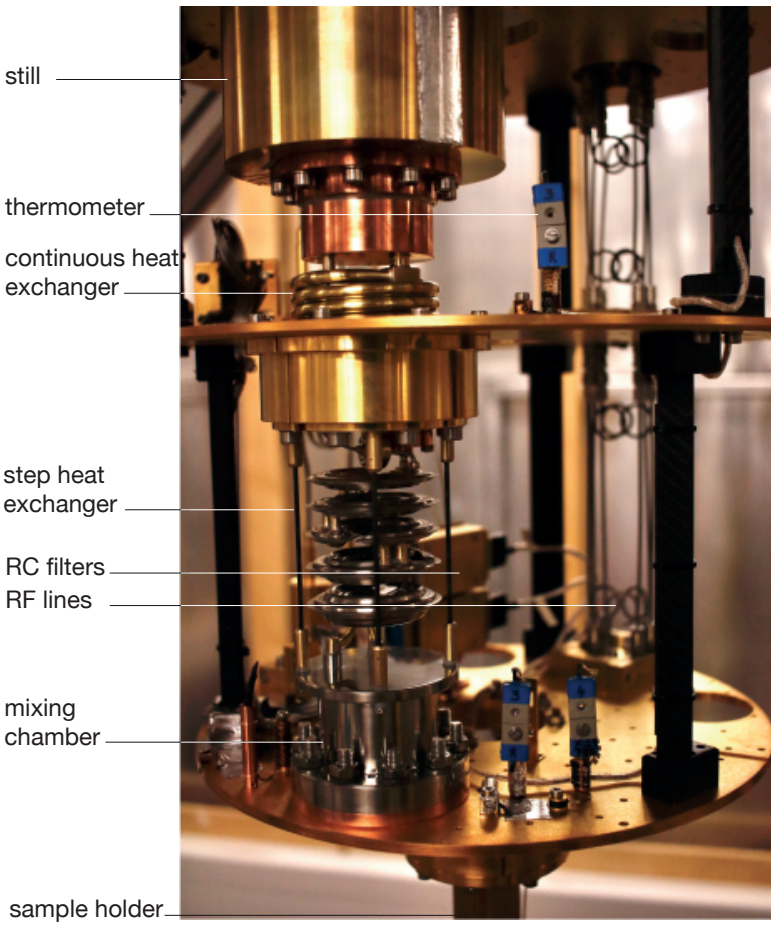

Fig. 5.6 Photograph of the inner dilution refrigerator circuit)

cold end of the tube, the pressure is reduced, and so is the temperature. The regenerator then absorbs heat from the hot end. In the second step of the cycle (expansion), the compressor forces adiabatic expansion of the refrigerant gas to cool it further. Through the regenerator, heat is further absorbed. This cycle is then repeated, allowing to cool the system down. Importantly, there is no liquid-gas interface in a pulse tube cooler because the operating pressures are above the critical pressures.

This mechanism describes only the original pulse-tube cooler. In practice, improvements include using rotary valve compressors, second inlets to reduce the mass flow into the regenerator, or multiple cooling stages [219–222]. State-of-the-art pulse tube coolers can reach 15 K to 20 K using a single stage or about 2 K with a dual-stage. Our system is composed of two pulse tube coolers. One is located at the first stage level (PT1) and operates below 50 K. The other one is placed at the second stage (PT2) and operates below 4 K. There is also a heat exchanger underneath the top plate to extract heat from the incoming gas before it reaches the pulse tube coolers. Additional cooling power is used for precooling the still and MC via a precool loop filled with the mixture. As soon as the system reaches 20 K, the precool loop is evacuated using a turbo pump, and this part of the circuit is shut with valves.

5.4.2 Condensing

Once the precooling circuit has been emptied, the condensing enables cooling down to base temperature after the precooling. The mixture is compressed using the ^{3}He compressor and passed through heat exchangers located on the PT stage to cool the gas around 4 K. Subsequently, the mixture is condensed using a Joule-Thompson stage. It is based on the following principle: an expanding gas performs work against its own internal forces. The Joule-Thompson stage comprises a heat exchanger located inside the still pumping line and a small nozzle (the impedance) through which the gas undergoes an isenthalpic expansion without moving parts. The nozzle performs no work: $W = 0$. As a result, one may write the conservation of enthalpy in this reversible heat exchange process:

$$W = H_1 - H_2 = (U_1 + p_1 V_1) - (U_2 + p_2 V_2) = 0, \tag{5.6}$$

and therefore for a real gas:

$$H = U(T) + pV = U(T) + RT. \tag{5.7}$$

As the enthalpy is constant and does not depend on pressure or volume, a temperature change must occur. In the dilution refrigerator, the condensing is done via two different steps: i) when cooling down the system to about 1.3 K, circulating the mixture through the dilution refrigerator will allow cooling rapidly to the phase separation line around 470 mK. ii) As soon as the dilution refrigerator's temperature is around 600 mK, the still is warmed up to 700 mK to start the distillation process. Then the temperature drops to a base level of 7 mK. During the circulation, the ^{3}He–^{4}He mixture can be contaminated with other gases (O_2, N_2). These impurities may block the impedance and therefore need to be filtered. Filtering is achieved with two traps filled with a high surface area adsorbent, cooled by liquid ^{4}He (internal trap) or liquid nitrogen (external trap, requiring refilling in liquid nitrogen every week).

5.4.3 Pumping

It is necessary to have the system at low enough pressure to limit convection. At relatively high temperatures, this is achieved by pumping the OVC with a turbo pump during cooling. In the K temperature range, the vapour pressure of all substances (except He) is so low that surfaces in the OVC are efficient pumps. Below 10 K, pumping on the OVC is counterproductive as cold surfaces condense the remaining gas molecules and improve the vacuum by several

orders of magnitude. This is so efficient that it may pump contaminants from the pumping station into the cryostat.

5.5 Thermal anchoring of electronic devices

Multiple factors may increase the temperature of the device measured. First, thermal radiations consist, by nature, of incoherent electromagnetic waves propagating in free space. Appropriate shielding both outside and inside the refrigerator prevents electromagnetic radiations in the sample. Second, the wiring may be a loophole for thermally excited electromagnetic fields to leak into the sample. Transfer of heat via phonons in the wires would there occur like waveguides. In order to prevent this, it is necessary to provide proper thermal anchoring and electromagnetic filtering in the wiring.

Samples are attached to the MC close to the dilute phase outflow, where the temperature is minimal, through a dual-board PCB-based sample holder system designed during the PhD. The PCB system is composed of a motherboard permanently connected to the sample puck and an exchangeable daughterboard, on which the sample is glued and wire-bonded. This system accommodates the connection of the device measured while ensuring thermalisation. Additional thermalisation of electrons at different stages of the dilution refrigerator are necessary to ensure that the sample's temperature matches the mixing chamber temperature, as illustrated in figure 5.7.

In this setup, hot electrons enter the dilution refrigerator at room temperature. They are thermalised at different stages (PT1, PT2, Still, MC) in order to reduce the electron temperature. Wires are thermally anchored at all stages to dump heat into the continuously refrigerated plates. As a result, cooling of the sample is achieved through heat extraction via the wires; this is much more efficient than via the PCB. The wiring consists of constantan looms, a non-metallic copper-nickel allow with low thermal conductivity and a temperature-independent resistivity, therefore well suited for this application. As the sample seats on an insulating chip carrier in vacuum, thermal coupling to the mixing chambers occurs through the sample wires. The wire consists of pure copper between the MC and the sample holder for optimal thermalisation. At this stage, additional thermalisation and noise filtering are achieved using a homemade RC filter thermally anchored to the MC plate. It filters the noise from 150 kHz up to the GHz regime.

Outside the cryostat, the 24-wire cable connects to a breakout box with a shielded 2-channel twisted pair cable with Fischer connectors. Each channel then connects a BNC connector on the breakout box. Additional filtering occurs at the breakout box stage. The shield is used as a ground-carrying line to prevent ground loops. We use the magnet power supply ground as the common

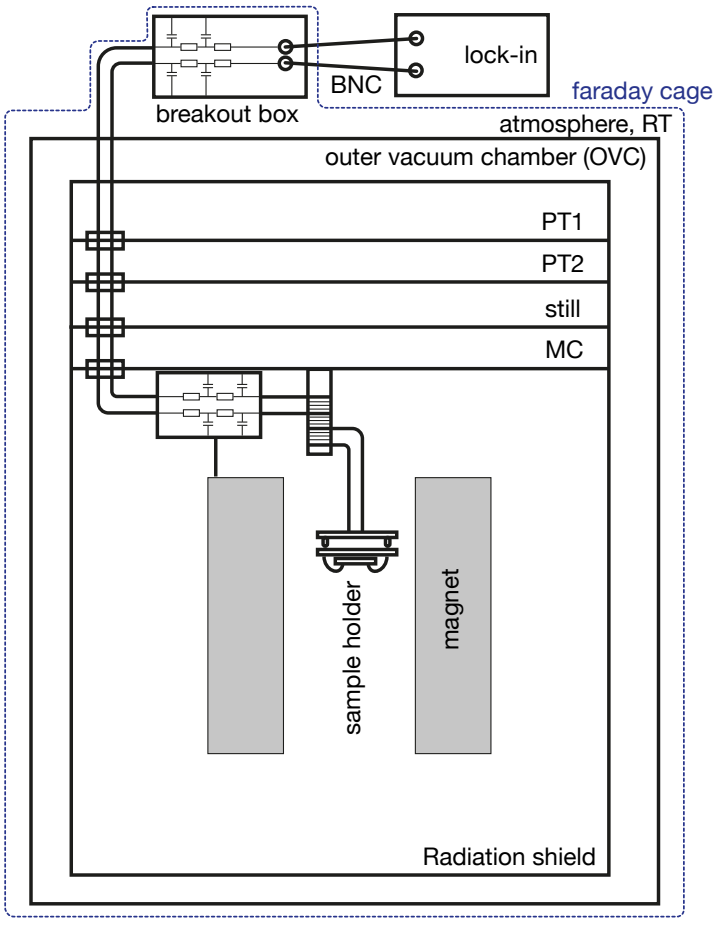

Fig. 5.7 Schematic of filtering scheme and thermal anchoring There is an RC filter PCB anchored on the MC plate and additional filtering at room temperature. The whole system is grounded with the magnet to avoid ground loops.

ground, with the dilution refrigerator, the breakout box and the ground pins of all the measuring equipment connected in series. All the racked instruments use electrically isolating mounting hardware. The background noise was tested using the spectrum analyser function of the Zurich Instrument MFLI lock-in amplifiers. The 50 Hz noise peak is 60 µV, much lower than the 300 µV limit for low electron temperature measurements usually considered acceptable [223]. I found that the instruments' sequential on and off switching did not considerably reduce the amplitude of the 50 Hz noise peak, thanks to the minimisation of ground loops.

5.6 Thermometry below 1K

Complete characterisation of a system's physical properties usually requires a temperature dependence measurement. Therefore, it is necessary to measure the temperature of our devices accurately. For this, one may use either a *primary* or *secondary* thermometer. A primary thermometer is used to measure the temperature without prior calibration. It is possible if a fundamental physical law describes the temperature dependence of the measured property. Conversely, a secondary thermometer must be calibrated to provide an accurate reading, but these are often easier to use. Here I present two techniques that have been used for low-temperature thermometry.

5.6.1 Phonon thermometry

The phonon temperature corresponds to the temperature of the MC plate thanks to good thermal anchoring between the electrical wires connected to the device and the MC. This temperature can be measured with a resistor thermometer, a secondary thermometer (therefore needs calibration). The temperature of the MC is acquired from a Lakeshore 372 AC resistance bridge based on lock-in amplification techniques with an AC excitation as low as 10 pA, allowing to measure the resistance of a metallic wire while minimising self-heating of the MC plate. Two different materials are used to measure the phonon temperature T_{mc}. Above 1.2 K, a thin-film ceramic zirconium oxynitride (Cernox) resistor is used because it has a linear temperature dependence between 1 K and room temperature, with minor changes in sensitivity under magnetic fields. Below 2 K, a thick-film chip resistor based on RuO_2 is used. It is a metal-ceramic composite consisting of an alloy of two RuO_2 conductive compounds with lead-silica glass on a ceramic substrate. RuO_2 resistors show non-metallic resistance characteristics. Thermal contact to the MC plate is ensured via epoxy, which could result in a relatively poor thermal link. In the millikelvin range, the mixing chamber temperature T_{mc} is measured from the RuO_2 resistor, supplied and calibrated by Oxford Instruments.

5.6.2 Electron thermometry

The wiring necessary to measure an electronic device may carry out noise, particularly in high frequencies, that can result in parasitic heating of the device under test. Additionally, the small AC excitation used to measure the device may result in Joule heating. Several techniques are available to account for the electron thermometry, consisting of measuring an electronic quantity directly related to the temperature: tunnel junctions between normal metal and superconductors (NIS) or two superconductors (SIS) and shot noise thermometry are some examples [14]. Here I used a Coulomb blockade thermometer (CBT) to measure the electron temperature. This measurement was carried out only once during my PhD, after several improvements to the dilution refrigerator system (better thermal anchoring, filtering, minimisation of ground loops).

For the purpose of thermometry, I used the CBT shown in figure 5.8, consisting of many small metallic islands connected in an array by tunnel junctions [224–226]. The conduction of this array is temperature dependent because of the balance between thermal excitations and single electrons tunnelling across the islands through an electrostatic barrier [14, 224–226]. This kind of device typically works over a decade of temperatures, for temperatures as low as 3.7 mK [224]. Conductance of the CBT is measured in a current-

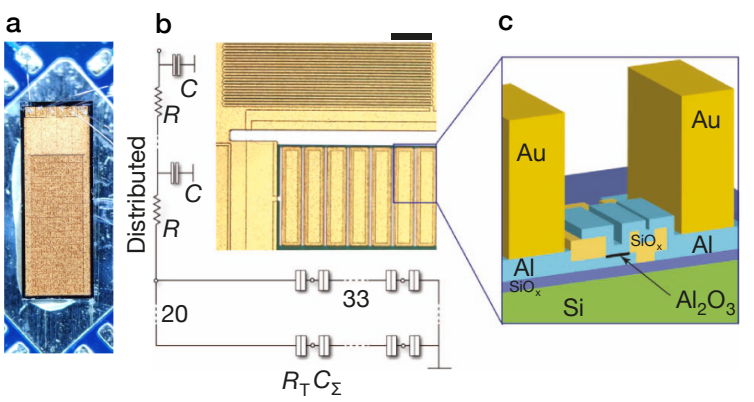

Fig. 5.8 Details of the CBT a) Optical photograph. **b)** optical micrograph (scale bar 10 µm) of the CBT with equivalent circuit diagram. **c)** Schematic cross-section with one Al_2O_3 junction between two Al islands with Au thermalisation blocks. (b) and (c) from ref. [224].

driven four-wire configuration, with the drive current provided by a custom amplifier. A small AC excitation (500 pA $\leq I_{ac} \leq$ 10 nA) is added to a DC bias (I_{dc}), allowing to measure the differential conductance G with a lock-in amplifier. A typical CBT's conductance dips around zero bias, with the dip becoming deeper and narrower at lower temperatures. It corresponds to the Coulomb blockade effect when the Coulomb energy $E_c = [(N-1)/N]\, e^2/C_\Sigma$ is much larger than the thermal energy $k_B T$ (where C_Σ is the capacitance of each island). Then the differential conductance can be described as [225]:

$$G = G_T \left(1 - \frac{E_C}{k_B T} g(x)\right), \tag{5.8}$$

where G_T is the asymptotic conductance at high bias voltage, $x = eV_{dc}/(Nk_B T)$, and N is the number of junctions. g is given by:

$$g(x) = \frac{x \sinh x - 4 \sinh^2(x/2)}{8 \sinh^4(x/2)}. \tag{5.9}$$

In practice, when $T_e = T_p$, one may approximate the full width at half maximum of the conductance dip with [224]:

$$V_{1/2} \approx 5.439 N k_B T/e. \tag{5.10}$$

Figure 5.9a shows the measured conductance G as a function of V_{dc} and the result of fitting $G(V_{dc})$ for different measurements. The warmest measurements (above 150 mK) allow calibration of the sensor and extract C_Σ =210 fF and G_T =108.3 µS. After calibrating the fit parameters, the same equation 5.8 is used to fit the coldest measurements. The resulting electron temperature is shown in figure 5.9b for 7 mK$\leq T_{mc} \leq$300 mK. The electronic temperature diverges from the mixing chamber temperature for $T_{mc} \leq$50 mK. When fixing the mixing chamber temperature T_{mc} =6.3 mK, lowering the AC input excitation decreases the minimal electronic temperature that can be achieved for currents above 5 nA (see inset, figure 5.9b). However, the electronic temperature saturates to $T_e \approx$35 mK for $I_{ac} \leq$5 nA.

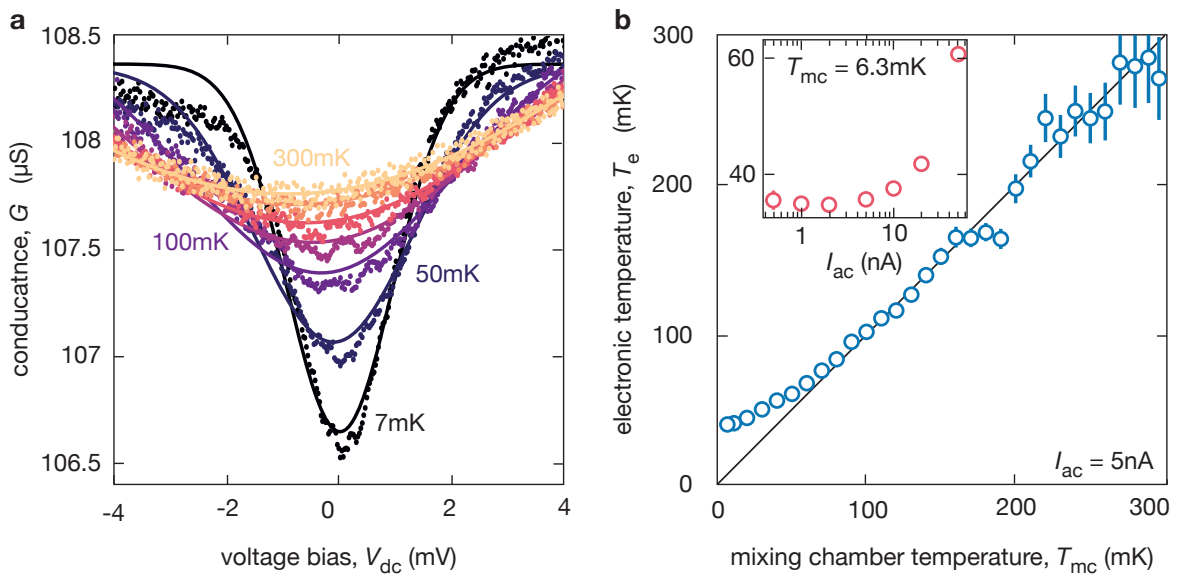

Fig. 5.9: CBT behaviour between 300 and 7mK a) CBT conductance $G(V_{\mathrm{dc}})$ for seven different temperatures. Symbols show measured values, and lines show best fits to the calculated ideal conductance. **b)** CBT electron temperature $T_{\mathrm{e}}(T_{\mathrm{mc}})$, showing that below 50 mK, the electronic temperature is sensibly higher than the MC phonon temperature. Inset: CBT electron temperature for different AC excitation currents at T_{mc} =6.3 mK.

5.6.3 Temperature control

In order to realise temperature-dependent measurements, controlled heat is applied to the MC plate. It is, in fact, more efficient not to regulate the refrigerator's temperature but to let it float and regulate the temperature of the sample holder or the plate thermally coupled to the MC. To achieve this, a signal from the thermometer is applied from the resistance bridge and adjusted from the temperature reading from the same thermometer. The difference is amplified and fed back to the heater through a proportional-integral-derivative (PID) controller. As the MC plate is heated rather than the sample directly, there is a substantial lag between the temperature reading on the RuO_2 thermometer and the internal temperature in the sample. For this reason, it is necessary to wait a few minutes after changing the temperature before being able to measure the electronic response.

Blank page

Part III
Effects of the moiré potential

Blank page

Chapter 6
Ballistic Brown-Zak fermions

As introduced in section 2.2.3, the relevant length scale in the presence of a large magnetic field is the magnetic length l_{B}. Here I show the emergence of a new family of quasiparticles, the Brown-Zak fermions whenever the magnetic length l_{B} (or multiples of) is commensurate with multiples of the lattice constant (λ_{sl}).

6.1 Magneto-Bloch states

6.1.1 Azbel's formulation

In crystalline solids, the translational invariance of the hamiltonian resulting from the periodic lattice potential allows charge carriers to propagate freely through the crystal lattice. This behaviour is described by Bloch's theorem: electronic states are delocalised over the crystal lattice. As a result, the spectrum is altered compared to a free electron system, as gaps appear on the edge of the Brillouin zone. In a magnetic field, the spectrum is modified into Landau levels. Cyclotron motion localises the charge carriers in closed orbits and the Bloch picture breaks down. A well-known consequence in metals and 2DEGs exposed to magnetic fields is a drop in conductivity.

However, one may explore the regime where the magnetic field B becomes strong enough so that the magnetic length is commensurable with the lattice periodicity. The relevant quantities here are the area of the lattice $\mathcal{A}$ and the flux penetrating that lattice unit cell, $\phi = \mathcal{A}B$. If p flux quanta are piercing q unit cells, one may write:

Results presented in this chapter have been published in:
J. Barrier, P. Kumaravadivel, R. Krishna-Kumar, L.A. Ponomarenko, N. Xin, M. Holwill, C. Mullan, M. Kim, R.V. Gorbachev, M.D. Thompson, J.R. Prance, T. Taniguchi, K. watanabe, I.V. Grigorieva, K.S. Novoselov, A. Mishchenko, V.I. Fal'ko, A.I. Berdyugin and A.K. Geim, "Long-range ballistic transport of Brown-Zak fermions in Graphene superlattices", Nat. Commun. **11**, 5756 (2020)

$$\frac{\mathcal{A}}{l_{\mathrm{B}}^2} = \frac{\phi}{\phi_0} = \frac{p}{q}, \tag{6.1}$$

with $p, q \in \mathbb{Z}$. By writing the Schrödinger equation for such a problem of Bloch electrons exposed to quantising magnetic fields (see [227]) Azbel demonstrated that the solutions have q eigenvalues and that for $\phi = p/q\phi_0$, there is an associated family of quasiparticles. In this thesis, they are referred to as Brown-Zak fermions. In practice, these quasiparticles recover a delocalised wave function, thereby forming new magnetic Bloch states, propagating along open trajectories, as if the magnetic field was absent. This is a consequence of the Aharonov-Bohm effect: an electron passing across q unit cells would acquire a phase shift that is a multiple of 2π, thus restoring the translational periodicity in high B. In general, the spectrum is dominated by localised states caused by Landau quantisation (see chapter 7) but at exactly rational values of the magnetic flux, the spectrum becomes continuous as a result of the emergence of magnetic Bloch states [194, 227–238].

6.1.2 Magnetic translation group

Let us consider the evolution of electron motion and energy dispersion upon increasing the magnetic field. At zero magnetic field, the electron wavefunction in a periodic lattice is delocalised in the whole crystal. It corresponds to Bloch states propagating freely throughout the lattice in straight trajectories. In finite B, electrons are subject to a Lorentz force thus move in a cyclotron motion. Their localisation is centred on the cyclotron orbit. In graphene, the cyclotron radius corresponding to this motion r_{c} writes:

$$r_{\mathrm{c}} = \frac{\hbar k_{\mathrm{f}}}{eB}, \tag{6.2}$$

where $k_{\mathrm{f}} = \sqrt{n\pi}$ is the Fermi wavevector, n is the charge carrier density. As B increases, r_{c} becomes smaller and smaller until Landau quantisation dramatically changes the energy dispersion. This formalism is valid only when r_{c} is much larger than the lattice spacing a, which results in highly degenerate energy levels with respect to their orbits' centre. In contrast, if r_{c} becomes so small that it becomes comparable to the distance between atoms in the lattice, the physics is dramatically different: the cyclotron motion has different energies depending on the position in the unit cell. This effect lifts the orbital degeneracy, with a dispersion resembling broadened LLs as in a continuous band, a phenomenon known as Harper broadening [239]. However, for specific magnetic fields, the cyclotron radius becomes commensurate with the lattice spacing, and translational symmetry of the Hamiltonian is restored. Consequently, the electron wave function in a magnetic field takes the form

of delocalised Bloch states: electrons start propagating in straight trajectories as if the magnetic field were absent, a theoretical result derived by Zak in 1964 [229]. Such a recovery of the translational symmetry of the electron wave functions occurs for many special magnetic field values, corresponding to $\phi/\phi_0 = p/q$ where ϕ is the magnetic flux, ϕ_0 the magnetic flux quantum and p and q are integer. This condition can correspond to the flux of a number p of flux quanta piercing a newly defined supercell that is q times larger than the lattice should be equal to the magnetic flux quantum.

6.1.3 Quantum oscillations

For usual graphene lattices, the nm-sized lattice constant would result in these magnetic Bloch states for magnetic fields in the order of 10 000 T. This is too large to be experimentally accessible and has for a long time reserved Brown-Zak fermions for theoretical studies. Nonetheless, the possibility to stack two different van der Waals crystals together has opened a new direction, enabling the creation of large-scale superlattices. For example, stacking graphene on top of hexagonal boron nitride with aligned crystallographic axes creates a moiré pattern giving rise to a periodic potential affecting the electronic spectrum of graphene. The superlattice thereby created has a relatively large lattice constant of ∼14 nm, allowing one flux quantum to penetrate through the superlattice unit cell for magnetic fields of only 30 T, experimentally accessible.

The superlattice spectrum is modified with the magnetic field and this becomes even stronger away from the main Dirac point. This results in conductivity maxima for magnetic fields $B = B_{p/q}$ corresponding to $\phi = \phi_0 p/q$ as the translational symmetry is restored. At low temperatures, these conductivity maxima are hidden in the rich spectrum of the Hofstadter butterfly, and become prominent at high temperatures, developing in a new set of $1/B$-periodic oscillations [194, 238] (see fig. 6.1).

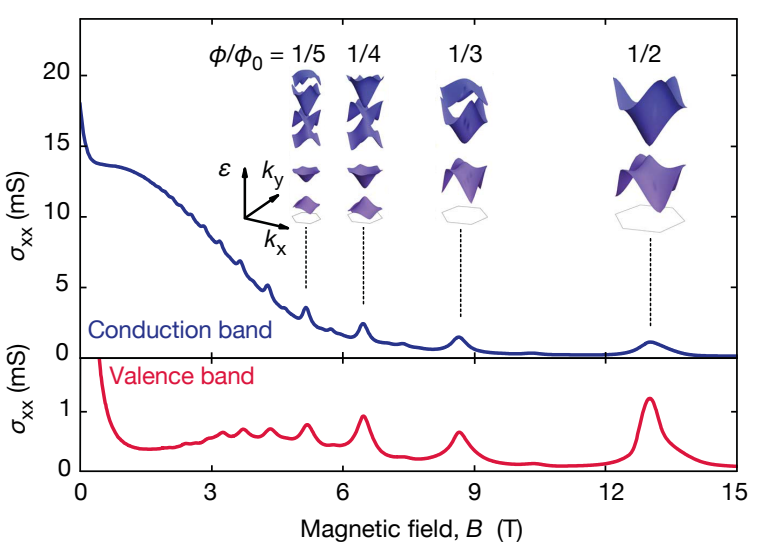

Fig. 6.1 Brown-Zak oscillations as recurring Bloch states at 100 K for electron and hole doping on a graphene superlattice. Inset: BZ minibands, shown as $E(\boldsymbol{k})$ inside the first Brillouin zone (indicated by the grey hexagons; their sizes decreases with increasing q). Data extracted from ref [194].

The quasiparticles residing in these rational fractions of the flux quantum are the Brown-Zak fermions (BZF), characterised by their own miniband spectra [194, 234–236, 238], different from the zero-B Dirac spectrum of graphene-on-hBN superlattices (see inset of figure 6.1 for the most prominent unit fractions). According to the group-theory analysis, these spectra can be reduced to the case of a zero effective magnetic field ($B_{\text{eff}} = B - B_{p/q} = 0$) by introducing new Bloch states and associated magnetic minibands, that are different for each p/q fraction. This concept was put forward by Brown and Zak [228, 229] who introduced the concept of magnetic translation group, predating the work of Hofstadter [231]. Each realisation of BZF has an additional q-fold degeneracy [10, 227–237]. This is equivalent to saying that each BZ fermion contains q equivalent mini-valleys. This degeneracy is additional to the 4-fold spin and valley degeneracy of graphene's original Dirac spectrum. These spectral properties will be experimentally proven in chapter 7. In the next sections, we demonstrate that BZFs are Bloch quasiparticles — like electrons in solids or Dirac fermions, and at $B = Bp/q$, they propagate through the superlattice as if the applied magnetic field is zero.

6.2 Experimental measurements of Graphene superlattices

Here I report the observation of BZFs with different p and q on high-quality graphene superlattices, fabricated using the dry transfer method (see appendix A), where the graphene layer is carefully aligned with one of the encapsulating hBN sheets, using one of the crystallographic edges [107]. For clarity of the measurement, a second encapsulating hBN crystal is intentionally misaligned to dodge competing moiré patterns [240–242]. The stack made therein was placed on an oxidised Si wafer, allowing us to apply back-gate voltage V_{g} to control the carrier density n (see chap 4). Multiple devices were studied but only two are shown in this chapter to highlight characteristic effects.

6.2.1 Zero-field behaviour

The first step in the characterisation of our devices consists in measuring the longitudinal resistivity ρ_{xx} at zero B, as well as the Hall resistivity ρ_{xy} in small magnetic fields (non quantising, i.e. below 0.1 T at T_{mc} =10 mK, allowing us to extract the $n(V_{\text{g}})$ dependence for all voltages except close to the neutrality points and van Hove singularities, corresponding to densities where ρ_{xy} reverses its sign and can no longer be described by the standard dependence $\rho_{\text{xy}} = B/ne$. An example of the zero-field longitudinal resistivity is shown

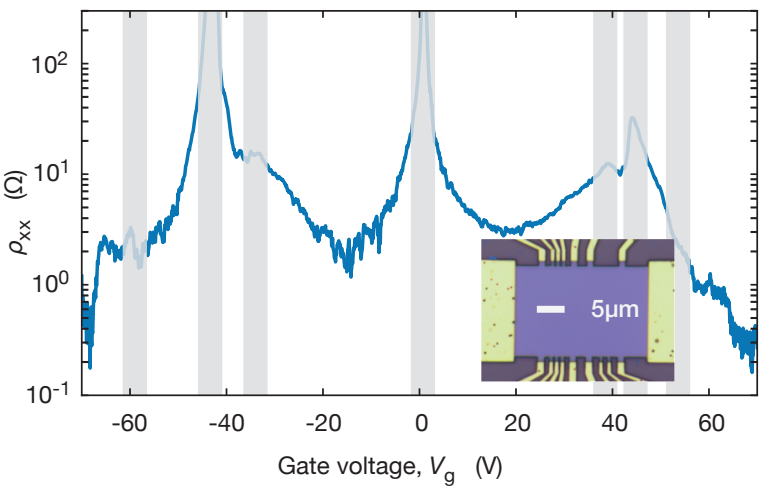

Fig. 6.2 Characterisation of device D1 with width W =17 µm. Longitudinal resitivity $R_{xx}(V_g)$ for the characteristic device shown in inset (optical micrograph)

in figure 6.2. Three peaks in ρ_{xx} can be observed at 0 V, 45 V and −45 V. The high-voltage peaks provide an unambiguous indication of the superlattice reconstruction of graphene's spectrum [105, 106, 238]; they are referred as secondary Dirac points. Note that the Dirac point for positive V_g (electron doping) is blunter than for negative V_g (hole doping), in agreement with theoretical work demonstrating that the effect of hBN alignment on the band structure is stronger in the valence band [105–110].

All studied devices exhibit mobilities $\mu = (\rho_{xx} ne)^{-1}$ in the order of $1 \times 10^6\,\mathrm{cm^2\,V^{-1}\,s^{-1}}$ (fig. 6.3a), reduced from ideality, by edge scattering due to finite W between 2 µm to 17 µm. However, the high quality of the devices can be corroborated using transverse magnetic measurements at low B (see figure 6.3b). In these conditions, the observation of resistance oscillations — due to transverse magnetic focusing — confirms that the Dirac fermions travel ballistically across the devices, along skipping orbits that extend over several hundreds of superlattice unit cells [243, 244]. This measurement also provides information about the Fermi surface topography for clean metals (including graphene superlattices) and agrees with the measurements previously reported [243].

Another quantity of interest is the mean free path ℓ. For Dirac fermions, the mean free path is calculated using the standard formula of the Drude model:

$$\sigma_{xx} = g\frac{e^2}{h}\left(\frac{k_F \ell}{2}\right), \tag{6.3}$$

where the Fermi wave vector $k_F = (4\pi/g)^{1/2}$ takes into account the degeneracy g of the Dirac fermions, that is 4 to account for the two-fold spin and valley degeneracies. As a result, one may write the mean free path as:

$$\ell = \frac{2}{\rho_{xx}}\frac{\hbar}{e^2}\sqrt{\frac{\pi}{4n}}. \tag{6.4}$$

The mean free path for the same characteristic device is shown in figure 6.3. The mean free path at $B = 0$ reaches distances >20 µm, which implies ballistic transport, limited by the device width W rather than impurity scattering.

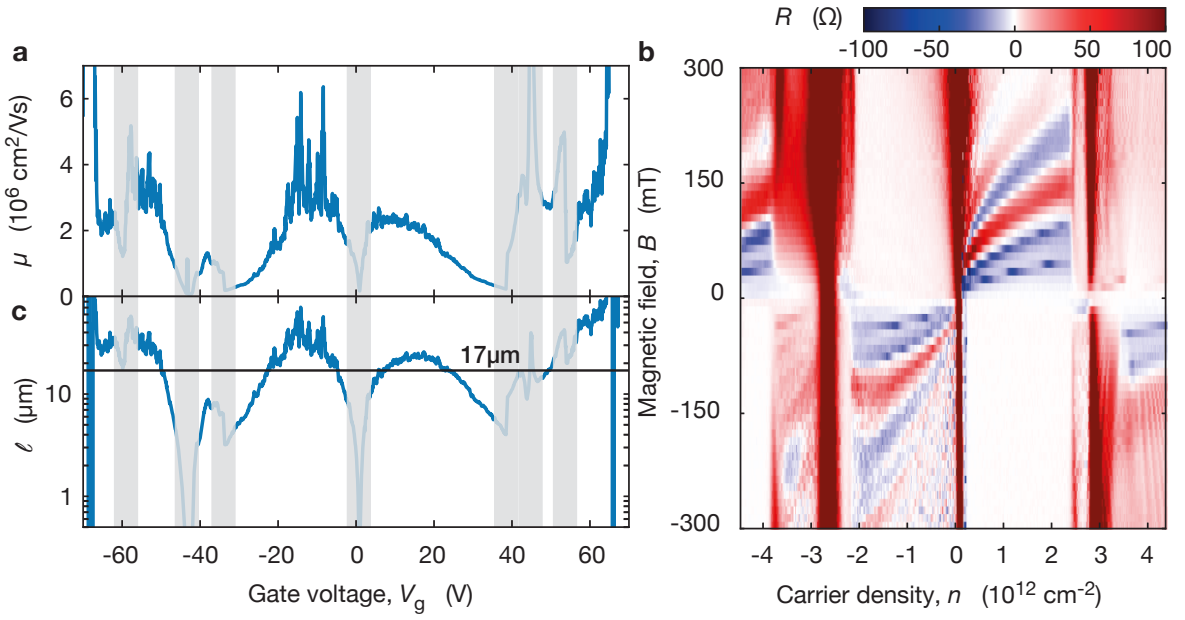

Fig. 6.3: Characterisation of device D1 a) mobility from the Drude formula. **b)** Transverse magnetic focusing measured using contacts separated by 1.5 µm (closest contacts of D1). **c)** mean free path calculated with equation 6.4. Semitransparent vertical strips in (a) and (c) indicate the doping regions around NPs and vHS where n could not be extracted directly from Hall measurements with charge inhomogeneity playing a role. measured at $B = 0$ (a,c) and T_{mc} =10 mK.

6.2.2 Direct observation Brown-Zak fermions

Figure 6.4 shows a map of the longitudinal conductivity $\sigma_{\mathrm{xx}} = \rho_{\mathrm{xx}}/(\rho_{\mathrm{xx}}^2 + \rho_{\mathrm{xy}}^2)$ as a function of V_{g} and B in fields up to 18 T. The dark features on this map can be understood in terms of the Hofstadter spectrum for Dirac fermions in moiré superlattices [107–113, 231] and are the focus of chapter 7. Here, the feature of interest is the appearance of high mobility Brown-Zak fermions (BZF) in high (quantising) magnetic fields.

We focus here on the high conductivity features. There are numerous Landau levels (LLs) spreading from the main and secondary NPs (miniband edges) which are located at V_{g} near 0 and ±45 V, and other pronounced funneling features near the vHS for $V_{\mathrm{g}} \approx -60\,\mathrm{V}$, $-35\,\mathrm{V}$, 40 V and 55 V in both hole (−) and electron (+) parts of the spectrum. More important, one may see on the conductivity map (fig 6.4) bright, horizontal yellow streaks, occurring at $\phi/\phi_0 = p/q$ where $p, q \in \mathbb{Z}$. At high temperatures (e.g. above 100 K), Landau quantisation is strongly suppressed and these high conductivity horizontal bands become the dominant transport feature [194, 238], broadening along the B axis as the temperature is increased. These were previously named Brown-Zak oscillations, and can be understood as the giant giant magnetoresistance of Brown-Zak fermions in a small effective field B_{eff}. The conductivity maxima correspond to zeros in ρ_{xy}, reflecting the recovery of translational symmetry (p flux quanta penetrate through q superlattice unit cells) and the emergence of Bloch states experiencing zero B_{eff}. Along with each horizontal streak, a

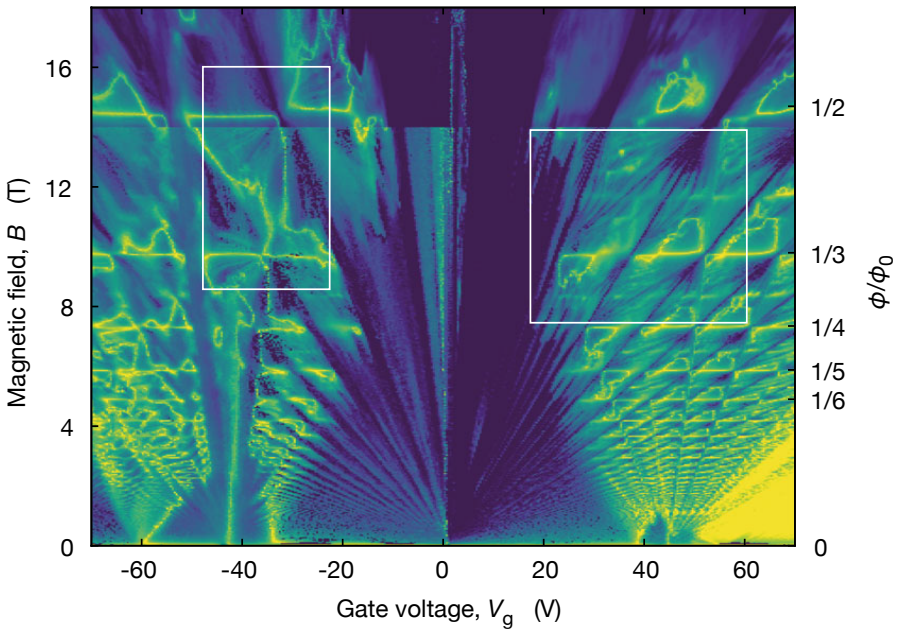

Fig. 6.4: longitudinal conductivity $\sigma_{xx}(V_g, B)$ of device D1 measured by sweeping V_g and varying B in small steps of 40 mT. T_{mc} =10 mK and 250 mK below and above 14 T, respectively. Indigo-to-yellow colours: log scale truncated between 38 nS and 16 mS for B <14 T and between 4 nS and 0.4 mS above 14 T. White rectangles are shown in finer details in chapter 7.

notable feature is the presence of numerous NPs and vHS, reflecting different realisations of BZFs at each $B_{p/q}$. Additionally, one can find a repetitive triangular pattern (seen most clearly between 2 T to 12 T at positive V_g in figure 6.4). These triangles are made of horizontal streaks at zero B_{eff} and vertical streaks emerging from NPs for BZF and slanted streaks originating from vHS. It is understood that the slanted streak corresponds to second-order realisations of BZFs in a reduced Moiré unit cell.

6.3 Ballistic transport of BZF

6.3.1 Mobility and mean free path

To evaluate the mobility of Brown-Zak fermions, I used the standard formula $\mu = \sigma_{xx}/n_{BZF}e$ where n_{BZF} is the carrier density of BZFs and $\sigma_{xx} = 1/\rho_{xx}$. This latter expression does not contain ρ_{xy} because the effective magnetic field B_{eff} acting on BZF is zero for $\phi = \phi_0 p/q$. The difficulty resides in evaluating n_{BZF} for a given V_g. To do so, I first used Hall measurements at small fields B ≤0.1 T to determine the geometrical capacitance and then use the longitudinal conductivity map around the p/q fraction of interest to identify the position of the neutrality points as V_g at which Landau mini-fans converge. vHS can be identified from Hall effect measurements as V_g corresponding to a change of sign in ρ_{xy} without exhibiting mini-fans (see chap. 7). As n_{BZF} varies

linearly across NPs and exhibits jumps at the vHSs, the known geometrical capacitance allows one to reconstruct $n_{\mathrm{BZF}}(V_{\mathrm{g}})$ as shown in figure 6.5.

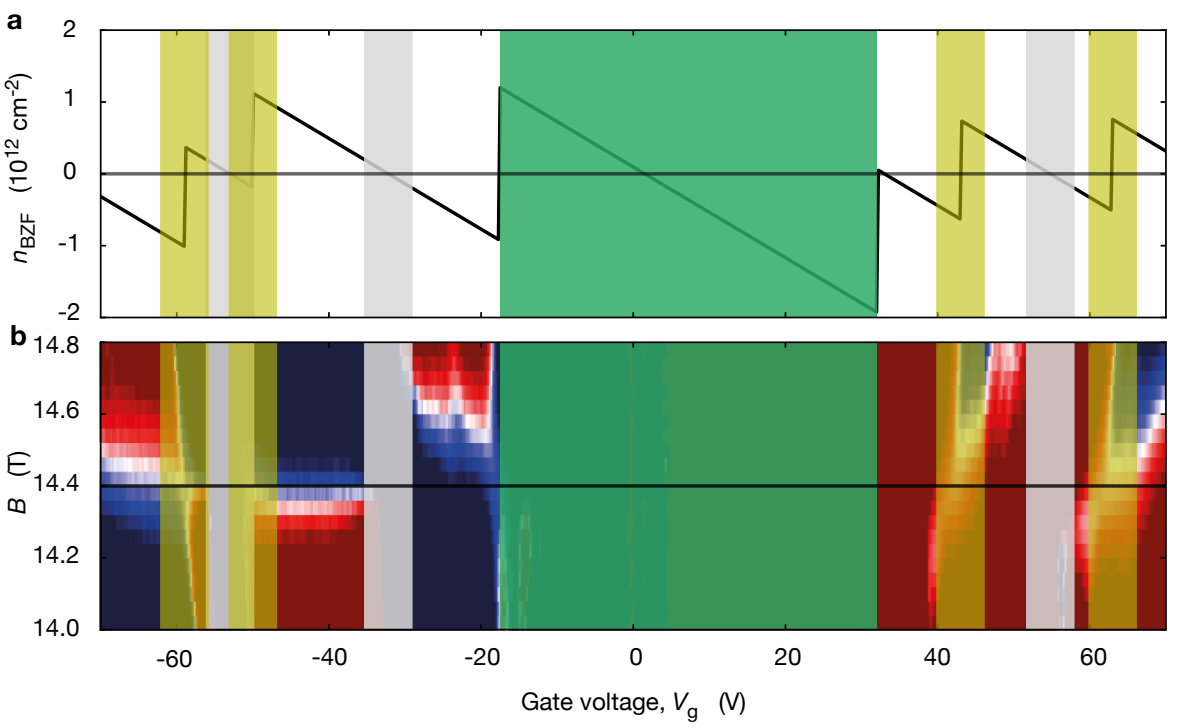

Fig. 6.5: Evaluating density of BZFs on device D1. a) Dependence of n_{BZF} on gate voltage at $\phi/\phi_0 = 1/2$ for the same device. **b)** measured maps for the Hall resistivity around $\phi/\phi_0 = 1/2$. colour scheme: blue and red represent negative and positive ρ_{xy}, respectively. Regions around NPs are indicated by the grey semi-transparent strips. The yellow strips mark vHS. The central green area covers the region dominated by the quantum Hall effect of Dirac fermions from the main graphene spectrum.

From this, the mean free path ℓ can be calculated using the formula of equation 6.4, replacing g by the BZF degeneracy and n by n_{BZF}:

$$\ell = \frac{2}{\rho_{\mathrm{xx}}} \frac{\hbar}{e^2} \sqrt{\frac{\pi}{g n_{\mathrm{BZF}}}}. \tag{6.5}$$

Here BZF have an additional mini-valley degeneracy [10, 227–237], equal to q (thas is, $g = 4 \times 2 = 8$ for the case of $\phi/\phi_0 = 1/2$), a result that will be proven experimentally in chapter 7. Using $g = 4q$ one can extract μ and ℓ from the measured longitudinal resistivity, as shown in figure 6.6, for different occurrences of BZF ($\phi/\phi_0 = 1/2$, $1/3$ and $1/4$). Here it is clear that away from the NPs and vHS, BZF exhibit μ reaching a few $10^6\,\mathrm{cm^2\,V^{-1}\,s^{-1}}$, comparable to μ of Dirac fermions in zero B. Additionally, the mean free path of BZF exceeds 10 µm, marginally smaller than ℓ of Dirac fermions, possibly a result of inhomogeneities within the device, combined with the difficulty of experimentally controlling the magnetic field precisely so that $B = B_{p/q}$. Surprisingly, mobilities for BZF with the larger q remain on the order of $10^6\,\mathrm{cm^2\,V^{-1}\,s^{-1}}$ and their mean free path approaches values comparable to the device width $W = 17\,\mu\mathrm{m}$, suggesting ballistic transport with a notable contribution from edge scattering.

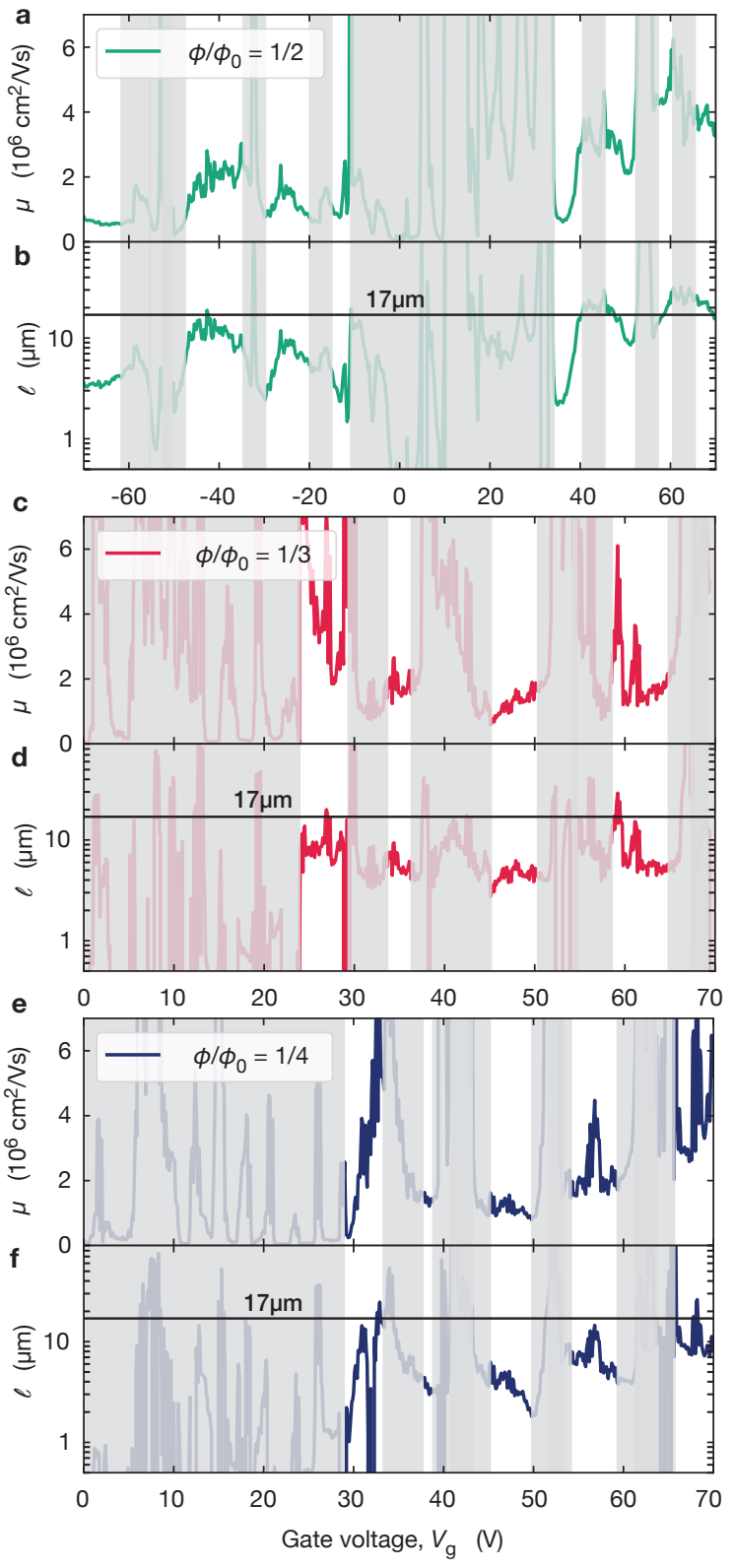

Fig. 6.6 Ballistic transport of BZFs on device D1: Mobility (a, c, e) and mean free path (b, d, f) of BZF for unit fractions of the flux quantum at 10 mK, for $\phi/\phi_0 = 1/2$ (a,b), $\phi/\phi_0 = 1/3$ (c,d) and $\phi/\phi_0 = 1/4$ (e, f). For 1/3 and 1/4 we show the data for positive voltages only because the vHS could accurately be identified only for electron doping.

6.3.2 Negative bend resistance

The ballisticity of BZF can be confirmed using the bend resistance geometry [6, 91] (see paragraph 2.2.2.1). Here we adapted the geometry to be used on Hall bar devices (see fig 6.7a). This allows one to detect if charge carriers can move ballistically over the entire channel width W with straight trajectories connecting current and voltage contacts. In these conditions, ballistic transport gives rise to the negative sign of the bend resistance R_b, in contrast to the conventional positive sign for a diffusive (ohmic) transport.

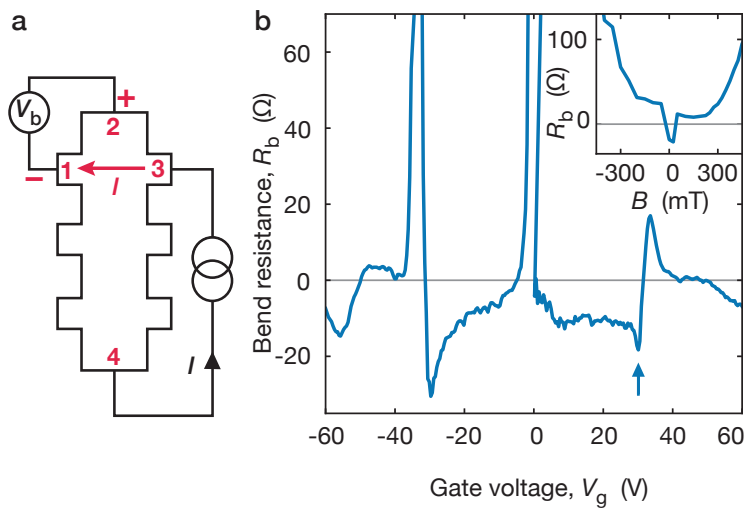

Fig. 6.7: Ballistic transport over micrometre distances. a) Schematic of bend resistance measurements. Current I is applied between contacts 3 and 4, and voltage V_b is measured between 2 and 1, yielding the bend resistance $R_\mathrm{b} = V_\mathrm{b}/I$. The voltage is positive for diffusive transport but becomes negative if charge carriers move directly from current injecting contact 3 into voltage probe 1 (as shown by the red arrow). **b)** bend resistance for Dirac fermions in zero B, measured on device D2 with $W = 4\,\mu\mathrm{m}$. Inset: $R_\mathrm{b}(B)$ taken at the minimum indicated by the arrow in the main plot.

Figure 6.7b shows measurements of device D2 (W =4 µm) in the bend resistance geometry. As expected from the long ℓ of Dirac fermions, R_b is negative in zero B everywhere away from NPs and vHS. Additionally, finite magnetic fields B bend the Dirac fermions trajectories, resulting in a rapid reversal of the sign of R_b with increasing B (see inset of fig. 6.7b). This measurement can be understood as follows (see section 2.2.2.1 for more details). For simplicity let us consider positive charge carriers (hole doping regime). In the case of ballistic transport, holes injected from contact 3 (see fig. 6.7a) travel along distances exceeding W hence can reach contact 1 without scattering. As a result, an extra positive charge would be accumulated near contact 1, and the voltage difference $V_{21} = V_2 - V_1$ will be negative. However, if the transport is diffusive, holes from contact 3 would travel along the lines of the electric field, and accumulate at contact 4 thus the sign of V_{21} should be conventional (positive). This consideration is also valid for electrons and therefore, negative R_b means that ballistic transport is occurring over distances larger than W.

6.3.3 Negative bend resistance of BZF

Concerning ballistic transport of BZF, the devices also exhibit negative R_b in high $B = B_{p/q}$, an evidence of straight trajectories over distances of several µm. Figure 6.8 shows the measured bend resistance R_b as a function of gate voltage and magnetic field. Negative R_b is observed in profound pockets around B corresponding to ϕ/ϕ_0 =1/2, 1/3, 1/4 and 1/5. This is the regime where the

existence of BZF experiencing $B_{\mathrm{eff}} = 0$ was previously demonstrated [194] from maxima in σ_{xx} and zeros in ρ_{xy}. Interestingly, negative pockets can only be observed for unit fractions $1/q$ of ϕ_0 with q from 2 to 5. Despite the relatively small size W of the device, no evidence for ballistic transport could be observed in this geometry for high-order BZF ($p > 1$).

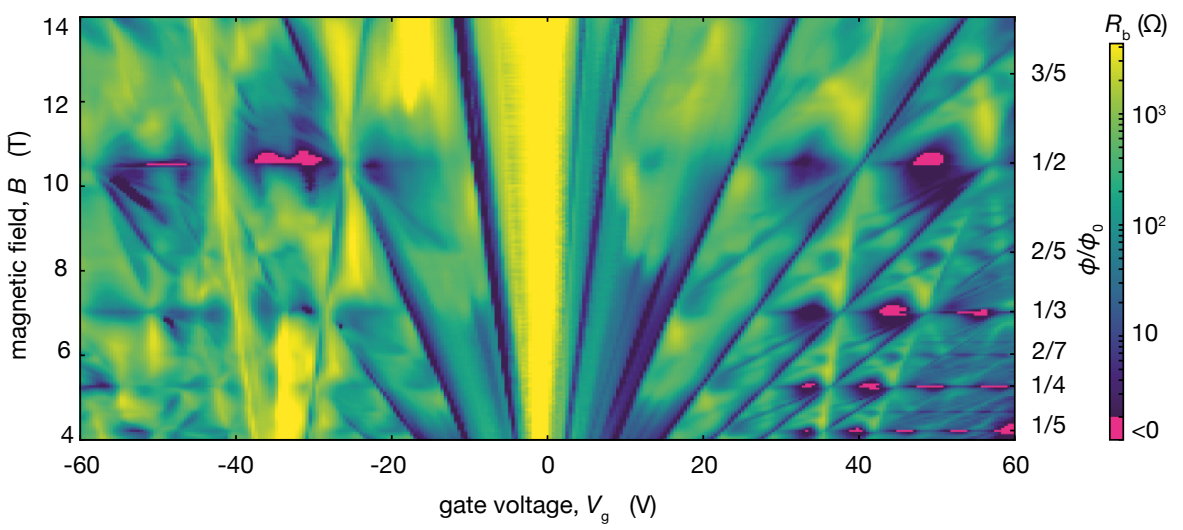

Fig. 6.8: Ballistic transport of BZF map $R_{\mathrm{b}}(V_{\mathrm{g}}, B)$ for device D2. B was changed in steps of 50 mT. Pockets of negative R_{b} appear along $\phi/\phi_0 = 1/q$ and are seen in magenta. The resistance quickly increases and changes sign for small $B_{\mathrm{eff}} = B - B_{p/q}$.

At fields $B = B_{p/q}$, BZFs move through the superlattice as if there was no external magnetic field. As a result, the negative bend resistance is observed. This possibility of ballistic transport was suggested using numerical simulations [111], and the profound negative R_{b} observed here proves this conjecture unequivocally. These pockets are located between NPs and vHS for BZF, similar to Dirac fermions. Away from these exact $B_{p/q}$ values, BZF experience non-zero $B_{\mathrm{eff}} = B - B_{p/q}$, which bends their trajectories, therefore replicate the usual magneto-transport effects of charge carriers in conventional 2D electron systems. As a result, the negative bend resistance vanishes quickly upon increasing the field. This feature is similar to the case of other Bloch quasiparticles (electrons, Dirac fermions, etc.).

Let me now comment on the observation of negative R_{b} only for unit fractions of the flux. As an example, a negative R_{b} pocket can be seen in figure 6.8 at the flux fraction $\phi/\phi_0 = 1/5$, but the signal is positive for 2/5 and 3/5. This can be attributed to the effective mass of BZFs that depends strongly on p/q (electronic spectra differ in different magnetic minibands [105, 194, 238]). Particularly, a consequence is that the mobility μ is much lower for BZF with $p > 1$, which could directly result in the absence of ballistic transfer for these fractions.

Note that the negative signals shown here are robust and characteristic of the geometry. We measured a corresponding map of ρ_{xx} (see chapter 7, fig. 7.6) in the same device, showing that the longitudinal resistance always remains

positive. Additionally, for some devices, negative resistance can be observed away from $\phi/\phi_0 = 1/q$. Unlike ballistic transfer resistance at unit flux fractions, these negative signals are not reproducible for all contact configurations and are usual in the quantum Hall effect regime using narrow (mesoscopic) devices [245].

Finally, the ballistic transport of BZF is found to be slightly sensitive to the temperature T: the pockets of negative R_b disappear universally above 30 K to 50 K, as shown in figure 6.9. This dependence is generally expected because the mean free path ℓ of BZF becomes shorter at higher T. Nonetheless, exact scattering mechanisms are unknown and could be non-trivial such as, for example, Umklapp electron-electron scattering [246, 247]. Overall, this could require further investigation well beyond the scope of this work.

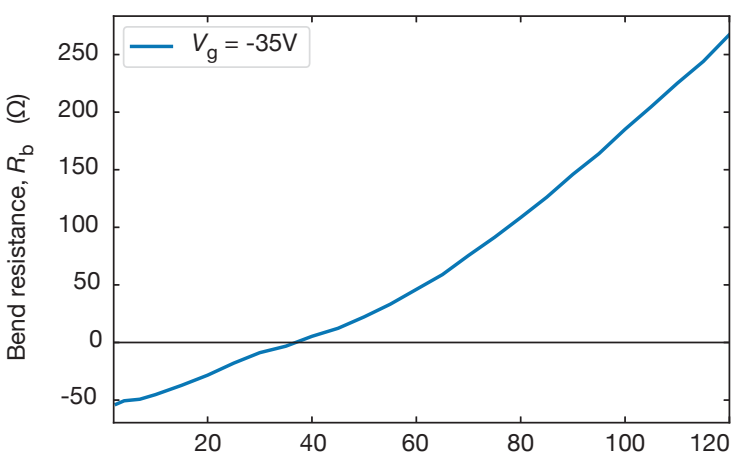

Fig. 6.9 Temperature dependence of BZF's ballistic transport example of the bend resistance measured at $\phi/\phi_0 = 1/2$ using device D3 with $W = 2\,\mu\mathrm{m}$

Conclusion

Graphene superlattices allow studying electronic transport under strong magnetic fields, in a regime where the magnetic length is commensurable with the lattice constant. Here I have shown that under such conditions, transport is dominated by a family of Bloch quasiparticles, the Brown-Zak fermions (BZF) with high mobility and mean free path. Studying further the electronic transport for this family of quasiparticles, I demonstrated that they have ballistic trajectories up to several microns for unit fractions of the magnetic flux in a wide range of temperatures.

Chapter 7
Landau quantisation of Brown-Zak fermions

Whenever the magnetic flux ϕ through the superlattice unit cell is commensurate with the magnetic flux quantum ϕ_0, charge carriers (Brown-Zak fermions) behave as if the applied magnetic field was absent. Their quantisation, described by the Hofstadter butterfly, depicts quantum states developed from intermixing of the field-induced spectrum (Landau levels) with the superlattice-related gaps (Bloch bands). This study necessitates low temperatures to prevent smearing of the most fragile gaps. In this chapter, we discuss the general picture of non-interacting electrons in graphene superlattices, corresponding to the Hofstadter butterfly. Particularly, we characterise Brown-Zak fermions (BZF) through their mini-valley degeneracy, extracted from Landau fans in non-zero B_{eff}.

7.1 The Hofstadter-Wannier picture

7.1.1 Spectrum of Bloch electrons in a magnetic field

If one refers to the problem first enunciated by Azbel [227] (see equation 6.1), it is possible to calculate the eigenvalues — the spectrum — numerically. This was first done and plotted by Hofstadter [231] on a square lattice as a function of the reduced flux $\alpha = \phi/\phi_0$ and the energy ε, showing the fractal structure of the Hofstadter butterfly (see fig 7.1).

In this spectrum, it appears that energy bands cluster into groups of bands, that in turn cluster into larger groups, forming the recursive structure of the butterfly. The element of interest here is the white regions between the eigen-

---

Results presented in this chapter have been published in:
J. Barrier, P. Kumaravadivel, R. Krishna-Kumar, L.A. Ponomarenko, N. Xin, M. Holwill, C. Mullan, M. Kim, R.V. Gorbachev, M.D. Thompson, J.R. Prance, T. Taniguchi, K. watanabe, I.V. Grigorieva, K.S. Novoselov, A. Mishchenko, V.I. Fal'ko, A.I. Berdyugin and A.K. Geim, "Long-range ballistic transport of Brown-Zak fermions in Graphene superlattices", Nat. Commun. **11**, 5756 (2020)

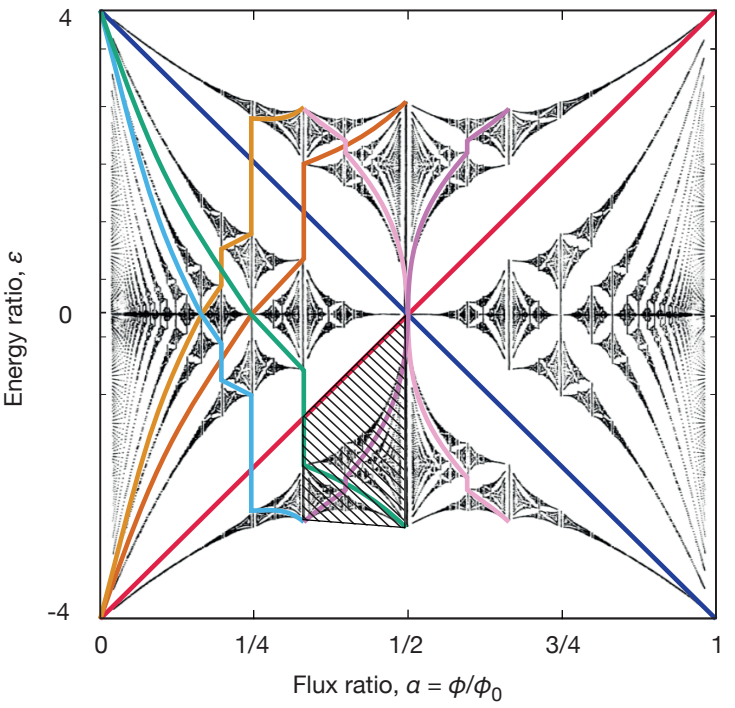

Fig. 7.1 Hofstadter butterfly on a square lattice black dots show the eigenvalues. Colour lines show the gaps between main bands, cf fig 7.2. Hatched zone is an example of a cell in the Hofstadter model.

values (black dots), corresponding to gaps. The main energy bands are the Landau levels. For low flux ratios α, the Landau levels are seen as sharp energy bands, and as α is increased, these bands acquire an internal structure of subbands, each located inside a cell (see fig 7.1). A few other interesting information can be extracted from this diagram: a) whenever $\alpha = p/q$ (the regime of Brown-Zak fermions highlighted earlier), the Bloch band breaks into p distinct subbands per cell (and q bands for all energies). b) spectrum(α) = spectrum($\alpha + N$). c) spectrum(α) = spectrum($-\alpha$) and d) the spectrum is symmetric in energy. Additionally, filling a band corresponds to increasing the hall conductivity σ_{xy} by 1. As a result, the Hofstadter butterfly can be seen as a phase diagram for non-interacting electrons [248].

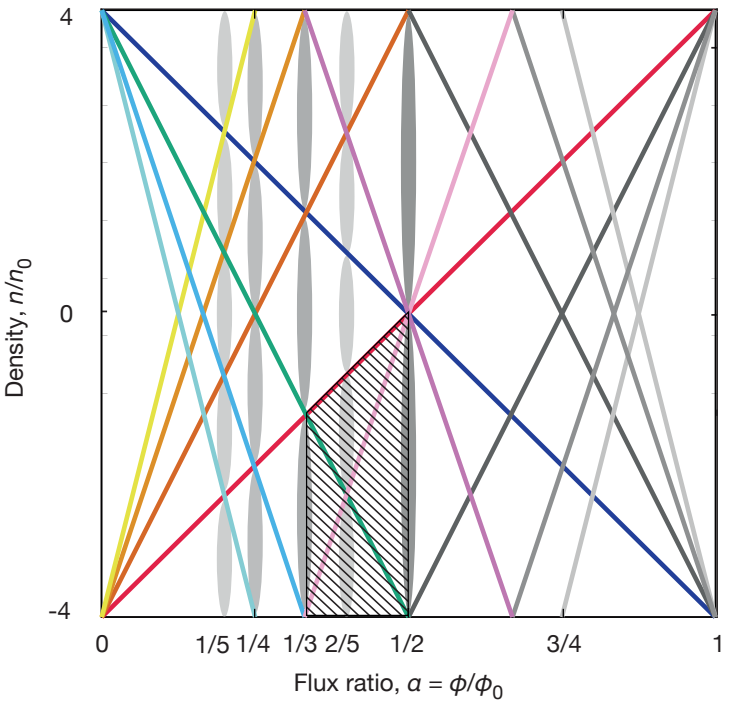

Fig. 7.2 Wannier diagram on a square lattice, constructed based on the Hofstadter butterfly. lines correspond to the same colour as in fig 7.1, corresponding to gaps (LLs). grey ellipses correspond to fraction p/q, a region where BZFs are found.

However, the interpretation of measurements in light of the Hofstadter butterfly can be complicated at a first sight. To overcome this issue, a transformation to plot the non-interacting electron model of the Hofstadter butterfly as a function of measurable quantities was introduced [230]. Indeed, the problem is simplified when plotting the gaps as a function of the normalised electron density n/n_0 in a magnetic field (or, more exactly the flux ratio α), which is the Wannier diagram. The zig-zag gaps of the Hofstadter butterfly, carrying a charge t per unit cell, are constrained to linear trajectories in the Wannier diagram. Figure 7.2 shows the Wannier diagram of a square lattice for the first 4 Landau levels and sublevels. Here, the red line (navy) corresponds, as in the Hofstadter butterfly, to 1 electron (hole) per unit cell. The brown (green), orange (blue) and yellow (teal) correspond to 2, 3, and 4 electrons (holes) per unit cell, respectively.

All the spectral gaps follow linear trajectories in the Wanier diagram, and are described by the dimensionless diophantine equation:

$$\frac{n}{n_0} = t\frac{\phi}{\phi_0} + s, \tag{7.1}$$

where $s, t \in \mathbb{Z}$. When $s = 0$, one describes Landau quantisation: t corresponds to the filling factor and is related to the Hall conductance. Parameter s corresponds to the Bloch band filling factor resulting from the crystal periodicity; it can be seen as the total number of electrons a band can accept. Other states can be seen, shown as purple and pink lines in figures 7.1 and 7.2. These states emerge from cell edges and correspond to $s > 1$. In our measurements, they are seen as self-similar Landau levels originating from the Landau quantisation of Brown-Zak fermions (BZF).

7.1.2 Wannier diagram in graphene superlattices

The case of graphene is different from a square lattice. First, the lattice is hexagonal with two inequivalent sites. Second, each of these sites corresponds to K points where two bands (conduction and valence band) join together, forming the general Dirac cones. As a result, the construction of the Wannier diagram for the hexagonal lattice must take into account these two features. In such a context, the Hofstadter butterfly is more complicated to calculate and not necessary for understanding. Note though, that it is no longer periodic in B, nor is it symmetric relative to n/n_0.

In that case, the linear dispersion of massless Dirac fermions results in Landau levels (LLs) for energies $E_\mathrm{t}(B) = \mathrm{sign}(t)v_\mathrm{F}\sqrt{2\hbar|teB|}$, with a peculiarity that is the existence of a zero-energy LL [53, 54] (see chap. 3). As a result, the diophantine equation for LL gaps of graphene (eq. 7.1) is modified by taking into account a half-integer slope $t+1/2$ corresponding to the Berry phase [249]:

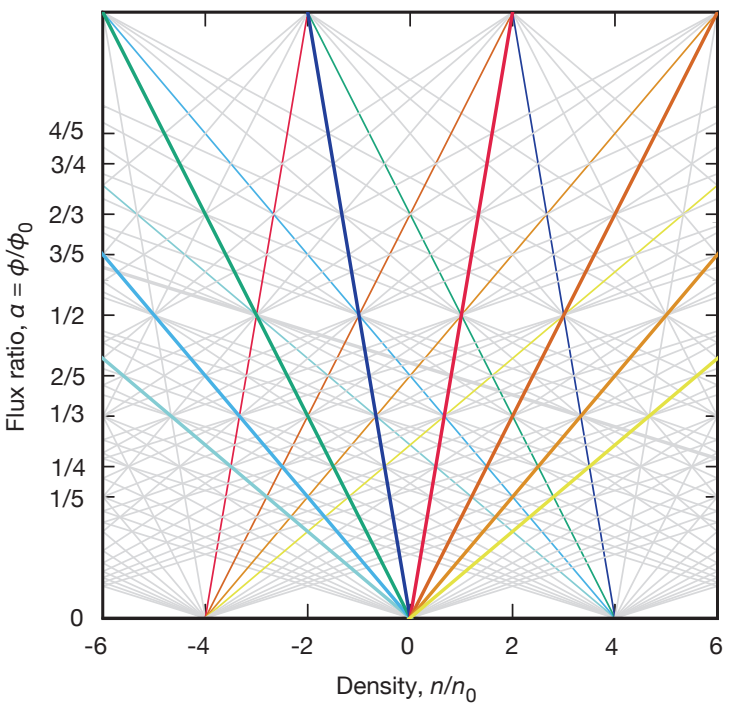

Fig. 7.3 Wannier diagram for graphene where the VB and CB touch at the Fermi level.

$$\frac{n}{n_0} = g\left(\left(t + \frac{1}{2}\right)\frac{\phi}{\phi_0} + s\right) \tag{7.2}$$

Where, for the case of Dirac fermions, $g = 4$ and the quantum Hall conductance can be expressed as $\sigma_{\mathrm{xy}} = g(t + 1/2)e^2/h$. For graphene superlattices with a superlattice constant $\lambda_{\mathrm{sl}} \approx 14\,\mathrm{nm}$, the regime of the Hofstadter-Wannier model is accessible through transport measurements in varying carrier densities and magnetic fields. In the Quantum Hall effect regime, spectral gaps appear as minima in the longitudinal conductance σ_{xx} and plateaus in the transverse Hall conductance σ_{xy} quantised in units of e^2/h. As a result, each miniband can be viewed as LLs of BZF minibands in effective magnetic fields $B_{\mathrm{eff}} = B - \phi_0 p/qS$. These features are unique and unambiguous signatures of the Hofstadter energy spectrum, distinct from the conventional integer quantum Hall effect.

The first features observable in graphene superlattices are a set of conductance minima fanning out from the second-generation Dirac fermions (see figure 6.4 around $\pm 45\,\mathrm{V}$). Counterintuitively, these are not LLs emerging from second-generation Dirac fermions but represent Hofstadter minibands [110]. At even higher magnetic fields, other sets of minima can be observed that cannot be traced back to either the main or secondary NPs [110–113]. I will show in this chapter that these states originate from the degeneracy lifting of BZF minibands. As a result, the complex pattern of figure 6.4 cannot be interpreted only in terms of Landau quantisation of the Dirac spectrum, or purely to the Hofstadter-Wannier model, but is specific to BZF in small magnetic fields $B_{\mathrm{eff}} = B - B_{p/q}$.

7.2 Degeneracy of Brown-Zak fermions

7.2.1 The Wannier-diagram as BZF Landau mini-fans

Chapter 6 introduced high mobility BZFs in graphene superlattices. The high mobility results in Landau quantisation in small $B_{\text{eff}} = B - B_{p/q} < 1\,\text{T}$. This Landau quantisation allows to experimentally find the spectral degeneracy g for different occurences of BZF at various p/q. To do so, figure 7.4 shows a high-resolution σ_{xx} map between $\phi/\phi_0 = 1/2$ and $1/4$.

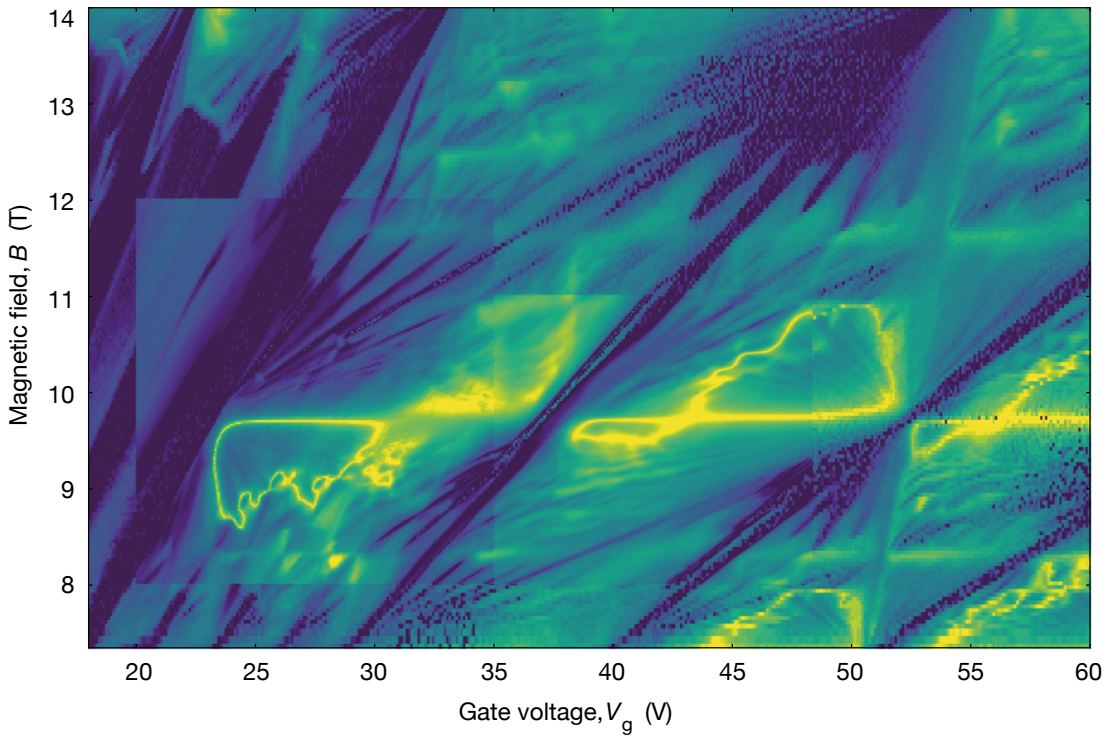

Fig. 7.4: Landau quantisation of BZF. High resolution map $\sigma_{\text{xx}}(V_{\text{g}}, B)$ on device D1 for the electron-doped region indicated in figure 6.4 by the white rectangle. B is varied in steps of 10 mT to 20 mT around $q = 3$ and 40 mT to 80 mT in other regions (resulting in contrast discontinuities. Logarithmic colour scale: indigo (230 nS) to yellow (7.8 mS).

One can see many Landau mini-fans originating from NPs, for different realisations of BZFs. As an example, we note that there are three profound mini-fans spreading from $B \approx 9.7\,\text{T}$ ($\phi/\phi_0 = 1/3$) for both $B_{\text{eff}} > 0$ and < 0. For clarity in the analysis, this conductivity map is replotted in figure 7.5 by tracing the most pronounced minima in σ_{xx}. There, each minimum can be described by an integer filling factor ν, corresponding to gt where g is the degeneracy and t the integer of the Diophantine equation. As a result, ν can be found from the minimum's slope.

In the Wannier diagram of figure 7.5, it is possible to identify LLs originating from the Dirac spectrum of the graphene superlattice, shown as black lines for filling indices 6, 10, 14, and 18. Second, we note that the 4-fold degeneracy of the Dirac fermion is broken, likely from many-body gaps as a result of quantum

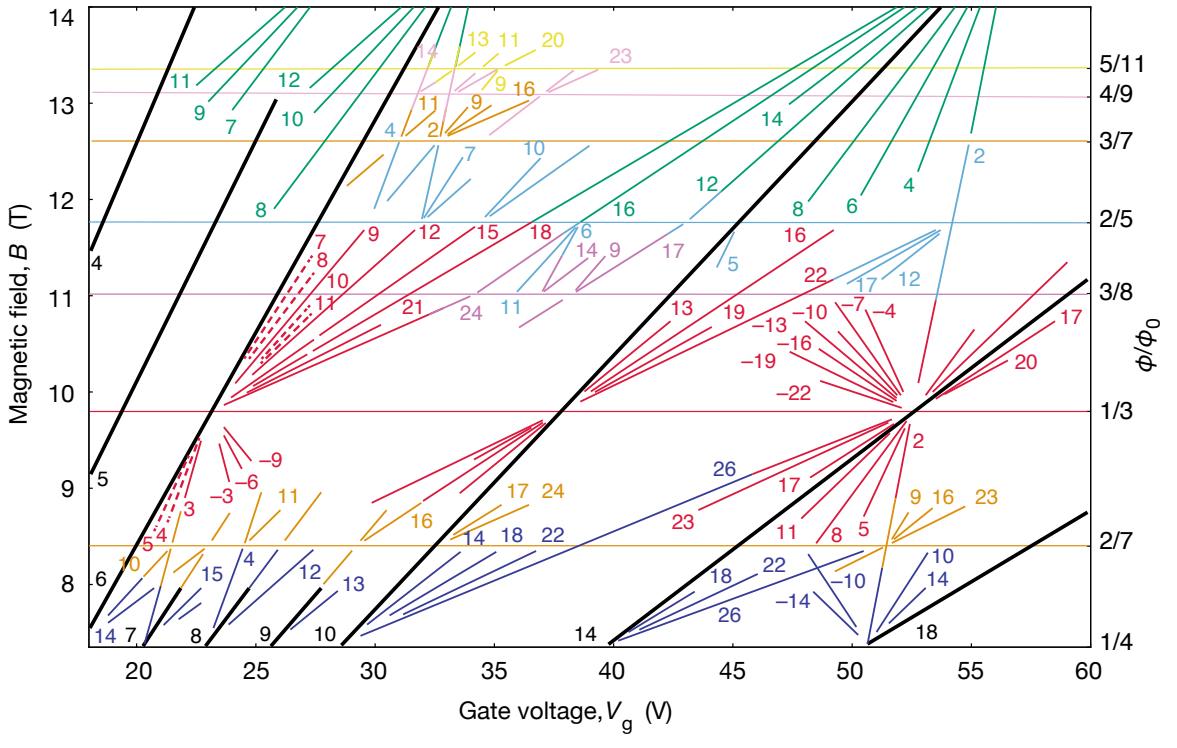

Fig. 7.5: Landau quantisation in BZF minibands: minima from 7.4 shown schematically. Colour-coded numbers are filling factors for corresponding Landau levels. Thick black lines correspond to the main sequence of LLs for graphene's Dirac spectrum (spin and valley degeneracy lifted). Green, red, navy, blue, orange, magenta, pink and yellow lines correspond to q =2,3,4,5,7,8,9 and 11, resp. Dashed red lines: minima due to mini-valley degeneracy.

Hall ferromagnetism (black lines, filling indices 4,5, 7, 8 , 9). Importantly, we focus on the LLs for BZF realisation at q =2, 3, 4, 5, 7, 8, 9 and 11, and for p =1, 2, 3, 4 and 5, shown as coloured fans. The difference in ν between the nearest LLs yields directly their degeneracy g. For example, all LLs observed for $\phi/\phi_0 = 1/2$ were separated by $\Delta\nu = 2$ whereas those at $\phi/\phi_0 = 1/3$ and $1/4$ by $\Delta\nu = 3$ and 4, respectively. As a result, the observed degeneracy of BZF at p/q is equal to q. A more detailed observation of figure 7.5 allows us to find that the degeneracy for the fraction p/q is equal to q independently of the numerator p. This q-fold degeneracy corresponds to the case where both spin and valley degeneracies are broken, as shown from the LL from the main Dirac spectrum corresponding to consecutive integer ν. When the spin and valley degeneracies are not broken — that is, at higher temperature — the degeneracy of BZF is indeed $4q$. In figure 7.6 we show the fan at 2 K, much higher than 10 mK in fig 7.5. At that temperature, the Dirac fermions of the main spectrum show a lifted spin and valley degeneracies at relatively strong B of 3 T. At lower fields B <3 T the interaction-induced gaps are smeared. This is similar for BZFs visible at 2 K. They only reach effective fields $|B_{\text{eff}}|$ <2 T, which does not allow the lifting of spin and valley degeneracies. As a result, the observed degeneracy of BZF is $4q$ at 2 K. This can be explained using the group theory of irreducible representations. A group corresponding to a p/q fraction of the magnetic flux is non-abelian, because of Aharonov-Bohm

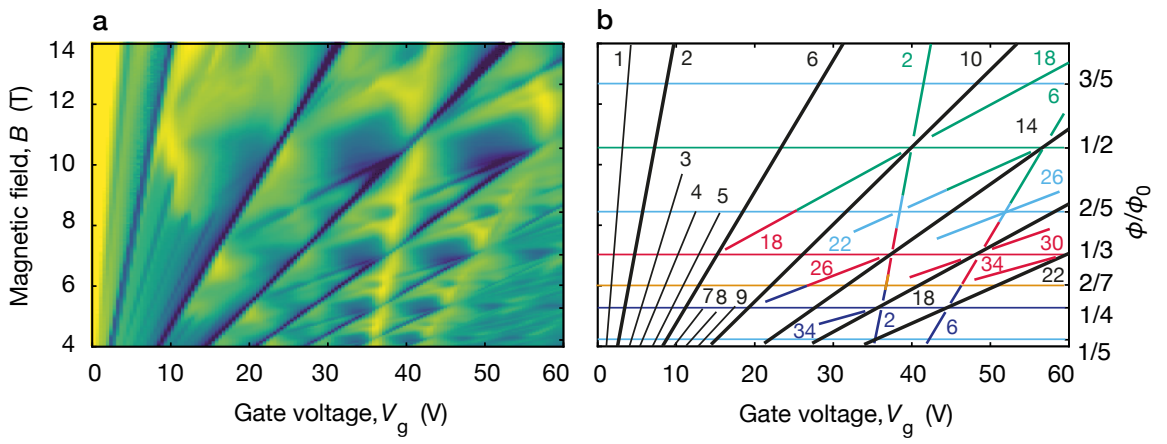

Fig. 7.6: Longitudinal resistance for ballistic BZF at a higher temperature. a) $R_{xx}(V_g, B)$ measured for device D2, with same colour scale as in figure 6.8. **b)** minima found in the longitudinal conductivity are shown schematically with the same colour coding as in figure 7.5. Thin black lines mark LLs with lifted spin and valley degeneracy for Dirac fermions of the main spectrum.

phases acquired upon translations in non-colinear directions. However, this group contains an abelian subgroup of translational symmetries, corresponding to a magnetic superlattice with a supercell that is q times larger. As a result, each realisation of BZF should have a q-fold degeneracy, taking the form of q mini-valleys in the magnetic mini-Brillouin zone, with an area that is q times smaller than the moiré superlattice Brillouin zone at $B = 0$. This comes on top of the spin and valley degeneracy of graphene's Dirac spectrum. As a result, the full degeneracy of BZF is $4q$ where 4 corresponds to 2 spins and 2 valleys. Lifting these degeneracies at ultra-low temperatures (as in figs 7.4 and 7.5) results in an observed q-fold degeneracy.

Additionally, the measured Hall conductance also exhibits quantised values in steps of qe^2/h, a further proof of the q-fold degeneracy of Brown-Zak fermions. As an example, figure 7.7 shows a zoom-in around $\phi/\phi_0 = 1/3$, showing steps $\Delta\sigma_{xy} = 3$.

7.2.2 Lifting mini-valley degeneracy

Looking in detail at figures 7.4 and 7.7, one can distinguish a notable exception to the single-particle Hofstadter-Wannier gap sequence with a q-fold degeneracy. There are additional quantum Hall effect minima, shown with dashed lines in figure 7.5. These LLs of BZF with q =3 are separated only by $\Delta\nu$ =1 so that all consecutive LLs from 3 to 12 are visible on the fan diagram. In theory, LLs with $\Delta\nu = 1$ do not exist within the single-particle Hofstadter-Wannier model [112, 113, 230, 231]. These fragile minima are attributed to BZ states with lifted mini-valley degeneracy. The quantum Hall effect for σ_{xy} = 7, 8, 10 e^2/h (see fig. 7.7 is further evidence of the observed degeneracy lifting.

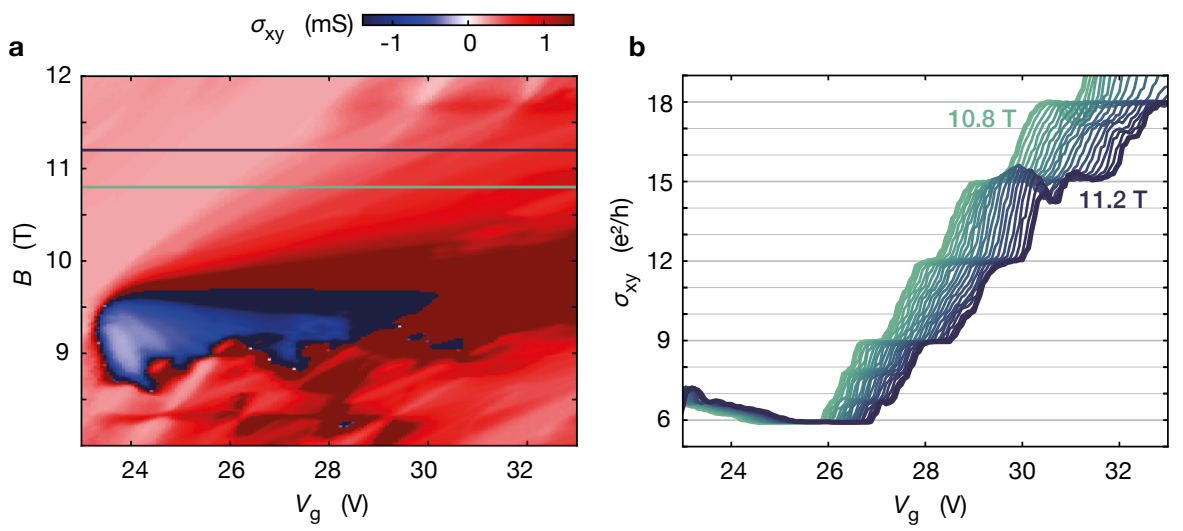

Fig. 7.7: Quantised Hall conductance of BZF on device D1. a) σ_{xy} around $\phi/\phi_0 = 1/3$. **b)** Hall conductivity as a function of gate voltage at a number of constant B within the field interval around 11T (colour-coded in (a)).

One can see well-developed plateaus with quantised values, fully consistent with the filling factors reported in 7.5. This lifting of all the degeneracies of BZF at low T involves very small energy gaps, as further emphasised by the rapid disappearance of these features with increasing T. Indeed these additional minima could not be resolved at 2 K, and also disappeared rapidly with increasing excitation current. For example, figure 7.8 shows the Landau mini-fan around $\phi/\phi_0 = 1/3$ for currents of 10 nA and 100 nA. In the lower current measurements, the minima associated with the lifted mini-valley degeneracy are lifted. At higher currents, one can observe the complete smearing of the degeneracy-lifted gaps as a result of an increase in the electronic temperature.

Let me comment on the fact that this degeneracy lifting has been observed previously and referred to as either the Fractional Bloch quantum Hall effect (FBQHE) [112] or symmetry-broken Chern insulators (SBCI) [113]. Both these denominations are confusing as they suggest that these states appear either spontaneously or through many-body physics. In theory, the mechanisms underlying the mini-valley degeneracy lifting is unclear and would require further studies to be fully resolved. A few hypotheses can nonetheless be made based on localisation of BZF states at ultra-low temperatures. The degeneracy lifting can happen via mini-valley mixing, due to the formation of charge-density waves that are commensurate with the magnetic superlattice (composed of q unit cells of the underlying moiré pattern), or a Wigner crystal [250] (states localised in a region of the magnetic supercell). Alternatively, this may occur because of spontaneous mini-valley polarisation of the BZF LLs, a phenomenon analogous to the isospin ferromagnetism in graphene [110]. In that case, BZF states would localise in the momentum space around one of the mini-valleys but would remain delocalised in the magnetic supercell.

According to the group theory of irreducible representations for the group of translation in a magnetic field [228, 229],

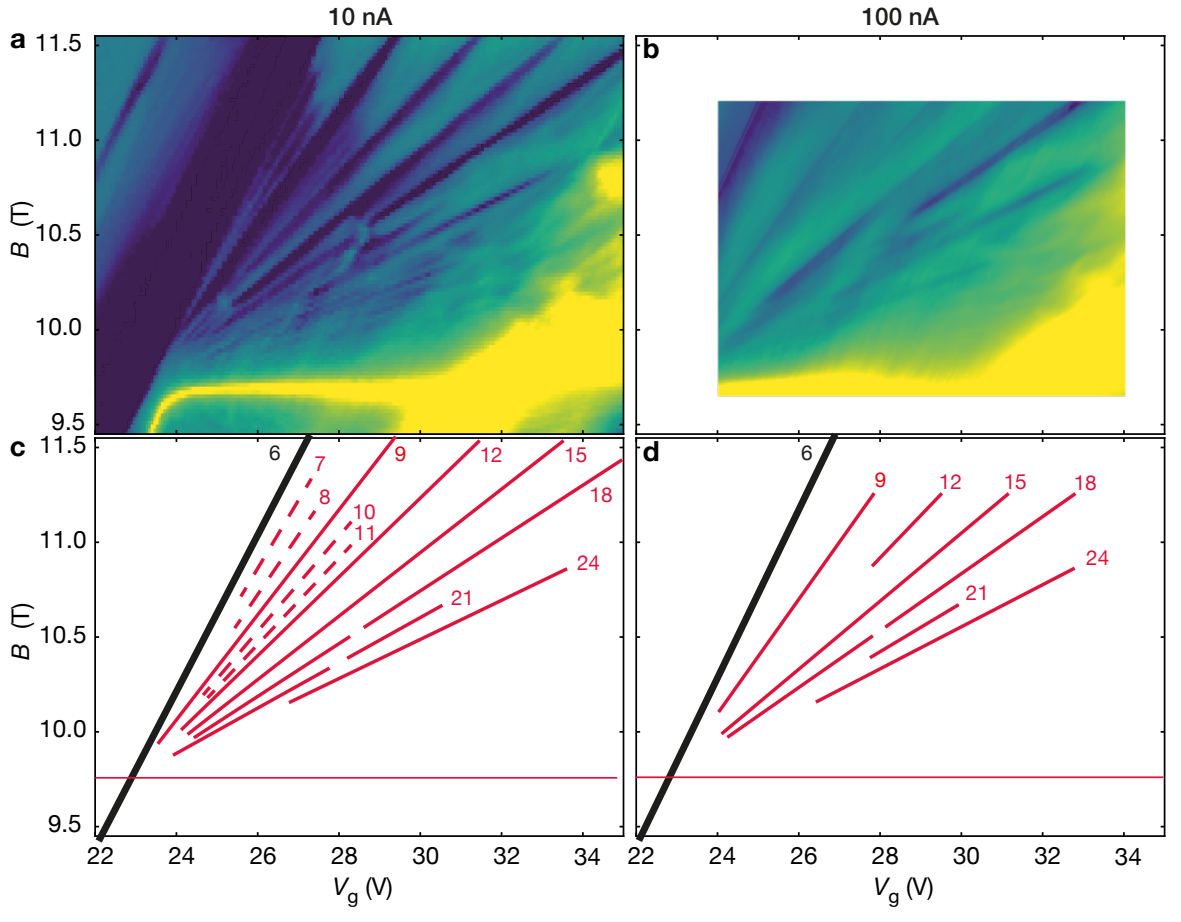

Fig. 7.8: Landau mini-fans in device D1 for different excitation currents. a and b) $\sigma_{xx}(B, V_g)$ at $T_{mc} = 10\,\text{mK}$ for $I_{ac} = 10\,\text{nA}$ and $100\,\text{nA}$, resp. Indigo-to-yellow log scale: $310\,\text{nS}$ to $780\,\mu\text{S}$. **c and d)** minima found in (a) and (b) shown schematically. Colour-coded numbers are the filling factors for the nearby LLs. Thick black lines = main sequence of LLs for graphene's Dirac spectrum.

7.3 Anomalous behaviours

On the electron side of the $V_g - B$ map, most of the features follow the described behaviour. However, some Landau mini-fans in the electron ($V_g < 0$) exhibit highly anomalous behaviour at low T that cannot be understood within the Hofstadter-Wannier model, or by considering LLs of non-interacting BZF. To the best of my knowledge, this behaviour has not been reported before, and understanding will be needed. Figure 7.9 shows an example of anomalous BZF behaviour.

In both the considerations of the Hofstadter-Wannier model and LLs of non-interacting BZF, LLs should evolve linearly in V_g and B, as detailed so far. The linear dependence comes from the fact that the density of state on each BZF LL is proportional to $B_{\text{eff}} = B - B_{p/q}$. Note that our devices are gated through the Si/SiO_2 wafer substrate, and the relatively long ($\sim$300 nm) distance from the graphene to the gate allows us to neglect the quantum capacitance corrections [251, 252], therefore $n \propto V_g$. Figure 7.9 shows that some BZF LLs exhibit bending and staircase-like features in the case of hole doping. These two anomalous features appear away from the NPs, in the region closer

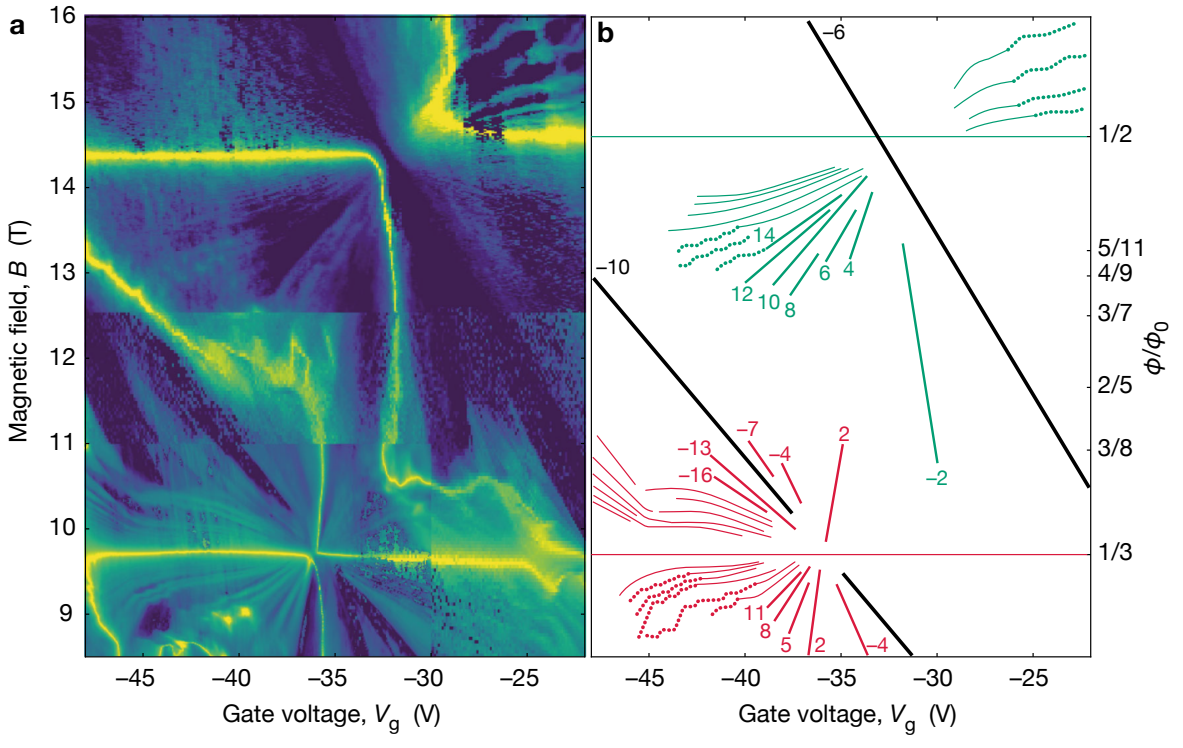

Fig. 7.9: Anomalous behaviour of BZF's LLs. a) High resolution $\sigma_{xx}(V_g, B)$ for the hole-doped region of device D1 marked in fig. 6.4. The measurements below B =12.5 T carried out at T_{mc} =10 mK and at 250 mK above. B applied in steps of 16 mT to 40 mT beove and below 12.5 T, resp (except for lower corner: data acquired at resolutions of 10 mT, see contrast discontinuities). log scale indigo (310 nS) to yellow (0.3 mS). **b)** Schematics for the conductance minima found in (a). Same colour coding as in fig 7.5. Solid lines indicate LLs evolving as expected, linearly in B and V_g. Thin curves indicate the anomalous bending. Dotted curves show the staircase-like features for some LLs. All the anomalous features are highly reproducible and do not depend on the measurement step size.

to the BZF's vHS. It would be reasonable to expect that these effects come as a result of strong electron-electron interactions, as they play a role in other experimental observations (e.g. lifting the spectral degeneracies) for the BZF occuring in the same fractions p/q. Note that the bending occurs towards the gate-voltage axis therefore usual suspects like negative compressibility fail at explaining our results. In that case, the LLs would bend towards the B axis. As a result, these anomalous behaviours are possible as a result of the interplay between BZF's LL with other quantised states originating from the nearby vHS leading to a redistribution of charge carriers between states with light and heavy effective masses. Another explanation could be the localisation of electrons within some parts of the magnetic supercell, as its size becomes notably larger than the magnetic length l_B at external fields B >10 T. This would be consistent with the Wigner crystallisation already mentioned [250]. Sadly no other features could be found to decipher the origins of these anomalies.

Conclusion

Here I have shown that in small $B_{\text{eff}} = B - B_{p/q} < 2\,\text{T}$, Brown-Zak fermions (BZF) develop their own Landau levels (LL), forming the general structure of the Wannier diagram. In-depth analysis of the LLs sequence allowed to resolve the spectral degeneracy of p/q occurrences of BZF as $4q$, degeneracy that can be fully lifted when electron-electron interactions are strong enough. Surprisingly, the additional mini-valley degeneracy can also be lifted, resulting in $\Delta\nu = 1$ for some instances of BZF. Additionally, we report two anomalous behaviours (bending and staircase-like feature) that cannot be understood at present.

Blank page

Chapter 8
Proximity effect in quantum Hall channels

When a normal metal N is placed between two superconducting electrodes S, it becomes possible to induce a supercurrent into the normal metal via Andreev bound states. It consists in transferring Cooper pairs between the two opposite electrodes via simultaneous Andreev reflectinos: an electron of the normal metal can be converted into a hole with opposite momentum and transfer a Cooper pair into the superconductor [12,32–35]. In the presence of a magnetic field, electron and hole trajectories bend, and the picture breaks down as their momentum and position no longer coincide at the NS interface [36]. The detail of this mechanism is explained in sections 2.3.2.3 and 3.3.2.

In ballistic systems however, electrons' and holes' trajectories can occasionally return to the same position after multiple bounces on mesoscopic edges [36], yielding switching currents of $\sim$50 nA under magnetic fields as high as 0.5 T. This is below the quantum Hall (QH) regime, in which proximity superconductivity is expected to allow for the observation of exications with non-trivial braiding statistics, like Majorana fermions or non-abelian anyons [253–256] but so far remains to be observed. In the QH regime, electrons and holes propagate in the same direction on the same side of the device, which does not support Andreev bound states, unless one manages to couple oppositely propagating edge states. To do so, chiral Andreev edge states (CAES) in the superconducting sheath [44, 169–173, 257–260] were exploited can be exploited. Early searches for these CAES in semiconductor heterostructures focused on the suppression of zero-bias peaks [176,177] and on magnetoconductance oscillations [178–181]. Graphene-based Josephson junctions with increased contact transparency [36, 91, 160–163] have enabled observations of similar phenomena corresponding to edge-mediated supercurrent [**?**,182], interpreted later as CAES [261]. In Hall bars with superconducting fingers, CAES have been observed as crossed Andreev reflection in the LL $\nu = 2$ [184] through negative differential resistance; inter-Landau level Andreev reflection in the zeroth LL [185] or interferences of Chiral Andreev edge states [186, 187]. This strategy requires two edges to carry a supercurrent, and results in switching

Results presented in this chapter will be submitted for publication

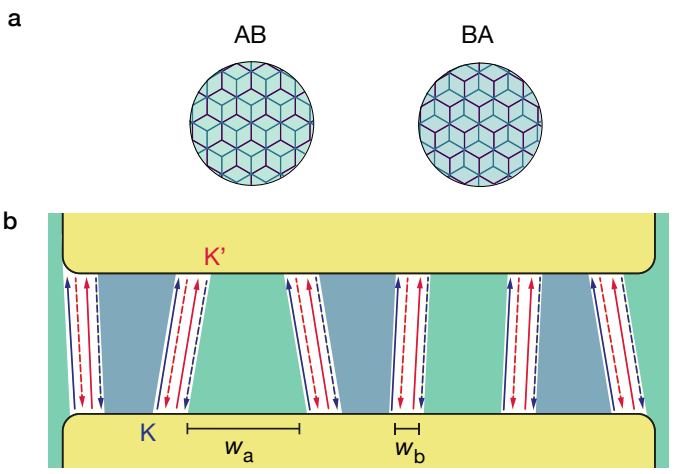

Fig. 8.1 mtBG superlattice structure. a) lattice structure of AB and BA domains. **b)** Geometry in our device: w_a is the average lateral size of the Bernal domains; w_b is the average width of the domain walls.

currents of a few nA at 1 T [182]. In principle, narrow devices would allow for increased coupling between opposite edges but at the expense of increased backscattering. To overcome that Sisyphean task, I suggest in this chapter a new geometry where edge states are carried along valley-polarised channels. This is similar to topological insulators in which each edge supports electrons' and holes' trajectories in both directions therefore carries its own supercurrent [200, 262–264], but in which superconductivity is destroyed by weak fields of ∼10 mT, an effect attributed to time-reversal symmetry breaking in the edge channels, detroying their helicity [262].

8.1 Device geometry

8.1.1 Minimally twisted bilayer graphene

Twisted bilayer graphene is a rich platform, in which considerable change in the electronic structure can be achieved through minute variations of the twist angle between the two graphene layers by virtue of the delicate interplay between strain-induced long-range superlattice effects and interlayer hybridisation (see section 3.2.2.2. For mtBG with twist angles <0.4°, internal strains tend to maximise the extension of energetically-favourable Bernal stacking at the detriment of AA-stacked regions. This atomic reconstruction forces the superlattice in large (µm-wide) triangular domains with uniform, alternating Bernal stacking, separated by sharp AB/BA domain walls and AA vertices [131–134] (see section 3.2.2.1. Figure 8.1a shows the lattice of such domains. Their structure is represented in figure 8.1b. The width of these domains can reach a few 100 nm, depending on the twist angle. The domain boundary width is independent of the twist angle and typically between 6 nm and 9 nm. As a result, these domain walls can behave as perfect 1D quantum wires. Electrostatic gating or external magnetic fields can break the inversion symmetry in individual Bernal domains. As a result, mtBG's Berry curvature changes sign between Bernal

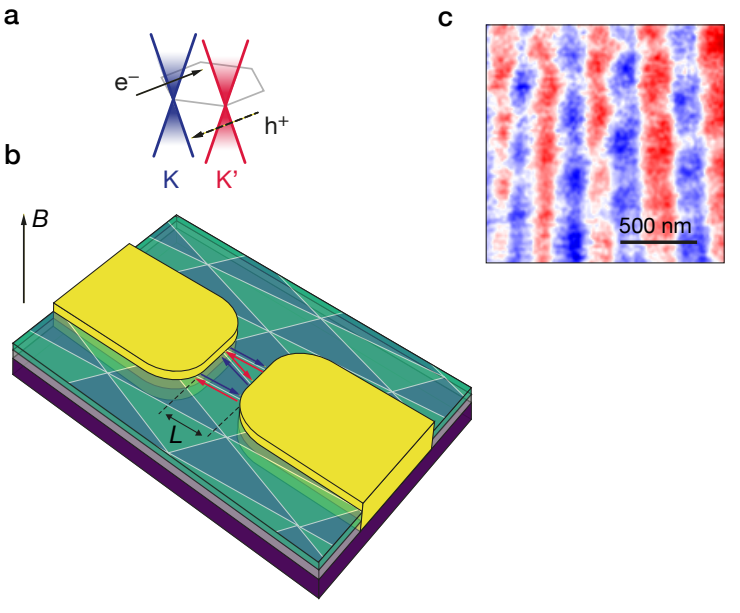

Fig. 8.2 Josephson junctions made with mtBG a) in the proposed Andreev reflection an electron in valley K of the mini-Brillouin zone is reflected as a hole in valley K' and reciprocally. **b)** geometry of the fabricated device. **c)** Example of photocurrent measurement enabling identification of AB/BA domains and corresponding boundaries.

domains, allowing counter-propagating valley-polarised 1D helical modes in the domain walls [77, 78, 131–134, 136–139, 265–268]. Four gapless 1D modes propagate on each side of the domain boundary, with opposite directions for valleys K and K', forming a network of 1D metallic states protected topologically against backscattering. Transport in this network is characterised by a Luttinger liquid behaviour [269] which is expected to widen interest in this class of twisted systems. At high magnetic fields, electronic transport in the DWs is expected to be slighly different, as the domain bulk can be gapped by cyclotron motion, and the DW would act as individual device edges. Their width of a few nA alows electrons' and holes' trajectories joining at a spot smaller than the superconducting coherence length.

8.1.2 Josephson junctions and device characterisation

Here I present a Josephson junction where the mtBG domain walls are proximitised. I make use of the valley-polarised helical network, a system in which Andreev processes reflect an electron from valley K (K') into a hole in valley K' (K respectively) [270] on the same channel (see figure 8.2a). For this reason, the degeneracy of DWs under a magnetic field is 4.

Figure 8.2b shows a schematic of the devices used. In order to neutralise competing edge states at the device-vacuum interface, we designed devices with a *semi-corbino* geometry, instead of the conventional Josephson junction geometry. Our devices are formed of narrow constrictions along selected AB/BA domain boundaries, preventing any coherence losses, while the edges of the graphene flakes remain unetched to maximise the distance between contacts and eventually suppress the supercurrent along the device edges [271]. Stacks were fabricated using the standard dry transfer procedure (see appendix A). Before designing the superconducting contacts, photocurrent measurements

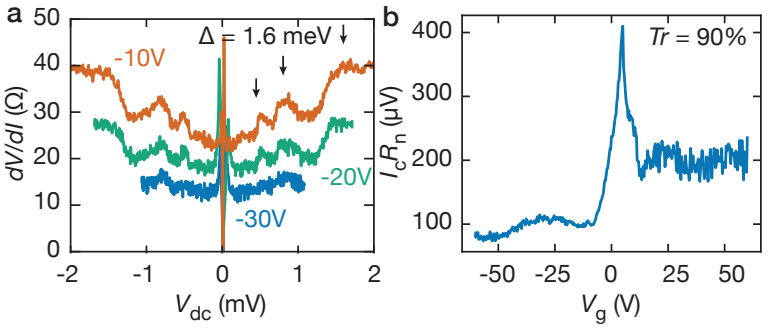

Fig. 8.3 Contact transparency in junction J2 with multiple domain walls. a) MAR seen through $dV/dI(V_{\mathrm{dc}})$. Arrows indicate the multiple andreev reflections corresponding to $2\Delta/3$, Δ and 2Δ from left to right. **b)** $I_{\mathrm{c}}R_{\mathrm{n}}(V_{\mathrm{g}}) \ll \Delta$ despite good transparency.

were carried out to select domains of interest on hBN-encapsulated mtBG heterostructures, following the method described in ref. [272]. An example of such measurement is shown in fig. 8.2c. The superconducting electrodes are made of sputtered NbTi allow, with upper critical field $H_{\mathrm{c2}} = 9.9\,\mathrm{T}$ and a critical temperature of $T_{\mathrm{c}} = 7\,\mathrm{K}$. The device length is chosen between 100 nm and 200 nm for all the devices because the conductivity of 1D channels was shown to deviate from the quantised value of $4e^2/h$ for longer channels [77]. All our devices show a pronounced proximity effect with a non-zero critical current I_{c} at the neutrality point, slowly increasing with $|V_{\mathrm{g}}|$, with a gap $2\Delta \approx 1.6\,\mathrm{meV}$, and an $I_{\mathrm{c}}R_{\mathrm{n}}$ product of about 200 µV, orders of magnitude below Δ. It is usually possible to characterise the contact transparency by comparing the $I_{\mathrm{c}}R_{\mathrm{n}}$ product to the superconducting gap measured from MAR (see, e.g., chap. 4). Here, it would result in suboptimal contacts and MAR should not be observable at low transparencies, therefore the low $I_{\mathrm{c}}R_{\mathrm{n}}$ values must come from a different mechanism. In the case of Josephson junctions made with multiple, parallel conduction channels, R_{n} should be smaller. Indeed, we find that the Sharvin formula of equation 4.24 should be rewritten as:

$$R_{\mathrm{q}} = \frac{1}{g\,(M + 4N)}\,\frac{h}{e^2} \tag{8.1}$$

Where $g = 4$ is the degeneracy, N is the number of Bernal domain walls between the two contacts and M is the number of propagating modes defined in equation 4.24. In brackets, the first term corresponds to the number of electron modes inside the Bernal domains, and the second term corresponds to the number of conducting modes in the channels (4, as found experimentally in domain walls [77, 78]). Injecting equation 8.1 into 4.25 we find the contact transparency. Figure 8.3 shows an example of MAR in a junction with 8 domain walls as well as a comparison between $I_{\mathrm{c}}R_{\mathrm{n}}$ and the superconducting gap on the same junction, yielding a contact transparency of 90 % despite low $I_{\mathrm{c}}R_{\mathrm{n}}$.

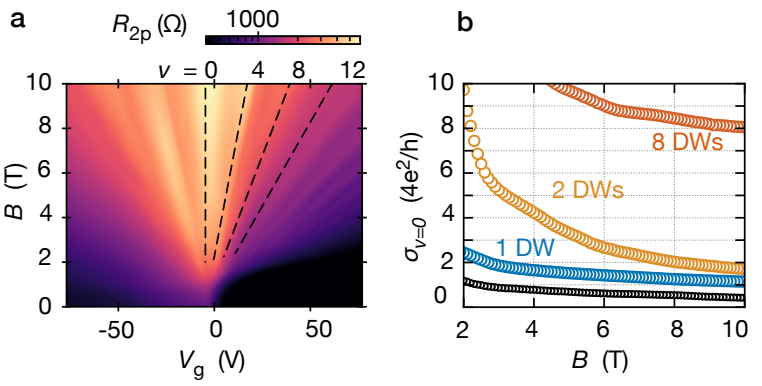

Fig. 8.4 High temperature transport: a) $R_{2p}(V_g, B)$ in junction J3 with 2DWs, at T_{mc} =10 K with LLs as dashed lines and **b)** Conductivity of the $\nu = 0$ LL as a function of the magnetic field for junctions J3, J4 and J5. Number of DWs found from SNOM is indicated. Black dots: JJ with no DW (J8).

8.1.3 Number of channels

I studied 8 Josephson junctions where the helical channels of mtBG are proximitised. After characterising the number of channels using photocurrent measurements we measure the transport properties above the critical field of the superconductor. Figure 8.4a shows a fan diagram measured for junction D5 at T_{mc} =10 K> T_c. The Landau levels appear as resistance maxima [273] for filling factors $\nu \equiv nh/eB = \pm 4$, 8, and 12, consistent with the four-fold valley degeneracy of bilayer graphene with a Berry phase 2π. The resistance maxima in the normal state have a relatively low resistance of $\sim 100\,\Omega$, orders of magnitude below the resistance quantum $R_K = h/e^2 \approx 25.8\,k\Omega$. It corresponds to the normal transport through the device edges combined with several 1D channels formed by AB/BA domain walls. These have a 4-fold degeneracy to account for spins and valleys propagating on each side of the boundary in opposite direction [77, 78, 131–134, 136–139, 265–268] but with a propagation direction fixed by the QH effect. As a consequence, the conductance in the normal state corresponds to:

$$\sigma_{LL} = \nu(4N + g_{LL})\frac{e^2}{h} \tag{8.2}$$

Where ν is the Filling factor of the considered LL, N is the number of domain boundaries in the junction and g_{LL} the degeneracy of the Landau level of interest. From this equation, it is possible to extract the number of domain walls, representing 1D channels, in each of our devices. This confirms the photocurrent measurements and is used for the characterisation of the contact transparency. Figure 8.4b shows the number of channels as a function of the conductance of the LL $\nu = 4$. In the following, we focus on devices J1 and J2 with multiple and 1 domain walls, respectively.

8.2 Supercurrent at low B

I started by measuring the supercurrent under small magnetic fields. Figure 8.5 shows the differential resistance dV/dI as a function of the magnetic field B <40 mT and the current bias I_{dc} for device D1 with one domain wall (DW). This was measured for a gate bias of 35 V, a carrier density at which the AB and BA domains should be partially gapped, while the domain walls should be weakly metallic. The critical current at small magnetic fields B <10 mT is modulated with the periodicity of a conventional single-slit response (see equation 2.52), where the periodicity of the oscillations should correspond to the magnetic flux penetrating the junction area. The periodicity of oscillations is 1.7 mT, corresponding to an area $\mathcal{A}_{\mathrm{J}}$ =1.2 µm^2, relatively large compared to the size of the device (0.3 µm^2). By taking into account the London penetration depth of NbTi thin films λ_{L} ≈350 nm, the effective area is reduced to 0.34 µm^2, which is close to the junction area. These oscillations are shown as a solid white line in figure 8.5. At magnetic fields B >10 mT, one can see deviations from the conventional oscillatory Fraunhofer diffraction pattern. Instead, the supercurrent follows a set of random oscillations, somehow limited by a constant value of the switching current $I_{\mathrm{S}} \approx 100$ nA. This supercurrent is attributed to the supercurrent flowing along the device mesoscopic edges and on the DW. As the magnetic field is varied, the critical current oscillates and the superconducting phase difference becomes position-dependent, revealing the spatial distribution $J_{\mathrm{s}}(x)$ of the supercurrent. To extract it from the measured switching current $I_{\mathrm{S}}(B)$, I follow the Dynes-Fulton approach adapted for 2D Josephson junctions (see section 4.5.2). The result is shown in the inset of figure 8.5. It is clear here that a small portion of the supercurrent is propagating away from the narrow strip of the junction, as evidenced by non-zero current density for $|x|$ >0.75 µm. Most of the supercurrent is propagating in the bulk of the junction, with two ears corresponding to the mesoscopic edges. At such magnetic fields, the presence of a DW has no discernable effect on the reconstructed supercurrent.

One can note, however, that when wultiple DW are present within the junctions, these act as device edges, and no supercurrent can be seen away from the narrow strip of the junction. On top of that, devices with multiple DW show a highly inhomogeneous reconstructed $J_{\mathrm{s}}(x)$ with peaks representing 50 % of the average current in the junction strip. This is attributed to inhomogeneous transport between semi-gapped Bernal domains and metallic conduction channels.

Overall, the reconstructed supercurrent spatial density shows that the small-field supercurrent originates from conduction in individual aligned domains, with small contributions from the device edges. On top of that, DWs allow separation between proximitised and non-proximitised regions. The contribu-

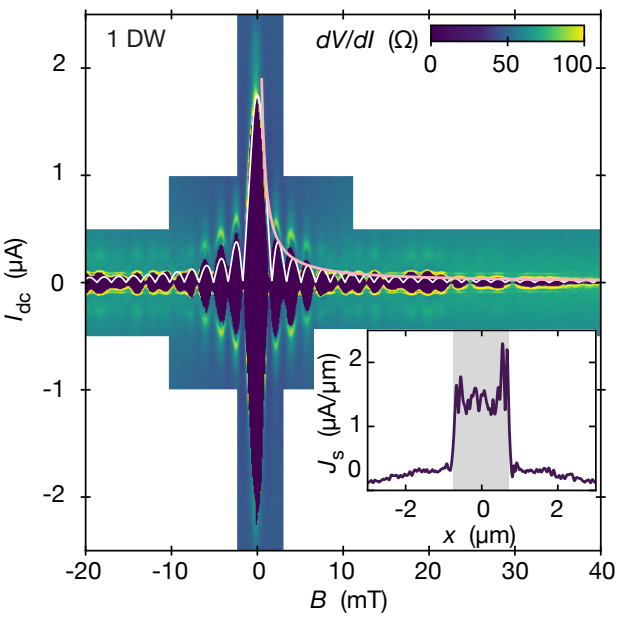

Fig. 8.5 Supercurrent at low magnetic fields: $dV/dI(B, I_{\mathrm{d}}c)$ at T_{mc} =20 mK on device J1 with 1 domain wall. White curve: Fraunhofer diffraction pattern for a usual 2D junction of the same dimensions. pink curve: $1/B$ enveloppe for the same dimensions. Inset: reconstruction using the Dynes-Fulton method.

tion from edge states is analogue to the previously described regime where proximity superconductivity persists under the aegis of cyclotron motion and edge scattering [36]. It should be noted that the method we used presents limitations, as it assumes a homogeneous supercurrent along the length of the junction, which means perpendicular Andreev processes relative to the contact edge, and a sinusoidal current-phase relation (CPR). The former is not guaranteed because of the triangular nature of the Bernal domains; the latter either as the critical current does not reach zero. This does not affect our conclusions thanks to the presence of sharp behaviour change around 10 mT.

8.3 Supercurrent at quantizing B

8.3.1 Field dependence

In small magnetic fields, the Bernal domains are only weakly gapped with the displacement field induced by a single gate. To fully break the time-reversal symmetry, gap these domains and force transport in DWs, we apply a much larger perpendicular magnetic field to our junctions of a few T. Under these conditions, the maximum supercurrent flowing through a junction is modulated by the magnetic flux, with a period corresponding to the flux quantum $\Phi_0 = h/2e$ where h is the Planck constant and $2e$ is the charge of a Cooper pair. According to the results of section 2.3.2.3, the supercurrent in a 2D Josephson junction should vanish above weak magnetic fields B^* (see eq. 2.56) as our device is edgeless.

Figure 8.6 shows the supercurrent B-dependence of device D2 with 8 domain boundaries. The proximity effect withstands magnetic fields up to 8 T, a field comparable to the critical field of the superconducting electrodes, suggesting

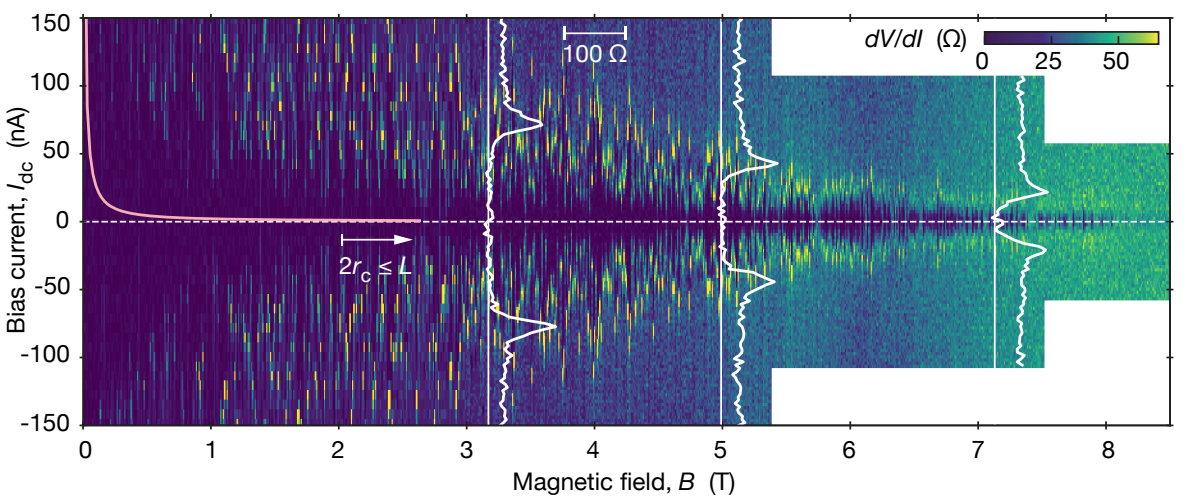

Fig. 8.6: Supercurrent in high B $dV/dI(B, I_{\mathrm{dc}})$ at V_{g} =20 V, showing supercurrent persisting at B in exces of 8 T. White arrow indicates the quantising field for the gate voltage. White curves show line cuts show the $dV/dI(I_{\mathrm{dc}})$ profile for various B indicated by thin wite lines. Pink curve is the profile described by equation 8.3. Measured in device J2 with multiple DWs.

its 1D nature with tight lateral confinement, an effect consistent with propagation in the network of domain walls. In all our devices, the proximity effect persisted up to 6 T at least. At high magnetic fields, this behaviour is different from usual graphene Josephson junctions in the quantum Hall regime [169–186] where edge channels conduct the supercurrent through chiral Andreev edge states. This is because the 1D domain walls are valley polarise and can carry out electrons and holes on the same channel with opposite momentum, contrary to chiral Andreev edge states that necessitate two edges with a possible loss of coherence. As a result, this is a similar situation to quantum spin Hall Andreev states [200, 262–264] where each 1D state supports its own supercurrent. Unfortunately, a supercurrent in the quantum spin Hall edge under a magnetic field was never reported.

In our measurements, the supercurrent persists well above the theoretical envelope for 2D josephson junctions, shown as a solid pink line:

$$I_{\mathrm{c}}^{envelope}(B) = \frac{\alpha}{e} \frac{\Delta(B)}{R_{\mathrm{n}}(B)\pi\Phi/\phi_0} \tag{8.3}$$

Where $\alpha \approx 2.1$, and $\Delta(B) = \Delta(0)\sqrt{1-(B/B_{\mathrm{c}})^2}$ is the superconducting gap and $R_{\mathrm{n}}(B)$ is the resistance in the normal state, experimentally measured at 10 K (see fig. 8.4). This trend results from the gapped bulk in the QH regime (above 2 T, see fig. 8.6), preventing the flow of a supercurrent [36, 161, 162,178]. It is worth noting that the critical current is systematically above the theoretical envelope: $I_{\mathrm{c}}(B) > I_{\mathrm{c}}^{envelope}(B)$. This is different from the known case of a chiral Andreev states-mediated supercurrent [169–186] for which only a small number of superconducting pockets can be observed above $I_{\mathrm{c}}^{envelope}$. This measurement shows a fast modulation of the supercurrent. This is due

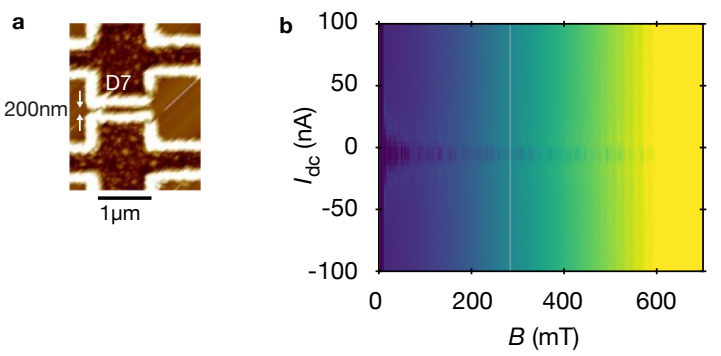

Fig. 8.7 Control measurement on a Bernal junction (J8) **a)** atomic force micrograph of the device used. **b)** $dV/dI(B, I_{\mathrm{dc}})$ at V_{g} =20 V bilayer. Color scale: indigo (0 Ω) to yellow (500 Ω).

to interferences between DWs that can be resolved for magnetic fields smaller than the one shown here.

To support this statement, we measured a control device made with Bernal bilayer graphene (shown in figure 8.7). This device shows no supercurrent above 400 mT. Equally, the uniqueness of our mtBG system can be witnessed by measuring other type of junctions. Josephson junctions including domain boundaries formed by a wrinkle in the graphene layer or by a step in the hBN substrate did not show any sign of a supercurrent above 0.25 T. In the literature, attempts to couple edge states in bilayer with an n-doped top layer and a p-doped bottom layer did not result in any high-field supercurrent [274].

8.3.2 Shapiro steps

A further evidence of the Josephson effect persisting up to high magnetic fields is the presence of Shapiro steps in the device. In the presence of a microwave excitation, phase locking between the RF field and the Josephson supercurrent gives rise to constant-voltage Shapiro steps in the $V(I)$ characteristics, with a step size $V_{\mathrm{n}} = nhf_{\mathrm{rf}}/2e$, where f_{rf} is the microwave frequency and $n \in \mathbb{Z}$. The presence of such steps is an unequivocal consequence of the Josephson effect. At B =5 T and f =3 GHz, we observe steps with a high $\Delta V = 6.2\,\mu\mathrm{V}$, consistent with the Cooper pair tunneling. It can be seen as minima with $0 \leq |n| \leq 3$ in the differential resistance map as a function of the RF amplitude V_{rf} (fig. 8.8a). In a conventional Josephson junction, the evolution of the Shapiro step width ΔI_{n} should follow a Bessel function pattern: $\Delta I_{\mathrm{n}} \propto |J_{\mathrm{n}}(2eV_{\mathrm{rf}}/hf)|$ where J_{n} is the nth Bessel function. Figure 8.8b shows a quantitative comparison of the width of the Shapiro steps $\Delta I_{\mathrm{n}}(V_{\mathrm{rf}})$ for n =0, 1, 2 and 3. We observe that the Shapiro plateaux can be perfectly described by Bessel functions. We note, however, that CPR oscillations with different frequencies may contribute to this width, resulting from the coexistence of 2π-periodic and a 4π-periodic Josephson current in the topological state [275]. For multichannel wires, it is indeed not possible to observe only the 4π-periodic supercurrent and to distinguish topological excitations. This system is analogous to a periodic array

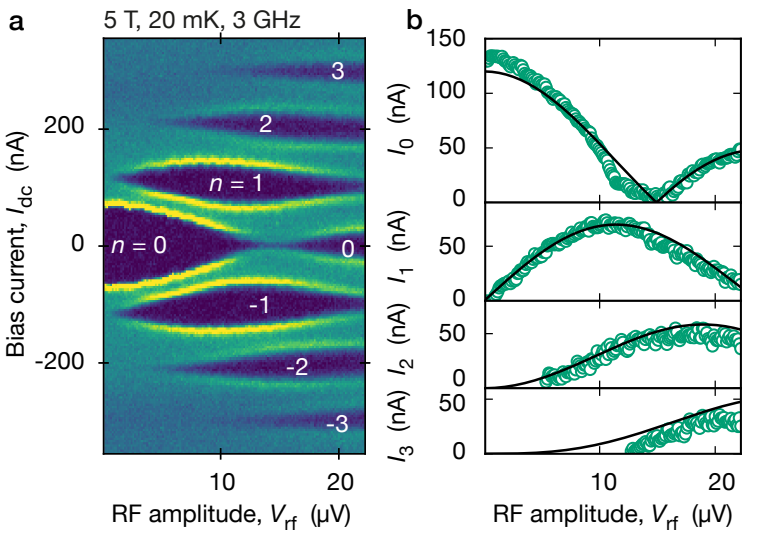

Fig. 8.8 Shapiro steps at 5T in device J2 at $V_g = 18\,V$. **a)** $dV/dI(V_{rf}, I_{dc}$ showing clear Shapiro spikes and zero resistance pockets. Color scale: indigo ($0\,\Omega$) to yellow ($70\,\Omega$) and **b)** Bessel function fit of the Shapiro steps for n =0, 1, 2 and 3.

of Josephson junctions [276], allowing Josephson vortices to flow through the array. Note that the high magnetic field periodicity of the critical current may be a result of pinning and hopping of vortices through the junction, an effect that could be exploited to search for non-trivial excitations [277, 278].

8.3.3 Quantum oscillations at large B

Further analysis of the current propagation can be carried out by looking at the high magnetic field response. Figure 8.9 shows the switching current B dependence for different Josephson junctions in the QH regime. Figure 8.9a shows a typical bilayer graphene Josephson junction (J5), for which we do not observe any supercurrent, but small pockets with non-linear IV characteristics. This corresponds to proximity superconductivity carried out by the edges of the device, coupled via CAES [182]. This is contrasting with devices containing DWs. Each DW is able to carry out its own supercurrent, with electrons and holes propagating on each side. As the superconducting coherence length of NbTi is $\sim$6 nm, similar to the width of individual DWs, and therefore, simple Andreev bound states are allowed to carry exist. Figure 8.9b shows the B response of a Josephson junction (device J1) containing a single DW. In this small range of magnetic fields (40 mT, there is a constant supercurrent, corresponding to almost perfect Andreev bound states within a metallic nano-wire formed by the DW. One can also explore the case of multiple domain walls. Figure 8.9c shows a junction containing two DWs and figure 8.9d one containing multiple DWs, at magnetic fields deep into the QH regime. For the case of the junction containing two DWs, there are oscillations with aperiodicity of 2.2 mT, corresponding to an area of $9 \times 10^{-13}\,m^2$. Taking into account the London penetration depth, it corresponds to the area delimited by two DWs separated by 400 nm, much smaller than the junction width (1.5 μm). Here, the coupling between two DWs is ensured via CAES propagating on the superconducting

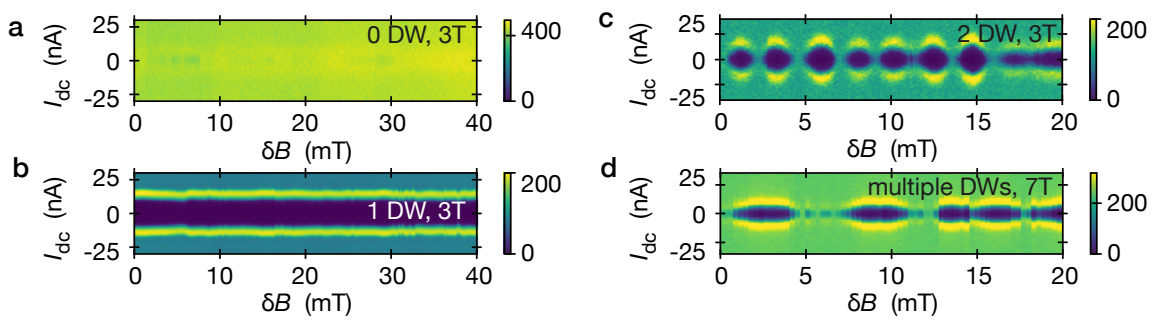

Fig. 8.9: High field periodicity of the critical current measured in devices J8, J1, J3 and J2 at base temperature T_{mc} =10 mK.

sheath between the two edge states. When the number of DWs is increased, multiple oscillations coexist at small field. For this reason, it is necessary to look at high magnetic fields to understand the length scale of interest. Indeed, at small magnetic fields, DWs with different spacing can couple together, resulting in multiple areas penetrated by a flux quantum, and therefore multiple oscillations periodicity. At 7 T (as shown in figure 8.9d), only the closest DWs can interract together, and the oscillation periodicity is 5 mT, corresponding to the area delimited by two DW separated by 180 nm (taking into account the London penetration depth).

8.3.4 Ballistic transport in individual DWs

We focus here on device J1 with 1 domain wall. Figure 8.10a shows the gate dependence at B =0 T. This gate dependence is typical for bilayer graphene Josephson junction. For hole doping (V_{g} <0 V, we observe Fabry-Pérot (FP) oscillations, a sign of ballistic transport within the bilayer graphene strip. However, no FP oscillations are visible for electron doping (V_{g} >0 V), a sign of good contact transparency. This is consistent with previous reports on ballistic, long, graphene Josephson junctions [36,163]. Turning on the magnetic field, one can look at intermediate fields of 1.2 T. Fabry-Pérot oscillations emerge for $V_{\mathrm{g}} < 25$ V, which corresponds to gate voltage at which the cyclotron diameter $2r_{\mathrm{c}}$ is smaller than the junction length L. Note that above that region, oscillations are still visible, but they appear randomly as coupling can also happen with the junction edges. At much higher magnetic fields of 3 T, FP oscillations become more visible. Figure 8.10b shows that at high bias ($I_{\mathrm{dc}} \approx$ 20 nA), the supercurrent is supressed, highlighitng the low-resistance QH features described earlier. At low DC biases, the proximity effect is visible for all positive V_{g} (fig. 8.10b), with clear oscillations of the switching current as a function of the gate voltage: FP oscillations along the DW. Further example of such oscillations can be seen in the fan diagram at I_{dc} =0 nA, showing that the zero-bias resistance oscillates, with resistance minima that match the critical

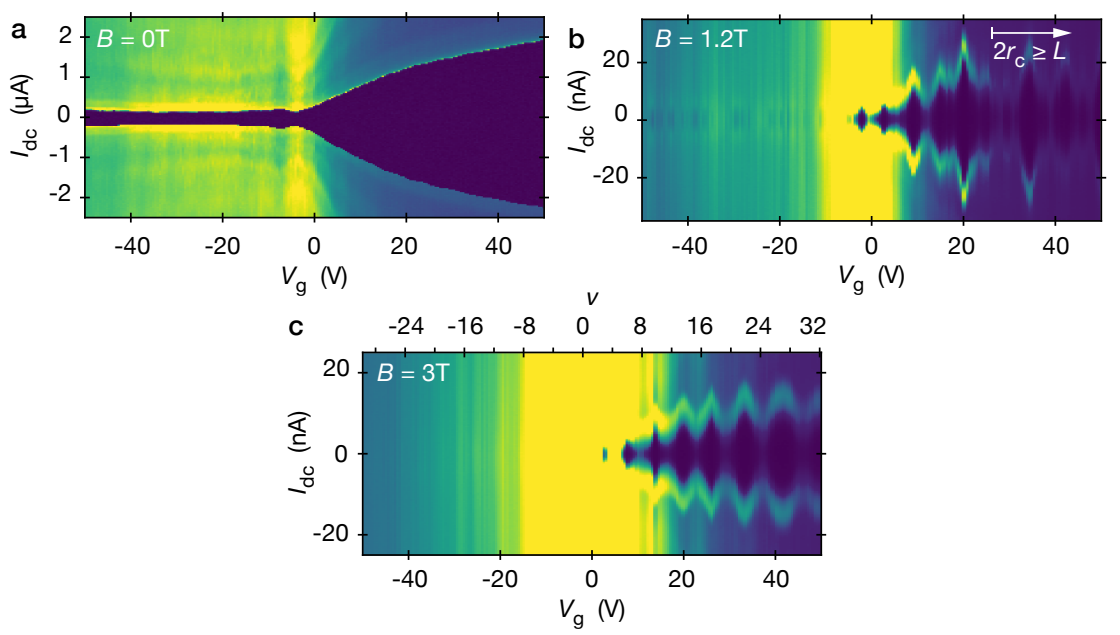

Fig. 8.10: Fabry-Pérot oscillations at different magnetic fiedls on device J1 with 1 DW: $dV/dI(V_g, I_{dc})$. at 0 T (a), 1.2 T (b) 3 T (c). colour scales: indigo (0 Ω) to yellow (260 Ω in a, 500 Ω in b and 800 Ω in c).

current maxima (fig. 8.11a to c), highlighting the Fabry-Pérot nature of such oscillations.

Finally, the FP oscillations do not follow a $1/\sqrt{n}$ dependence as expected for the case of a 2DEG, but rather $1/n$. This is a behaviour expected for the case of 1D metallic wires, as shown in figure 8.11d. There might be, however, additional contribution and coupling between the 2D bulk and 1D edges. Further theoretical studies might give more insight into the nature of such FP oscillations. Such a fit, however, gives a cavity length of L =240 nm, corresponding to a DW oriented between the two superconducting electrodes at a non-zero angle, if one considers the Fermi velocity of the Dirac spectrum. Overall, the presence of FP oscillations appearing in the Quantum Hall regime shows ballistic motion of the electrons and holes trajectories forming the Andreev bound states in the DWs.

8.3.5 Further characterisation of the proximity effect in DWs

To better understand the properties of the proximity effect in the DWs, I study their dependence with temperature. The superconducting coherence length of NbTi is ≈6 nm and the length of the junction around 200 nm, therefore we are in the case of long Josephson junction. In this case, temperature should play little role, except for reducing the superconducting gap at $k_B T$ comparable to Δ. In the current-phase relation, the gap Δ shoud be substituted with the Thouless energy E_{Th} [36, 279], and the critical current should be limited by E_{Th} rather than Δ. Indeed, figure 8.12a shows that at B =0 T, the critical cur-

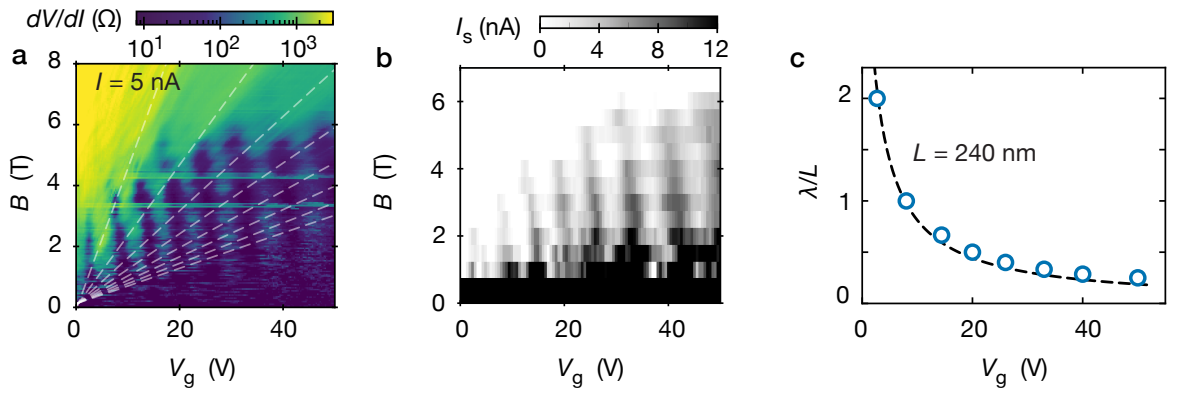

Fig. 8.11: Characterisation of Fabry-Pérot oscillations in individual DWs. a) zero bias differential resistance. **b)** critical current and **c)** characteristic lengthscale of the FP cavity. Measured on device J1 with 1 DW.

rent evolves with the expected long junction behaviour: $I_{\mathrm{C}} \propto \exp(-k_{\mathrm{B}}T/E_{\mathrm{Th}})$ where $E_{\mathrm{Th}} = \hbar v_{\mathrm{F}}/L$ [280], and the temperature dependence saturates at low temperatures, when $k_{\mathrm{B}}T$ becomes comparable to E_{Th} =0.1 meV (1.2 K). Figure 8.12b shows an example of the temperature dependence at high magnetic field (3 T), where the proximity effect seems to persists up to 2 K. One can define the switching current I_{S} as the current for which $R(I_{\mathrm{S}}) = R_{\mathrm{N}}/2$. The switching current dependence is shown in figure as a white dashed line in figure 8.12b. This dependence differs qualitatively from the one at B =0 T, and does not evolve as a function of E_{Th} anymore —or at least, not the E_{Th} as defined for the case of a 2DEG. This shape resembles the dependence for a short junction.

Here, there can be different interpretations for the observed phenomenon. On the one hand, convex shapes are usually a sign of transport in short junctions, a definition usually written in terms of the device length: $L \gg \xi$, where ξ is the superconducting coherence length. There is also another equivalent definition for the short junction limit in terms of the Thouless energy: $E_{\mathrm{Th}} \gg \Delta_0$ [281, 282]. If we define E_{Th} as: $E_{\mathrm{Th}} = \hbar v_{\mathrm{f}}/l_\phi$, where l_ϕ is the coherence length in the junction and v_{f} is taken as in the Dirac spectrum v_{f} $\sim 10^6\,\mathrm{m\,s^{-1}}$, then we get $E_{\mathrm{Th}} \sim 10$ meV which is much larger than $\Delta_0 \approx 1$ meV. As a result, the fits with a ballistic short-junction model would be considered, as shown in figure 8.12c, for different temperatures. The short junction fit writes as follows:

$$I_{\mathrm{S}}(\phi, T) = \frac{\pi\Delta(T)}{2eR_{\mathrm{N}}} \frac{\sin\phi}{\sqrt{1-\tau\sin^2\phi/2}} \tanh\left(\frac{\Delta(T)}{2k_{\mathrm{B}}T}\sqrt{1-\tau\sin^2\phi/2}\right), \qquad (8.4)$$

where $\Delta(T) \approx \Delta_0\sqrt{1-(T/T_{\mathrm{C}})^2}$, ϕ is the phase difference between the two superconductors, τ the transmission coefficient of the SN interface, and R_{N} the normal state resistance [279, 280] . For a usual junction, the critical current corresponds to the value of ϕ that maximises $I_{\mathrm{S}}(T)$. On the other

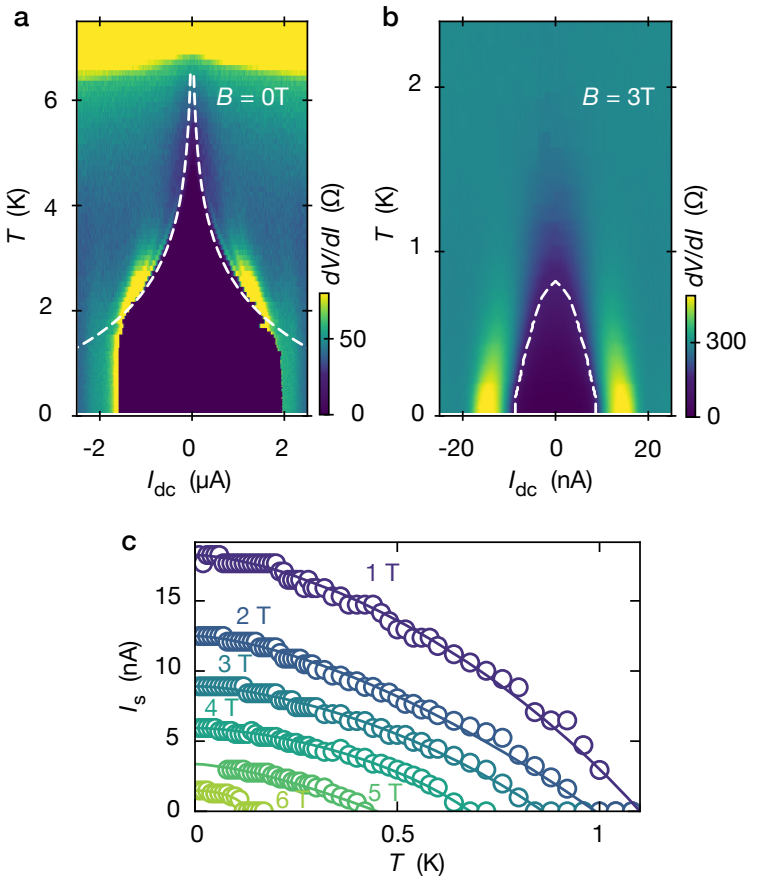

Fig. 8.12 Temperature dependence of the critical current. a) $\rho_{xx}(I_{dc}, T)$ at $B = 0\,\mathrm{T}$ measured in J1 with 1DW. **b)** same at $B = 3\,\mathrm{T}$. **c)** $I_S(T)$ for different magnetic fields. solid line: fit with eq. 8.4. Mearused on device J1 with 1DW.

hand, the effective transparency of the NS interface should be taken as 1 in the case of figure 8.12c, as the measurements were done in a resonance (standing wave condition) of the Fabry-Pérot oscillations, corresponding to $V_g = 33\,\mathrm{V}$. Therefore, when fitting for parameter Δ_0, we find that in the QH regime, $\Delta_0 = 0.25\,\mathrm{meV}$, suggesting that the nature of the superconductor changes. Indeed, it was predicted that the proximity of an s-wave superconductor with a topological insulator would result in the creation of a p-wave superconductor [283]. Here, the proximity of NbTi with the quantum Hall topological insulator created by DWs might change the nature of the superconductor and create a p-wave superconductor with different properties. This hypothesis would need more theoretical and experimental studies to be validated.

Conclusion

In this chapter, I demonstrated robust Josephson coupling along 1D edges in the quantum Hall regime. I showed that in such structures, the proximity effect persists deep into the quantum Hall regime. The magnetic-field oscillations of the supercurrent are consistent with Andreev bound states in very narrow channels. Further characterisation provides evidence for the ballistic nature of such junctions, and for enhanced coupling between two superconductors. This could open new research directions in the search for topological excitations in the quantum Hall regime. In addition, it could be a platform for new devices, such as SQUID magnetometers operating at high B.

Part IV
Effects of electron correlations on the band structure

Blank page

Chapter 9
Correlated states and van Hove singularities

In twisted bilayer graphene, flat bands emerged as a platform for the exploration of electronic interaction, appearing close to the magic angle (see paragraph 3.2.2.2). In most condensed matter systems, the variety of quantum phases is usually the result of strong electronic interactions breaking the underlying symmetries. The variety of different phases in magic-angle twisted bilayer graphene (MA-tBG) suggests that the flat band results in low-symmetry states in the many-body spectrum, stabilised by external parameters (pressure, strain, electric and magnetic fields, etc.) [152], but, as I am writing this thesis, the nature of the interaction-driven symmetry breaking is not yet understood. The non-trivial topological properties of the low-energy spectrum of MA-tBG are revealed through the lifting of their degeneracies, by creating a gap between them [119, 152]. Particularly, the single-particle band structure of MA-tBG conforms to the sublattice C_2 and time-reversal T symmetries, protecting the Dirac point. The breaking of these symmetries can create a gap and give rise to Chern insulators, having a quantised Hall conductance. The C_2 sublattice symmetry can be broken by the alignment of MA-tBG with hBN substrate [124, 125]. The time-reversal T symmetry can be broken by applying strong magnetic fields [119, 150–152].

In this chapter, we propose a new system in which the sublattice C_2 symmetry is spontaneously broken. We stack a graphene monolayer on top of a Bernal-stacked graphene bilayer to create topological flat bands, as several theoretical studies predicted [284–286]. Narrow and topologically non-trivial valley-projected Moiré minibands emerge, breaking both the sublattice C_2 and interlayer mirror M_y symmetries [20, 287–290]. We show that the low crystal symmetry and the tunability of the band and topology make it a rich system

---

Results presented in this chapter have been published in:
S. Xu, M.M. Al Ezzi, N. Balakrishnan, A. Garcia-Ruiz, B. Tsim, C. Mullan, J. Barrier, N. Xin, B.A. Piot, T. Taniguchi, K. Watanabe, A. Carvalho, A. Mishchenko, A.K. Geim, V.I. Fal'ko, S. Adam, A.H. Castro Neto, K.S. Novoselov and Y. Shi, "Tunable van Hove singularities and correlated states in twisted monolayer-bilayer graphene", Nat. Phys. **17** (5), 619 (2021). Sections 9.4 and 9.5 have not been published.

for the exploration of correlated states. In this chapter, I present 4 devices, labeled M1 to M4.

9.1 Emergence of tunable correlated states

First, twisted monolayer-bilayer graphene (tMBG) can be fabricated with two mirror-symmetric configurations: either with the Bernal graphene bilayer on top or with the monolayer graphene on top. All our samples are double-gated (see section 4.2.2) therefore the overall $\rho_{xx}(V_{tg}, V_{bg})$ can be flipped through $V_g \to -V_g$ between these two symmetric configurations to observe the same results. This was corroborated experimentally [20]. For consistency, we define positive D when the electric field points from the monolayer to the bilayer.

Figure 9.1 shows the transport behaviour of a tMBG sample (M1) with angle 1.22° at 1.6 K. All the features are similar in the mK range but contact issues at lower temperatures result in a lack of clarity. There is a clear asymmetry with respect to D, related to the lack of symmetry in tMBG stacks [286]. There is also an asymmetry between the valence ($n < 0$) and conduction ($n > 0$) bands. Theory allowed us to unravel a few features from this map.

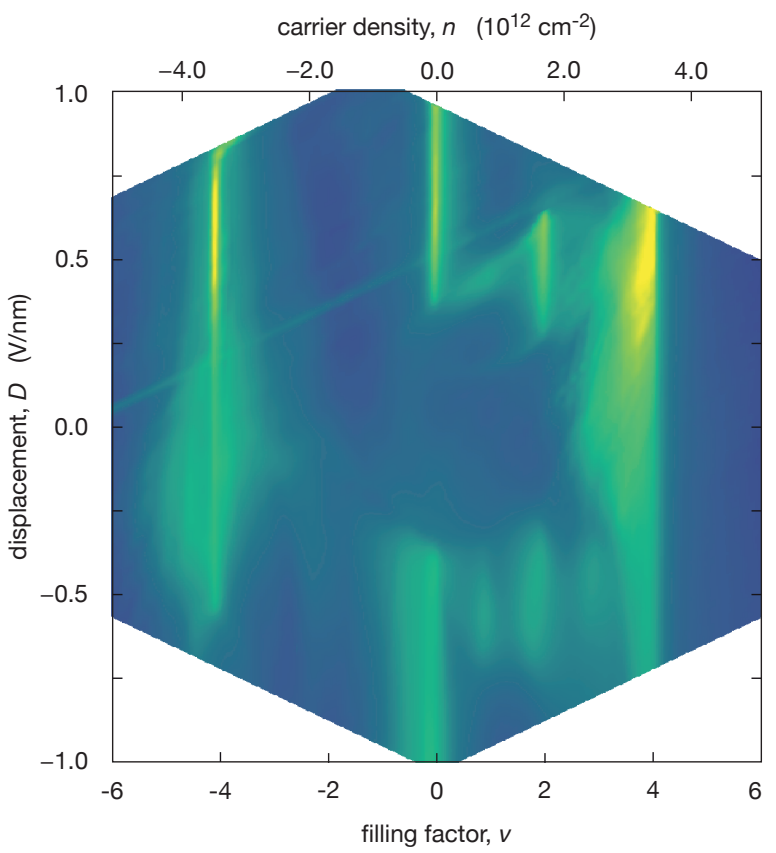

Fig. 9.1 resistivity of sample M1 with twist angle θ =1.22°, $\rho_{xx}(\nu, D)$ measured at $T = 1.6\,\mathrm{K}$ and $B = 0\,\mathrm{T}$. Logarithmic colorscale: indigo ($10\,\Omega$) to yellow ($10\,\mathrm{k}\Omega$).

9.1.1 Single-particle features

As in most graphene-based moiré superlattices, one may expect tMBG to present two secondary Dirac peaks at full-filling $\nu = \pm 4$. As the Bernal bilayer graphene component shows a gap opening under a perpendicular displacement field, it was also an expected feature in tMBG. Indeed, figure 9.1 shows high resistance features at $\nu = \pm 4$ as well as an increase in the resistivity for $\nu = 0$ at finite $|D|$ =0.4 V nm^{-1}. Indeed, these features are corroborated by calculations of the band structure with a continuum model [20, 289] (shown in figure 9.2).

These calculations combine the band structure of monolayer graphene with Bernal bilayer graphene, assuming that there are no interactions between the bands. These calculations for $D = 0$ (fig. 9.2, left panel) show clear bandgaps emerging at $\nu = \pm 4$, separating the low-energy bands (lowest conduction and valence bands shown as green and orange lines) from higher-energy bands (shown as black lines). When $D = 0.5\,\mathrm{V\,nm^{-1}}$ (fig. 9.2 right panel), the two band insulators change slightly: The bandgap Δ_{+4} at $\nu = +4$ increases slightly on the electron side, while the bandgap Δ_{-4} at $\nu = -4$ decreases on the hole side. This situation is reversed for negative D. Additionally, a gap Δ_0 is opened by D at the charge neutrality point (brown streak), consistent with the increased resistance in fig. 9.1. There is also a small but non-zero energy shift of the monolayer Dirac point E_{DS} that occurs even in the absence of

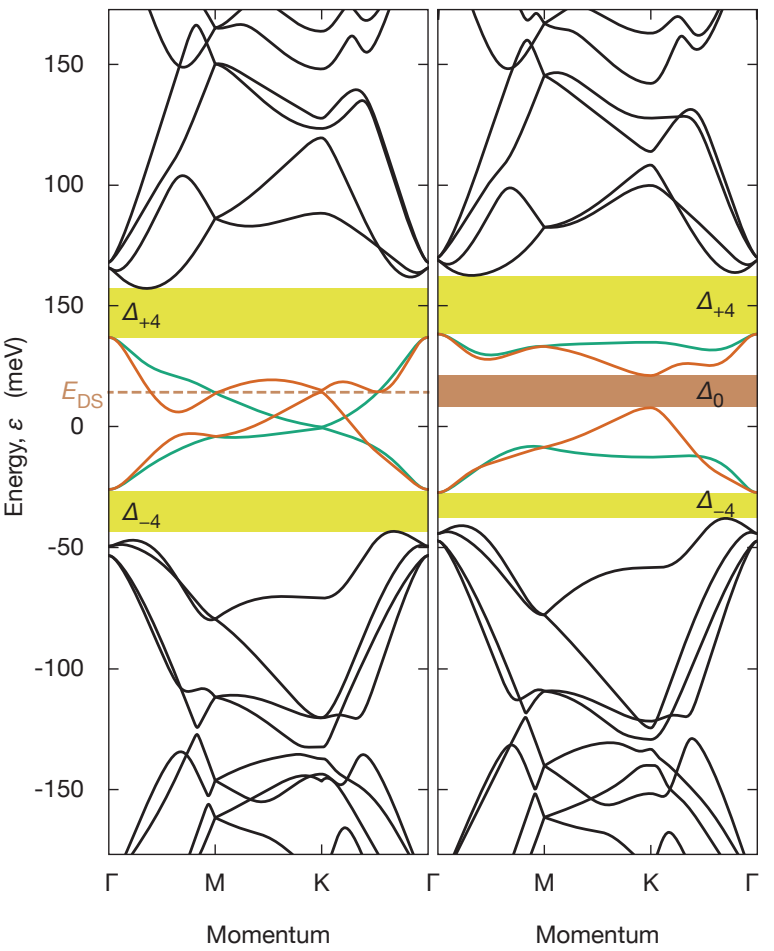

Fig. 9.2 calculated band structure of tMBG with $\theta = 1.22°$ for displacement fields $D = 0$ (left) and $0.5\,\mathrm{V\,nm^{-1}}$ (right). Yellow streaks indicate the bandgaps $\Delta_{\pm 4}$ at full filling and the brown region shows the gap Δ_0 at charge neutrality, opened upon application of D. Green and orange colours indicate the lowest energy bands for the K point residing at the bilayer and monolayer and corners, respectively. E_{DS} is the energy shift of the monolayer Dirac point. Data from ref. [20].

a displacement field D, resulting in an electron-hole asymmetry that will be discussed later. The displacement field D has two effects on the band structure [291]. Increasing the displacement field (in both directions) pushes the conduction band of the monolayer upwards and its valence band downwards with equal magnitude. For the bilayer band, a positive D results in an interlayer bias U, shifting the conduction band upward by $U/2$ and the valence band downward by $U/6$, and reciprocally for negative D. This explains the opening of a bandgap at charge neutrality after the bilayer conduction band is shifted upwards by a displacement field, while the resulting conduction band is very flat. The positive E_{DS} results in a smaller bandwidth in the conduction band than in the valence band.

9.1.2 Correlated states at integer fillings

However, some of the features in figure 9.1 cannot be explained by the single-particle picture in fig 9.2. There are indeed resistance peaks that emergy at fillings $\nu = 1$ and 2, strongly asymmetric for electrons and holes, as well as positive and negative D. Similar insulating states at fillings 1, 2 and 3, failing to be described with a single-particle picture have also been reported in twisted bilayer graphene (tBG) [145, 148], twisted double bilayer graphene (tDBG) [292–296]. Additionally, independent measurement of tMBG at the Universities of Washington (WA, USA) [289, 290] and Santa Barbara (CA, USA) [287, 288] support our conclusions. Indeed these states are similar to the correlated states originating from band flatness and band isolation in twisted double bilayer graphene [292], consistent with relatively flat bands in the valence band. Because of the electron-hole asymmetry of the band structure shown in figure 9.2, the bandwidth is much smaller in the conduction band compared to the hole band, concomitant with the observation of resistive states only for positive carrier densities. On top of that, we note that these insulating features have a much lower resistance for $D < 0$ than for $D > 0$, in contrast with twisted double bilayer graphene [292] where the correlated states are symmetric with respect to the sign of D.

9.1.3 Temperature dependence

These correlated states manifesting as resistivity peaks at commensurate fillings $\nu = 1$, 2 and 3 show qualitatively different behaviours for positive and negative D. The correlated state at $D > 0$ presents important resistances of $\approx$20 kΩ, while at $D < 0$, the resistance of 2.5 kΩ is much smaller. Here I dis-

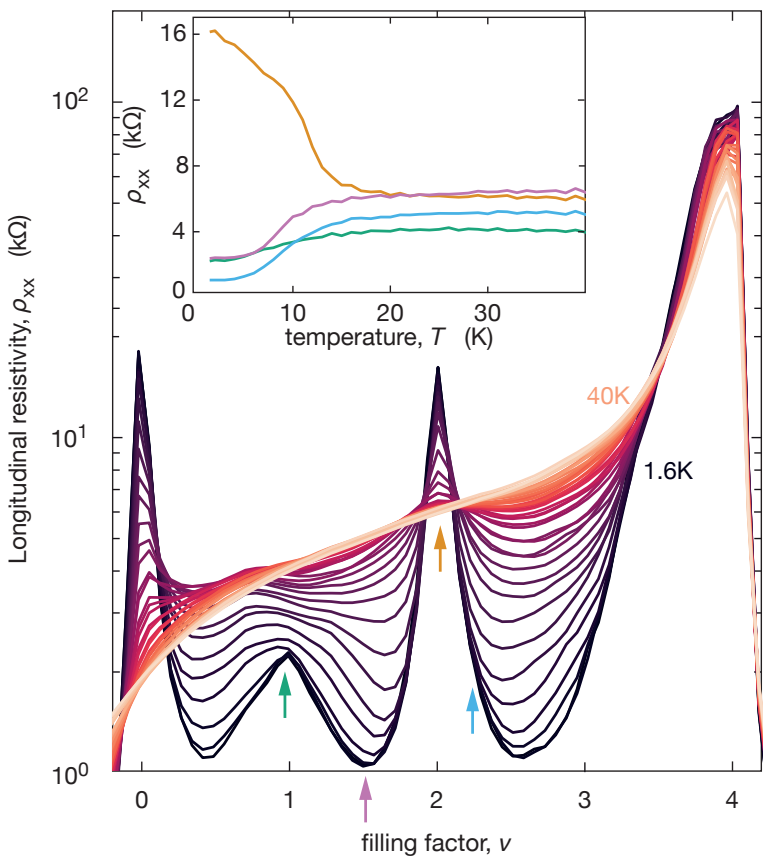

Fig. 9.3 Temperature dependence of the correlated states at $D = +0.45\,\mathrm{V\,nm^{-1}}$ on sample M1: $\rho_{xx}(\nu)$ with varying T. Inset: $\rho(T)$ acquired at the filling marked by coloured arrows in the main panel.

cuss the temperature dependence as a function of electron filling, at constant displacement.

9.1.3.1 Positive displacement

At positive D, there is a highly resistive state at half-filling in the conduction band surrounded by a stretched halo of increased resistance (see fig. 9.1). Figure 9.3 shows the temperature dependence of ρ_{xx} at D =0.5 $\mathrm{V\,nm^{-1}}$. This shows insulating behaviours at half-filling (see inset) whereas, at all other fillings, the behaviour is metallic (defined as increasing ρ with T). We note that measurements of the localised density of state (LDOS) for positive displacements in the same system indicate a phase behaviour similar to twisted double bilayer graphene [289]. This behaviour is probably arising as a consequence of symmetry breaking within a flat conduction band. Additionally, it was shown that energy gaps appear when an in-plane magnetic field is applied, an effect that could indicate the emergence of a spin-polarised ordering at $\nu = 2$ [289, 290]. All these observations correspond to the behaviour of correlated insulators and metallic states in twisted double bilayer graphene (tDBG) [292–296], suggesting that the phase diagram of tMBG is similar to that of tDBG with the same twist angles, and the weak differences appear as a result of the absence of a weakly charged fourth graphene sheet.

Slightly away from half-filling, the resistivity drops abruptly as the temperature is lowered (see inset, fig. 9.3). This abrupt drop is present in regions of the phase diagram in which the magnitude or the sign of the Hall density

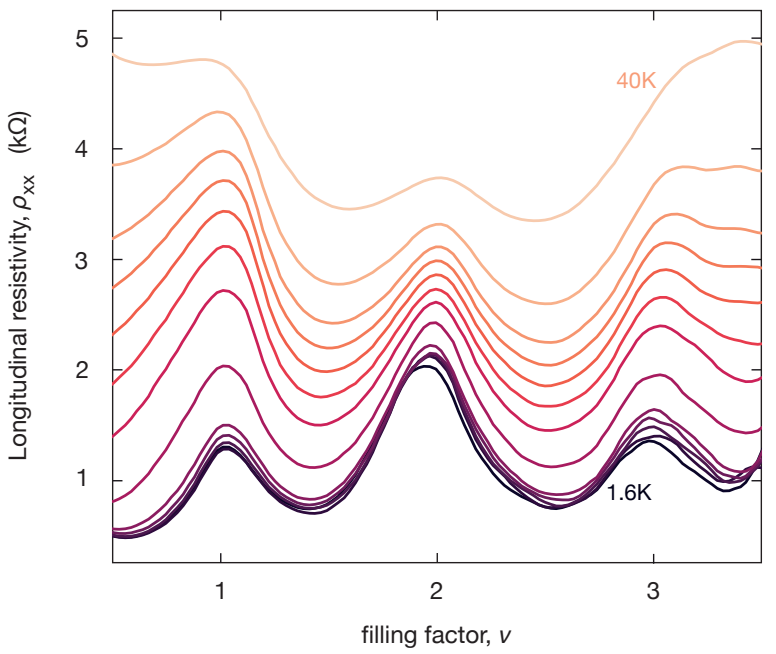

Fig. 9.4 Temperature dependence of the correlated states at $D = -0.45\,\mathrm{V\,nm^{-1}}$ on sample M1: $\rho_{xx}(\nu)$ with varying T.

n_H deviates from the single-particle picture expectation (see below). This is similar to tDBG, in which insulators deviating from the single-particle picture were interpreted as correlated states for fractional fillings. The emergence of these states was attributed to band flatness and band isolation of the low-energy conduction band from its neighbouring bands. Many studies in twisted bilayer graphene close to the magic angle have shown that the spin and valley degeneracies are lifted as a result of electron correlations, giving rise to similar correlated states at integer numbers of electron and hole fillings. Here there is no sign of any insulating state for hole dopping. Indeed, calculations with a continuum model have shown that the bandwidth is much higher in the valence band [20, 289]. This absence of flat band with a much higher Fermi velocity would be the reason for the lack of a correlated insulating state at $n < 0$.

9.1.3.2 Negative displacement

At negative displacement, there are three states with increased resistance, all appearing for integer fillings of the conduction band. Figure 9.4 shows the temperature dependence of ρ_{xx} in the conduction band for $D = -0.45\,\mathrm{V\,nm^{-1}}$. All these states are characterised by a metallic behaviour and a low resistivity ($\sim$1 kΩ) at low temperatures. The behaviour for the insulating state at half-filling ($\nu = 2$) is monotonic with temperature. It corresponds to a semimetallic behaviour. However, the metallic resistive states at $\nu = 1$ and 3 do not show such a monotonic behaviour. Their resistance increases with rising T below $\approx$20 K and decreases at higher temperatures. In this region of negative displacement fields, LDOS measurements have shown great similarities with the phase behaviour of tBG for similar angles [289]. There are, however, some differences as the resistivity depends on details of the band structure. In this

type of correlated insulator, the band structure can be hard to understand. The peak amplitude of all these three correlated states at integer fillings decreases with increasing temperature. This is consistent with the expectation that electron-electron interactions weaken with temperature. Resultingly, the three integer-filling metallic resistive states are attributed to strongly correlated electronic states. However, the non-monotonic behaviour could originate from the competition of different phenomena. Correlations are the principal suspect to explain the low resistivity and metallic temperature dependence. Here they could cause a partial gap opening and band overlap instead of a gap opening as is the case for positive displacements. Another possibility for this non-monotonic behaviour would be temperature-driven phase transitions, from a low-entropy liquid state to a large-entropy localised state. This effect is usually described by the Pomeranchuk effect and was reported in tBG [297, 298]. Full understanding would require further investigations.

Here again, calculations have shown that these states originate from flat bands. However, the local minimum bandwidth is flatter for a positive interlayer potential than for negative potentials. In our transport experiments, this results in flatter bands at $D > 0$ than $D < 0$. It coincides with the experimental observation that the correlated states at positive D are more robust than under negative D.

Finally, such correlation-mediated band insulators appear close to an integer number of electrons per moiré unit cell. This is similar to tBG, where the origin of the strongly correlated insulator is still debated. It was proposed that it could arise from the formation of Mott insulators [145], but this was impugned [154, 155]. Another possibility is the formation of a Wigner crystal [154], or because electron interactions can lift the spin and valley degeneracies [150]. For all these proposed mechanisms, insulating states are expected at integer electron and hole fillings because electron-electron interactions conserve momentum, and can only dissipate the current by Umklapp processes. This condition is only allowed when a moiré mini-band is completely filled [299].

9.2 van Hove singularities

To better understand the nature of these correlated insulators and the phase behaviour in tMBG, we study the response of the Hall coefficient under small perpendicular magnetic fields.

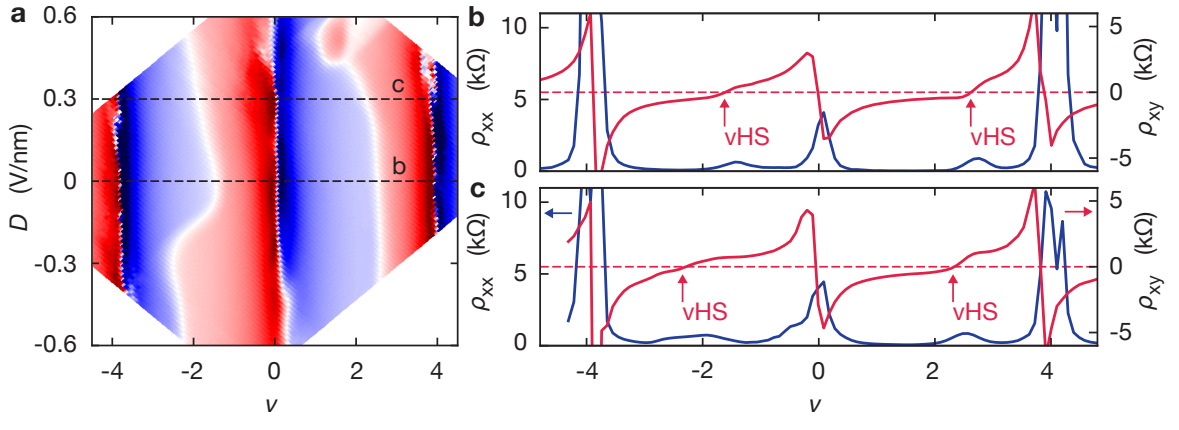

Fig. 9.5: vHS in sample M2 (tMBG with a 1.47° twist): a) $R_{xy}(n, D)$ at B =0.5 T and T_{mc} =1.6 K. Colour scale: blue (−4 kΩ) to red (4 kΩ). **b and c)** longitudinal (B =0 T) and Hall (B =0.5 T) resistivities for D =0 V nm^{-1} and 0.3 V nm^{-1}, respectively, showing vHS emerging at different densities.

9.2.1 Valence band

We first focus on the behaviour in the valence band. Figure 9.5a shows a $R_{xy}(n, D)$ map measured in a sample M2 with a twist angle θ =1.47°. There is a clear, abrupt change of sign at charge neutrality ($\nu = 0$) and full filling ($\nu = \pm 4$) that can be explained by the Fermi level passing through single-particle superlattice gaps (see section 3.2.1.1), accompanied by a change of carrier types. There is also a much less abrupt change of sign, occurring in an S-shape feature in the valence band and vertical line in the conduction band. Figure 9.5b and c give further information on this change of sign. It is identified as a change of the band curvature from electron- to hole-like with $\rho_{xy} = 0$. We attribute this change in the carrier type to van Hove singularities, spanning the whole D range that can be reached in our transport experiments. The position of the vHS changes with displacements, following the white S-shape of figure 9.5a. The presence of vHS in the valence band is consistent with the presence of two single-particle gaps at $\nu = 0$ and $\nu = -4$. The behaviour is different —much richer— in the conduction band.

9.2.2 Symmetry breaking in the conduction band

We now turn back to sample M1 shown previously. Figure 9.6 shows ρ_{xy} in the region corresponding to correlated states for integer $\nu > 0$ and $D > 0$, for three different temperatures. First, we focus on the behaviour at D = 0.45 V nm^{-1}. The behaviour deviates from the single-particle picture (see, e.g. the ρ_{xx} peaks at fillings $\nu = 1$ and 2 in figure 9.6). ρ_{xy} changes sign, for low temperatures, at filling $\nu = 1$ and 2, and for the highest temperatures, only around filling $\nu = 2$. The change of sign indicates a change of carrier type from hole-like to electron-like in the middle of the band. It was postulated

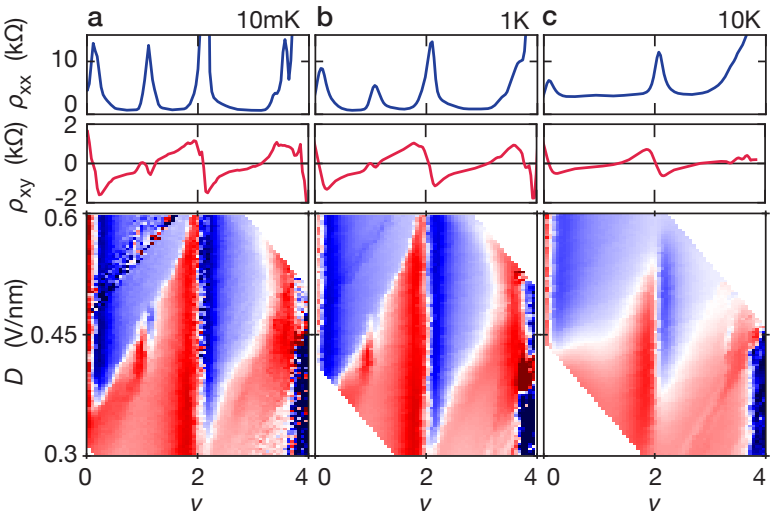

Fig. 9.6 vHS in the conduction band at positive displacement in sample M1 at T = 10 mK, 1 K and 10 K, a, b, c resp.) $\rho_{xx}(\nu)$ (top) and ρ_{xy} (middle) at D =0.45 V nm^{-1} Bottom pannels: $\rho_{xy}(\nu, D)$ Colour scale: blue (−2 kΩ) to red (2 kΩ).

[289] that the change of carriers is the result of symmetry breaking at half and quarter filling, with the formation of a new mini-band edge. The sign change of ρ_{xy} is happening within the halo of increased resistance introduced in section 9.1.3.1, suggesting spontaneously broken symmetry within the band. Looking at the larger picture, the ρ_{xy} change of sign happens only for a small range of displacement fields 0.4 < D <0.7 V nm^{-1}. This is in contrast with the previously reported sign change at $D < 0$ [289] where the three resistive features are all concomitant with sign changes in ρ_{xy} and features much more concentrated in a narrow range of D. As these states also have a low resistivity, it can be postulated that for $D < 0$, the correlated states indicate overlap between electron and hole-like bands when the Moiré unit cell hosts an integer number of electrons.

We attribute these sign changes to van Hove singularities resulting from band reconstruction as a result of strong correlations. These van Hove singularities indicate the formation of three new Fermi surfaces (Lifschitz transitions) when the conduction band hosts an integer number of electrons, similar to the behaviour of tDBG and tBG.

9.3 Evolution with twist angles

So far, I have shown two devices M1 and M2 with twists 1.22° and 1.47°. The first one shows correlated states at integer fillings of the conduction band, the second did not. Here we explore a wider range of twist angles and their influence on the correlated states. Figure 9.7 shows the evolution of the correlated states as a function of twist angle θ. We present 8 devices with twists 0.99°, 1.18°, 1.22°, 1.26°, 1.30°, 1.41°, 1.47° and 1.60°. Let us first discuss the correlated states at $D > 0$ (fig. 9.7a). For all the twist angles considered, there is a halo of somewhat increased resistance appearing between CNP and full-filling in a narrow range of displacement fields. For twists angles between 1.18° and 1.41° correlated insulators develop at integer fillings, between 0.3 < D <0.7 V nm^{-1}.

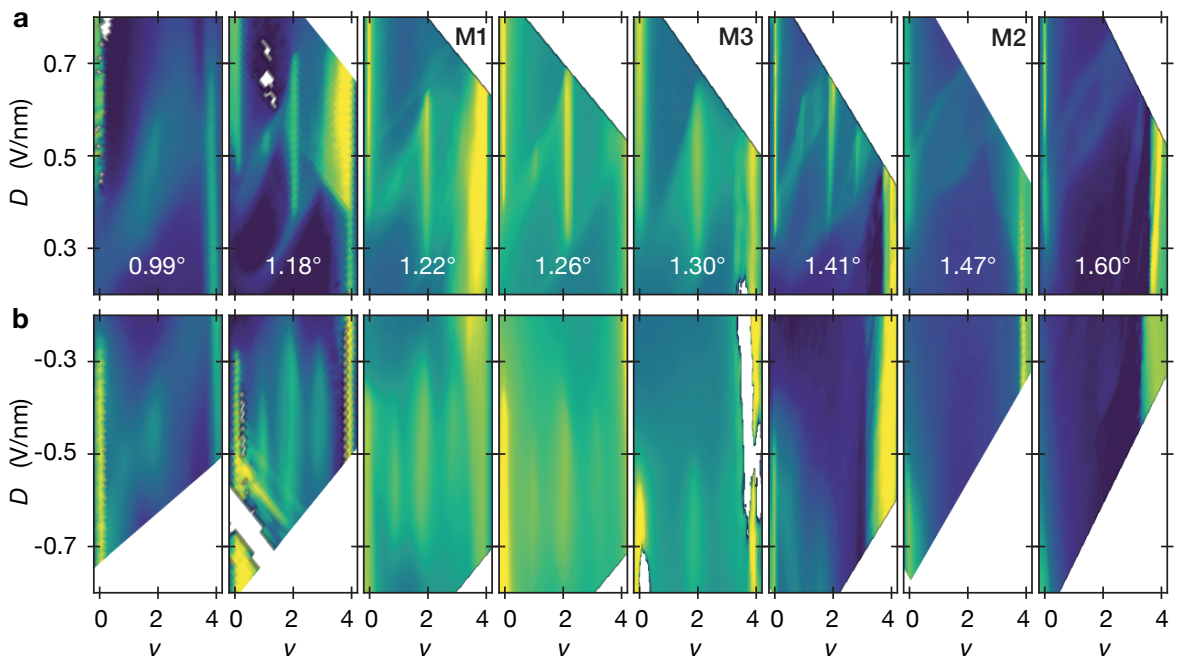

Fig. 9.7: evolution of the correlated states with twist angles for positive (a) and negative (b) displacements. $\rho_{xx}(\nu, D)$ measured at T =1.6K and B =0T for samples with varying twist angles θ. Logarithmic colour scale: indigo (20 Ω) to yellow (7 kΩ).

These states remain in the same range of displacement fields for all twist angles. Additionally, it seems that the correlated states at $\nu = 1$ and 3 are more stabilised for a range of twists between 1.26° and 1.41°. The resistance of these states is maximum between 1.22° and 1.26° and decreases with increasing θ above 1.26° and with decreasing θ below. Theory has shown [20] that the bandwidth minimum of the low energy conduction band at positive interlayer biases (corresponding to positive displacement fields) increases with θ between 0.9° and 1.6°, consistent with the observation that the correlated features at $D > 0$ fade away with increasing θ. The band isolation is also calculated to be maximised at 1.26°, consistent with our experimental observations.

Concerning negative D (shown in fig. 9.7b) the semimetallic resistive states appear most clearly for a small range of twists between 1.18° and 1.30°. They fade away below 1.18° and shift to higher displacements above 1.26°, to a point that they cannot be measured in our transport experiments. Theoretical calculations have shown that the position of the minimum of the low-energy conduction band shifts to larger energy [20]. This is in accordance with the shift of the correlated states to higher displacements. Additionally, this low-energy conduction band becomes less isolated from the high-energy conduction band as the gap Δ_{+4} decreases in energy, with increasing interlayer bias. The less isolated band at $D < 0$ than at $D > 0$ could explain the lower resistance observed at $D < 0$. Overall, the correlated states observed at integer fillings in the conduction and valence band can be explained by enhanced band hybridisation in a set of *magic* angles that flattens the band and increase electronic correlations.

9.4 Anomalous Hall effects & orbital magnetism

We now focus on the correlated states emerging at $D > 0$. Figure 9.8 shows the Hall resistivity ρ_{xy} as a function of the magnetic field for different temperatures, measured in device M3 with twist angle 1.30° at $\nu = 0.76$ and 1.6, and $D = 0.45\,\mathrm{V\,nm^{-1}}$. These states, in the halo of the insulating states at $\nu = 1$ and 2, exhibit a robust anomalous Hall effect with a large hysteresis with a large Hall angle $\rho_{xy}/\rho_{xx} \sim 10$ at $B = 0$. Contrary to other reports [287–290] we observe that the anomalous Hall effect decreases as one moves closer to $\nu = 1$ or 2. Figure 9.8 shows the temperature dependence of the anomalous Hall effect, showing its total suppression by raising the temperature above 5 K. The large Hall angle indicates that the transport is occurring predominantly through the edges. However, ρ_{xy} is not quantised and ρ_{xx} is still finite. This could be due to either disorder or a small gap, preventing the full development of the Chern insulator. This should be achieved when moving closer to integer filling, but our devices do not show such an effect. Indeed, previous reports noted that the insulators at integer filling were trivial, and the anomalous Hall effect was observed upon doping from $\nu = 1$, with no quantisation achieved [287–290]. There is, however, a very narrow range of angles around 1.25° for which a Chern insulator with $\mathcal{C} = 2$ and the Anomalous Hall effect approaching quantisation was observed [288].

Note that spin-orbit coupling is very low in graphene, therefore the anomalous Hall effect should not emerge from spin-ordered magnetism. Instead, it was proposed that the hysteretic behaviour in twisted graphene heterostructures could originate from orbital magnetism [124, 125, 128, 288, 290]. This ordering would be confirmed by additional reports that have shown that the magnetic ordering could be controlled and switched with sweeping n at $B = 0$, in addi-

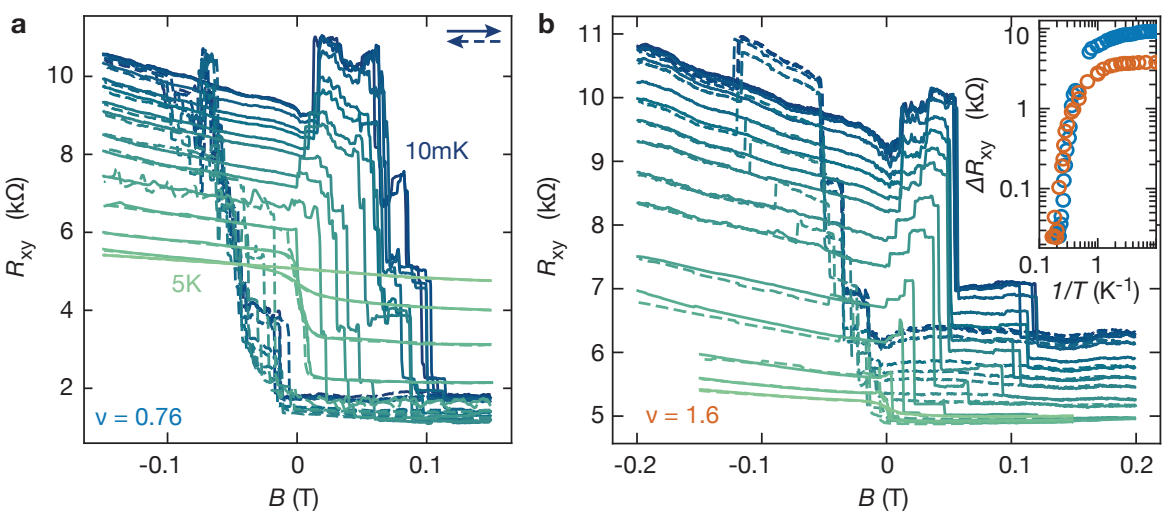

Fig. 9.8: Anomalous Hall effect in tMBG. $R_{xy}(B)$ hystereses cycles at different temperature for $\nu = 0.76$ (**a**) and $\nu = 1.60$(**b**) on device M3. Inset: amplitude of the Hall resistance as a function of $1/T$, showing activation gaps of 1.1 and 1.3 meV, resp.

tion to switching with B [288, 289]. This is a sign of unique orbital magnetism exhibited in twisted monolayer-bilayer graphene that would deserve further studies.

9.5 Correlated states beyond the Fermi surface edge

Away from the correlated states, we observed non-linear IV characteristics [20] resembling incipient superconductivity, with a sharp increase in the resistance with temperature. However, although this system shares some qualitative similarities with MA-tBG, superconductivity is absent and the non-linear IV curves are rather a signature of out-of-equilibrium anomalies. I first explain this effect in a single-particle picture for the general case of graphene superlattices, before showing data in tMBG.

9.5.1 The Dirac fluid away from equilibrium

In general metals, the electric response of a given system can be described by a small displacement of the Fermi surface in momentum space balancing acceleration of charge carriers with scattering-induced relaxation. In the general case of subsection 2.1.1, the displacement of the Fermi surface in momentum space is small: the drift velocity $\boldsymbol{v}_\mathrm{d}$ is negligible compared with the Fermi velocity $\boldsymbol{v}_\mathrm{f}$. In graphene, weak inelastic scattering allows to shift the Fermi surface far from equilibrium [300–302] As a result, it was recently made possible to shift the charge carriers within the topmost partially filled band along the applied electric field E resulting in the production of extra carriers through interband transitions [115]. This happens in the Dirac fluid, a relativistic plasma of massless electrons and holes. Whereas at high carrier densities, the drift velocity in graphene is only limited by phonon emission [303, 304], this is not the case for low n, close to the neutrality point, where thermal excitations allow non-negligible displacements of the Fermi surface. This regime shows a universal behaviour at high bias (see figure 9.9 and ref. [115]). At relatively high biases ($j \lesssim 10\,\mu\mathrm{A}\,\mu\mathrm{m}^{-1}$) the superlattice exhibits linear IV characteristic, followed by a rapid switching into a high-resistance state: the dV/dI shows a pronounced peak for a critical current density j_c and decreases at higher biases. $j_\mathrm{c} \approx nev_\mathrm{f}$ corresponds to the transition between a low- and high-resistance state, where $v_\mathrm{d} \approx v_\mathrm{f}$. For $j > j_\mathrm{c}$ it was shown that a Schwinger-like effect consisting of particle-antiparticle creation occurs in the Dirac fluid [115].

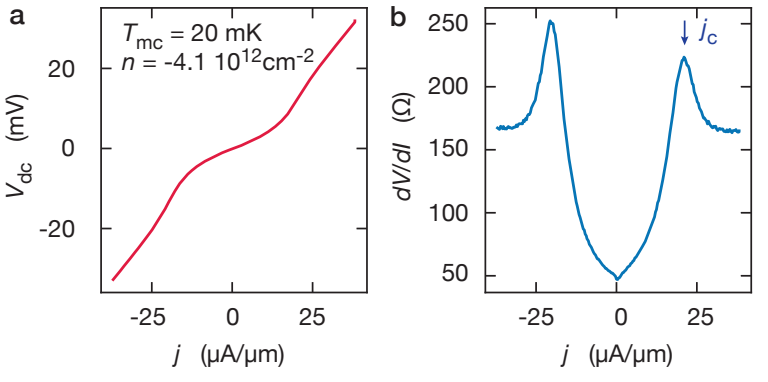

Fig. 9.9 Non-linear transport in a graphene superlattice (device D3). a) I-V characteristic as a function of the current density j, and **b)** corresponding dV/dI curve.

9.5.1.1 Secondary Dirac fermions

Here we focus on the behaviour close to secondary Dirac points (DP) of graphene superlattices where the Fermi velocity v_f is expected to be lower as a result of narrow electronic bands, a feature that should enhance the visibility of out-of-equilibrium criticalities. I chose to focus on the hole side as the Dirac point is more pronounced and leads to enhanced resistance (see, for example, fig. 3.7 in section 3.2.1.1). In this region, the non-linear IV characteristics evolve in such a manner than the two peaks at j_c merge for $n = -n_0$ where n_0 is the density of the secondary DP found at $4.01 \times 10^{12}\,\mathrm{cm}^{-1}$, as shown in figure 9.10.

At finite biases close to the secondary DP, the Fermi velocity was calculated to be half of the value of the main Dirac point [114]. This translates into $j_\mathrm{f} = v_\mathrm{f}^{2DP}/n_\mathrm{s}e$ where $v_\mathrm{f}^{2DP} \approx 5 \times 10^5\,\mathrm{m\,s}^{-1}$ and n_s is the carrier density in the region of interest. n_s is different from the total density n induced by the gate and is found by taking into account the presence of vHS in the band structure: $n_\mathrm{s} = C_\mathrm{g}(V_\mathrm{g} - V_\mathrm{2DP})/e = C_\mathrm{g}V_\mathrm{g}/e + n_0$ (see details in section 6.2), where V_2DP is the gate voltage at which the secondary DP is measured. Additionally, it is possible to evaluate the drift velocity v_d corresponding to the maxima j_c. These are shown as white dots in the map of figure 9.10, whereas the current $j_\mathrm{f}(n)$ corresponding to the calculated Fermi velocity is shown as a dashed line. Here the maxima are found for v_d much smaller than v_f.

In order to get more insight into the critical behaviour, I show the extracted drift velocity v_d calculated for the maxima at j_c in figure 9.11a. The found v_d corresponds to several $10^4\,\mathrm{m\,s}^{-1}$, an order of magnitude below the calculated Fermi velocity. Close to the secondary neutrality point at $\nu = -1$, the drift velocity shows a sharp peak, and evidence of rapidly decreasing v_d away from the secondary DP. Additionally, v_d is smaller for the electron-like miniband than for the hole-like miniband. This can be explained by a higher bandwidth on the hole-side miniband. As the band structure flattens away from the secondary Dirac point, one may expect v_d to decrease further as the density is tuned away from n_0 [115] but my measurements do not allow to confirm or refute this hypothesis. Overall, a better understanding of this critical transport char-

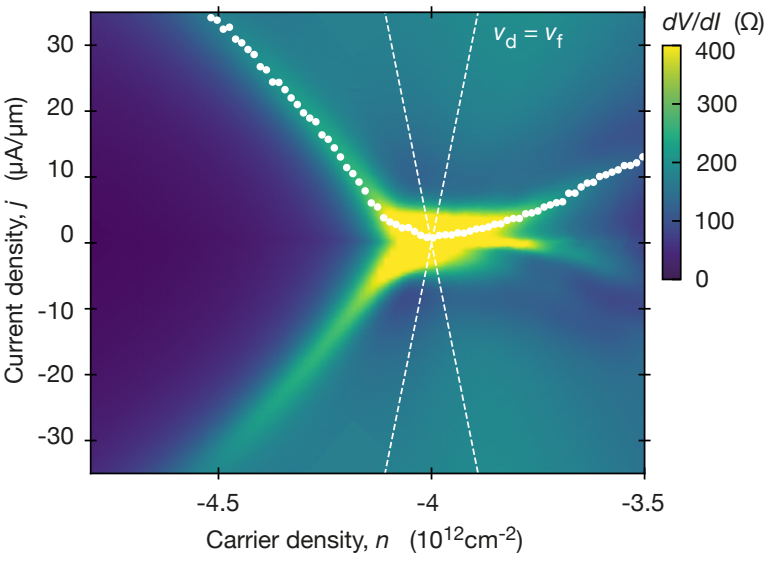

Fig. 9.10 High bias regime close to the secondary DP in device D3: dV/dI as a function of j and n for the same superlattice of figure 9.9. Measured at T_{mc} =20 mK. White dots indicate the position of j_{c}, dashed lines indicate the current $j_{\mathrm{f}}(n)$ corresponding to the Fermi velocity calculated in the secondary DP of a graphene-hBN heterostructure.

acteristic near the secondary Dirac point would require specific calculations of the electronic spectrum.

At the secondary Dirac point, the behaviour can be understood via a Schwinger-like particle-antiparticle production as follows. At relatively low biases, the resistance drops dramatically, attributed E-induced interband carriers generation along the e–h puddle boundaries [115, 305]. The minimum of the differential resistance dV/dI occurs for a relatively low critical current of $\sim$10 µA µm^{-1}, five times smaller than close to the main Dirac point in graphene point contacts [115]. At higher current densities, the resistance gradually increases again. In this case, E can move the electrons from the valence bend to the conduction band, with extra electrons and holes created by interband transitions. At these biases, the apparent drift velocity exceeds the maximum possible Fermi velocity: $v_{\mathrm{d}} = j/ne > v_{\mathrm{f}}$. This is made possible thanks to the extra electrons and holes, generated at a rate $\propto E^{3/2}$ in the Schwinger-like mechanism, adding a density Δn on top of the gate-induced n. Accounting for electron-hole annihilation (recombination processes that bring the electronic system back into equilibrium), the concentration of extra carriers can be found $\Delta n \propto V^{3/2}$ if $\Delta n \ll n$. This translates into the current $\Delta n e v_{\mathrm{f}} \propto V^{3/2}$ and therefore we measure $dV/dI \propto j^{1/3}$, as shown by the dashed line in figure 9.11b. This behaviour is expected to be similar at all densities (not only close to a DP) for a current above j_{c}. For $j \lesssim j_{\mathrm{c}}$ carriers move at maximum velocity and saturate at v_{f} explaining the peak separating the regime of a weakly dissipative fluid-like flow to a strongly dissipative electron-hole plasma.

9.5.2 The case of Brown-Zak fermions

This behaviour is similar for Brown-Zak fermions, which can be seen as replicas of the Dirac spectrum in a magnetic supercell. Figure 9.12 shows similar high-

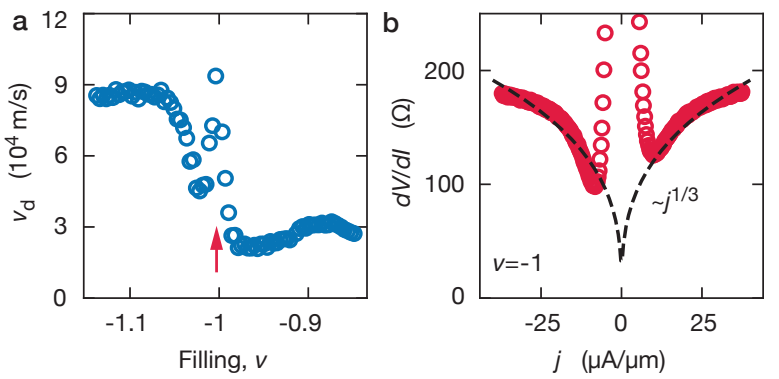

Fig. 9.11 Non-linear transport near the secondary Dirac point in device D3. a) drift velocity at j_c as a function of the filling $\nu = n/n_0$. **b)** dV/dI at the secondary DP (red arrow in panel a).

bias transport in a graphene superlattice for $B = p/qB_{\phi_0}$ with $p/q = 1/3$. Whereas in graphene, $j_c = nev_f$ is valid for a wide range of carrier densities n, this is not the case in graphene superlattices as a result of band reconstruction in the mini Brillouin zone. As a result, the group velocity of charge carriers decreases rapidly away from the secondary Dirac point and drops close to the van Hove singularities.

In the case of Brown-Zak fermions, there are several neutrality points (NP) occuring for all Landau filling fractions $\nu = \pm 2, \pm 6, \pm 10, \pm 14, \pm 18$ (as shown in figure 9.12), with van Hove singularities occuring between each of these neutrality points (see chapter 7 for more details). Consequently, there is a small range of n_{BZF} around each of these NPs for which j_c evolves linearly as $j_c \approx n_{\mathrm{BZF}} e v_f$ where n_{BZF} is calculated in section 6.3.1. In that case, the presence of vHSs between two consecutive NPs would deviate from the linear behaviour of $j_c(n_{\mathrm{BZF}})$. Indeed, the non-linearity would correspond on one side of the vHS to electron-like BZF and, on the other side, to hole-like BZF. These electron and hole-like pairs do not cancel out at large biases but contribute to the high-bias behaviour. This results in bell-shaped features, interconnecting different NPs of the BZF.

Additionally, the BZF have verry narrow minibands, and therefore a low v_f and the onset of high-bias transition is expected at small j. Indeed, the switching transition occurs at $j_d \lesssim 20\,\mu\mathrm{A}\,\mu\mathrm{m}^{-1}$, 10 times smaller than at zero magnetic fields. Aronud each NP, v_f is found between $3 \times 10^3\,\mathrm{m\,s}^{-1}$ and $5 \times 10^3\,\mathrm{m\,s}^{-1}$, an order of magnitude smaller than the characteristic v_f of several $10^4\,\mathrm{m\,s}^{-1}$ for superlattices at zero field. This translates into relatively small minibands widths of ≈10 meV, expected from band structure calculations [105, 194].

9.5.3 High bias behaviour in tMBG

It becomes reasonable to expect similar non-linearities to appear in tMBG, with Dirac cones merging at ν =-4, 0 and 4, and remain unaffected in the

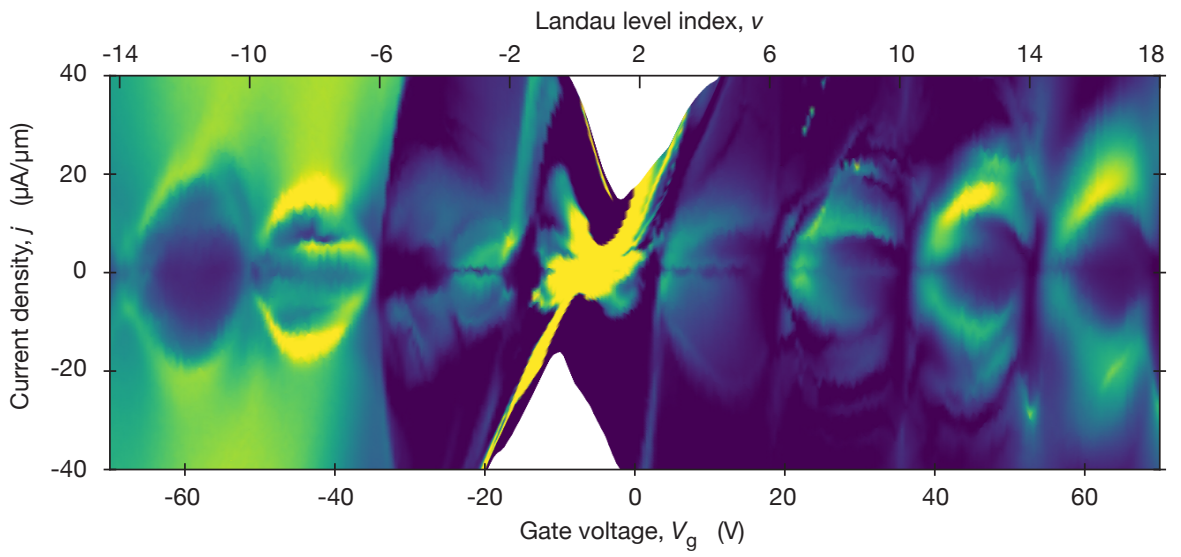

Fig. 9.12: Non-linear transport at $B = B_{\phi_0}/3$ in device D3 $dV/dI(V_g, j)$ in a graphene-hBN superlattice at T_{mc} =20 mK. Colour scale: indigo (50 Ω) to yellow (2.4 kΩ).

region of the correlated insulators, as a large number of carriers and very low Fermi velocity would need much larger fields to be driven out-of-equilibrium.

9.5.3.1 Slow Fermi velocity

Figure 9.13a sows a $dV/dI(\nu, j)$ map, measured for D =0.45 V nm^{-1} in device M4 with a twist angle of 1.2° device. A number of features can be observed and are sketched on figure 9.13b.

First, we focus on the valence band ($\nu < 0$). The signal shows a low resistance at small biases, corresponding to the regions indicated in navy in figure 9.13b, with a constant resistance ($dV/dI \lesssim$2 kΩ). This signal then increases dramatically to a pronounced peak for a certain value j_{c2} (red curve in fig. 9.13b), consistent with the observations in graphene superlattices detailed above. For $j > j_{c2}$, the Schwinger mechanism of electron-hole pair generation is still valid.

The behaviour is different in the conduction band, where multiple non-linearities can be observed. Close to full filling, the transition between the high and low-resistance follows $j_c \approx nev_f$ with v_f =500 m s^{-1}, a value found through calculations with a continuum model [20] and indicated as a white dashed line in fig 9.13a. This very slow Fermi velocity is reduced by more than three orders of magnitude compared with the Fermi velocity of monolayer graphene (10^6 m s^{-1}) and two orders of magnitude compared with the Fermi velocity close to the secondary DP of graphene superlattices (see fig. 9.11). It is nonetheless consistent with reports in tBG at 1.23° [115] and translates into a bandwidth of ∼10 meV, consistent with band structure calculations [20]. However, contrary to the twisted bilayer graphene system where the high-resistivity j_c branches merge at charge neutrality, there is no evidence of such an effect in

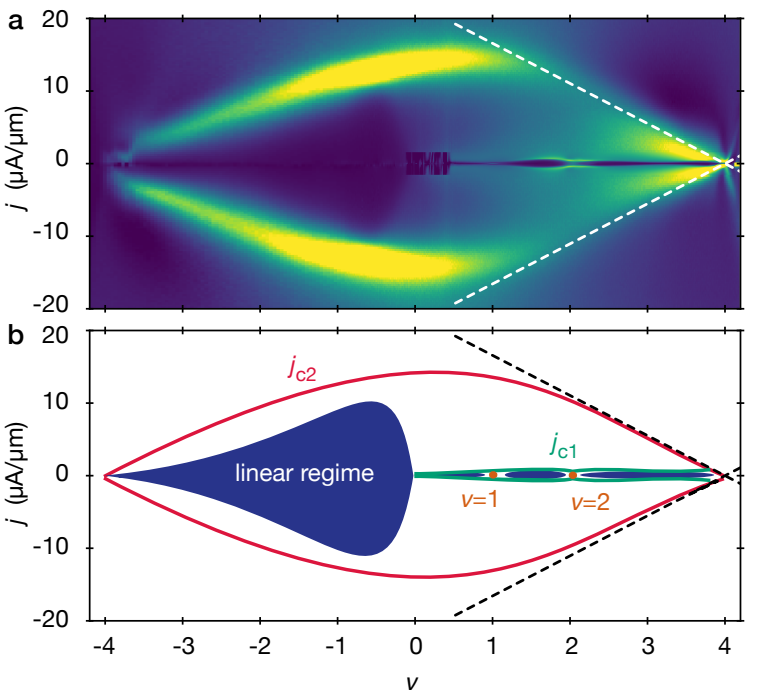

Fig. 9.13 Non-linearities in tMBG. a) $dV/dI(\nu, j)$ measured at constant $D = 0.45\,\mathrm{V\,nm^{-1}}$ in device M6 with a 1.2° twist angle at $T_{\mathrm{mc}} = 20\,\mathrm{mK}$. Colour scale: indigo (0 Ω) to yellow (10 kΩ). Dashed white line: calculated j_{f} for $\nu = 4$. **b)** Schematic of the behaviour in (a).

tMBG, for a wide range of displacement fields between 0.2 and $0.55\,\mathrm{V\,nm^{-1}}$. This could be explained by two different mechanisms. The insulating state at $\nu = 2$ could be different from charge neutrality and instead host relatively flat bands. This seems counter-intuitive as single-particle calculations show the emergence of a resistive state at CNP, but the nature of this state was recently challenged and is still under debate [287, 290]. A second possibility is a competition between conducting channels in tMBG. At $D > 0$, the density of states is dominated by the contribution from the bilayer, so that the outer layer of the bilayer concentrates most of the electronic charges [128]. As a result, at high biases, the electric field shifts the Fermi sea from the bilayer, leaving the electronic structure of the monolayer untouched. This could reorganise the spectrum, as non-linear behaviour is virtually unreachable in monolayer graphene. This hypothesis is corroborated by measurement at $D < 0$ (not shown), in which the two branches of j_{c2} merge at $\nu = 0$, similar to twisted bilayer graphene.

In the range $0 < \nu < 4$ the spectrum is subject to multiple Lifshitz transitions and van Hove singularities and many-body reconstruction of the spectrum. There, the high-bias transport regime is more complex. In addition to the critical current j_{c2} at $\sim 20\,\mathrm{\mu A\,\mu m^{-1}}$, there is another resistance maximum depending weakly on the density, at $j_{\mathrm{c1}} \approx 1\,\mathrm{\mu A\,\mu m^{-1}}$ (shown as a green line in fig. 9.13b). Interestingly, the resistance peak at j_{c1} is more pronounced around $\nu = 2$, where it displays a constriction but doesn't merge in the insulating state. Rather, there are small but noticeable maxima, seen as a zero-bias peak, emerging for $\nu = 1$ and 2. Note that in this regime, j_{c1} is very low ($\approx 1\,\mathrm{\mu A\,\mu m^{-1}}$), corresponding to Fermi velocities of a few $\mathrm{m\,s^{-1}}$. This results in very flat bandwidths in the range of ~ 0.1–$1\,\mathrm{meV}$, an experimental evidence of the flat bands leading to strong correlations at integer fillings.

9.5.3.2 Charge transfer in a nested Fermi surface

Here I try to understand the high-bias behaviour of the correlated insulator at $\nu = 2$. Note that in this region, the band structure possesses a Lifschitz transition, reshaping the band structure [20]. Figure 9.14a shows the non-linear behaviour at $\nu = 2$. At small bias, there is a small zero-bias peak as the Hall density is reset. In a usual neutrality point, the initial drop is attributed to electron-hole puddles, and small E generate interband carriers along the puddle boundary, enhancing the conductivity. Here the system presents similarities as the carrier density is reset by the Lifschitz transition, so it is reasonable to expect a similar mechanism. As the field is increased further, there is a minimum in dV/dI at $j \approx 100\,\mathrm{nA\,\mu m^{-1}}$, followed by a rapid increase and a peak at a very low critical current of $j_{c1} = 450\,\mathrm{nA\,\mu m^{-1}}$ and a minimum at $\sim 1\,\mathrm{\mu A\,\mu m^{-1}}$. At higher biases, there is once again, an increase followed by a gradual drop of the resistance, before the onset of j_{c2}.

Figure 9.14b shows the temperature dependence of the non-linearities. The zero-bias peak is the most fragile feature and disappears around 3 K. Upon increase of the temperature, j_{c1} appears to be constant over a temperature range between 20 mK and 6 K, before being smeared by heating, evidence of a transition from Schwinger-dominated transport to normal transport as additional electron-hole pairs are thermally excited. Note that these two temperature scales are smaller than the range over which the correlated state at $\nu = 2$ is observed (see, eg. fig. 9.3). However, the resulting $k_B T$ is in the order of 0.5 meV which corresponds to a very narrow bandwidth expected in this regime of strongly correlated electrons. These non-linearities at a small j_{c1} could be associated with very flat bands that even a small electric field can shift out of equilibrium. Over the range of this measurement, I am not able to distinguish any variation in j_{c2}, therefore we can expect it to be associated with an unreconstructed band with a larger bandwidth.

To understand better the origin of these features, figure 9.14c shows the Fermi surface at $\nu = 2$ for a 1.22° twist angle, calculated with a single particle model. As the carrier density is reset by the Lifshitz transition at $\nu = 2$, a multi-pocket Fermi surface merges into a single Fermi surface. This results in a nested Fermi surface, where a small portion is encircling K_{BG} of the mini Brillouin zone corresponding to the K point of the bilayer Brillouin zone, corresponding to localised electron wavefunctions in the bilayer. The first peak j_{c1} would correspond to this portion of the Fermi surface, where the group velocity is minimal (see fig. 9.14c). As the field is increased, the effects on the rest of the Fermi surface surrounding Γ become more pronounced, resulting in the criticality observed at j_{c2}. Importantly, the maximum group velocity is calculated in the large Fermi pocket encircling Γ for all densities, corresponding to a uniform distribution of the electron wavefunction across all three layers.

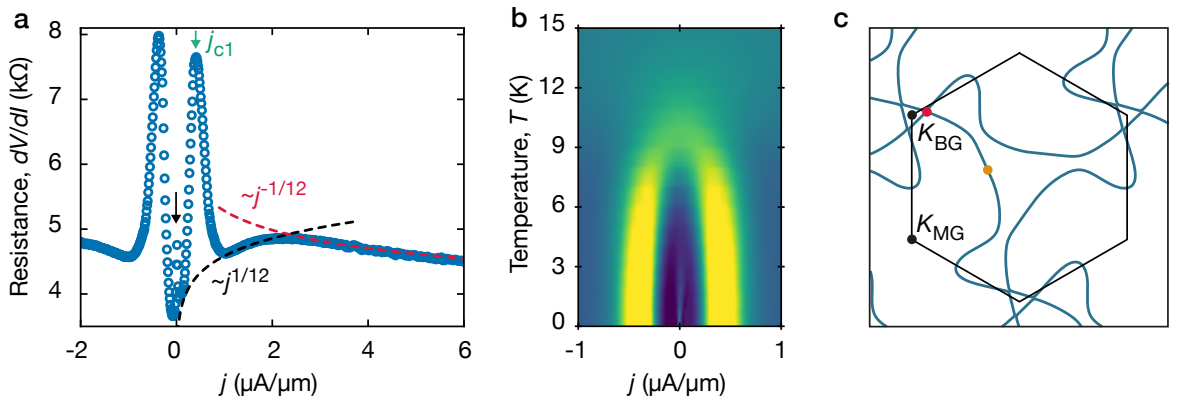

Fig. 9.14: Nested Fermi surface measured in device M6. a) non-linearities at a function of the current density, for ν =2 and D =0.45 V nm^{-1}. Dashed lines correspond to best-exponent fits. **b)** Temperature dependence for the curve shown in panel (a). Colour scale: indigo (3.8 kΩ) to yellow (6.5 kΩ). **c)** Fermi surface at $\nu = 2$ and D =0.44 V nm^{-1}, extracted from [20]. The red dot correspond to the location of the minimum Fermi velocity; the orange dot to the maximum.

The high-bias behaviour is expected to be described by $dV/dI \propto j^{\alpha}$, where $\alpha = 1/3$ for a Schwinger mechanism. It is found that the best-fit exponent for the creation of carriers above j_{c1} is close to 1/12 (see fig. 9.14a), much smaller than for a Schwinger mechanism, therefore, suggesting a different mechanism. This exponent could be related to Zener-Klein tunnelling, where α was shown to be comprised between 0 and $-1/3$ at the graphene neutrality point [305]. In that case, the exponent is related to tunnelling between different energy bands and defect scattering. This is consistent with the analysis above, where the different high-bias features correspond to charges being driven from the low-energy subband around K_{BG} to the high-energy subband around Γ. As the bias is increased, annihilation of carriers follows the same power law and therefore likely corresponds to the inverse mechanism, transferring carriers back from the high-energy- to the low-energy subband.

9.5.3.3 Field-induced Band reconstruction

To appreciate the competition between wavefunctions localised at the monolayer and at the bilayer in the band structure, I measured the displacement dependence of the low-bias non-linearities at constant $\nu = 2$, shown in figure 9.15a. The displacement field is expected to shift the weight of the wavefunction from the monolayer to the bilayer, therefore shifting the energy of the K_{MG} and K_{BG} points with respect to each other. The zero-bias peak, corresponding to the correlated state at $\nu = 2$ can be resolved for a finite range of D between 0.3 V nm^{-1} and 0.5 V nm^{-1} below which the transport regime is linear as expected from the absence of correlated insulators and the dV/dI peaks occuring at j_{c1} are more pronounced above $D = 0.4$ V nm^{-1}. Between 0.3 V nm^{-1}

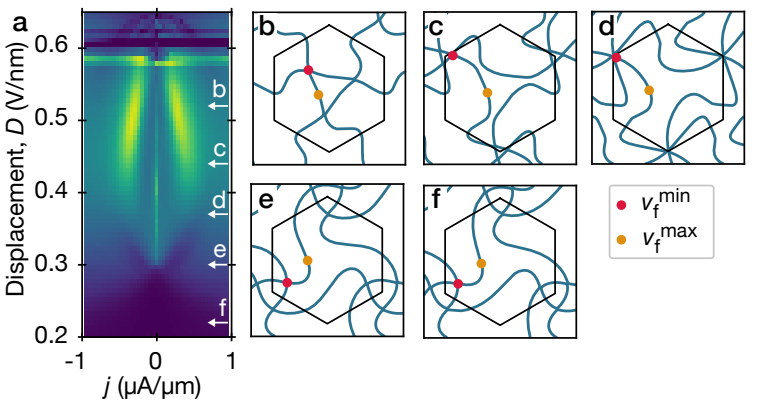

Fig. 9.15 Field-induced band reconstruction en device M6. a) $\rho_{xx}(j, D)$ at $\nu = 2$. Colour scale: indigo (0 Ω) to yellow (10 kΩ). **b** to **f)** Fermi surface at D indicated in panel (a).

and $0.4\,\mathrm{V\,nm^{-1}}$, the high-bias regime corresponds to a drop of the resistance, different from the usual maxima observed in graphene superlattices [115].

These features can be interpreted with the variation of the Fermi surface with D (fig. 9.15 b to f). At relatively high displacements of $0.52\,\mathrm{V\,nm^{-1}}$ and $0.44\,\mathrm{V\,nm^{-1}}$ (b and c), a small Fermi pocket is centred around K_{BG}, while at lower displacements of $0.3\,\mathrm{V\,nm^{-1}}$ and $0.22\,\mathrm{V\,nm^{-1}}$ (e and f) small Fermi pockets are centred around K_{MG}. This suggests that over this range of displacement fields, a Lifschitz-like transition occurs, moving the Fermi surface from the bilayer to the monolayer corner of the mini Brillouin zone.

Note that in this region, the Fermi velocity cannot be calculated easily because of the resetting of the Hall conductance at $\nu = 2$, leading to unknown n. It is nonetheless expected to be very low as the bandwidth is found $\lesssim$1 meV. Overall, the correlated insulator at $\nu = 2$ may result from partial polarisation of K_{BG} and K_{MG} with respect to the layers, leading to a condensate of electrons and holes. Here, vHSs result in many-body reconstruction of the spectrum so the single-particle calculations of the Fermi surface can only be used as a guide.

Conclusion

In this chapter, I introduced twisted monolayer-bilayer graphene (tMBG), a system that exhibits a variety of effects as a result of the absence of inversion symmetry. Correlated states emerge at integer fillings of the conduction band upon application of a displacement field for a small range of twist angles, a result of symmetry breaking and interlayer hybridisation. In the vicinity of these correlated states, the anomalous Hall effect can be observed. Finally, the presence of both monolayer- and bilayer-like subbands results in a strong interplay of states at some displacement fields. Measurements of non-linear transport at high bias allow us to extract a very low Fermi velocity that explains the many-body phenomena, with consequences being debated [306]. Further studies may explore the nature of the correlated state at $\nu = 2$ as it shows similarities with the recently measured BCS-BEC crossover in MA-tBG [307], even though superconductivity is absent in tMBG.

Chapter 10
Flat band superconductivity via proximity screening

The use of metals in proximity with a studied system is a widely used platform for the control of electron-electron interactions. This induces additional screening and suppresses Coulomb interaction in the studied system [98, 247, 308–310]. In van der Waals heterostructures, there are two different approaches for this proximity screening. The first is to place a metallic system (e.g. multilayer graphene) close enough to the heterostructure with a thin hBN layer to decouple this multilayer graphene from the studied heterostructure via interlayer distance. In this case, it is possible to decrease the thickness of the dielectric spacer to increase the magnitude of screening. There is another approach that consists in using a virtual spacer of zero thickness and decoupling the two systems by a large angle [311–317]. This translates into a large momentum mismatch between the two K points of the two subsystems. The previous chapter was focused on multilayer systems with a small twist angle so that the wavefunctions from each layer overlap and hybridise between the two Dirac cones of the two subsystems. In this chapter I propose a different kind of heterostructures, using large angles to decouple two subsystems and induce screening of the Coulomb interactions with effects on relatively flat bands.

10.1 Decoupling with a large twist angle

Here I introduce the effects of high-angles on transport measurements in relatively simple systems. Let's consider a system of two layers of graphene stacked together at a very large angle $\sim 10°$. An example of a lattice of such a heterostructure is shown in figure 10.1a. When the two layers are stacked with a large twist angle, there is no long-range Moiré superlattice. The two Dirac cones of the two monolayers are spaced in momentum space by a distance proportional to the twist angle – large at high angles. As a result, the two Dirac cones can be considered non-interacting and could be studied independently. These sorts of heterostructures can be fabricated using the usual method, and

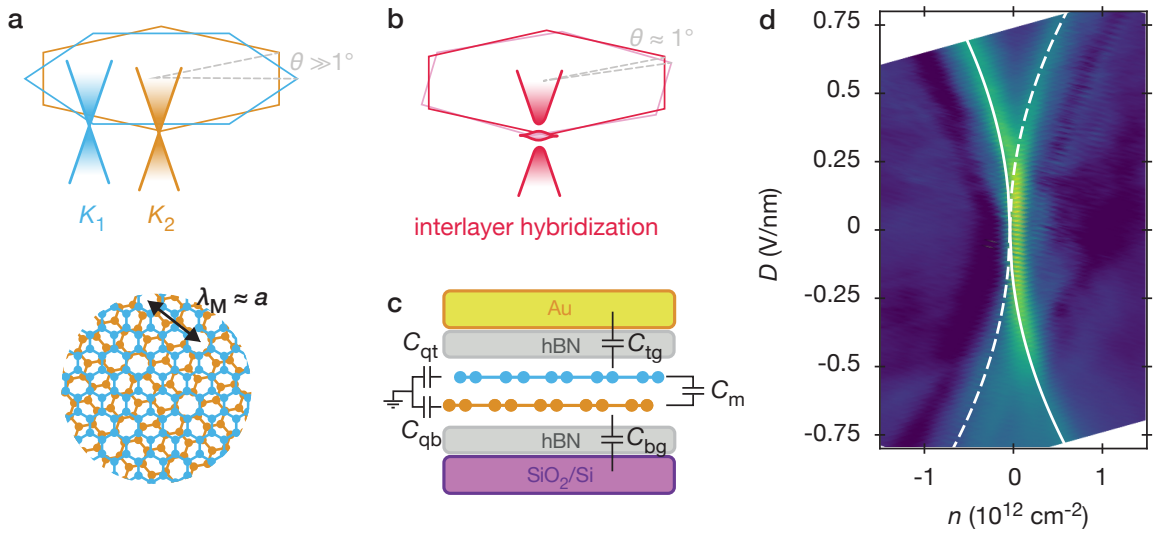

Fig. 10.1: Transport properties of large-angle bilayer graphene. a) Sketch of two graphene layers twisted with a large angle. top: in reciprocal space: the two Dirac cones are far away. bottom: in real space, the moiré wavelength λ_{M} is comparable with the interatomic distance a. **b)** For small angle twisted bilayer graphene, interlayer hibridisation results in flat bands. **c)** Electrostatic model used in the chapter and **d)** $\rho_{\mathrm{xx}}(n, D)$ calculated with the inter-layer capacitance model. Logarithmic colour scale: indigo (16 Ω) to yellow(400 Ω).

Raman spectroscopy during the fabrication process is performed to verify that the two layers are decoupled.

In such a system, tuning the top gate affects mostly the density of state in the top layer, while varying the bottom gate predominantly affects the density of state in the bottom layer. Figure 10.1b shows the different capacitances involved in this system. C_{tg} and C_{bg} correspond to the geometric capacitances of the top and bottom graphene to the top and bottom gate, respectively. They can be found using the usual methods: one can use atomic force microscopy to find the thickness of the hBN layers or use Hall measurements in a small magnetic field (see subsection 4.4.2). The capacitance between the two graphene sheets is C_{m}. The quantum capacitances C_{qt} and C_{qb} of the top and bottom layers are proportional to the density of states at the Fermi energy in the top and bottom layers, respectively: $C_{\mathrm{qt}} = e^2\mathcal{N}_{\mathrm{s,t}}(E_{\mathrm{f}})$ and $C_{\mathrm{qb}} = e^2\mathcal{N}_{\mathrm{s,b}}(E_{\mathrm{f}})$ where $\mathcal{N}_{\mathrm{s,t}}$ and $\mathcal{N}_{\mathrm{s,r}}$ represent the density of state of the top and bottom layer, respectively [315]. As in usual double-gated systems, the slope of the zero-density line in the $(V_{\mathrm{tg}}, V_{\mathrm{bg}})$ map is given by $-C_{\mathrm{b}}/C_{\mathrm{t}}$ (see section 4.2.2). The influence of the interlayer and quantum capacitances can be appreciated in transport measurements. Figure 10.1c shows the resistivity $\rho_{\mathrm{xx}}(n, D)$, where the density and displacements are calculated with gate thicknesses found through atomic force microscopy. There are notable features to observe on this map. First, there is a high-resistivity peak at $n = 0$ and $|D| < 0.25\,\mathrm{V\,nm^{-1}}$, corresponding to the two independent Dirac points, evolving as a function of both n and D. Second, this high-resistivity peak is split at large displacements $|D| > 0.25\,\mathrm{V\,nm^{-1}}$. The finite interlayer capacitance —originating from the finite

electronic thickness of graphene— is responsible for the splitting of this peak into two branches [315].

The variations of these NPs in the $(V_{\mathrm{tg}}, V_{\mathrm{bg}})$ space can be described as ridges following the equations [315]:

$$\left.\frac{\partial V_{\mathrm{tg}}}{\partial V_{\mathrm{bg}}}\right|_{\mathrm{n_b}=0} \approx -\frac{C_{\mathrm{bg}}}{C_{\mathrm{tg}}}\left(1+\frac{C_{\mathrm{qt}}}{C_{\mathrm{m}}}\right) \tag{10.1}$$

$$\left.\frac{\partial V_{\mathrm{bg}}}{\partial V_{\mathrm{tg}}}\right|_{\mathrm{n_t}=0} \approx -\frac{C_{\mathrm{tg}}}{C_{\mathrm{bg}}}\left(1+\frac{C_{\mathrm{qb}}}{C_{\mathrm{m}}}\right) \tag{10.2}$$

This can be expressed as trajectories of the CNPs:

$$V_{\mathrm{tg}}|_{\mathrm{n_b}=0} = -\frac{-C_{\mathrm{bg}}}{C_{\mathrm{tg}}}\left(1+\frac{C_{\mathrm{qt}}}{C_{\mathrm{m}}}\right)V_{\mathrm{bg}} + \mathrm{const.} \tag{10.3}$$

$$V_{\mathrm{bg}}|_{\mathrm{n_t}=0} = -\frac{-C_{\mathrm{tg}}}{C_{\mathrm{bg}}}\left(1+\frac{C_{\mathrm{qb}}}{C_{\mathrm{m}}}\right)V_{\mathrm{tg}} + \mathrm{const.} \tag{10.4}$$

Combining these equations with equations 4.6 and 4.7 we get the trajectories in the (n, D) space, approximating $C_{\mathrm{qt}} = C_{\mathrm{qb}} = C_{\mathrm{q}}$:

$$D_{\mathrm{CNP}} \approx \frac{e}{\epsilon_0}\frac{C_{\mathrm{m}}}{C_{\mathrm{q}}} n_{\mathrm{CNP}} + D_0, \tag{10.5}$$

where n_{CNP} and D_{CNP} are the coordinaters of the two charge neutrality points (CNP) for the two independent layers.

As a result, for high-angle twisted bilayer graphene, the splitting in n is given by $C_{\mathrm{q}}/C_{\mathrm{m}}$. This behaviour is non-linear as $C_{\mathrm{q}} \propto \sqrt{n}$, therefore $|D_{\mathrm{CNP}}| \propto \sqrt{|n|}$. This behaviour is different in high-angle twisted double bilayer graphene for which $C_{\mathrm{q}} = \mathrm{const}$. Figure 10.2 shows a sketch of the zero-density lines for high-angle tBG and tDBG in the $(V_{\mathrm{tg}}, V_{\mathrm{bg}})$ space. In such a map, the line with slope $-C_{\mathrm{tg}}/C_{\mathrm{bg}}$ corresponds to the gating condition where the total charge carrier density vanishes. In this map, the CNP from each graphene layers is found to depart from the $n_{\mathrm{tot}} = 0$ line as $\sqrt{|n|}$ and the CNP from each bilayer follows linear trajectories. Multiple experimental studies confirm these calculations [314–317]

10.2 Twisted tetralayer graphene

10.2.1 Description of the device

Twisted monolayer and bilayer graphene can be seen as model systems for high-angle heterostructures. Here I propose to explore a more complex heterostructure, composed of two twisted bilayers (tBG), stacked together with a large angle ($\approx$10°), so that the electronic structure is decoupled. Here I describe sample S1, combining two twisted bilayers: the bottom bilayer is twisted

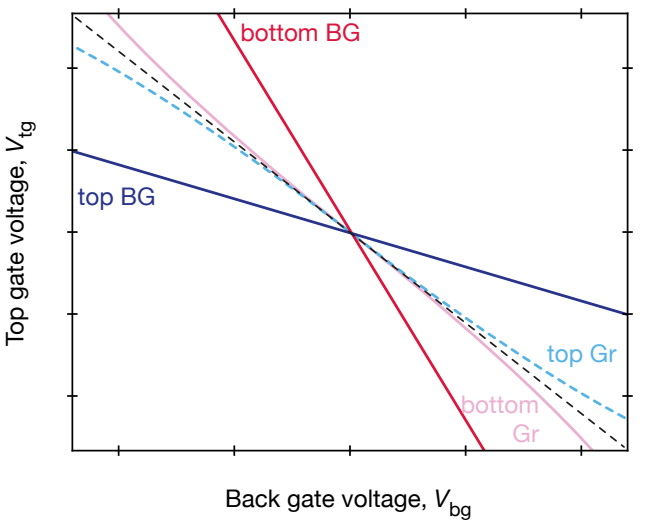

Fig. 10.2 Zero-density lines for high-angle systems: tBG (pink and light blue lines) and tDBG (red and navy lines). Black dashed line represents $n_{\mathrm{tot}} = 0$.

bilayer graphene with a 1.25° angle, close to the magic angle but sufficiently far enough that superconductivity and correlated states have, so far, not been observed at this angle. This bottom subsystem is referred to as MA-tBG. The top bilayer is a twisted bilayer graphene with a twist angle of 0.4°. At this angle, the lattice is expected to reconstruct into giant alternating Bernal domains [131–134]. This top bilayer is referred to as mtBG. The twist angles in the two subsystems were extracted from the positions of secondary DPs and BZFs.

This system is analogue to a recently reported heterostructure in which a thin hBN spacer was used between an MA-tBG layer and a Bernal bilayer graphene layer [310]. This hBN spacer was used to decouple electronically the MA-tBG from the Bernal BG and at the same time screen the Coulomb interaction of MA-tBG resulting in enhancement of the superconductivity and weakening of insulating states. Here, the large twist angle has the same effect as the thin hBN spacer. In this system, the two gates can be used to simultaneously control the carrier density n and the displacement field D in both layers. Owing to the large twist angle, the two subsystems are relatively independent of one another therefore it is possible to access a space of constant densities and displacement relative to each bilayer. This is a relatively different system from small-angle twisted tetralayers [318–320] because it cannot be treated as a uniform system but encompasses two distinct subsystems influencing each other. To the extent of my knowledge, this is the first use of large angle heterostructures to tune strongly correlated electronic systems.

10.2.2 Screening of electron-electron interactions

Understanding the role of Coulomb interactions is detrimental to identifying the nature of the correlated state in magic-angle twisted bilayer graphene [310]. In particular, MA-tBG shows a phase diagram resembling that of cuprates,

with correlated insulators close to superconducting phases. Recent studies invalidated this hypothesis by showing that correlated insulators and superconducting phases could appear independently of one another. Here, screening electron-electron interactions should reduce the influence of Coulomb interactions and stabilise superconductivity. Sample S1 that I show here comprises a bottom bilayer close to the magic angle and screening electron-electron interactions could help the understanding of the emergence of electronic phases around the magic angle [150, 151, 310, 321].

To understand the impact of screening from the top twisted bilayer on the bottom MA-tBG, we compare transport measurements with a double-gated twisted bilayer graphene device fabricated in the same conditions (sample S2). The position of secondary neutrality points and BZF in this device reveal a twist angle of 1.23°, similar to the 1.25° of the 4-layer heterostructure. Figure 10.3 shows both resistivities ρ at 2 K and 50 K. We note that at 2 K the resistivity is an order of magnitude smaller in the 4-layer graphene at the secondary DPs. This lowered resistance is likely due to parallel conduction in both the MA-tBG and mTBG bilayers.

At elevated temperatures, Umklapp electron-electron scattering is expected to dominate the resistivity of graphene heterostructures [246]. In twisted bilayer graphene, $\rho(T)$ can be described quantitatively by Umklapp e^-–e^- scattering, i.e., should rapidly increase as $\Delta\rho \propto T^2$. In figure 10.3, this is visible through a 10-fold increase of the resistivity at 50 K compared to 2 K. In the tetralayer heterostructure, the presence of an additional bilayer twisted with a large angle strongly suppresses $\Delta\rho(50\,\mathrm{K})$ by a factor > 5. The suppression of high-temperature resistivity is most visible close full filling ($\nu = 4$) where the resistivity is suppressed by a factor ∼50.

The suppression of the resistivity in this tetralayer heterostructure is attributed to suppressed Umklapp e^-–e^- scattering, as a result of enhanced Coulomb screening. The presence of the top bilayer strongly screens Coulomb

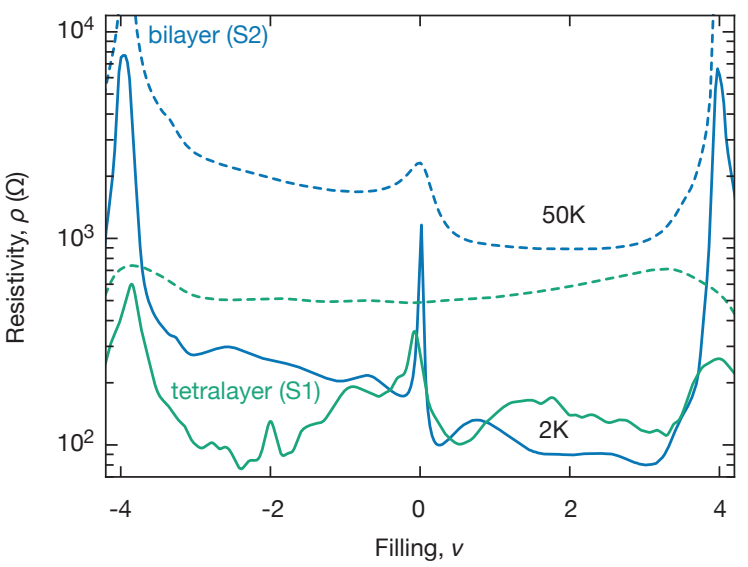

Fig. 10.3 Suppression of umklapp e–e scattering in large-angle tetralayer graphene $\rho(\nu)$ of 1.2° twisted bilayer graphene and 1.2°, 10° and 0.4° twisted tetralayer graphene for T =2 K (solid lines) and 50 K (dashed lines).

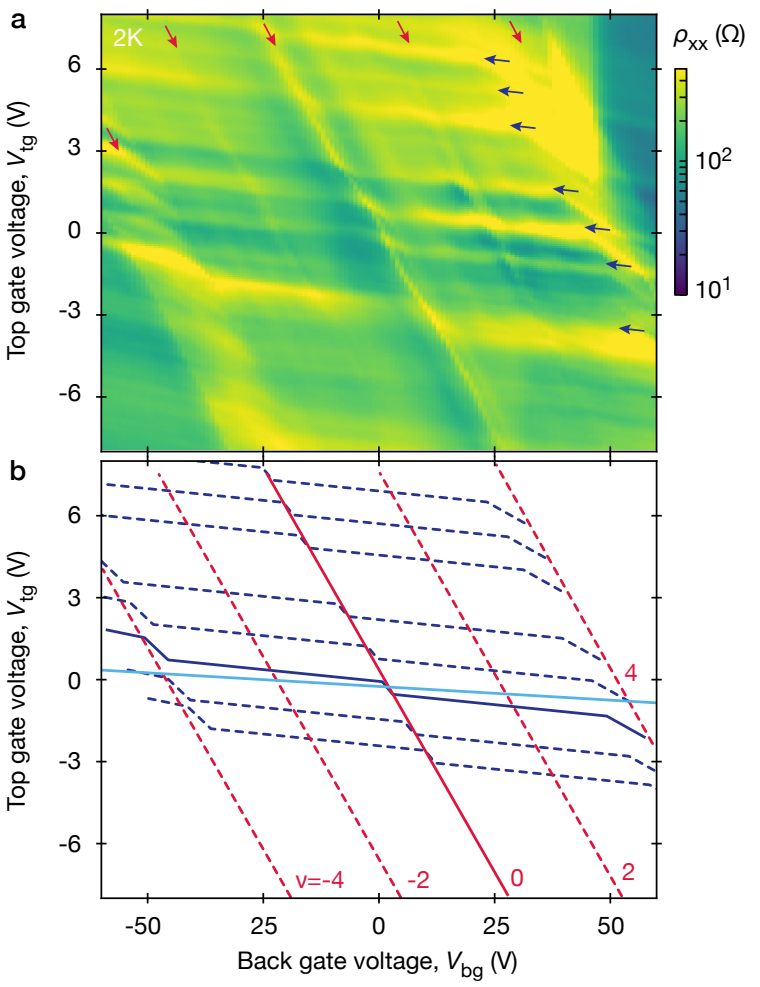

Fig. 10.4 Gate-tunable transport in weakly coupled tetralayer graphene (device S1). **a)** $\rho_{xx}(V_{tg}, V_{bg})$ measured at 2 K. Red (navy) arrows denote resistivity features corresponding to the bottom MA-tBG (top mtBG). White dashed line: cut at which figures 10.3 and 10.6 were measured, corresponding to constant displacement in the bottom MA-tBG. **b)** Schematic of the constant filling lines on each bilayers. solid lines show zero-density lines for the top (navy) and bottom (red) bilayers; dashed lines show non-zero constant density lines.

interactions, which enhances electron correlations. A consequence of this is the presence of small resistance peaks appearing close to $\nu = \pm 2$, attributed to correlated insulators [145] visible in the low-temperature characteristic of figure 10.3, but absent in S2 at all temperatures. Lower temperatures are expected to enhance the resolution of these metallic resistive states.

10.2.3 Transport in weakly coupled layers

Figure 10.4a shows a resistivity gate dependence measured at 2 K. There are multiple features observable from this gate map, sketched in figure 10.4b. There are slanted resistance maxima, indicated with navy and red lines. As shown previously for the case of high-angle twisted double bilayer graphene, these lines correspond to constant-density features in the top bilayer (mtBG) and the bottom bilayer (MA-tBG). The trajectories of the constant-density lines of the MA-tBG (shown in red) are straight lines in the (V_{tg}, V_{bg}) space. The trajectories corresponding to constant-density lines of the mtBG (shown in navy) are a succession of discontinuous segments, shifting by a few volts on the top gate whenever they intersect constant density lines of the MA-tBG. The linear behaviour can be explained similarly to high-angle twisted double bilayer graphene. The discontinuous behaviour is analogous to transport

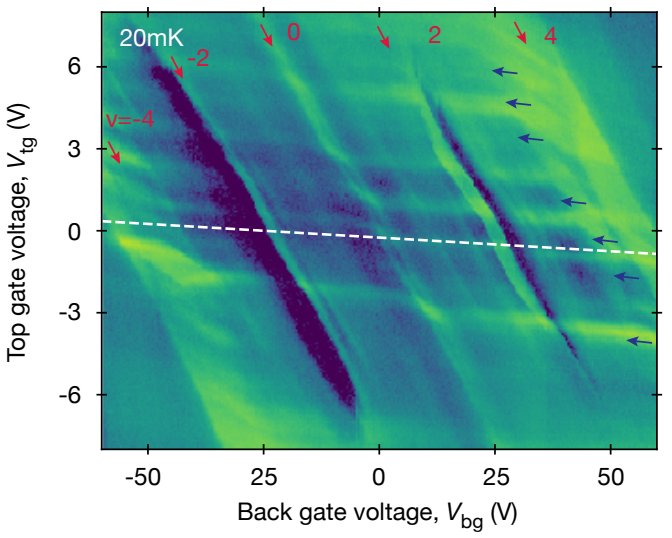

Fig. 10.5 $\rho_{xx}(V_{tg}, V_{bg})$ **in weakly coupled tetralayer graphene (S1) at** 20 mK. Same colour scale as in figure 10.4.

data in screened magic-angle twisted bilayer graphene [310], where distortions of transport features occur whenever the screening BLG is fully insulating, leading to unscreened behaviour. Here, these distortions happen when the resistance of MA-tBG is higher suggesting the same mechanism.

From this electronic measurement, we find $C_{tg}/C_{bg} \approx 3.4$, in agreement with the expected slope considering the measured thickness of top and bottom hBN via atomic force microscopy. We can also extract the geometric capacitance between the two bilayers, and find C_m =6.4 µF cm^{-2}, a value comparable to the observed capacitance between two single-layer graphene sheets (7.5 µF cm^{-2}) [315], and approximately double as the capacitance between two bilayers (3.5 µF cm^{-2}) [314], probably due to the additional twists between individual layers.

10.3 Incipient superconductivity

10.3.1 Ultra-low temperature transport

Figure 10.5 shows the resistivity measured at $T_{mc} = 20$ mK. It should be compared with figure 10.4a with which it shares the colour scale, enabling better visualisation of the resistance difference. In most of the (V_{tg}, V_{bg}) space, the resistance drops homogeneously by a factor 3, consistent with increasing electron-electron interactions at ultra-low temperatures. Note, however, that the suppression of the resistance between 2 K and 20 mK is much greater than between 50 K and 2 K, a further sign of screened electron-electron scattering in our 4-layer device.

There is another important feature, noticed as indigo streaks close to $\nu_{MA-tBG} = \pm 2$, corresponding to zero-resistance. We attribute these streaks to superconductivity for the following reasons. In twisted bilayer graphene systems close to the magic angle, superconductivity has been observed close

to the correlated states for fillings $2 \leq |\nu| \leq 3$ [148–151]. Notably, the superconducting dome at negative doping was found to be consistently stronger for a wide range of twist angles. For some angles far from the magic angle superconductivity was only observed for hole doping. This is consistent with the measurements of figure 10.5 that show a broader zero-resistivity streak for $\nu \approx -2$ than for $\nu \approx 2$. For this reason, the indigo streaks in figure 10.5 is attributed to superconductivity. Further characterisation is provided later in this chapter. Additionally, superconductivity is expected to appear in twisted bilayer graphene close to the magic angle, with a critical temperature decreasing dramatically as the angle is moved away from the magic angle condition [321]. To the extent of my knowledge, the highest angle at which superconductivity was reported is 1.18° [321], much lower than the 1.25° of device S1. Importantly, no sign of zero resistance could be observed at our lowest temperature in S2 with twist angle of1.23°, neither for electron and hole doping. Correlated insulators at half-filling were also absent at low temperatures.

10.3.2 Unconventional superconductivity

We now aim to characterise the superconductivity in weakly coupled tetralayer graphene (S1). Figure 10.6a shows the resistivity measured along with the white dashed line in figure 10.4. This line is chosen to be in a region of small $D_{\mathrm{MA-tBG}}$, and without any high-resistance features originating from the top bilayer, so that its influence is minimal [310]. We observe resistive metallic states for filling factors $\nu_{\mathrm{MA-tBG}}$ = -4, -2, 0, 2, 3 and 4. The resistance of these states is much lower than the resistance of correlated and insulating states reported in magic-angle bilayers [150] but is comparable with magic-angle tetralayers [320]. As explained above, this is because an additional bilayer offers a parallel conduction system.

We observe superconducting domains for $2 \leq |\nu_{\mathrm{MA-tBG}}| \leq 3$, highlighted as blue stripes in figure 10.6. The superconductivity is spread over a wide range of densities, encompassing the whole range between correlated insulators at $|\nu_{\mathrm{MA-tBG}}| = 2$ and 3. The behaviour for electron-doping is consistent with previous reports, where superconductivity was observed mostly close to correlated insulators, suggesting in early reports that the insulating and superconducting orders could share a common origin as in cuprates. However, measurements in screened devices [151, 310, 321] have shown that when the strength of Coulomb interaction is tuned, superconductivity can be decoupled from the correlated insulators. This suggests that correlated insulators and superconductivity could be two phenomena competing with each other. In our device, hole-side doping shows a relatively weak metallic-insulating phase at $\nu = -2$ and no insulating phase at all at $\nu = -3$, consistent with observa-

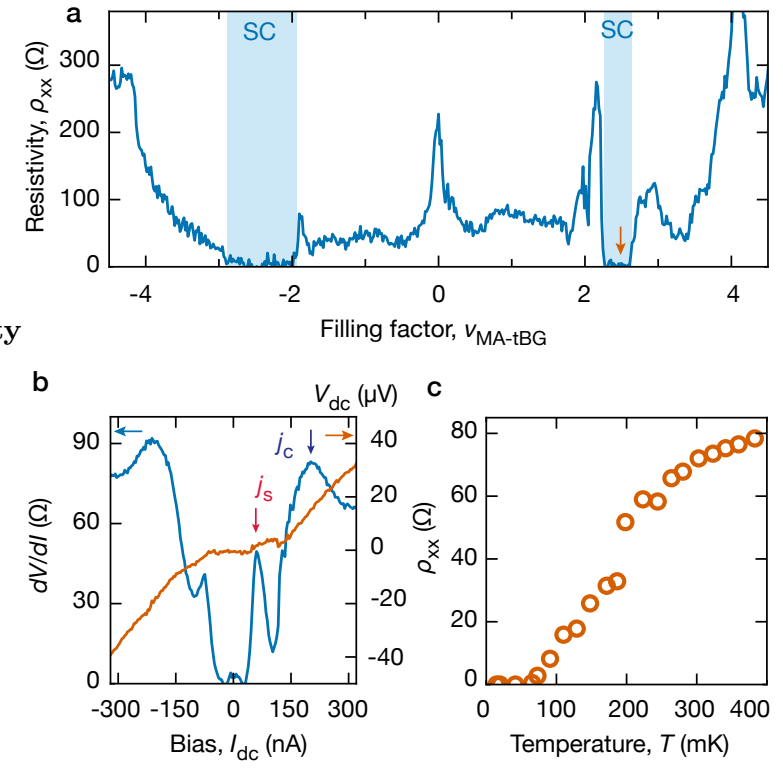

Fig. 10.6 Superconductivity in weakly coupled tetralayer graphene (S1): a) $\rho_{xx}(\nu)$ measured at 20 mK along the white dashed line of figure 10.4. **b)** $dV/dI(I_{dc})$ measured for density corresponding to the brown arrow of (a). **c)** $\rho_{xx}(T)$ at the same point.

tions in screened devices. The amplitude of correlated insulators is decreased by screening, while superconductivity increases from the decreasing Coulomb interaction.

We now explore the superconducting behaviour close to $\nu = +2$. Figure 10.6b shows the differential resistance dV/dI and the DC voltage V_{dc} measured as a function of the DC bias current I_{dc} for $n = 1.63\,\mathrm{cm}^{-2}$. At low biases $I_{dc} < 100\,\mathrm{nA}$, we observe a non-linear behaviour characteristic of superconductivity, with a rapid increase of the differential resistance for $I_{dc} \approx 50\,\mathrm{nA}$, corresponding to the switching current of the superconducting phase. As the bias current is further increased, non-linearities emerge, characterised by a much broader peak in dV/dI with a maximum at $I_{dc} = 200\,\mathrm{nA}$. This non-linear behaviour corresponds to a critical shift of the Fermi surface in the normal state, as explained in the previous chapter. Figure 10.6c shows the resistivity temperature-dependence measured at $I_{dc} = 0$ at the same density of $1.63 \times 10^{12}\,\mathrm{cm}^{-2}$. We observe a rapid increase of the resistivity for temperatures $> 100\,\mathrm{mK}$. It corresponds to a thermal activation energy of $\sim 10\,\mu\mathrm{eV}$. Similarly, in small magnetic fields, the superconductivity disappears around 3 mT (not shown). Taking this value as the critical field H_{c2}, one can estimate the superconducting coherence length $\xi_0 = \sqrt{\phi_0 / 2\pi H_{c2}} \sim 330\,\mathrm{nm}$. This is 6 times larger than superconducting coherence lengths reported in MA-tBG [150,293], probably resulting from electrostatic gating suppressing charge inhomogeneities and enabling superconducting correlations at larger distances. It is also possible to use the uncertainty principle to estimate the superconducting coherence length with Pippard's argument. In that case, one gets $\xi_0 \sim \Delta x \sim \hbar v_f / k_B T_c \sim 76\,\mathrm{nm}$. This is somehow smaller than the coherence length measured from B_c, and closer to previously reported coherence lengths in MA-tBG [150, 293].

From these measured ξ_0, it is possible to find the pairing gap Δ from the BCS relation: $\Delta \sim \hbar v_\mathrm{f}/\xi_0$. Using $v_\mathrm{f} \sim 1000\,\mathrm{m\,s^{-1}}$, the superconducting gap is found $\Delta \sim 1\,\mu\mathrm{eV}$ (or $8\,\mu\mathrm{eV}$ with Pippard's argument), therefore the ratio $\Delta/k_\mathrm{B}T$ is about 0.1 to 1, which is much smaller than the ratio of 1.73 expected in conventional superconductors, but somehow consistent with MA-tBG [307]. These energy scales suggest rather fragile superconductivity with an unconventional behaviour, and superconducting correlations persisting over rather long length scales, probability as a result of the Coulomb screening induced by the top mtBG layer. In that sense, screening could shift the competition between electron-phonon coupling with Coulomb interactions in favour of the electron-phonon coupling, therefore strengthening the Cooper pair formation and superconductivity. This mechanism, however, appears to be inconsistent with the finding of unconventional $\Delta/k_\mathrm{B}T$ ratio. Alternatively, the screening of Coulomb interaction could modify some properties of the MA-tBG band, such as the bandwidth or the size of the Fermi surface, resulting in a flatter band that favours strong correlations.

Note that the non-linearities corresponding to a critical shift of the Fermi surface are visible for magnetic fields in excess of 500 mT and temperatures above 400 mK, as expected from the Schwinger mechanism [115].

10.3.3 Displacement dependence of the superconductivity

In order to acquire a better understanding of the influence of the screening from the top mtBG on the superconducting behaviour, we study the superconducting streak in the $(n_\mathrm{MA-tBG}, D_\mathrm{MA-tBG})$ space. This corresponds to a region of constant density and displacement fields applied to the bottom bilayer. For a strongly coupled heterostructure, the displacement field between the different layers can be found using equation 4.7. In weakly coupled systems, the top bilayer acts as a gate on the bottom layer, therefore if we want to study the bottom bilayer, it is necessary to replace $C_\mathrm{tg}V_\mathrm{tg}$ in eq. 4.7 with $C_\mathrm{m}V_\mathrm{mtBG}$, where C_m is the measured interlayer capacitance between the two weakly coupled bilayers and V_mtBG is the electrical potential of the top layer. Additionally, the Fermi energy in the top layer is [314]:

$$E_\mathrm{f,t} = eV_\mathrm{mtBG} = \frac{\hbar^2}{2m^*}\pi n_\mathrm{mtBG} = \frac{e^2}{C_\mathrm{qt}} n_\mathrm{mtBG} \tag{10.6}$$

Therefore, $V_\mathrm{mtBG} = en_\mathrm{t}/C_\mathrm{qt}$ and the displacement calculated on the bottom bilayer can be rewritten as:

$$D_\mathrm{MA-tBG} = \frac{1}{2\epsilon_0}\left(\frac{C_\mathrm{m}}{C_\mathrm{q}} e n_\mathrm{mtBG} - C_\mathrm{bg}V_\mathrm{bg}\right) \tag{10.7}$$

Which can be written as:

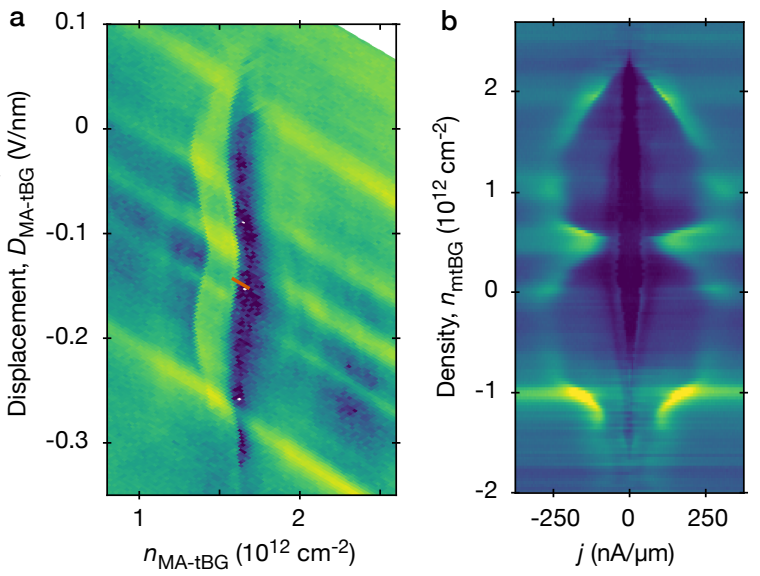

Fig. 10.7 Superconductivity in screened MA-tBG (S1). a) $\rho_{xx}(n_{\mathrm{mA-tBG}}, D_{\mathrm{MA-tBG}})$. Logarithmic color map: indigo (10 Ω to yellow (290 Ω). **b)** $dV/dI(j, n_{\mathrm{mtBG}})$. Colormap indigo (0 Ω) to yellow (500 Ω).

$$D_{\mathrm{MA-tBG}} = \frac{1}{2\epsilon_0}\left(C_{\mathrm{eff}} V_{\mathrm{tg}} - C_{\mathrm{bg}} V_{\mathrm{bg}}\right) \tag{10.8}$$

Where $C_{\mathrm{eff}} = C_{\mathrm{m}} C_{\mathrm{mtBG}}/C_{\mathrm{q}}$ with C_{mtBG} the capacitance of the top bilayer. Similarly, n can be found as:

$$n_{\mathrm{MA-tBG}} = \frac{C_{\mathrm{eff}} V_{\mathrm{tg}} + C_{\mathrm{bg}} V_{\mathrm{bg}}}{e} \tag{10.9}$$

Here, I find C_{eff} =330 μF m^{-2}. Figure 10.7a shows the ρ_{xx} map of figure 10.5 rearranged in the $(n_{\mathrm{MB-tBG}}, D_{\mathrm{MA-tBG}})$ space. Here we find that the superconducting behaviour varies in a small range of n in an inverted 3 shape, as the resistance of the normal state changes with D. This is due to varying screening as a result of varying resistance of the top mtBG. More impressive, the superconductivity disappears above $D_{\mathrm{MA-tBG}} = 0.03\,\mathrm{V\,nm^{-1}}$ and below $-0.3\,\mathrm{V\,nm^{-1}}$. To the extent of my knowledge, this is the first time that such a field-dependence of superconductivity is reported, either in unscreened or screened magic-angle twisted bilayer graphene devices. This could result from enhanced screening in a narrow range of V_{tg}, as the resistance of the top mtBG is relatively low. As V_{tg} (and thus, $D_{\mathrm{MA-tBG}}$) is moved into a high-resistance region of mtBG, the electron screening is reduced, and the magnitude of the Coulomb interaction increases again to compete with the electron-phonon coupling and superconductivity is destroyed as the band is not flat enough. In the hypothesis of an unconventional behaviour of the superconducting pocket, screening would flatten the band, resulting in superconductivity, and as Coulomb screening is reduced at high D, the bandwidth would increase and superconductivity is destroyed.

To corroborate this hypothesis, figure 10.7b shows a $dV/dI(j, n_{\mathrm{mtBG}})$ map, giving more insights into the interplay between superconductivity and the Fermi velocity, and the influence of the density of state in the top bilayer. We find that the critical shift of the Fermi surface happens for j comparable to the superconducting switching current density j_{s} around 3 densities in the

top bilayer: $n_{\mathrm{ntBG}} = -1 \times 10^{12}\,\mathrm{cm}^{-2}$, $0.5 \times 10^{12}\,\mathrm{cm}^{-2}$ and $2.2 \times 10^{12}\,\mathrm{cm}^{-2}$. At high charge density, the superconductivity appears to be limited by the E-induced critical shift of the Fermi surface. This would be consistent with a restructuration of the Fermi surface leading to increased superconductivity under high screening, while the ground (unscreened) state corresponds to a metallic layer, consistent with unconventional superconductivity.

10.4 Superconductivity at the edge of the Fermi surface

We now focus on the peaks at high bias corresponding to the critical shift of the Fermi surface. Figure 10.8a shows the resistivity as a function of the current density j and the density $n_{\mathrm{MA-tBG}}$, close to $\nu = 2$. This corresponds to sweeping the back-gate across the brown line of figure 10.7a. For $n_{\mathrm{MA-tBG}}$ away from half-filling, the superconducting non-linearities are present for $|j| < 50\,\mathrm{nA\,\mu m}^{-1}$, consistent with the results above. Importantly, the switching current remains constant at all densities where a superconducting behaviour is observed. For carrier densities $n_{\mathrm{MA-tBG}} > 1.65 \times 10^{12}\,\mathrm{cm}^{-2}$, the critical shift of the Fermi surface happens at constant $j_{\mathrm{c}} \approx 200\,\mathrm{nA\,\mu m}^{-1}$. As the carrier density is tuned closer to half-filling, the j_{c} maxima decrease to form a zero-bias peak at half-filling.

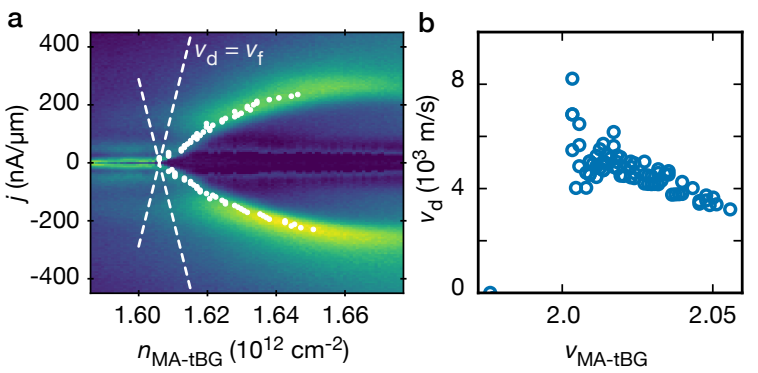

Fig. 10.8 Fermi-surface limited superconductivity. a) $dV/dI(n_{\mathrm{MA-tBG}}, j)$ along the brown line of figure 10.7a ($D = -0.15\,\mathrm{V\,cm}^{-1}$). Colour scale: indigo ($0\,\Omega$) to yellow ($400\,\Omega$). Dashed lines show the calculated Fermi velocity. **b)** extracted $v_{\mathrm{d}}(\nu_{\mathrm{MA-tBG}})$.

In such a system, it is relatively complicated to estimate theoretically the Fermi velocity owing to the influence of screening. In unscreened twisted bilayer graphene with a 1.23° twist angle, $v_{\mathrm{f}} = 3 \times 10^4\,\mathrm{m\,s}^{-1}$ close to charge neutrality and $4 \times 10^5\,\mathrm{m\,s}^{-1}$ at full filling [115]. However, as a flatter band emerge from interlayer hybridisation, the Fermi velocity is expected to be much lower close to half-filling. Figure 10.8a shows $j_{\mathrm{f}}(n_{\mathrm{MA-tBG}})$ corresponding to $v_{\mathrm{f}} = 3 \times 10^4\,\mathrm{m\,s}^{-1}$ as white dashed lines, an upper bound of the expected Fermi velocity. Indeed, it appears that the drift velocity v_{d} at $\nu = 2$ is much lower, as shown by the white dots in fig. 10.8a. In figure 10.8b, I show the corresponding v_{d}, in-

creasing as ν moves closer to 2 on the electron side and diverging for $\nu = 2$. Evidence of the flatter band is found through $v_\mathrm{d} \approx 4 \times 10^3\,\mathrm{m\,s^{-1}}$ that is an order of magnitude below estimations close to charge neutrality, but consistent with observations in magic-angle graphene [307]. At densities corresponding to hole-like doping of this correlated insulator, a zero-bias peak appears instead of a symmetric maximum. This behaviour is not yet understood and would necessitate further studies.

Interestingly, it appears that the zero-resistance behaviourattributed to unconventional superconductivity is destroyed when the critical current j_c, corresponding to out-of-equilibrium non-linear criticalities, reaches a current density close to the superconducting switching current j_s. This mechanism could open new directions to further the understanding of superconductivity in twisted bilayer graphene. Indeed it was suggested that the coincidence of j_s and j_c results from the same current-limiting mechanism in the superconducting and normal state, which means that the group velocity limit in the Dirac fluid would also limit the current density in the superconducting phase [307]. For completeness, let me mention an alternative explanation: the critical shift of the Fermi surface could correspond to a feature of the top bilayer. This possibility was ruled out as the variation of the gate was chosen so that it does not cross any resistance peak attributed to the top mtBG, and therefore change in the density of states from the top twisted bilayer graphene.

Conclusion

In this chapter, I introduced a new system to study the influence of screening and parallel bands on superconductivity, based on high-angle van der Waals heterostructures. The addition of a graphene bilayer at a large angle on top of a twisted bilayer close to the magic angle results in increased Coulomb screening in a narrow range of top gate voltage, thus inducing superconductivity for a finite range of displacement fields. The superconductivity was found to share unconventional characteristics, therefore increased Coulomb screening is likely to flatten the band, leading to the emergence of correlated insulators and superconducting pockets. Still, the superconducting switching current appears to be limited by the Fermi velocity, a limiting mechanism similar to relativistic superfluids [322]. This kind of high-angle structure can be generalised to potentially any stack and allow further studies on the influence of screening and parallel systems on strongly correlated states.

Blank page

Chapter 11
Summary

In this thesis, I demonstrated several novel transport phenomena unique to graphene heterostructures. Even eighteen years after the discovery of graphene, when most of the field has been ploughed and harrowed, there is still room for emerging physics if one chooses not to dig deeper but rather start forming one's own furrow on the other side of the fence. Here, a few factors enabled new research: improvement of fabrication techniques, access to ultra-low temperatures, and the creation of novel heterostructures with different twist angles.

The improved fabrication techniques and availability of high-quality samples with high mobility allowed us to reduce the disorder and lift all degeneracies. It enabled observation of high-mobility Brown-Zak fermions (chapter 6) and further understanding of the Hofstadter's butterfly (chapter 7). Accessing low temperatures with a dilution refrigerator to measure high-quality samples allowed us to lift all the degeneracies of Brown-Zak fermions (BZF). On this matter, I observed for the first time a few features such as mini-Landau fans of BZF evolving into bent trajectories or staircase-like characteristics.

More importantly, creating new kinds of heterostructures allowed me to observe other effects. For example, a significant part of the research on graphene heterostructures in the past four years focused on magic-angle devices. Instead of making similar devices, we chose to explore much smaller angles, i.e. minimally twisted bilayer graphene (mtBG), where the lattice reconstructs, creating a network of topologically protected channels. The use of superconducting leads to induce a proximity effect in mtBG domain walls (chapter 8 revealed the persistence of supercurrent in impressively high magnetic fields. When graphene sheets are twisted with slighly larger angles, the two Dirac cones are spaced in momentum close enough so that the neighbouring bands hybridise into flat bands, a harbinger of unique phenomena. I explored a different system combining two heterogeneous band structures: twisted monolayer bilayer graphene (tMBG, chapter 9). In this system, flat bands result in the emergence of correlated insulators at integer fillings of the conduction band upon application of a displacement field. I explored the anomalous Hall effect in these states and their Fermi velocity in a non-linear transport regime. Fi-

nally, I explored another system: high angle twisted tetralayer graphene, where the high angle decouples two bilayer subsystems and screens the Coulomb interaction (chapter 10). It results in superconductivity in a finite range of displacement fields. I explored this regime and its limitation when the Fermi velocity becomes comparable to the superconducting condensate velocity.

As for future works, fundamental questions remain. Some of them would only be answered through incremental advances. In the case of Brown-Zak fermions, for example, we still understand poorly the bending of the Landau levels and the staircase-like features at high magnetic fields. In this case, theoretical studies should be essential to identify possible mechanisms. In the same system, other directions would also deserve a more careful look: how do the high-conductivity slanted streaks emerge? High-order BZFs certainly play a role in forming these states. What is the Landau quantisation of secondary Dirac fermions and their Berry phase? So far, we lack experimental evidence. There is no question that the combination of large, high-quality devices and ultra-low temperatures will be instrumental in answering these questions. Concerning the other projects (proximity superconductivity in the 1D topological network of mtBG, correlated states of tMBG or superconductivity in tetralayer graphene), one can imagine fundamental developments. For example, the proximitised helical states can be a basis for topologically protected superconducting qubits. Another idea would consist in inducing spin-orbit coupling through proximity with a heavy metal, for example, by adding transition metal dichalcogenides to the stack. What happens in this system if the spin-degeneracy of the domain walls is lifted? As for the correlated states of mtBG, one can imagine inducing superconductivity into the stack via proximity with a superconducting finger to explore the interplay of anomalous Hall effect and superconductivity. The diversity of potential studies with high-angle heterostructure is unlimited. For example, one may imagine twisting two magic-angle graphene layers at a high angle. What would be the resulting feature? What about two mtBG layers stacked with a high angle? Could it create a high-order topological network? Based on this thesis, the possibilities of potential experimental systems and research directions are infinite, so the experienced reader will undoubtedly come up with their own idea.

Appendix A
Fabrication of mesoscopic devices

The results presented in this thesis come after significant efforts to improve the fabrication of van der Waals heterostructure. Good contacts are necessary to observe the desired results. For example, high contact resistance can blur the observation of low resistance features; low-transparency graphene-superconductor interfaces can hamper observation of the zero resistance. Fabrication of suitable interfaces is a relatively complex method explained here. In this appendix, I use the following acronyms:

PDMS polydimethylsiloxane
PMMA polymethyl methacrylate
PPC polypropylene carbonate

A.1 Exfoliation

Two-dimensional materials — a fortiori graphene — are extracted from a parent bulk compound, consisting of multiple layers bound together by van der Waals forces. These interlayer forces are weak compared to the in-plane covalent bonds (or ionic for some compounds), making the different layers easily peeled off from one another with various physical or chemical methods. The highest quality yield stems from micromechanical exfoliation.

Exfoliation involves using low-tack adhesive tape[1] to exfoliate the material and cleaved it onto silicon-oxide substrates. To do so, a piece of tape is placed onto a layered material to peel off the first few layers and then repeatedly folded on itself to thin down the layers stuck to the adhesive. Next, the tape is brought in contact with a clean substrate, such as a Si/SiO_2 wafer. The tape is

During my PhD, I spent the first 6 months fabricating devices, which did not yield any data presented in this thesis. The following section lists the method I used, and combines information from other people who fabricated the devices shown in this thesis.

[1] Low-tack is generally used for graphene/hBN, while high-tack can exfoliate more fragile materials such as transition metal dichalcogenides.

then slowly peeled from the substrate to leave a freshly cleaved material on top of it. There are a few parameters that influence the quality and the maximum lateral dimensions of monolayers. First, the size of the parent crystal limits the maximum layer size. A second limiting factor is the crystal adhesion to a substrate and the easiness of release from the tape. Controlling the depositon- or peel-angle can avoid this limit. Third, the substrate-crystal surface chemistry may influence the quality of the exfoliated layers. Plasma/O_2 activation can enhance it. Fourth, there are other less controlled factors, like surface roughness of the substrate or humidity conditions. The most important here is the parent bulk crystal's quality and low defect density. Graphene is exfoliated from highly oriented pyrolitic graphite from NGS Naturgraphit GmbH. hBN crystals are grown by Kenji Watanabe and Takashi Taniguchi [88].

The resulting crystals can then be identified and selected through visible light optical microscopy. The optical contrast of 2D materials is seen through Fabry-Pérot cavities between the 2D material and the dielectric (SiO_2 layer). Graphene monolayers are most visible for oxide substrates of thickness $\sim$290 nm. Additionally, green band-pass filters can improve the optical contrast. With these techniques, it is possible to select flakes depending upon their thicknesses, as different thicknesses have different absorption or refraction coefficients to incident light. When the colour contrast is not enough to distinguish flakes of different thicknesses, one can use Raman spectroscopy or atomic force microscopy to identify the different layer thicknesses.

The exfoliation with adhesives may leave some residues on the 2D materials. This contamination prevents one from obtaining atomically thin interfaces while stacking different layers; it may create bubbles or cracks, or limit electronic properties. There are a few methods to clean the stacks. Annealing at 300 °C to 500 °C in an inert gas (H_2, Ar) or vacuum for several hours would vaporise or decompose most contaminants. This works well for hBN, but other 2D materials may not be stable at such high temperatures. Graphene, for example, may detach from the SiO_2 substrate and roll-up. Another method uses contact-mode AFM to clean the material by scanning the tip. It is, however, a rarely used process as very lengthy. Finally, the encapsulation of flakes within hBN results in a *self-cleaning* mechanism, agglomerating impurities into bubbles, allowing one to pattern a device into bubble-free areas.

A.2 Stacking

Vertical assembly of van der Waals heterostructures is performed using a micromanipulator system consisting of the following. A rotating hotplate is placed on an X-Y micrometre stage under an optical microscope. A transfer arm is placed between the microscope optics and the heating stage and is attached

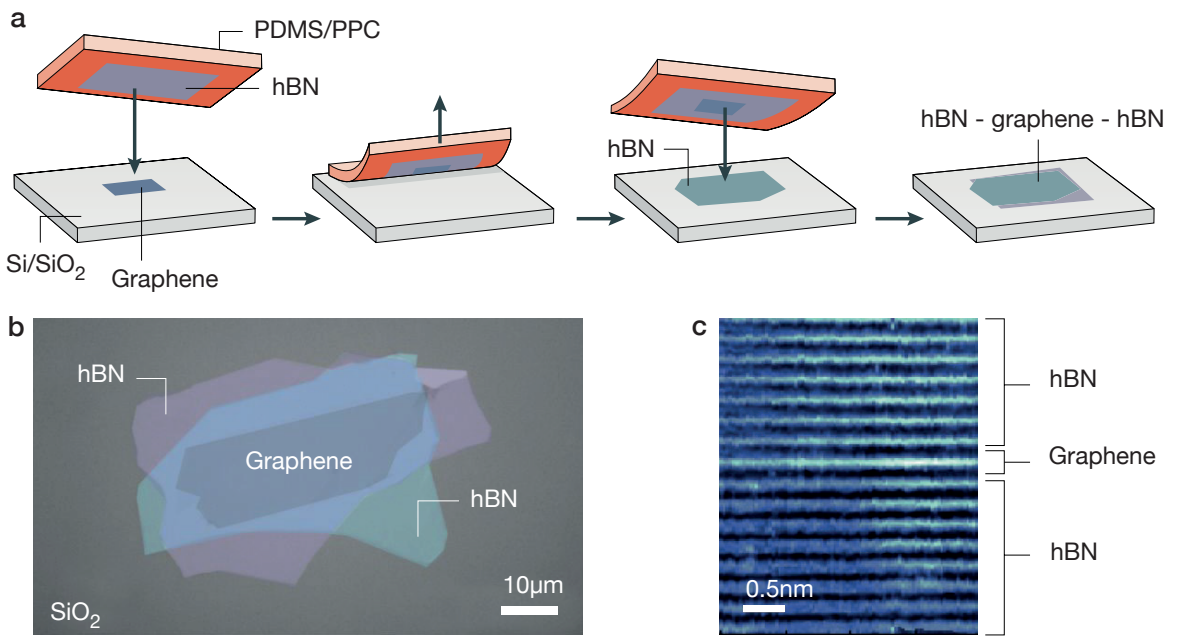

Fig. A.1: Fabrication of van der Waals heterostructures a) polymer stamping technique used to pick-up and assemble the different flakes sequentially. **b)** optical micrograph of a completed stack of graphene encapsulated between two hBN flakes. **c)** high-resolution transmission electron micrograph of hBN-graphene-hBN stack. Figure adapted from refs [87, 160].

to an X-Y-Z micrometre stage. Once graphene and hBN crystals are exfoliated separately on appropriate substratse, they can be picked up using a PPC polymer film on a PDMS elastomer stamp. This stamp can easily be realised on a microscope slide attached to the transfer arm so that the flake pick-up can be seen under the microscope (see fig. A.1a). This stamp allows for peeling an hBN flake directly off the SiO_2 substrate and henceforth placed over a graphene flake and brought in contact with it. Heating the graphene's SiO_2 substrate favours van der Waals adhesion between the hBN flake and the graphene layer. Graphene is peeled off its substrate when the elastomer stamp is moved up. This stack can then be placed on top of another material to compose a complex van der Waals heterostructure. The composite structure can later be deposited on a pristine Si/SiO_2 wafer for device processing. Figure A.1b shows an example of a simple van der Waals heterostructure. Figure A.1c shows a section of the heterostructure, resulting in an atomically sharp, impurity-free interface.

A.3 Lithography and contact deposition

Metal leads need to contact the van der Waals heterostructures for the sake of electronic measurements. 1D edge contacts have substantially lower contact resistance than the standard surface contact [91,160]. Therefore this technique is essentially used for the devices presented in this thesis. A positive resist such

as PMMA is used. Upon irradiation, it will undergo chain scission, lowering the cross-link density and increasing the resist embrittlement. After coating the substrate-heterostructure device, e-beam lithography with an EVO-MA10 scanning electron microscope is performed to selectively expose the resist, with a resolution limited to 50 nm to 100 nm. In order to minimise the lithography time, small and large parts of the contacts are exposed separately so that the beam dose is adjusted for varying resulution. Several factors affect the sharpness and the resolution of the final exposed pattern. The most important is electrons scattering through the resist, broadening the exposed region. This lowers the resolution but, in turn, makes the lift-off step easier: carefully selecting the resist thickness is necessary.

In order to optimise the undercut profile and the resolution of the exposed trenches, two resist with different molecular weights are used. The first layer is a solution containing 3 % 495K PMMA, spin-coated at 3000 rpm and annealed at 150 °C for 5 min. The second layer is a solution containing 3 % 950K PMMA and is spin-coated using the same conditions. The combined thickness of the resist is ∼220 nm. The large molecular weight layer acts as a buffer to limit the electron scattering in the underneath layer.

Contacts can then be developed into a 3:1 mixture of IPA and deionised water. Placing the device in a beaker for 30 s is sufficient to dissolve and wash away the regions with lower cross-linking. The device is then cleaned for 30 s in IPA and blown with nitrogen. Metal is then deposited in the contact trenches. There are different techniques: thermal evaporation, e-beam evaporation and sputtering. E-beam evaporation is the method with the highest purity and thus lowest contact resistance. We use a Moorfield e-beam evaporation system to direct an electron beam at a metal target under a high vacuum ($<5\times10^{-6}$ mbar). The kinetic energy of electrons is converted into thermal energy, causing sublimation of the metal. The generated metal vapour is then condensed onto the sample. Chromium is first used as a thin (3 nm to 5 nm) adhesion-enhancing layer before gold or other superconducting metals (40 nm). For usual devices, gold gives good contact to graphene; therefore is the most common choice. Superconductors enabling high-transparency Josephson junctions are MoRe or NbTi. The last fabrication step is the lift-off: the PMMA resist is dissolved in acetone for ∼1 h, removing the metal layer above it. The stack is transferred in IPA for cleaning and dried with nitrogen gas.

References

1. C. Kittel, *Introduction to solid state physics Eighth edition* (Wiley, 2005)
2. N.W. Ashcroft, N.D. Mermin, *Solid state physics* (Holt-Saunders, 1976)
3. D. Pines, P. Nozières, *Theory of quantum liquids, v1. Normal Fermi liquids* (Addison-Wesley, 1998)
4. S. Datta, *Electronic transport in mesoscopic systems* (Cambridge University Press, 1997)
5. Y. Imry, *Introduction to mesoscopic physics*. 2 (Oxford University Press, 2002)
6. C.W.J. Beenakker, H. van Houten, in *Solid State Physics*, vol. 44 (Elsevier, 1991), pp. 1–228
7. Y. Aharonov, D. Bohm, Physical Review **115**(3), 485 (1959)
8. D.Y. Sharvin, Y.V. Sharvin, JETP Lett **34**(272) (1981)
9. R.A. Webb, S. Washburn, C. Umbach, R. Laibowitz, Physical Review Letters **54**(25), 2696 (1985)
10. L.D. Landau, E.M. Lifshitz, L.P. Pitaevskii, *Statistical physics Part 2 - The theory of the condensed state*, vol. 9 (Pergamon Press, 1980)
11. D. Schoenberg, *Magnetic oscillations in metals* (Cambridge University Press, 1984)
12. M. Tinkham, *Introduction to superconductivity* (Courier Corporation, 2004)
13. G. Deutscher, P. De Gennes, in *Superconductivity*, vol. 2, ed. by R. Parks (Marcel Dekker, New York, 1969), chap. 17, p. 1005
14. C. Enss, S. Hunklinger, *Low-Temperature Physics* (Springer, 2005)
15. K.v. Klitzing, G. Dorda, M. Pepper, Physical review letters **45**(6), 494 (1980)
16. A.K. Geim, I.V. Grigorieva, Nature **499**(7459), 419 (2013)
17. A.F. Young, Y. Zhang, P. Kim, in *Physics of Graphene*, ed. by H. Aoki, M.S. Dresselhaus (Springer, 2014), pp. 3–27
18. K. Novoselov, A. Mishchenko, A. Carvalho, A. Castro Neto, Science **353**(6298) (2016)
19. J. Barrier, P. Kumaravadivel, R. Krishna-Kumar, L.A. Ponomarenko, N. Xin, M. Holwill, C. Mullan, M. Kim, R.V. Gorbachev, M.D. Thompson, J.R. Prance, T. Taniguchi, K. Watanabe, I.V. Grigorieva, K.S. Novoselov, A. Mishchenko, V.I. Fal'ko, A.I. Berdyugin, A.K. Geim, Nature Communications **11**, 5756 (2020)
20. S. Xu, M.M. Al Ezzi, N. Balakrishnan, A. Garcia-Ruiz, B. Tsim, C. Mullan, J. Barrier, N. Xin, B.A. Piot, T. Taniguchi, et al., Nature Physics **17**(5), 619 (2021)
21. B. Van Wees, H. Van Houten, C. Beenakker, J.G. Williamson, L. Kouwenhoven, D. Van der Marel, C. Foxon, Physical Review Letters **60**(9), 848 (1988)
22. M. Roukes, A. Scherer, S. Allen Jr, H.G. Craighead, R. Ruthen, E. Beebe, J. Harbison, Physical review letters **59**(26), 3011 (1987)
23. H.U. Baranger, A.D. Stone, Physical Review Letters **63**(4), 414 (1989)
24. C. Beenakker, H. Van Houten, Physical Review B **39**(14), 10445 (1989)

25. C. Ford, S. Washburn, M. Büttiker, C. Knoedler, J. Hong, Physical Review Letters **62**(23), 2724 (1989)
26. Y. Takagaki, K. Gamo, S. Namba, S. Ishida, S. Takaoka, K. Murase, K. Ishibashi, Y. Aoyagi, Solid State Communications **68**(12), 1051 (1988)
27. G. Timp, H. Baranger, P. DeVegvar, J. Cunningham, R. Howard, R. Behringer, P. Mankiewich, Physical Review Letters **60**(20), 2081 (1988)
28. C. Beenakker, H. Van Houten, Physical Review Letters **63**(17), 1857 (1989)
29. H. Van Houten, C. Beenakker, J. Williamson, M. Broekaart, P. Van Loosdrecht, B. Van Wees, J. Mooij, C. Foxon, J. Harris, Physical Review B **39**(12), 8556 (1989)
30. J. Spector, H. Stormer, K. Baldwin, L. Pfeiffer, K. West, Surface Science **228**, 283 (1990)
31. G. Blonder, M. Tinkham, T. Klapwijk, Physical Review B **25**(7), 4515 (1982)
32. B. Pannetier, H. Courtois, Journal of Low Temperature Physics **118**(5), 599 (2000)
33. T. Klapwijk, Journal of Superconductivity **17**(5), 593 (2004)
34. P.G. De Gennes, *Superconductivity of metals and alloys* (Westview Press, 1966)
35. B.D. Josephson, Reviews of Modern Physics **46**(2), 251 (1974)
36. M. Ben Shalom, M. Zhu, V. Fal'ko, A. Mishchenko, A. Kretinin, K. Novoselov, C. Woods, K. Watanabe, T. Taniguchi, A. Geim, J. Prance, Nature Physics **12**(4), 318 (2016)
37. V. Ambegaokar, A. Baratoff, Physical Review Letters **10**(11), 486 (1963)
38. R. Meservey, B. Schwartz, in *Superconductivity*, vol. 1, ed. by R. Parks (Marcel Dekker, New York, 1969), chap. 3, p. 141
39. I. Giaever, H. Hart Jr, K. Megerle, Physical Review **126**(3), 941 (1962)
40. P. Dubos, H. Courtois, B. Pannetier, F. Wilhelm, A. Zaikin, G. Schön, Physical Review B **63**(6), 064502 (2001)
41. M.D. Thompson, M. Ben Shalom, A. Geim, A. Matthews, J. White, Z. Melhem, Y.A. Pashkin, R.P. Haley, J.R. Prance, Applied Physics Letters **110**(16), 162602 (2017)
42. J. Rowell, Physical Review Letters **11**(5), 200 (1963)
43. I. Krylov, Y.V. Sharvin, Journal of Experimental and Theoretical Physics **64**, 946 (1973)
44. F. Giazotto, M. Governale, U. Zülicke, F. Beltram, Physical Review B **72**(5), 054518 (2005)
45. S. Shapiro, Physical Review Letters **11**(2), 80 (1963)
46. D. DiVincenzo, E. Mele, Physical Review B **29**(4), 1685 (1984)
47. G.W. Semenoff, Physical Review Letters **53**(26), 2449 (1984)
48. F.D.M. Haldane, Physical Review Letters **61**(18), 2015 (1988)
49. P.R. Wallace, Physical Review **71**(9), 622 (1947)
50. A.H. Castro Neto, F. Guinea, N.M.R. Peres, K.S. Novoselov, A.K. Geim, Reviews of Modern Physics **81**(1), 109 (2009)
51. K.S. Novoselov, A.K. Geim, S.V. Morozov, D. Jiang, Y. Zhang, S.V. Dubonos, I.V. Grigorieva, A.A. Firsov, Science **306**(5696), 666 (2004)
52. K.S. Novoselov, D. Jiang, F. Schedin, T. Booth, V. Khotkevich, S. Morozov, A.K. Geim, Proceedings of the National Academy of Sciences **102**(30), 10451 (2005)
53. K.S. Novoselov, A.K. Geim, S.V. Morozov, D. Jiang, M.I. Katsnelson, I. Grigorieva, S. Dubonos, A. Firsov, Nature **438**(7065), 197 (2005)
54. Y. Zhang, Y.W. Tan, H.L. Stormer, P. Kim, Nature **438**(7065), 201 (2005)
55. R.S. Deacon, K.C. Chuang, R.J. Nicholas, K.S. Novoselov, A.K. Geim, Physical Review B **76**(8), 081406 (2007)
56. J. Avila, I. Razado, S. Lorcy, R. Fleurier, E. Pichonat, D. Vignaud, X. Wallart, M.C. Asensio, Scientific Reports **3**(1), 1 (2013)

57. G. Mikitik, Y.V. Sharlai, Physical Review Letters **82**(10), 2147 (1999)
58. Y. Zheng, T. Ando, Physical Review B **65**(24), 245420 (2002)
59. V. Gusynin, S. Sharapov, Physical Review Letters **95**(14), 146801 (2005)
60. N.M.R. Peres, F. Guinea, A.H. Castro Neto, Annals of Physics **321**(7), 1559 (2006)
61. H. Suzuura, T. Ando, Physical Review Letters **89**(26), 266603 (2002)
62. F. Tikhonenko, D. Horsell, R. Gorbachev, A. Savchenko, Physical Review Letters **100**(5), 056802 (2008)
63. R.V. Gorbachev, J.C.W. Song, G.L. Yu, A.V. Kretinin, F. Withers, Y. Cao, A. Mishchenko, I.V. Grigorieva, K.S. Novoselov, L.S. Levitov, A.K. Geim, Science **346**(6208), 448 (2014)
64. K.S. Novoselov, E. McCann, S.V. Morozov, V.I. Fal'ko, M.I. Katsnelson, U. Zeitler, D. Jiang, F. Schedin, A.K. Geim, Nature Physics **2**(3), 177 (2006)
65. E. McCann, V.I. Fal'ko, Physical Review Letters **96**(8), 086805 (2006)
66. E. McCann, Physical Review B **74**(16), 161403 (2006)
67. J.B. Oostinga, H.B. Heersche, X. Liu, A.F. Morpurgo, L.M. Vandersypen, Nature Materials **7**(2), 151 (2008)
68. Y. Zhang, T.T. Tang, C. Girit, Z. Hao, M.C. Martin, A. Zettl, M.F. Crommie, Y.R. Shen, F. Wang, Nature **459**(7248), 820 (2009)
69. F. Xia, D.B. Farmer, Y.m. Lin, P. Avouris, Nano Letters **10**(2), 715 (2010)
70. K. Zou, J. Zhu, Physical Review B **82**(8), 081407 (2010)
71. T. Taychatanapat, P. Jarillo-Herrero, Physical Review Letters **105**(16), 166601 (2010)
72. J. Yan, M.S. Fuhrer, Nano Letters **10**(11), 4521 (2010)
73. Y.D. Lensky, J.C.W. Song, P. Samutpraphoot, L.S. Levitov, Physical Review Letters **114**(25), 256601 (2015)
74. G. Kirczenow, Physical Review B **92**(12), 125425 (2015)
75. M. Sui, G. Chen, L. Ma, W.Y. Shan, D. Tian, K. Watanabe, T. Taniguchi, X. Jin, W. Yao, D. Xiao, Y. Zhang, Nature Physics **11**(12), 1027 (2015)
76. Y. Shimazaki, M. Yamamoto, I.V. Borzenets, K. Watanabe, T. Taniguchi, S. Tarucha, Nature Physics **11**(12), 1032 (2015)
77. L. Ju, Z. Shi, N. Nair, Y. Lv, C. Jin, J. Velasco, C. Ojeda-Aristizabal, H.A. Bechtel, M.C. Martin, A. Zettl, J. Analytis, F. Wang, Nature **520**(7549), 650 (2015)
78. J. Li, K. Wang, K.J. McFaul, Z. Zern, Y. Ren, K. Watanabe, T. Taniguchi, Z. Qiao, J. Zhu, Nature Nanotechnology **11**(12), 1060 (2016)
79. J. Li, R.X. Zhang, Z. Yin, J. Zhang, K. Watanabe, T. Taniguchi, C. Liu, J. Zhu, Science **362**(6419), 1149 (2018)
80. T.L.M. Lane, M. Andjelković, J.R. Wallbank, L. Covaci, F.M. Peeters, V.I. Fal'ko, Physical Review B **97**(4), 045301 (2018)
81. H. Zhou, L. Holleis, Y. Saito, L. Cohen, W. Huynh, C.L. Patterson, F. Yang, T. Taniguchi, K. Watanabe, A.F. Young, Science **375**, 774 (2022)
82. Y. Lee, S. Che, J. Velasco Jr, D. Tran, J. Baima, F. Mauri, M. Calandra, M. Bockrath, C.N. Lau, arXiv preprint arXiv:1911.04450 (2019)
83. A. Kerelsky, C. Rubio-Verdú, L. Xian, D.M. Kennes, D. Halbertal, N. Finney, L. Song, S. Turkel, L. Wang, K. Watanabe, T. Taniguchi, J. Hone, C.R. Dean, D.N. Basov, A. Rubio, A.N. Pasupathy, Proceedings of the National Academy of Sciences **118**(4) (2021)
84. Y. Shi, S. Xu, Y. Yang, S. Slizovskiy, S.V. Morozov, S.K. Son, S. Ozdemir, C. Mullan, J. Barrier, J. Yin, A.I. Berdyugin, B.A. Piot, T. Taniguchi, K. Watanabe, V.I. Fal'ko, K.S. Novoselov, A.K.G. Geim, A. Mishchenko, Nature **584**, 210 (2020)
85. H. Zhou, T. Xie, A. Ghazaryan, T. Holder, J.R. Ehrets, E.M. Spanton, T. Taniguchi, K. Watanabe, E. Berg, M. Serbyn, A.F. Young, Nature **598**(7881), 429 (2021)

86. H. Zhou, T. Xie, T. Taniguchi, K. Watanabe, A.F. Young, Nature **598**(7881), 434 (2021)
87. M. Yankowitz, Q. Ma, P. Jarillo-Herrero, B.J. LeRoy, Nature Reviews Physics **1**(2), 112 (2019)
88. K. Watanabe, T. Taniguchi, H. Kanda, Nature Materials **3**(6), 404 (2004)
89. P. Zomer, S. Dash, N. Tombros, B. Van Wees, Applied Physics Letters **99**(23), 232104 (2011)
90. C.R. Dean, A.F. Young, I. Meric, C. Lee, L. Wang, S. Sorgenfrei, K. Watanabe, T. Taniguchi, P. Kim, K.L. Shepard, J. Hone, Nature Nanotechnology **5**(10), 722 (2010)
91. A.S. Mayorov, R.V. Gorbachev, S.V. Morozov, L. Britnell, R. Jalil, L.A. Ponomarenko, P. Blake, K.S. Novoselov, K. Watanabe, T. Taniguchi, A.K. Geim, Nano Letters **11**(6), 2396 (2011)
92. L. Ponomarenko, A. Geim, A. Zhukov, R. Jalil, S. Morozov, K. Novoselov, I. Grigorieva, E. Hill, V. Cheianov, V. Fal'Ko, K. Watanabe, T. Taniguchi, R.V. Gorbachev, Nature Physics **7**(12), 958 (2011)
93. I. Meric, C.R. Dean, N. Petrone, L. Wang, J. Hone, P. Kim, K.L. Shepard, Proceedings of the IEEE **101**(7), 1609 (2013)
94. G.H. Lee, Y.J. Yu, C. Lee, C. Dean, K.L. Shepard, P. Kim, J. Hone, Applied Physics Letters **99**(24), 243114 (2011)
95. L. Britnell, R.V. Gorbachev, R. Jalil, B.D. Belle, F. Schedin, M.I. Katsnelson, L. Eaves, S.V. Morozov, A.S. Mayorov, N.M. Peres, A.H. Castro Neto, J. Leist, A.K. Geim, L.A. Ponomarenko, K.S. Novoselov, Nano Letters **12**(3), 1707 (2012)
96. L. Britnell, R.V. Gorbachev, A.K. Geim, L.A. Ponomarenko, A. Mishchenko, M.T. Greenaway, T.M. Fromhold, K.S. Novoselov, L. Eaves, Nature Communications **4**(1), 1 (2013)
97. A. Mishchenko, J. Tu, Y. Cao, R.V. Gorbachev, J. Wallbank, M. Greenaway, V. Morozov, S. Morozov, M. Zhu, S. Wong, , F. Withers, C.R. Woods, Y.J. Kim, K. Watanabe, T. Taniguchi, E.E. Vdovin, O. Makarovsky, T.M. Fromhold, V.I. Fal'ko, A.K. Geim, L. Eaves, K.S. Novoselov, Nature Nanotechnology **9**(10), 808 (2014)
98. X. Liu, K. Watanabe, T. Taniguchi, B.I. Halperin, P. Kim, Nature Physics **13**(8), 746 (2017)
99. J. Li, T. Taniguchi, K. Watanabe, J. Hone, C. Dean, Nature Physics **13**(8), 751 (2017)
100. X. Liu, J. Li, K. Watanabe, T. Taniguchi, J. Hone, B.I. Halperin, P. Kim, C.R. Dean, Science **375**(6577), 205 (2022)
101. P. Kumaravadivel, M.T. Greenaway, D. Perello, A.I. Berdyugin, J. Birkbeck, J. Wengraf, S. Liu, J.H. Edgar, A.K. Geim, L. Eaves, R. Krishna Kumar, Nature communications **10**(3334) (2019)
102. M.T. Greenaway, P. Kumaravadivel, J. Wengraf, L.A. Ponomarenko, A.I. Berdyugin, J. Li, J.H. Edgar, R. Krishna Kumar, A.K. Geim, L. Eaves, Nature Communications **12**(6392) (2021)
103. L. Esaki, R. Tsu, IBM Journal of Research and Development **14**(1), 61 (1970)
104. S.C. Chen, R. Kraft, R. Danneau, K. Richter, M.H. Liu, Communications Physics **3**(71) (2020)
105. J.R. Wallbank, A.A. Patel, M. Mucha-Kruczyński, A.K. Geim, V.I. Fal'Ko, Physical Review B **87**(24), 245408 (2013)
106. M. Yankowitz, J. Xue, D. Cormode, J.D. Sanchez-Yamagishi, K. Watanabe, T. Taniguchi, P. Jarillo-Herrero, P. Jacquod, B.J. LeRoy, Nature Physics **8**(5), 382 (2012)

107. L.A. Ponomarenko, R.V. Gorbachev, G.L. Yu, D.C. Elias, R. Jalil, A.A. Patel, A. Mishchenko, A.S. Mayorov, C.R. Woods, J.R. Wallbank, M. Mucha-Kruczyński, B.A. Piot, M. Potemski, I.V. Grigorieva, K.S. Novoselov, F. Guinea, F.V. I, A.K. Geim, Nature **497**(7451), 594 (2013)
108. C.R. Dean, L. Wang, P. Maher, C. Forsythe, F. Ghahari, Y. Gao, J. Katoch, M. Ishigami, P. Moon, M. Koshino, T. Taniguchi, K. Watanabe, K. Shepard, J. Hone, P. Kim, Nature **497**(7451), 598 (2013)
109. B. Hunt, J.D. Sanchez-Yamagishi, A.F. Young, M. Yankowitz, B.J. LeRoy, K. Watanabe, T. Taniguchi, P. Moon, M. Koshino, P. Jarillo-Herrero, R.C. Ashoori, Science **340**(6139), 1427 (2013)
110. G. Yu, R. Gorbachev, J. Tu, A. Kretinin, Y. Cao, R. Jalil, F. Withers, L. Ponomarenko, B. Piot, M. Potemski, D.C. Elias, X. Chen, K. Watanabe, T. Taniguchi, I. Grigorieva, K.S. Novoselov, V.I. Fal'ko, A.K. Geim, A. Mishchenko, Nature Physics **10**(7), 525 (2014)
111. M. Diez, J. Dahlhaus, M. Wimmer, C. Beenakker, Physical Review Letters **112**(19), 196602 (2014)
112. L. Wang, Y. Gao, B. Wen, Z. Han, T. Taniguchi, K. Watanabe, M. Koshino, J. Hone, C.R. Dean, Science **350**(6265), 1231 (2015)
113. E.M. Spanton, A.A. Zibrov, H. Zhou, T. Taniguchi, K. Watanabe, M.P. Zaletel, A.F. Young, Science **360**(6384), 62 (2018)
114. C. Ortix, L. Yang, J. van den Brink, Physical Review B **86**(8), 081405 (2012)
115. A.I. Berdyugin, N. Xin, H. Gao, S. Slizovskiy, Z. Dong, S. Bhattacharjee, P. Kumaravadivel, S. Xu, L.A. Ponomarenko, M. Holwill, D.A. Bandurin, M. Kim, Y. Cao, M.T. Greenaway, K.S. Novoselov, I.V. Grigorieva, K. Watanabe, T. Taniguchi, V.I. Fal'ko, L.S. Levitov, R. Krishna Kumar, A.K. Geim, Science **375**(6579), 430 (2022)
116. W. Kohn, J. Luttinger, Physical Review Letters **15**(12), 524 (1965)
117. I.Y. Pomeranchuk, Soviet physics, JETP **8**, 361 (1958)
118. Y. Kim, P. Herlinger, P. Moon, M. Koshino, T. Taniguchi, K. Watanabe, J.H. Smet, Nano Letters **16**(8), 5053 (2016)
119. S. Wu, Z. Zhang, K. Watanabe, T. Taniguchi, E.Y. Andrei, Nature Materials **20**(4), 488 (2021)
120. A.V. Maharaj, I. Esterlis, Y. Zhang, B. Ramshaw, S. Kivelson, Physical Review B **96**(4), 045132 (2017)
121. C.R. Woods, L. Britnell, A. Eckmann, R.S. Ma, J.C. Lu, H.M. Guo, X. Lin, G.L. Yu, Y. Cao, R.V. Gorbachev, A.V. Kretinin, P. J, L.A. Ponomarenko, M.I. Katsnelson, Y.N. Gornostyrev, K. Watanabe, T. Taniguchi, C. Casiraghi, H.J. Gao, A.K. Geim, K.S. Novoselov, Nature Physics **10**(6), 451 (2014)
122. J. Li, C. Tan, S. Chen, Y. Zeng, T. Taniguchi, K. Watanabe, J. Hone, C. Dean, Science **358**(6363), 648 (2017)
123. A.A. Zibrov, C. Kometter, H. Zhou, E. Spanton, T. Taniguchi, K. Watanabe, M. Zaletel, A. Young, Nature **549**(7672), 360 (2017)
124. A.L. Sharpe, E.J. Fox, A.W. Barnard, J. Finney, K. Watanabe, T. Taniguchi, M. Kastner, D. Goldhaber-Gordon, Science **365**(6453), 605 (2019)
125. M. Serlin, C.L. Tschirhart, H. Polshyn, Y. Zhang, J. Zhu, K. Watanabe, T. Taniguchi, L. Balents, A.F. Young, Science **367**(6480), 900 (2020)
126. G. Chen, L. Jiang, S. Wu, B. Lyu, H. Li, B.L. Chittari, K. Watanabe, T. Taniguchi, Z. Shi, J. Jung, Y. Zhang, F. Wang, Nature Physics **15**(3), 237 (2019)
127. G. Chen, A.L. Sharpe, P. Gallagher, I.T. Rosen, E.J. Fox, L. Jiang, B. Lyu, H. Li, K. Watanabe, T. Taniguchi, , J. Jung, Z. Shi, D. Goldhaber-Gordon, Y. Zhang, F. Wang, Nature **572**(7768), 215 (2019)

128. G. Chen, A.L. Sharpe, E.J. Fox, Y.H. Zhang, S. Wang, L. Jiang, B. Lyu, H. Li, K. Watanabe, T. Taniguchi, Z. Shi, T. Senthil, D. Goldaber-Gordon, Y. Zhang, F. Wang, Nature **579**(7797), 56 (2020)
129. K. Uchida, S. Furuya, J.I. Iwata, A. Oshiyama, Physical Review B **90**(15), 155451 (2014)
130. N.N. Nam, M. Koshino, Physical Review B **96**(7), 075311 (2017)
131. H. Yoo, R. Engelke, S. Carr, S. Fang, K. Zhang, P. Cazeaux, S.H. Sung, R. Hovden, A.W. Tsen, T. Taniguchi, K. Watanabe, G.C. Yi, M. Kim, M. Luskin, E.B. Tadmor, E. Kaxiras, P. Kim, Nature Materials **18**(5), 448 (2019)
132. S. Huang, K. Kim, D.K. Efimkin, T. Lovorn, T. Taniguchi, K. Watanabe, A.H. MacDonald, E. Tutuc, B.J. LeRoy, Physical Review Letters **121**(3), 037702 (2018)
133. P. Rickhaus, J. Wallbank, S. Slizovskiy, R. Pisoni, H. Overweg, Y. Lee, M. Eich, M.H. Liu, K. Watanabe, T. Taniguchi, T. Ihn, K. Ensslin, Nano Letters **18**(11), 6725 (2018)
134. S. Xu, A. Berdyugin, P. Kumaravadivel, F. Guinea, R. Krishna Kumar, D. Bandurin, S. Morozov, W. Kuang, B. Tsim, S. Liu, J. Edgar, I. Grigorieva, V. Fal'ko, M. Kim, A. Geim, Nature communications **10**, 4008 (2019)
135. J.S. Alden, A.W. Tsen, P.Y. Huang, R. Hovden, L. Brown, J. Park, D.A. Muller, P.L. McEuen, Proceedings of the National Academy of Sciences **110**(28), 11256 (2013)
136. P. San-Jose, R.V. Gorbachev, A.K. Geim, K.S. Novoselov, F. Guinea, Nano Letters **14**(4), 2052 (2014)
137. I. Martin, Y.M. Blanter, A.F. Morpurgo, Physical Review Letters **100**(3), 036804 (2008)
138. F. Zhang, A.H. MacDonald, E.J. Mele, Proceedings of the National Academy of Sciences **110**(26), 10546 (2013)
139. P. San-Jose, E. Prada, Physical Review B **88**(12), 121408 (2013)
140. Z. Qiao, J. Jung, Q. Niu, A.H. MacDonald, Nano Letters **11**(8), 3453 (2011)
141. A.R. Wright, T. Hyart, Applied Physics Letters **98**(25), 251902 (2011)
142. A. Vaezi, Y. Liang, D.H. Ngai, L. Yang, E.A. Kim, Physical Review X **3**(2), 021018 (2013)
143. R. Bistritzer, A.H. MacDonald, Proceedings of the National Academy of Sciences **108**(30), 12233 (2011)
144. H. Isobe, N.F. Yuan, L. Fu, Physical Review X **8**(4), 041041 (2018)
145. Y. Cao, V. Fatemi, A. Demir, S. Fang, S.L. Tomarken, J.Y. Luo, J.D. Sanchez-Yamagishi, K. Watanabe, T. Taniguchi, E. Kaxiras, R.C. Ashoori, P. Jarillo-Herrero, Nature **556**(7699), 80 (2018)
146. D. Wong, K.P. Nuckolls, M. Oh, B. Lian, Y. Xie, S. Jeon, K. Watanabe, T. Taniguchi, B.A. Bernevig, A. Yazdani, Nature **582**(7811), 198 (2020)
147. U. Zondiner, A. Rozen, D. Rodan-Legrain, Y. Cao, R. Queiroz, T. Taniguchi, K. Watanabe, Y. Oreg, F. von Oppen, A. Stern, E. Berg, P. Jarillo-Herrero, S. Ilani, Nature **582**(7811), 203 (2020)
148. M. Yankowitz, S. Chen, H. Polshyn, Y. Zhang, K. Watanabe, T. Taniguchi, D. Graf, A.F. Young, C.R. Dean, Science **363**(6431), 1059 (2019)
149. Y. Cao, V. Fatemi, S. Fang, K. Watanabe, T. Taniguchi, E. Kaxiras, P. Jarillo-Herrero, Nature **556**(7699), 43 (2018)
150. X. Lu, P. Stepanov, W. Yang, M. Xie, M.A. Aamir, I. Das, C. Urgell, K. Watanabe, T. Taniguchi, G. Zhang, A. Bachtold, A.H. MacDonald, D.K. Efetov, Nature **574**(7780), 653 (2019)
151. P. Stepanov, I. Das, X. Lu, A. Fahimniya, K. Watanabe, T. Taniguchi, F.H. Koppens, J. Lischner, L. Levitov, D.K. Efetov, Nature **583**(7816), 375 (2020)
152. I. Das, X. Lu, J. Herzog-Arbeitman, Z.D. Song, K. Watanabe, T. Taniguchi, B.A. Bernevig, D.K. Efetov, Nature Physics **17**(3), 710 (2021)

153. H.C. Po, L. Zou, A. Vishwanath, T. Senthil, Physical Review X **8**(3), 031089 (2018)
154. B. Padhi, C. Setty, P.W. Phillips, Nano letters **18**(10), 6175 (2018)
155. J.M. Pizarro, M. Calderón, E. Bascones, Journal of Physics Communications **3**(3), 035024 (2019)
156. H.B. Heersche, P. Jarillo-Herrero, J.B. Oostinga, L.M. Vandersypen, A.F. Morpurgo, Nature **446**(7131), 56 (2007)
157. X. Du, I. Skachko, E.Y. Andrei, Physical Review B **77**(18), 184507 (2008)
158. F. Miao, S. Wijeratne, Y. Zhang, U.C. Coskun, W. Bao, C.N. Lau, Science **317**(5844), 1530 (2007)
159. P. Rickhaus, R. Maurand, M.H. Liu, M. Weiss, K. Richter, C. Schönenberger, Nature communications **4**(2342) (2013)
160. L. Wang, I. Meric, P.Y. Huang, Q. Gao, Y. Gao, H. Tran, T. Taniguchi, K. Watanabe, L.M. Campos, D.A. Muller, J. Guo, P. Kim, J. Hone, K.L. Shepard, C.R. Dean, Science **342**(6158), 614 (2013)
161. K. Komatsu, C. Li, S. Autier-Laurent, H. Bouchiat, S. Guéron, Physical Review B **86**(11), 115412 (2012)
162. P. Rickhaus, M. Weiss, L. Marot, C. Schönenberger, Nano Letters **12**(4), 1942 (2012)
163. V.E. Calado, S. Goswami, G. Nanda, M. Diez, A.R. Akhmerov, K. Watanabe, T. Taniguchi, T.M. Klapwijk, L.M.K. Vandersypen, Nature Nanotechnology **10**(9), 761 (2015)
164. P. Kumaravadivel, X. Du, Scientific Reports **6**(24274) (2016)
165. C.W.J. Beenakker, Physical Review Letters **97**(6), 067007 (2006)
166. C.W.J. Beenakker, Reviews of Modern Physics **80**(4), 1337 (2008)
167. D.K. Efetov, L. Wang, C. Handschin, K.B. Efetov, J. Shuang, R. Cava, T. Taniguchi, K. Watanabe, J. Hone, C.R. Dean, P. Kim, Nature Physics **12**(4), 328 (2016)
168. C.W.J. Beenakker, Physical Review Letters **67**(27), 3836 (1991)
169. M. Ma, A.Y. Zyuzin, Europhysics Letters **21**(9), 941 (1993)
170. Y. Takagaki, Physical Review B **57**(7), 4009 (1998)
171. H. Hoppe, U. Zülicke, G. Schön, Physical Review Letters **84**(8), 1804 (2000)
172. Y. Asano, T. Kato, Journal of the Physical Society of Japan **69**(4), 1125 (2000)
173. U. Zülicke, H. Hoppe, G. Schön, Physica B: Condensed Matter **298**(1-4), 453 (2001)
174. R.S.K. Mong, D.J. Clarke, J. Alicea, N.H. Lindner, P. Fendley, C. Nayak, Y. Oreg, A. Stern, E. Berg, K. Shtengel, M.P.A. Fisher, Physical Review X **4**(1), 011036 (2014)
175. X.L. Qi, T.L. Hughes, S.C. Zhang, Physical Review B **82**(18), 184516 (2010)
176. H. Takayanagi, T. Akazaki, Physica B: Condensed Matter **249**, 462 (1998)
177. D. Uhlisch, S. Lachenmann, T. Schäpers, A. Braginski, H. Lüth, J. Appenzeller, A.A. Golubov, A. Ustinov, Physical Review B **61**(18), 12463 (2000)
178. T.D. Moore, D. Williams, Physical Review B **59**(11), 7308 (1999)
179. J. Eroms, D. Weiss, J. De Boeck, G. Borghs, U. Zülicke, Physical Review Lretters **95**(10), 107001 (2005)
180. I.E. Batov, T. Schäpers, N.M. Chtchelkatchev, H. Hardtdegen, A.V. Ustinov, Physical Review B **76**(11), 115313 (2007)
181. Z. Wan, A. Kazakov, M.J. Manfra, L.N. Pfeiffer, K.W. West, L.P. Rokhinson, Nature Communications **6**(7426) (2015)
182. F. Amet, C.T. Ke, I.V. Borzenets, J. Wang, K. Watanabe, T. Taniguchi, R.S. Deacon, M. Yamamoto, Y. Bomze, S. Tarucha, G. Finkelstein, Science **352**(6288), 966 (2016)
183. A. Seredinski, A.W. Draelos, E.G. Arnault, M.T. Wei, H. Li, T. Fleming, K. Watanabe, T. Taniguchi, F. Amet, G. Finkelstein, Science Advances **5**(9), eaaw8693 (2019)
184. G.H. Lee, K.F. Huang, D.K. Efetov, D.S. Wei, S. Hart, T. Taniguchi, K. Watanabe, A. Yacoby, P. Kim, Nature Physics **13**(7), 693 (2017)

185. M.R. Sahu, X. Liu, A.K. Paul, S. Das, P. Raychaudhuri, J.K. Jain, A. Das, Physical Review Letters **121**(8), 086809 (2018)
186. L. Zhao, E.G. Arnault, A. Bondarev, A. Seredinski, T.F.Q. Larson, A.W. Draelos, H. Li, K. Watanabe, T. Taniguchi, F. Amet, et al., Nature Physics **16**(8), 862 (2020)
187. G.H. Park, M. Kim, K. Watanabe, T. Taniguchi, H.J. Lee, Scientific Reports **7**(10953) (2017)
188. M.N. Wilson, *Superconducting magnets* (1983)
189. N. Balshaw, *Practical cryogenics. and introduction to laboratory cryogenics* (1996)
190. D.A. Abanin, A.V. Shytov, L.S. Levitov, B.I. Halperin, Physical Review B **79**(3), 035304 (2009)
191. J. Balakrishnan, G. Kok Wai Koon, M. Jaiswal, A. Castro Neto, B. Özyilmaz, Nature Physics **9**(5), 284 (2013)
192. J.M. Ziman, *Principles of the Theory of Solids* (Cambridge University Press, 1972)
193. M.I. Katsnelson, A.K. Geim, Philosophical Transactions of the Royal Society A: Mathematical, Physical and Engineering Sciences **366**(1863), 195 (2008)
194. R. Krishna Kumar, X. Chen, G.H. Auton, A. Mishchenko, D.A. Bandurin, S.V. Morozov, Y. Cao, E. Khestanova, M.B. Shalom, A.V. Kretinin, K.S. Novoselov, L. Eaves, I.V. Grigorieva, L.A. Ponomarenko, V.I. Fal'ko, A.K. Geim, Science **357**(6347), 181 (2017)
195. M. Octavio, M. Tinkham, G. Blonder, T. Klapwijk, Physical Review B **27**(11), 6739 (1983)
196. H.Y. Gunel, N. Borgwardt, I.E. Batov, H. Hardtdegen, K. Sladek, G. Panaitov, D. Grutzmacher, T. Schapers, Nano Letters **14**(9), 4977 (2014)
197. K. Flensberg, J.B. Hansen, M. Octavio, Physical Review B **38**(13), 8707 (1988)
198. A. Lodder, Y.V. Nazarov, Physical Review B **58**(9), 5783 (1998)
199. R. Dynes, T. Fulton, Physical Review B **3**(9), 3015 (1971)
200. S. Hart, H. Ren, T. Wagner, P. Leubner, M. Mühlbauer, C. Brüne, H. Buhmann, L.W. Molenkamp, A. Yacoby, Nature Physics **10**(9), 638 (2014)
201. C. Swenson, Physical Review **79**(4), 626 (1950)
202. W. Halperin, F.B. Rasmussen, C. Archie, R. Richardson, Journal of Low Temperature Physics **31**(5), 617 (1978)
203. F. Pobell, *Matter and Methods at Low Temperatures* (Springer, 2007)
204. W. Keesom, K. Clusius, Proceedings of the Koninklijke Akademie van Wetenschappen te Amsterdam **35**, 307 (1932)
205. P. Kapitza, Nature **141**(3558), 74 (1938)
206. J.F. Allen, A. Misener, Nature **141**(3558), 75 (1938)
207. J.F. Annett, et al., *Superconductivity, superfluids and condensates*, vol. 5 (Oxford University Press, 2004)
208. D.R. Tilley, J. Tilley, *Superfluidity and superconductivity* (Routledge, 2019)
209. I.M. Khalatnikov, *An introduction to the theory of superfluidity* (CRC Press, 2018)
210. J. Wilks, D.S. Betts, *An introduction to liquid helium.* (Clarendon Press, 1987)
211. J. Bardeen, G. Baym, D. Pines, Physical Review Letters **17**(7), 372 (1966)
212. J. Bardeen, G. Baym, D. Pines, Physical Review **156**(1), 207 (1967)
213. O.V. Lounasmaa, *Experimental principles and methods below 1K* (academic Press, 1974)
214. H. London, G. Clarke, E. Mendoza, Physical Review **128**(5), 1992 (1962)
215. P. Das, R. de Bruyn Ouboter, K. Taconis, in *Proceedings on the 9th International Conference on Low Temperature Physics* (Plenum Press London, 1965)
216. A. Jones, C. Scheller, J. Prance, Y. Kalyoncu, D. Zumbühl, R. Haley, Journal of Low Temperature Physics **201**, 772 (2020)
217. D. Edwards, E. Ifft, R. Sarwinski, Physical Review **177**(1), 380 (1969)

218. W.E. Gifford, R. Longsworth, Advances in Cryogenic Engineering **10**, 69 (1965)
219. E. Mikulin, A. Tarasov, M. Shkrebyonock, in *Advances in Cryogenic Engineering* (Springer, 1984), pp. 629–637
220. S. Zhu, P. Wu, Z. Chen, W. Zhu, Y. Zhou, Cryogenics **30**, 257 (1990)
221. Y. Matsubara, J. Gao, Cryogenics **34**(4), 259 (1994)
222. N. Jiang, U. Lindemann, F. Giebeler, G. Thummes, Cryogenics **44**(11), 809 (2004)
223. H.O.H. Churchill, Quantum dots in gated nanowires and nanotubes. Ph.D. thesis, Harvard University (2012)
224. D.I. Bradley, R.E. George, D. Gunnarsson, R.P. Haley, H. Heikkinen, Y.A. Pashkin, J. Penttilä, J.R. Prance, M. Prunnila, L. Roschier, M. Sarsby, Nature communications **7**(10455) (2016)
225. J.P. Pekola, K.P. Hirvi, J.P. Kauppinen, M.A. Paalanen, Physical Review Letters **73**(21), 2903 (1994)
226. S. Farhangfar, K.P. Hirvi, J.P. Kauppinen, J.P. Pekola, J.J. Toppari, D.V. Averin, A.N. Korotkov, Journal of Low Temperature Physics **108**(1), 191 (1997)
227. M.Y. Azbel, Soviet Physics, JETP **19**(3), 634 (1964)
228. E. Brown, Physical Review **133**(4A), A1038 (1964)
229. J. Zak, Physical Review **134**(6A), A1602 (1964)
230. G.H. Wannier, Physica Status Solidi (B) **88**(2), 757 (1978)
231. D.R. Hofstadter, Physical Review B **14**(6), 2239 (1976)
232. P. Streda, Journal of Physics C: Solid State Physics **15**(36), L1299 (1982)
233. J.W. Rhim, K. Park, Physical Review B **86**(23), 235411 (2012)
234. R. Rammal, Journal de Physique **46**(8), 1345 (1985)
235. P. Delplace, G. Montambaux, Physical Review B **82**, 035438 (2010)
236. X. Chen, J.R. Wallbank, A.A. Patel, M. Mucha-Kruczyński, E. McCann, V.I. Fal'ko, Physical Review B **89**(7), 075401 (2014)
237. D.J. Thouless, M. Kohmoto, M.P. Nightingale, M. den Nijs, Physical Review Letters **49**(6), 405 (1982)
238. R. Krishna Kumar, A. Mishchenko, X. Chen, S. Pezzini, G.H. Auton, L.A. Ponomarenko, U. Zeitler, L. Eaves, V.I. Fal'ko, A.K. Geim, Proceedings of the National Academy of Sciences **115**(20), 5135 (2018)
239. P.G. Harper, Proceedings of the Physical Society. Section A **68**(10), 874 (1955)
240. L. Wang, S. Zihlmann, M.H. Liu, P. Makk, K. Watanabe, T. Taniguchi, A. Baumgartner, C. Schönenberger, Nano letters **19**(4), 2371 (2019)
241. Z. Wang, Y.B. Wang, J. Yin, E. Tóvári, Y. Yang, L. Lin, M. Holwill, J. Birkbeck, D.J. Perello, S. Xu, J. Zultak, R.V. Gorbachev, A.V. Kretinin, T. Taniguchi, K. Watanabe, S.V. Morozov, M. ANDELKOVIC, S.P. MILOVANOVIC, L. Covaci, F.M. Peeters, A. Mishchenko, A.K. Geim, K.S. Novoselov, V.I. Fal'ko, A. Knothe, C.R. Woods, Science Advances **5**(12), eaay8897 (2019)
242. N.R. Finney, M. Yankowitz, L. Muraleetharan, K. Watanabe, T. Taniguchi, C.R. Dean, J. Hone, Nature Nanotechnology **14**(11), 1029 (2019)
243. M. Lee, J.R. Wallbank, P. Gallagher, K. Watanabe, T. Taniguchi, V.I. Fal'ko, D. Goldhaber-Gordon, Science **353**(6307), 1526 (2016)
244. A.I. Berdyugin, B. Tsim, P. Kumaravadivel, S.G. Xu, A. Ceferino, A. Knothe, R. Krishna Kumar, T. Taniguchi, K. Watanabe, A. Geim, I.V. Grigorieva, V.I. Fal'ko, Science Advances **6**(16), eaay7838 (2020)
245. M. Büttiker, Physical Review B **38**(17), 12724 (1988)
246. J.R. Wallbank, R. Krishna Kumar, M. Holwill, Z. Wang, G.H. Auton, J. Birkbeck, A. Mishchenko, L.A. Ponomarenko, K. Watanabe, T. Taniguchi, K.S. Novoselopv, I.L. Aleiner, A.K. Geim, V.I. Fal'ko, Nature Physics **15**(1), 32 (2019)

247. M. Kim, S.G. Xu, A.I. Berdyugin, A. Principi, S. Slizovskiy, N. Xin, P. Kumaravadivel, W. Kuang, M. Hamer, R. Krishna Kumar, , R.V. Gorbachev, K. Watanabe, T. Taniguchi, I.V. Grigorieva, V.I. Fal'ko, M. Polini, A.K. Geim, Nature communications **11**(2339) (2020)
248. Y. Saito, J. Ge, L. Rademaker, K. Watanabe, T. Taniguchi, D.A. Abanin, A.F. Young, Nature Physics **17**(4), 478 (2021)
249. T. Fabian, M. Kausel, L. Linhart, J. Burgdörfer, F. Libisch, Physical Review B **106**(16), 165412 (2022)
250. A.M. DaSilva, J. Jung, A.H. MacDonald, Physical Review Letters **117**(3), 036802 (2016)
251. Z. Chen, J. Appenzeller, in *2008 IEEE International Electron Devices Meeting* (IEEE, 2008)
252. G.L. Yu, R. Jalil, B. Belle, A.S. Mayorov, P. Blake, F. Schedin, S.V. Morozov, L.A. Ponomarenko, F. Chiappini, S. Wiedmann, U. Zeitler, M.I. Katsnelson, A.K. Geim, K.S. Novoselov, D.C. Elias, Proceedings of the National Academy of Sciences **110**(9), 3282 (2013)
253. C. Chamon, R. Jackiw, Y. Nishida, S.Y. Pi, L. Santos, Physical Review B **81**(22), 224515 (2010)
254. I. Khaymovich, N. Chtchelkatchev, I. Shereshevskii, A. Mel'nikov, Europhysics Letters **91**(1), 17005 (2010)
255. R.P. Tiwari, U. Zülicke, C. Bruder, Physical Review Letters **110**(18), 186805 (2013)
256. O. Gamayun, J.A. Hutasoit, V.V. Cheianov, Physical Review B **96**(24), 241104 (2017)
257. M.P. Fisher, Physical Review B **49**(20), 14550 (1994)
258. Y. Asano, T. Yuito, Physical Review B **62**(11), 7477 (2000)
259. N. Chtchelkatchev, Journal of Experimental and Theoretical Physics Letters **73**(2), 94 (2001)
260. N.M. Chtchelkatchev, I.S. Burmistrov, Physical Review B **75**(21), 214510 (2007)
261. Y. Alavirad, J. Lee, Z.X. Lin, J.D. Sau, Physical Review B **98**(21), 214504 (2018)
262. I. Knez, R.R. Du, G. Sullivan, Physical Review Letters **109**(18), 186603 (2012)
263. J. Wiedenmann, E. Bocquillon, R.S. Deacon, S. Hartinger, O. Herrmann, T.M. Klapwijk, L. Maier, C. Ames, C. Brüne, C. Gould, A. Oiwa, K. Ishibashi, S. Tarucha, H. Buhmann, L.W. Molenkamp, Nature Communications **7**(10303) (2016)
264. E. Bocquillon, R.S. Deacon, J. Wiedenmann, P. Leubner, T.M. Klapwijk, C. Brüne, K. Ishibashi, H. Buhmann, L.W. Molenkamp, Nature Nanotechnology **12**(2), 137 (2017)
265. D.K. Efimkin, A.H. MacDonald, Physical Review B **98**(3), 035404 (2018)
266. A. Ramires, J.L. Lado, Physical Review Letters **121**(14), 146801 (2018)
267. X.C. Wu, C.M. Jian, C. Xu, Physical Review B **99**(16), 161405 (2019)
268. L.J. Yin, H. Jiang, J.B. Qiao, L. He, Nature Communications **7**(11760) (2016)
269. C. Chen, A.C. Neto, V.M. Pereira, Physical Review B **101**(16), 165431 (2020)
270. A.R. Akhmerov, C.W.J. Beenakker, Physical Review Letters **98**(15), 157003 (2007)
271. M.T. Wei, A.W. Draelos, A. Seredinski, C.T. Ke, H. Li, Y. Mehta, K. Watanabe, T. Taniguchi, M. Yamamoto, S. Tarucha, G. Finkelstein, F. Amet, I.V. Borzenets, Physical Review B **100**(12), 121403 (2019)
272. N.C.H. Hesp, I. Torre, D. Barcons-Ruiz, H.H. Sheinfux, K. Watanabe, T. Taniguchi, R.K. Kumar, F.H.L. Koppens, Nature Communications **12**(1640) (2021)
273. J.R. Williams, D.A. Abanin, L. DiCarlo, L.S. Levitov, C.M. Marcus, Physical Review B **80**(4), 045408 (2009)
274. D.I. Indolese, P. Karnatak, A. Kononov, R. Delagrange, R. Haller, L. Wang, P. Makk, K. Watanabe, T. Taniguchi, C. Schonenberger, Nano Letters **20**(10), 7129 (2020)

275. P. San-Jose, E. Prada, R. Aguado, Physical Review Letters **108**(25), 257001 (2012)
276. M. Rzchowski, S. Benz, M. Tinkham, C. Lobb, Physical Review B **42**(4), 2041 (1990)
277. J.D. Sau, R.M. Lutchyn, S. Tewari, S.D. Sarma, Physical Review Letters **104**(4), 040502 (2010)
278. G. Chaudhary, A.H. MacDonald, Physical Review B **101**(2), 024516 (2020)
279. A.A. Golubov, M.Y. Kupriyanov, E. Il'Ichev, Reviews of Modern Physics **76**(2), 411 (2004)
280. I.V. Borzenets, F. Amet, C.T. Ke, A.W. Draelos, M.T. Wei, A. Seredinski, K. Watanabe, T. Taniguchi, Y. Bomze, M. Yamamoto, S. Tarucha, G. Finkelstein, Physical Review Letters **117**, 237002 (2016)
281. C. Beenakker, in *Transport Phenomena in Mesoscopic Systems* (Springer, 1992), pp. 235–253
282. E.M. Spanton, M. Deng, S. Vaitiekėnas, P. Krogstrup, J. Nygård, C.M. Marcus, K.A. Moler, Nature Physics **13**(12), 1177 (2017)
283. L. Fu, C.L. Kane, Physical Review Letters **100**(9), 096407 (2008)
284. Y. Park, B.L. Chittari, J. Jung, Physical Review B **102**(3), 035411 (2020)
285. L. Rademaker, I.V. Protopopov, D.A. Abanin, Physical Review Research **2**(3), 033150 (2020)
286. Z. Ma, S. Li, Y.W. Zheng, M.M. Xiao, H. Jiang, J.H. Gao, X.C. Xie, Science Bulletin **66**(1), 18 (2021)
287. H. Polshyn, Y. Zhang, M.A. Kumar, T. Soejima, P. Ledwith, K. Watanabe, T. Taniguchi, A. Vishwanath, M.P. Zaletel, A.F. Young, Nature Physics **18**(1), 42 (2022)
288. H. Polshyn, J. Zhu, M. Kumar, Y. Zhang, F. Yang, C. Tschirhart, M. Serlin, K. Watanabe, T. Taniguchi, A. MacDonald, A.F. Young, Nature **588**(7836), 66 (2020)
289. S. Chen, M. He, Y.H. Zhang, V. Hsieh, Z. Fei, K. Watanabe, T. Taniguchi, D.H. Cobden, X. Xu, C.R. Dean, M. Yankowitz, Nature Physics **17**(3), 374 (2021)
290. M. He, Y.H. Zhang, Y. Li, Z. Fei, K. Watanabe, T. Taniguchi, X. Xu, M. Yankowitz, Nature Communications **12**(4727) (2021)
291. E.S. Morell, M. Pacheco, L. Chico, L. Brey, Physical Review B **87**(12), 125414 (2013)
292. G.W. Burg, J. Zhu, T. Taniguchi, K. Watanabe, A.H. MacDonald, E. Tutuc, Physical review letters **123**(19), 197702 (2019)
293. Y. Cao, D. Rodan-Legrain, O. Rubies-Bigorda, J.M. Park, K. Watanabe, T. Taniguchi, P. Jarillo-Herrero, Nature **583**(7815), 215 (2020)
294. X. Liu, Z. Hao, E. Khalaf, J.Y. Lee, Y. Ronen, H. Yoo, D.H. Najafabadi, K. Watanabe, T. Taniguchi, A. Vishwanath, P. Kim, Nature **583**(7815), 221 (2020)
295. C. Shen, Y. Chu, Q. Wu, N. Li, S. Wang, Y. Zhao, J. Tang, J. Liu, J. Tian, K. Watanabe, T. Taniguchi, R. Yang, Z. Yang Meng, D. Shi, O.V. Yazyev, G. Zhang, Nature Physics **16**(5), 520 (2020)
296. M. He, Y. Li, J. Cai, Y. Liu, K. Watanabe, T. Taniguchi, X. Xu, M. Yankowitz, Nature Physics **17**(1), 26 (2021)
297. A. Rozen, J.M. Park, U. Zondiner, Y. Cao, D. Rodan-Legrain, T. Taniguchi, K. Watanabe, Y. Oreg, A. Stern, E. Berg, P. Jarillo-Herrero, S. Ilani, Nature **592**(7853), 214 (2021)
298. Y. Saito, F. Yang, J. Ge, X. Liu, T. Taniguchi, K. Watanabe, J. Li, E. Berg, A.F. Young, Nature **592**(7853), 220 (2021)
299. T. Giamarchi, Physical Review B **44**(7), 2905 (1991)
300. L. Fritz, J. Schmalian, M. Müller, S. Sachdev, Physical Review B **78**(8), 085416 (2008)
301. J. Crossno, J.K. Shi, K. Wang, X. Liu, A. Harzheim, A. Lucas, S. Sachdev, P. Kim, T. Taniguchi, K. Watanabe, T.A. Ohki, K.C. Fong, Science **351**(6277), 1058 (2016)

302. P. Gallagher, C.S. Yang, T. Lyu, F. Tian, R. Kou, H. Zhang, K. Watanabe, T. Taniguchi, F. Wang, Science **364**(6436), 158 (2019)
303. I. Meric, M.Y. Han, A.F. Young, B. Ozyilmaz, P. Kim, K.L. Shepard, Nature Nanotechnology **3**(11), 654 (2008)
304. M.A. Yamoah, W. Yang, E. Pop, D. Goldhaber-Gordon, ACS Nano **11**(10), 9914 (2017)
305. N. Vandecasteele, A. Barreiro, M. Lazzeri, A. Bachtold, F. Mauri, Physical Review B **82**(4), 045416 (2010)
306. F. Xie, Z. Song, B. Lian, B.A. Bernevig, Physical Review Letters **124**(16), 167002 (2020)
307. H. Tian, S. Che, T. Xu, P. Cheung, K. Watanabe, T. Taniguchi, M. Randeria, F. Zhang, C.N. Lau, M.W. Bockrath, arXiv preprint at arXiv:2112.13401 (2021)
308. R.V. Gorbachev, A.K. Geim, M.I. Katsnelson, K.S. Novoselov, T. Tudorovskiy, I.V. Grigorieva, A.H. MacDonald, S.V. Morozov, K. Watanabe, T. Taniguchi, L.A. Ponomarenko, Nature Physics **8**(12), 896 (2012)
309. M.T. Greenaway, E.E. Vdovin, A. Mishchenko, O. Makarovsky, A. Patanè, J.R. Wallbank, Y. Cao, A.V. Kretinin, M.J. Zhu, S.V. Morozov, V.I. Fal'ko, K.S. Novoselov, A.K. Geim, T.M. Fromhold, L. Eaves, Nature Physics **11**(12), 1057 (2015)
310. X. Liu, Z. Wang, K. Watanabe, T. Taniguchi, O. Vafek, J.I.A. Li, Science **371**(6535), 1261 (2021)
311. A. Luican, G. Li, A. Reina, J. Kong, R.R. Nair, K.S. Novoselov, A.K. Geim, E.Y. Andrei, Physical Review Letters **106**(12), 126802 (2011)
312. J.D. Sanchez-Yamagishi, T. Taychatanapat, K. Watanabe, T. Taniguchi, A. Yacoby, P. Jarillo-Herrero, Physical Review Letters **108**(7), 076601 (2012)
313. J.D. Sanchez-Yamagishi, J.Y. Luo, A.F. Young, B.M. Hunt, K. Watanabe, T. Taniguchi, R.C. Ashoori, P. Jarillo-Herrero, Nature Nanotechnology **12**(2), 118 (2017)
314. P. Rickhaus, G. Zheng, J.L. Lado, Y. Lee, A. Kurzmann, M. Eich, R. Pisoni, C. Tong, R. Garreis, C. Gold, M. Masseroni, T. Taniguchi, K. Watanabe, T. Ihn, K. Ensslin, Nano Letters **19**(12), 8821 (2019)
315. P. Rickhaus, M.H. Liu, M. Kurpas, A. Kurzmann, Y. Lee, H. Overweg, M. Eich, R. Pisoni, T. Taniguchi, K. Watanabe, et al., Science advances **6**(11), eaay8409 (2020)
316. P. Rickhaus, F.K. de Vries, J. Zhu, E. Portoles, G. Zheng, M. Masseroni, A. Kurzmann, T. Taniguchi, K. Watanabe, A.H. MacDonald, T. Ihn, K. Ensslin, Science **373**(6560), 1257 (2021)
317. S. Slizovskiy, A. Garcia-Ruiz, A.I. Berdyugin, N. Xin, T. Taniguchi, K. Watanabe, A.K. Geim, N.D. Drummond, V.I. Fal'ko, Nano Letters **21**(15), 6678 (2021)
318. T. Cea, N.R. Walet, F. Guinea, Nano Letters **19**(12), 8683 (2019)
319. J.M. Park, Y. Cao, L. Xia, S. Sun, K. Watanabe, T. Taniguchi, P. Jarillo-Herrero, Nature Materials **21**(7), 877 (2022)
320. G.W. Burg, E. Khalaf, Y. Wang, K. Watanabe, T. Taniguchi, E. Tutuc, Nature Materials **21**(7), 884 (2022)
321. Y. Saito, J. Ge, K. Watanabe, T. Taniguchi, A.F. Young, Nature Physics **16**(9), 926 (2020)
322. Y. Nishida, H. Abuki, Physical Review D **72**(9), 096004 (2005)